A PRECISION OPTICAL TRAPPING ASSAY: MEASURING THE CONFORMATIONAL DYNAMICS OF SINGLE E. COLI RECBCD HELICASES

by

Ashley R. Carter

B.S. & B.S.E., University of Michigan, 2002

M.S., University of Colorado, 2007

A thesis submitted to the

Faculty of the Graduate School of the

University of Colorado in partial fulfillment

of the requirements for the degree of

Doctor of Philosophy

Department of Physics

2008

This thesis entitled:
A PRECISION OPTICAL TRAPPING ASSAY: MEASURING THE CONFORMATIONAL DYNAMICS OF SINGLE E. COLI RECBCD HELICASES
written by Ashley R. Carter
has been approved for the Department of Physics

Thomas Perkins, Department of Molecular, Cellular, and Developmental Biology and Department of Physics (Lecturer)

Konrad Lehnert, Department of Physics

Date

The final copy of this thesis has been examined by the signatories, and we find that both the content and the form meet acceptable presentation standards of scholarly work in the above mentioned discipline.

Carter, Ashley R. (Ph.D., Physics)

A PRECISION OPTICAL TRAPPING ASSAY: MEASURING THE CONFORMATIONAL DYNAMICS OF SINGLE E. COLI RECBCD HELICASES

Thesis directed by Professor Thomas Perkins, Department of Molecular, Cellular, and Developmental Biology and Department of Physics (Lecturer)

Helicases are enzymes that unwind double-stranded nucleic acids [e.g., deoxyribonucleic acid (DNA)]. Unwinding occurs by converting chemical energy [e.g., adenosine triphosphate (ATP) hydrolysis] into a translocation-induced unwinding event, although the exact mechanism of how ATP is coupled to unwinding along DNA is unknown. The first step in understanding this mechanism is to determine the step size of movement. Structural data suggests that the mechanical step size of unwinding is one base-pair (bp) for each ATP molecule hydrolyzed, while biochemical data suggests that the rate-limited kinetic step size for unwinding is multiple base-pairs ($\sim$4 bp). To address this question, we directly measured the translocation step size of a helicase, the E. coli RecBCD helicase, using a single molecule assay. Previous single-molecule measurements of RecBCD failed to resolve steps due to limited resolution ($\sim$6 bp). We increased resolution to 1 bp in a precision optical trapping assay by actively stabilizing the microscope and reducing multiple types of trap laser noise. With this precision assay, we observed both forwards and backwards steps that were variable in size and had an average step size of 4.4 bp. The variability and multiple base-pair step size are in part due to ATP-independent, $\pm$3 bp conformational dynamics in the RecBCD-DNA complex. Thus, our results support a mechanism in which the RecBCD helicase has a variable step size; the average of which quantitatively agrees with the previously determined kinetic step size.

Dedication

I would like to dedicate this thesis to my husband Greg. Only he knows the blood, sweat, and tears that have gone into this colossal undertaking.

Acknowledgements

This work was supported by an Optical Science and Engineering Program Fellowship (a part of the National Science Foundation Interdisciplinary Graduate Education Research Traineeship), a National Physical Science Consortium Fellowship, a Physik Instrumente NanoInnovation Grant, the National Science Foundation (Phy-0404286 and Phy-1551010), a Burrows Wellcome Fund Career Award in the Biomedical Sciences (TTP), a W.M. Keck Initiative in the RNA Sciences, and NIST.

I would like to acknowledge several parties for their support in building the instruments. Gavin King was the chief designer and builder of the AFM experiment and was crucial in the building of the back-scattered detection experiment. In addition, Allison Churnside worked extensively on the AFM FPGA control electronics. Early design and building of the optical tweezers instrument was carried out by Lora Nugent-Glandorf and Amanda Carpenter. Design of the photodiode and servo electronics circuits was the work of Jan Hall and Terry Brown. Carl Sauer designed and built custom electronics for detection by the quadrant photodiodes, servo systems for maintaining laser intensity, anti-aliasing filters, break-out boxes for voltage signals, and offset amplifiers. Mike Whitmore built custom electronics for laser diode temperature and current controllers. Dave Tegart built our power supply bin. James Fung-A-Fat and Paul Beckingham provided advice on filtering and detection of electronic signals. Blaine Horner, Kim Hagen, and Tracy Keep were responsible for building custom microscope parts and Hans Green machined our very intricate optical tweezers detection

arm and AFM assembly. Alan Patee and Gavin King did an excellent job designing the AFM assembly.

I would like to thank several people for support in nanofabrication of the fiducial marks. Early nanofabrication advice was given by Dan Schmidt and David Alchenberger. In addition, Theresa Ulrich and Wayne Halsey were responsible for patterning holes on microscope cover glass and were aided by Amanda Carpenter. David Alchenberger was responsible for early fabrication of low-index glass posts, while Gavin King helped determine protocols for fabricating low-index glass posts and was chiefly responsible for fabricating silicon disks with a shadow mask. Hern Paik aided shadow mask development. Yeonee Seol helped make a repository of silicon disk slides.

I would like to acknowledge several people for their help in software design. Allison Churnside designed software for FPGA control and AFM imaging along with Louisa Eberle. Gavin King helped write the AFM software, as well as software for stabilizing the sample using back-scattered detection. Yeonee Seol, Amanda Carpenter, and Lora Glandorf helped design many of the optical tweezers calibration programs. Specific thanks to Yeonee Seol for the DNA hairpin experiment software and Amanda Carpenter for the PZT mirror calibration software.

There are many people that helped with the biological assays. Martha Hosotani helped perform all of the RecBCD assays and was instrumental in running the experiment. RecBCD assays on chi sites were aided by Jessica Rouge. Wayne Halsey prepared all of the DNA and gave advice on assay preparation. Yeonee Seol prepared the DNA hairpin assay. Hung-Wen Li and Hsiu-Fang Fan purified the biotinylated RecBCD enzyme. Lora Nugent-Glandorf, Yeonee Seol, Amanda Carpenter, Martha Hosotani, Justin Kuczynski, and Theresa Ulrich helped to make buffers and reagents, determine lab protocols on surface preparation, bead preparation, bead-DNA binding, and other assay preparations.

I would like to thank several people for their efforts on analyzing the experi-

mental data. Many thanks go to Marileen Dogterom, Koen Visscher, and Ben Kalafut for providing step finding algorithms. In addition, Martha Hosotani was very helpful in analyzing the RecBCD data, and Betsy Siewert aided in providing early programs to analyze DNA elasticity and length data. Andy Leifer was also helpful in programming a scaled power spectral density function. Thanks also go to the computing staff, especially James Raith and Mike Paige for keeping my computer running and Jim McKown and Peter Ruprecht for maintaining perknas.

I would like to thank my committee members: Konrad Lehnert, Henry Kapteyn, Margaret Murnane, and Art Pardi for reading my thesis and guiding my graduate career. I would also like to thank other mentors who guided my research or advised me: Meredith Betterton, David Wilson, Peter Rosenthal, Jeff Orszak, Dana Anderson, Myron Campbell, Young-Kee Kim, Hung-Wen Li, Keith Schwab, and Mark Manheimer.

I would like to also thank my friends and family for encouragement over the years: Lily, Nikita, Dad, Mom, Nic, Bub, Ryan, Marme, Papaw, Grandma, Grandpa, Mum, Pop, Susan, Jimbag, Mike H., Betty, Jessica, Owen, Evan, Bill, Patricia, Meredith, Mike P., Laura, Mark, Emily, Kevin, Amanda, Marty, Martha, Allison, Keith, Juan, Kirk, Carl, Christine, Ariel, Allison, Hern, Justin, Yeonee, Wayne, Lora, Gavin, Andy, Julie, Vasilly, Stephanie, Adam, Jen, Janet, and of course my husband Greg.

Finally, I would like to thank the most important person in my graduate career, my advisor Thomas Perkins. If I were to mention everything that he has done it would probably fill my entire thesis. He has been involved in the conception, funding, instrumental design and building, software design, biological assay development, data taking, analysis, and publication for all of my experimental results. He has mentored me through six years of graduate school with Tuesday night experimental sessions, dinners at the Sunflower and the Med, beer at the Sink and Catacombs, Biophysical Society Annual Meetings, and countless hours spent rewriting all of my manuscripts. I am grateful for his support, friendship, and understanding. Thank you Tom.

Contents

Chapter

Figures

Figure

Chapter 1

Introduction

Helicases are ubiquitous enzymes that are present in almost every cellular process involving nucleic acids, either DNA (deoxyribonucleic acid) or RNA (ribonucleic acid) [65, 93, 111]. As an initial step in nucleic acid metabolism, helicases must unwind double-stranded nucleic acids into their constituent single strands by translocating along the nucleic acid template and disrupting the bonds between the two strands. Helicase research has focused on answering the basic scientific question of how these enzymes are able to convert chemical energy into the mechanical work of movement and strand separation [65, 66, 93, 111]. This is often difficult due to the exquisitely small movements of helicases, Ångstroms to nanometers [3, 19, 24, 28, 30, 61, 68, 67, 83, 109, 125, 142], and the monumental task of synchronizing an ensemble of helicases to measure the time-dependent process of chemical energy conversion to movement [12]. With the advent of single-molecule studies in the last fifteen years, the dynamics of unwinding can be tracked in individual helicase molecules [19, 28, 83], removing the need for synchronicity. Plus, in the last three years, the tracking of single molecules has reached the Ångstrom-scale [1, 76, 83], making it the right time to answer this basic scientific question. Our research focuses on directly measuring the unwinding of DNA by the RecBCD helicase found in *E. coli* using a precision optical trapping assay. These measurements offer insight into the mechanism of helicase unwinding and shed light on the first steps of many DNA processes.

While the double helix structure of DNA allows for stable packaging of the genome, this double helix must be unwound into its two complementary strands for any DNA metabolism to occur [65, 93, 111]. DNA structure has four bases (cytosine, C; guanine, G; adenine, A; and thymine, T) that are linked into strands via a backbone of alternating deoxyribose sugars and phosphate groups (Fig. 1.1). This backbone is antisymmetric such that the 3' end of DNA has a terminal hydroxyl group from a deoxyribose sugar ring while the 5' end terminates with a phosphate group. The strands are joined through multiple hydrogen bonds in Watson-Crick, complementary base-pairs (A with T, 2 hydrogen bonds; G with C, 3 hydrogen bonds) to form the double helix. The sequence of bases forms a genetic "code" that gives instructions on how to build proteins. The code is "read" when (*i*) DNA is copied into RNA in transcription and (*ii*) the RNA is translated into a sequence of amino acids, the building blocks of proteins, during translation. To pass along the genetic code, DNA undergoes replication, where the double-stranded DNA molecule is copied to form two double-stranded molecules. Processing also occurs during repair or in recombination, a pathway that allows for the breakage and rejoining of two double-stranded DNA molecules such that genetic information can be swapped or double-stranded breaks can be repaired. During all of these processes the double helix of DNA must be unwound to expose the underlying bases.

Helicases are enzymes that unwind either DNA or RNA by translocating along the nucleic acid and disrupting the hydrogen-bonding of the base-pairs [41, 65, 66, 93, 111]; as such, helicases are employed in almost every process in the cell that involves nucleic acids, from transcription and translation to DNA recombination [65]. This highly diverse functionality leads to a number of mechanistic and structural differences between helicases. Helicases bind to various substrates (single- or double-stranded, RNA or DNA), move along the nucleic acid in different directions (3' to 5' or 5' to 3'), and belong to one of six structural super families (SF1-SF6) [38, 111]. SF1 and SF2 helicases are structurally similar and contain two "RecA-like" folds, while SF3-SF6 helicases are

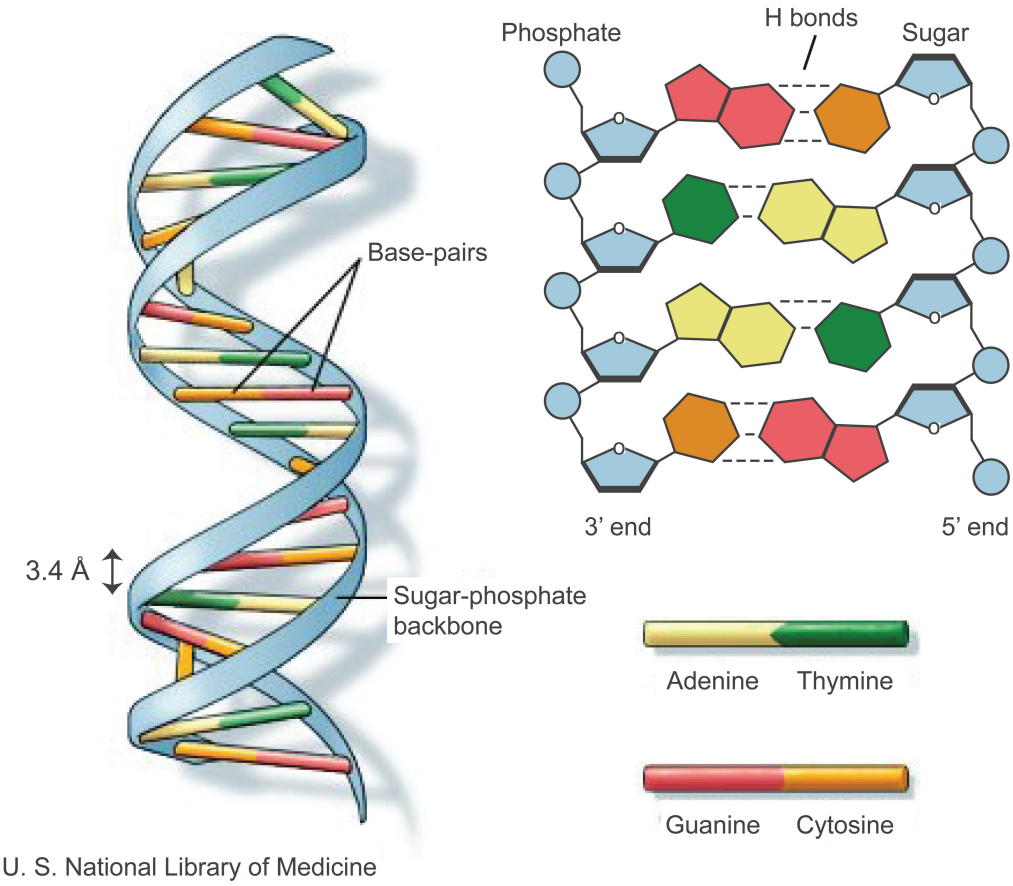

Figure 1.1: DNA structure. Two DNA strands are twisted together to form a double helix. Each strand contains nitrogenous bases and a backbone of repeating sugar and phosphate groups. Strands are held together through weak hydrogen bonding of the bases that must be disrupted for unwinding to occur. Figure credit: adapted from the U. S. National Library of Medicine.

composed of six "RecA-" or "AAA$^+$-like" folds that form a hexameric ring. Additionally, within each super family there are further structural motifs that subdivide them. However, in all cases helicases are motor proteins that convert chemical energy from the hydrolysis of a nucleoside triphosphate, generally adenine triphosphate (ATP), into mechanical work, which both translocates the helicase and unwinds the nucleic acid duplex. This leads to several structural similarities among the super families, termed core domains [111]. These core domains consist of a pocket for the binding and hydrolysis of the nucleoside triphosphate and an "arginine finger" for coupling of chemical energy into a physical conformational movement of the enzyme. The differences between helicases support the diverse functionality needed for nucleic acid metabolism, while the helicase similarities allow for the coupling of chemical energy into the unwinding of the nucleic acid duplex.

An important and basic question in helicase research is how helicases convert chemical energy from ATP hydrolysis into a translocation along the nucleic acid [65, 66, 93, 111]. Since we are interested in this question as it applies to the SF1 helicase, RecBCD, we will focus on SF1 or SF2 helicases moving along DNA. Previously, x-ray crystallography has been used to observe helicase-DNA complexes in different stages of ATP hydrolysis. In this way these structural studies have postulated a 1 base-pair (bp, 3.4 Å) movement of the helicase along the DNA given the hydrolysis of one ATP molecule [13, 61, 125, 141]. This movement per ATP is the mechanical step size. Additionally, biochemical assays have been used to measure the kinetically rate-limited translocation step by synchronizing an ensemble of helicase molecules moving along DNA. This rate-limited translocation is the kinetic step size. Under conditions where ATP is rate-limiting one would expect that the rate-limited translocation and the translocation per ATP would be the same; that is to say the kinetic step size would equal the mechanical step size of 1 bp. However, measurements of the kinetic step size in these conditions have yielded multiple base-pair steps, typically $\sim$4 bp [24, 28, 68, 67, 124].

Thus, there is a conundrum in the field as to why the ATP-limited kinetic step size does not correspond to the mechanical step size.

Currently, there are two leading models to explain the observed data [66]: the inchworm model [124] and the Brownian ratchet model [62]. In the inchworm model, there are multiple ATP hydrolysis events that rapidly occur before a slower, rate-limited process moves the helicase by the same multiple of base-pairs, allowing for a mechanical step size of 1 bp and a multiple base-pair kinetic step size. The model is termed inchworm because it assumes that the rapid ATP hydrolysis events move one section of the helicase along the DNA by 1 bp until the tension in the helicase allows for a large conformational change that moves the rest of the molecule. There is some evidence for this model. The SF1 helicase, UvrD, has a kinetic step size of 4 bp with 4 ATP hydrolysis events per step [124], and the SF2 helicase, NS3, has a 3 bp rate-limited translocation step with 3 faster kinetic steps per rate-limited step [83]. In the other leading model, the Brownian ratchet model, the helicase weakly binds the DNA when bound to ATP and moves forward when thermal fluctuations disrupt the hydrogen bonds between the DNA bases. Once forward, ATP is hydrolyzed and the helicase tightly binds the DNA preventing the rebonding of the bases. In this model the energy from ATP hydrolysis and the thermal bath are used to affect movement, allowing for a multiple base-pair kinetic step size. This model was proposed after the SF2 helicase, NS3h, was shown to unwind several base-pairs without ATP [62]. While other models are conceivable to explain the observations, these two models are the most popular.

All of the models that explain helicase unwinding can be classified as either active or passive [66]. Generally, one might think that an active helicase is an enzyme that uses ATP, while a passive helicase does not require an energy source, but since all helicases require a nucleoside triphosphate for unwinding to occur, active and passive have taken on different meanings. An active helicase uses a mechanism to actively melt the bonds between base-pairs while a passive helicase is an enzyme that waits for

thermal fluctuations to open the bonds (Fig. 1.2). In this terminology, the inchworm model is an example of an active helicase model, and the Brownian ratchet model is an example of a passive helicase model.

Our goal was to measure DNA unwinding by a particular helicase, RecBCD, and determine which model, if any, best describe RecBCD unwinding. More specifically, we measured the translocation step at rate-limiting ATP concentrations using a single-molecule technique [15]. By observing translocation at rate-limiting ATP we hoped to confirm or refute previous data showing multiple base-pair steps. By using a single-molecule technique we could directly measure RecBCD movement without synchronizing an ensemble of helicases and without measuring an average translocation. Both the previous structural and biochemical studies measure an ensemble of molecules and are limited to an average measurement. Averages in populations are sometimes misleading because they smear out dynamic fluctuations, obscure multimodal behavior, and mask rare but interesting events [12]. A direct measurement of RecBCD motion revealed the actual kinetic step size and suggested a model to reconcile the structurally determined mechanical step size with biochemical measurements.

In addition, measurements of RecBCD gave us insight into how a complex protein processes DNA. RecBCD is a multifunctional enzyme in *E. coli* responsible for both excising foreign DNA and repairing double-stranded DNA breaks through the DNA recombination pathway [56, 59, 112]. When RecBCD binds blunt end DNA, it uses its helicase function to unwind the DNA while digesting the double-strands with a nuclease until it recognizes a specific sequence only present in *E. coli* DNA, the chi site (Fig. 1.3 **A**). During chi site recognition the enzyme pauses [114], then after chi recognition it switches tasks from that of foreign DNA excision to DNA repair. The helicase slows down, the nuclease cleaves only one strand, and the enzyme begins to load the protein RecA to form a filament that is targeted for DNA recombination [110, 114]. This complex function leads to a complex structure (Fig. 1.3 **B**). RecBCD is a heterotrimer

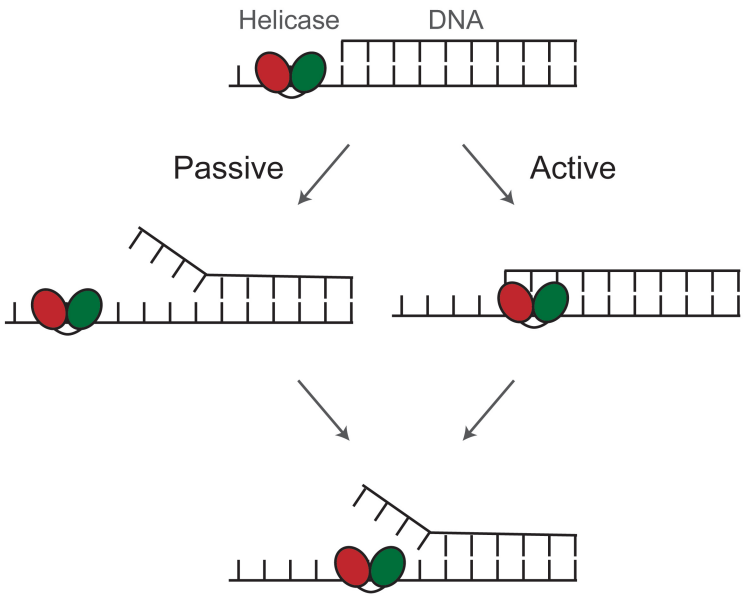

Figure 1.2: Models of DNA unwinding. In an active unwinding model the helicase opens the DNA bonds, while in a passive unwinding model thermal energy disrupts bonding between the two strands.

with two motor domains, RecB and RecD, that translocate along opposite polarity DNA strands and are each SF1 helicases [110]. Unlike other motor protein domains which generally work together to move the enzyme, RecB and RecD are decoupled from one another and move at different rates [25, 26, 122]. Before chi recognition RecD is faster, and thus the lead helicase, whereas after chi recognition RecB is faster [122]. The RecC subunit is intimately coupled to RecB and contains the domain for chi recognition along with a "pin" structure that contacts the double-stranded DNA [110]. The nuclease domain is found in the RecB subunit [110]. This complex structure allows for one of the highest unwinding rates, 1 kbp/s, and processivities (number of base-pairs unwound in a single binding event), 36–48 kbp, though the reason for both are unknown [66]. Future direct measurements of RecBCD movement may elucidate this functional behavior of the enzyme.

To directly measure single-molecule RecBCD motion, we used a precision optical trapping assay (Fig. 1.4) [18]. Previous measurements of individual RecBCD molecules using optical trapping techniques were limited by a 20-Å resolution [96]. In the previous experiment, a DNA molecule ($\sim$2.4 μm) was stretched between two points: a RecBCD helicase biochemically linked to the surface and a micron-sized polystyrene bead. Bead position relative to the trap center was measured by a detection laser. As RecBCD unwound the DNA, the bead was pulled toward the helicase and the corresponding bead motion was used to calculate the change in DNA length. Since step sizes in DNA length could be as small as 1 bp or 3.4 Å, we needed to reduce the 20-Å noise in the assay. There were three main sources of noise. The first source of noise was Brownian motion of the bead, which has a zero-mean, and therefore, can be averaged away given enough time [18, 94]. The second source of noise was microscope drift between the surface (where RecBCD is attached) and the objective (which controls movement of the optical trap, and thus, the bead) [89]. To reduce this surface-based noise, we actively stabilized the microscope to 1 Å in 3D (bandwidth, Δf = 1–25 Hz) [17] by

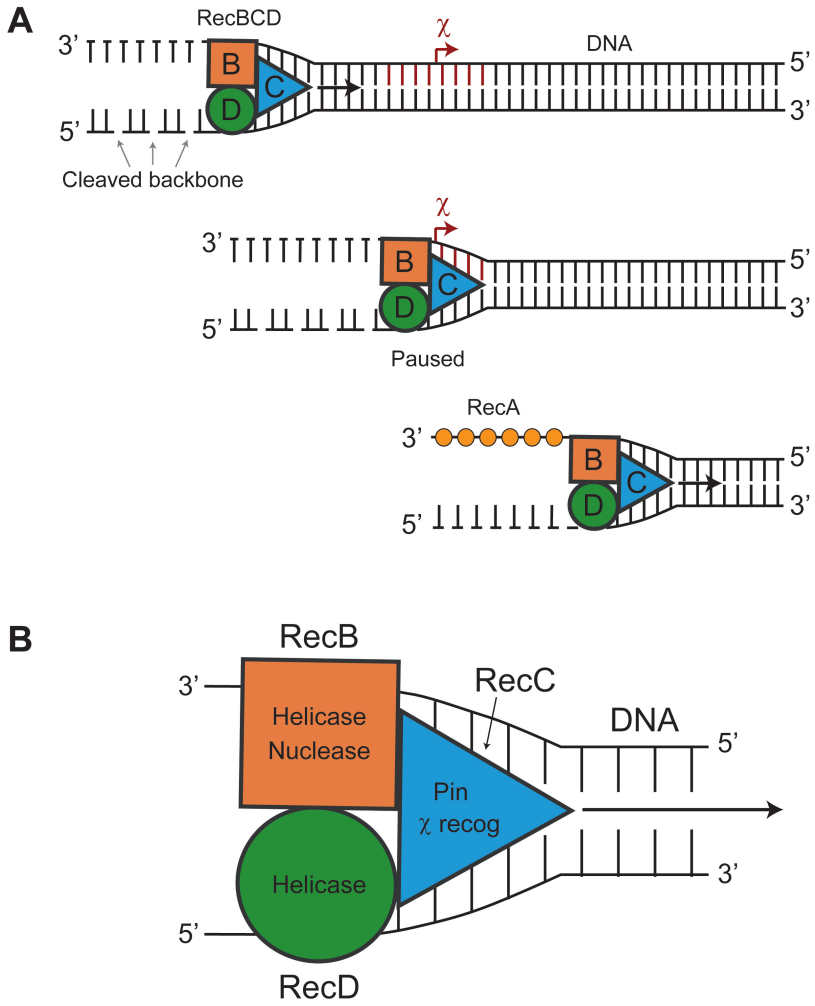

Figure 1.3: RecBCD structure and function. (**A**) RecBCD is a complex helicase built for processing double-stranded DNA breaks in *E. coli* . When RecBCD binds a blunt DNA end, it unwinds and digests the double-stranded DNA until it reaches a specific sequence only present in *E. coli* DNA, a chi site (χ). After chi site recognition, RecBCD slows down, deregulates DNA digestion, and loads RecA. (**B**) To perform these complicated tasks RecBCD has two helicase motor domains, one in the RecB subunit and the other in RecD that bind the DNA with opposite polarity and move at different speeds. The RecC subunit contains a "pin" structure which contacts the double-stranded DNA and acts as the separation point for the duplex. RecC also has the amino acids that recognize the chi site. RecB contains the nuclease domain that digests the DNA. Figure adapted from Singleton et al. [110].

measuring the position of a fiducial mark on the surface (fabricated post) and using this position in a feedback loop to the stage controller to keep fiducial mark position (and hence surface position) constant [17, 16]. Finally, the last source of noise was the lasers. Pointing instability causes a movement of the trapped bead with respect to the detection laser and intensity noise in the trap causes both movement of the trapped bead, if under load, and fluctuations in the force on the bead [18]. To counteract laser noise, we also used an active stabilization technique that reduced pointing instability to 0.5 Å (rms, Δf = 0.03–100 Hz) and intensity noise to ∼0.01% (rms, Δf = 0.2– 2000 Hz) [18]. The resulting optical trapping assay with both surface and laser stabilization was capable of resolving 1 bp motions along DNA [18]. In comparison with other high resolution techniques [1, 76], this method is surface-coupled for easier assay development, reduces fluctuations in force, and allows for high-resolution positional data after force perturbations.

Using this precision optical trapping assay we were able to measure RecBCD motility with sub-nanometer resolution. We observed that RecBCD moved both forward and backward at low ATP concentrations. Steps were variably sized with an average step of 4.4 bp, agreeing with the previously measured biochemical kinetic step size of 4 bp [68, 67]. In addition, there were large (±3 bp) fluctuations that occurred at higher frequencies than RecBCD stepping. These fluctuations were ATP-independent and were only present when single-stranded DNA engaged the RecD helicase, indicating that the fluctuations were actually conformational dynamics of the RecBCD-DNA complex. RecBCD-DNA conformational dynamics were not affected by the presence of an ATP-analog or mutations in the ATP-binding pocket, suggesting that the conformational dynamics are not movements within the enzyme of the ATP-binding pocket. However, the conformational dynamics were dependent on the sequence of the upstream base-pairs, indicating that RecBCD is interacting with the upstream double-stranded DNA in the absence of ATP and unwinding it. The different conformations are then

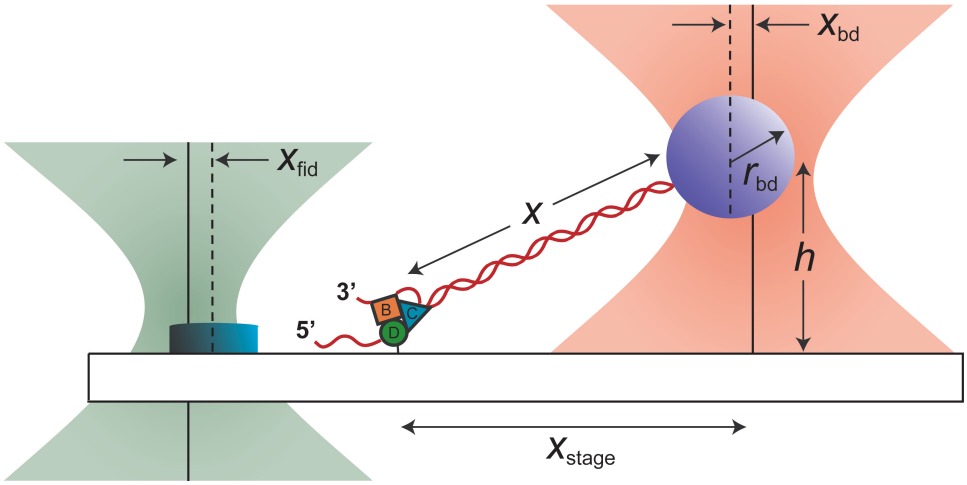

Figure 1.4: Precision optical trapping assay to measure RecBCD motion. A DNA molecule is stretched between the RecBCD helicase and an optically trapped bead. One detection laser (*pink*) measures the bead position (x_{bd}), which is used to calculate DNA length. The other detection laser (*green*) measures the position of a fiducial mark (x_{fid}), which is used to stabilize the surface. The trap laser (*not shown*) is also stabilized to reduce multiple types of laser noise.

translocations of RecBCD along the DNA template even in the absence of ATP. These data suggest a model for helicase movement where the enzyme is able to move in multiple base-pair steps without ATP and uses the chemical energy of ATP to drive forward motion. Thus, our findings are consistent with helicase models with large multi-base-pair steps [66], but not with models that require an ATP-rate-limited, translocational step size of 1 bp [13, 61, 125].

Further explanation for these findings can be found in the remaining pages of the document. The general experimental technique for building the instrument, preparing the biological assay, taking the data, and analyzing the output traces can be found in Ch. 2. In Ch. 3, active stabilization of the microscope to 1 Å is discussed and closely follows the publication in *Applied Optics* by Carter et al. [17]. A modified version of this stabilization technique can be used to stabilize an atomic force microscope (AFM). This diversion from the main topic is dealt with in Ch. 4 and closely follows the publication in *Optics Express* by Carter et al. [16] and the submitted work by King, Carter et al. [51]. In Ch. 5, we discuss active stabilization of the trap laser to $\sim$0.01% and the application of both trap and microscope stabilization to an optical trapping assay. The result is a precision optical trapping assay sensitive to 1 bp motion along DNA. This chapter closely mimics the submitted work by Carter et al. [18]. The last topic covered in Ch. 6 is measurements of RecBCD movement and conformational dynamics, which draws from information in the prepared work by Carter et al. [15].

Chapter 2

Experimental technique

One of the most important themes in this work is that by actively stabilizing both the microscope and the lasers we can achieve Ångstrom-scale sensitivity in an optical trapping experiment. Moreover, it is this active stabilization that allows for precision studies of the RecBCD helicase and gives rise to an ultrastable AFM. In this chapter we detail the experimental techniques of these stabilized assays: the optics and electronics that make up the instruments (Section 2.1), the preparation of the biological samples (Section 2.2), the software routines for data collection (Section 2.3), and the methods to analyze the data (Section 2.4).

2.1 Instruments

2.1.1 Optical trapping microscope

Our highly stable optical-trapping system, based on earlier work [17, 89], consisted of a high-powered, neodymium-doped yttrium orthovanadate crystal laser (Spectra-Physics, Millennia IR, 10 W, $\lambda = 1064$ nm) for trapping and two diode lasers (Blue Sky Research, VPSL, 50 mW, $\lambda = 785$ nm and 850 nm, line width = $\sim$0.5 nm FWHM) for detecting bead motion and stage drift (Fig. 2.1 and Fig. 2.2). All three lasers were coupled into the microscope (Nikon, TE-2000) using dichroic mirrors (Chroma) and focused by a high numerical aperture objective (Nikon, PlanAPO-100X-IR, numerical aperture = 1.4). In the image plane, the two diode lasers were positioned so as to scatter

light off either a fiducial mark or an optically trapped bead. Both the forward-scattered light and the incident beams were collected by the condenser and were imaged onto a quadrant photodiode (QPD, PerkinElmer Optoelectronics, YAG-444-4A) to detect position [100, 128]. The lasers were separately translated in the image plane by piezoelectric, lead zirconate titanate (PZT) mirrors (Physik Instrumente, S-330.2SL) that were placed in a conjugate plane to the back-focal-plane of the objective. Pure rotations in this plane lead to pure translations in the image plane. We translated the sample using a 3D, closed-loop PZT stage (Physik Instrumente, P517.3CD). This instrument was also used to stabilize a microscope to 1 Å (see Ch. 3). In this incarnation, both of the diode lasers measured stage drift, while the trap laser was not used.

The apparatus was designed to both passively and actively minimize mechanical, thermal, and laser noise. The trap laser head was mounted on a research-grade optical table (TMC), while the diode pump lasers were housed in a different room to minimize acoustical and thermal noise. The fan in the trap laser head unit was disabled and replaced with an always-on, ducted, 18.6-L/s fan to reduce 0.4-Hz intensity noise caused by transient heating of the neodymium-doped yttrium orthovanadate crystal. The diode lasers were both current and temperature stabilized. The current controller electronics consisted of a proportional-integral servo controller capable of 25 ppm/ °C at 137 mA, 5 VDC (similar to 505B, Newport). Diode laser temperature controller electronics consisted of a proportional-integral-differential servo controller capable of ±1 millidegree at ±2 A, 6 VDC (similar to 350B, Newport). The temperature controller variables were set by the Ziegler-Nichols closed-loop tuning method [143]. All three lasers were actively stabilized (see Section 2.1.4) to reduce pointing, mode, polarization, and intensity noise. We passed each laser through an acousto-optic modulator (AOM; Isomet, 1205C-2, lead molybdate crystal) to modulate intensity; a single-mode, polarization-maintaining fiber (OZ optics, SMJ-A3A4P-3S-1064-6/125-3AS-3-1) and a polarizing beam splitter (Newport, 10FC16PB) to convert pointing, mode, and polarization noise into intensity

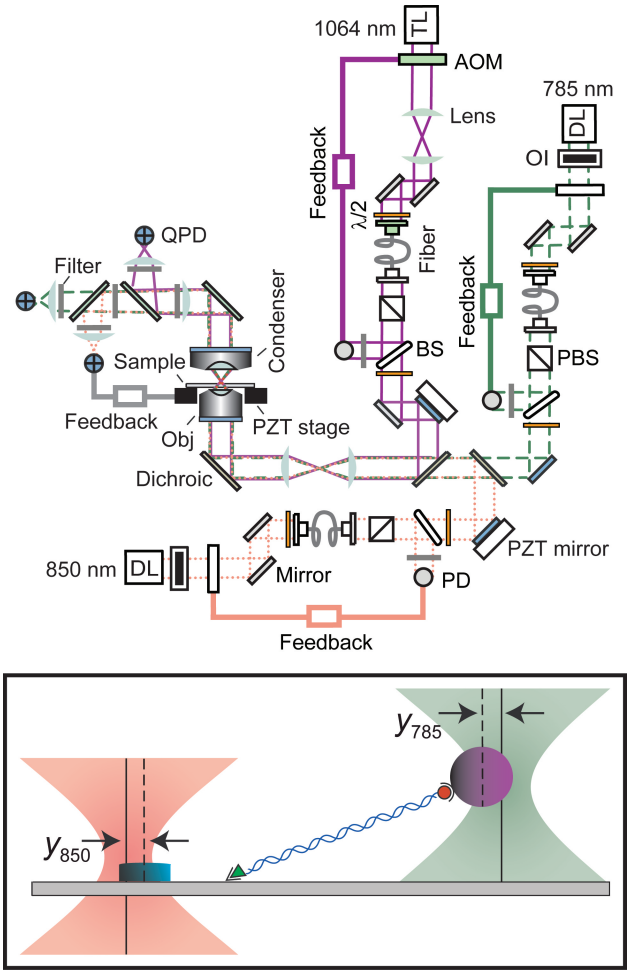

Figure 2.1: Diagram of the optical trapping microscope. The trap laser (TL) and two diode lasers (DL, $\lambda = 785$ nm and 850 nm) were actively stabilized (see Section 2.1.4) by a feedback loop using an acousto-optic modulator (AOM). All three lasers were then coupled into the microscope via dichroic mirrors and were focused by the objective (Obj). In the image plane (*black box*), the two diode lasers scattered off either a fiducial mark or an optically trapped bead, and the forward scattered light was imaged onto a quadrant photodiode (QPD). Each laser was independently translated in the imaging plane by mirrors in a plane conjugate to the back-focal-plane of the objective. Acronyms represent the following: polarizing beam splitter (PBS), optical isolator (OI), photodiode (PD), piezo-electric (PZT, lead zirconate titanate), half-wave plate ($\lambda/2$) and beam sampler (BS). Blue-shaded components and green-shaded components are in optically conjugate planes.

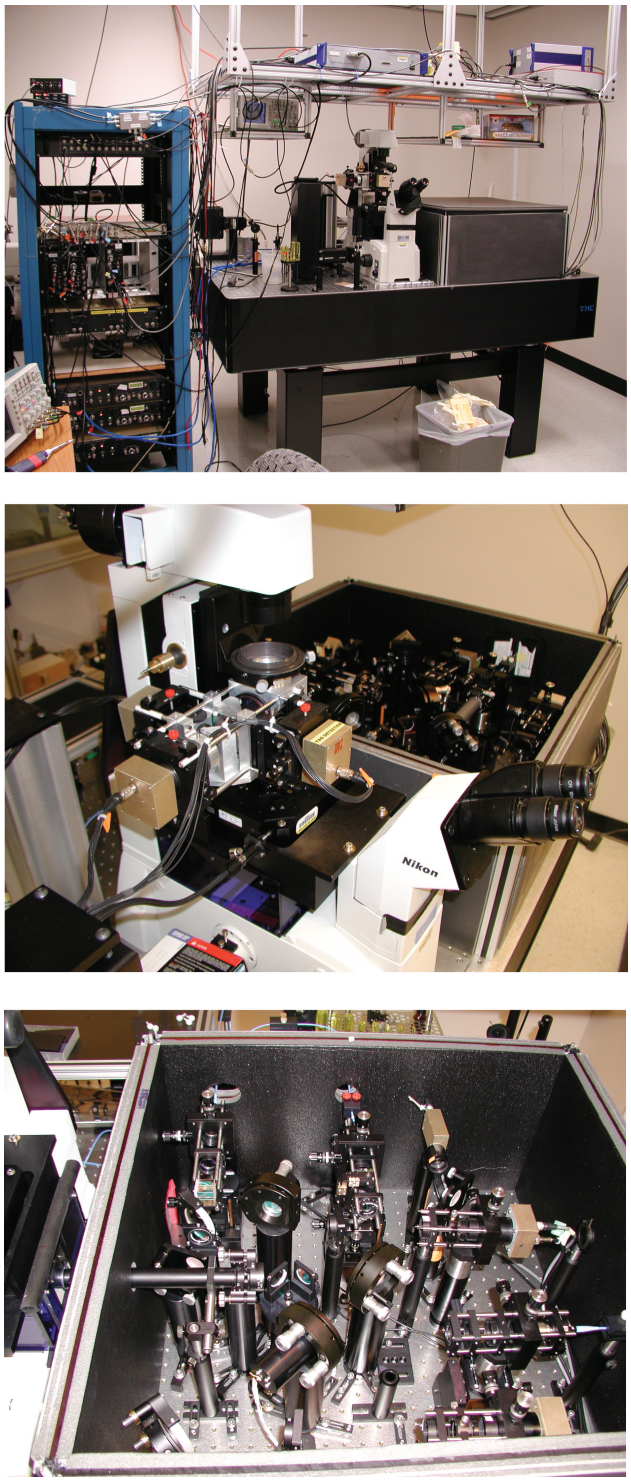

Figure 2.2: Pictures of the optical trapping microscope. *Top.* Optical trapping instrument. *Middle.* Zoom-in of the microscope and detector arm. *Bottom.* Zoom-in of the laser optics before the microscope.

noise; a beam sampler (Newport, 20B10NC) and photodiode to measure the intensity; and an electronic feedback loop to the AOM to minimize the resulting intensity noise. We improved the mechanical stability of the microscope by stiffening the condenser pillar with an aluminum trapezoid (12.5-mm thick). Also, the objective and stage were mounted with custom-built monolithic parts, and the whole apparatus was mounted on a research-grade optical table, separate from the trap laser. Cables to and from the microscope were stress-relieved using monolithic mounts, and multiple cables were tied together to increase stiffness. We supported the detection optics directly off the vertical condenser pillar with a 0.15-m cage assembly. Thermal noise was reduced by coupling the lamp to the microscope with a liquid light guide (Roffin, 3-mm diameter). To minimize laser noise, optics external to the microscope were mounted on 38-mm-diameter monolithic posts (where possible), enclosed in a box, and the beam path was further enclosed in 25-mm-diameter tubing (where possible). We also reduced the beam path length before the microscope to $\sim$1 m. Measurements were made in an acoustically quiet (NC30), temperature-regulated room ($\pm 0.2\,^{\circ}\mathrm{C}$). For a detailed list of custom parts see Appendix D.

Vibrational testing suggested that the current limitations in the mechanical stability of our system are the fiber launches and the QPDs. In vibrational testing, the position of a fiducial mark was measured (see Section 2.3.4) as different optical or mechanical components were tapped lightly by hand. In general, the system was passively reducing enough noise if tapping did not create more than 2-nm spikes at 100 Hz. For this test, a normal noise level was 0.2 nm peak-to-peak at 100 Hz for the lateral directions and 0.5 nm peak-to-peak at 100 Hz for the axial direction. Components that show larger noise levels than 2 nm needed to be mechanically tightened or stress-relieved. After vibrational testing, the system needed to mechanically settle (usually over a day or so) before actual measurements could be made. For the optical trapping microscope, the main sources of noise were the fiber launches and the QPDs. The fiber launch sta-

bility directly couples into the pointing stability of the laser, and the QPD is held by a long attachment to the condenser lens (see Appendix D) creating unwanted motion. To improve the optical design of these components in the AFM application, we switched to a back-scattered detection (BSD) scheme with the QPDs firmly mounted to the optical table, removing the need for optics attached to the condenser lens. We also launched both lasers from the same fiber (see Section 2.1.2), increasing the differential pointing stability.

2.1.2 Modified microscope for the AFM application

We modified our general microscope design for the AFM application (Fig. 2.3 and Fig. 2.4). In the optical trapping microscope we detected forward-scattered light, however this detection scheme is not compatible with AFM due to limited or poor quality optical access opposite of the imaging objective. BSD, initially demonstrated over 10 years ago for optically trapped beads [33], is a viable alternative. In our BSD setup, two stabilized diode lasers (see Section 2.1.4; Lumics, $\sim$100 mW, λ = 810 nm and 845 nm) were focused at the image plane and the back-scattered light was collected using a single, high numerical aperture objective. BSD often suffers from inefficient use of light (0.02-0.1%) [44], with prior work separating BSD signals from the incident light via partially reflective mirrors that decreased the power of both the incident and back-scattered light [44, 50, 49]. While increasing the laser power would increase the amount of back-scattered light, a low laser power minimizes potential perturbation in future applications. For instance, in an application involving AFM where we want to measure the position of a metal-coated cantilever in vacuum, deflection due to laser heating can be substantial (1 nm/μW) [4, 6]. Thus, we sought to minimize laser noise while maximizing the efficiency of photon collection. To do so, both lasers were directed into the back of the microscope objective using a dichroic mirror [17]. Efficient collection of the back-scattered signal was achieved using an optical isolator, which consisted of a

polarizing beam splitter and a quarter-wave plate. We further increased this efficiency by under-filling our 10-mm-diameter QPD with a 6-mm back-scattered beam, in contrast to previous experiments that used an overfilled QPD [33] or BSD in combination with a reflective element [50, 49] to deduce vertical position. As a result, with only 1.3 mW incident upon the objective (and 60% of that at the sample [88]), we achieved a high collection efficiency (5%) of the input light at the QPD. This efficiency enabled us to use low laser power (800 μW at the laser focus) while achieving high sensitivity (see Ch. 4). Independent control of both lasers in the sample plane was achieved with two separate mirrors in a conjugate plane to the back-focal-plane of the objective.

In verifying microscope stabilization, we used one laser to detect sample position (810 nm) and the other laser as an independent verification (845 nm). However, in the AFM application, we stabilized the sample with respect to the AFM tip, where both the sample and the tip were detected by lasers. We therefore introduced two lasers that by design share a largely collinear beam path. Common-mode noise (e.g., mechanical motion of the fiber tip) was suppressed in this differential measurement scheme. Thus, the differential stability between the lasers will be the ultimate limitation [19 pm laterally, 73 pm vertically, Δf = 0.1–50 Hz, see Ch. 4].

For the AFM application, we custom-built an AFM assembly that mounted directly onto the optical microscope frame. Detailed drawings of the AFM assembly that contain the AFM tip are presented elsewhere [20]. In the AFM application, we separately measured the position of the AFM tip and a fiducial mark on the sample with two diode lasers and back-scattered detection, as discussed above. Sample and tip position were controlled with a pair of 3D, closed-loop PZT stages (Physik Instrumente, P363.3CD and P733.3DD), which were both mounted on coarse-positioning stages. The six axes of motion (i.e., x, y, z on both stages) were controlled with custom software (National Instruments, LabVIEW 8.5) and a field programmable gate array card (National Instruments, PCI-7833R). Commercial silicon and silicon-nitride tips were used [Mikro-

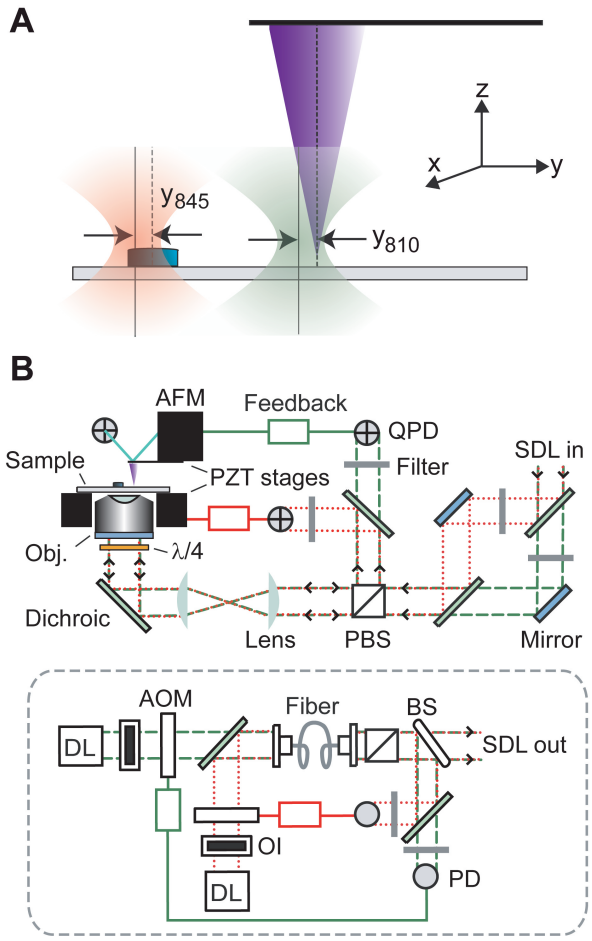

Figure 2.3: Diagram of the atomic force microscope (AFM). (**A**) Detailed view of the image plane where the AFM tip and sample positions were detected by focused lasers scattering off a fiducial mark on the sample and the apex of the tip. (**B**) Two diode lasers (DL) were actively stabilized by the combination of optics shown in the gray box. The stabilized diode lasers (SDL) were coupled into the microscope similar to Figure 2.1. Because the AFM tip is in the forward-scattered direction, the back-scattered light was imaged onto the QPD. The combination of the polarizing beam splitter (PBS) and quarter-wave plate ($\lambda/4$) led to highly efficient back-scattered detection. Each laser was independently translated in the imaging plane by mirrors in a plane conjugate to the back-focal-plane of the objective. Acronyms represent the following: optical isolator (OI), acousto-optic modulator (AOM), photodiode (PD), piezo-electric (PZT, lead zirconate titanate), half-wave plate ($\lambda/2$) and beam sampler (BS). Blue-shaded components are in optically conjugate planes.

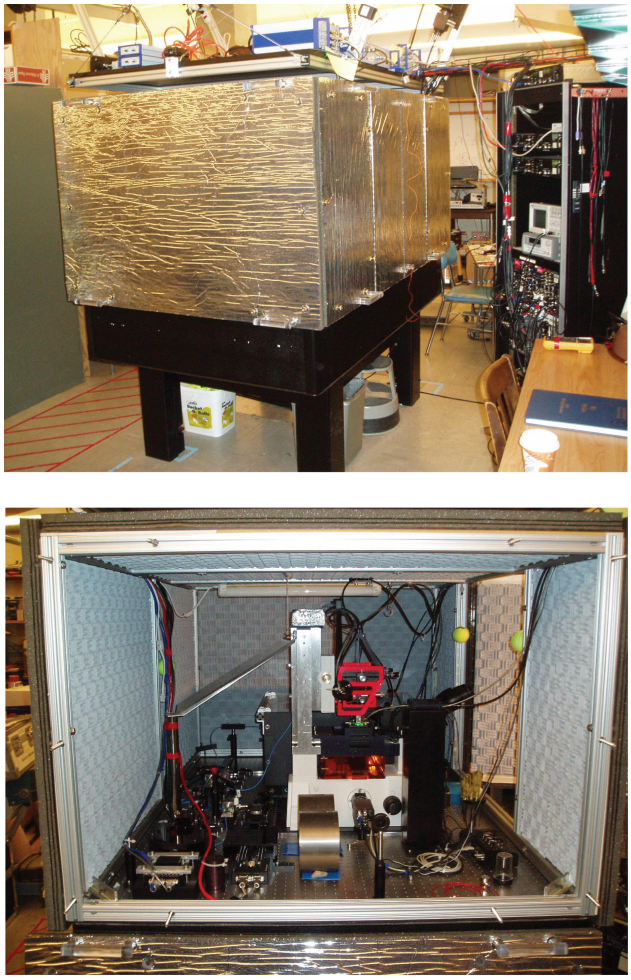

Figure 2.4: Pictures of the AFM. *Top.* AFM instrument. *Bottom.* Inside the acoustically isolated box is the microscope and laser optics.

Mash, CSC38/noAl (stiffness = 0.08 N/m); Veeco, DNP-S (stiffness = 0.06 N/m)]. For AFM imaging, we deduced cantilever deflection via a third diode laser (λ = 785 nm) in a standard optical-lever geometry [75]. More specifically, we reflected the 785-nm laser off the back side of the AFM cantilever and detected its deflection with a QPD. We calibrated each cantilever by contacting the AFM tip to the cover slip, yielding a typical sensitivity of ∼30 mV/nm. To minimize thermally induced cantilever deflection [6], we used cantilevers without a metallic coating (or removed the metallic coating chemically). Nonetheless, we maintained a deflection sensitivity of <20 pm (rms, Δf = 0.1–1000 Hz). We deduced the mechanical response time (∼100 μs) of the silicon nitride cantilever by measuring the resonance width (FWHM) of the thermally driven fundamental resonance peak in air.

As in the optical trapping microscope, the AFM apparatus was constructed such that passive and active stabilization reduced mechanical, thermal, and laser noise. There were a few instrumental differences. To further reduce mechanical vibrations, an optical breadboard (TMC, 77-113, 91.6-mm-tall with adapter) was mounted on the optical table as a riser to shorten mount height. In addition, the microscope pillar was replaced by a 0.4 m X 0.18 m X 0.09 m monolithic aluminum column. We also placed lead bricks in strategic locations on the optical table to more equally distribute the table weight; we did not see an appreciable difference in stability by doing this. The whole assembly was enclosed by a custom-built, acoustically isolated box. To image the sample, the mercury lamp was replaced by a gooseneck light-emitting diode (McMaster-Carr, 6799T1). The room was not temperature-regulated, but during experiments the air-handling system was turned off, all of the doors were closed, and the room temperature was allowed to equilibrate.

2.1.3 Detection electronics

The position of the fiducial mark or trapped bead was detected by a QPD (250 kHz bandwidth with custom electronics; ∼40 μW laser power at detector). Lateral motion was deduced from the normalized intensity difference on the QPD while vertical motion was deduced by the sum signal – the total light falling upon the four quadrants of the QPD. The normalized differences, as well as the offset-amplified sum signal, were digitized using 16 bits at either 4 or 10 kHz, and the resulting voltages were converted to positions (see Section 2.3.1). More specifically, the four currents from each QPD were converted into voltages using a transimpedance amplifer with a resistance of 100 kΩ. Then a summing and subtraction circuit using operational amplifiers (similar to the circuit in the UDT application note "Quadrant/Bi Cell Photodiode", Fig. 2.5) generated the x (left quadrants - right quadrants), y (top quadrants - bottom quadrants), and z (sum of all quadrants) voltage signals. The x and y signals were normalized by division to reduce the effect of amplitude changes on the QPD. The voltages were then filtered with an 8th-order, low-pass, elliptic filter (Frequency Devices), and digitized with a 16-bit, 20-V-range data acquisition card (National Instruments, PCI-6052E). In the modified microscope for AFM, the data acquisition card was upgraded to an 18-bit data card (National Instruments, M-series High Accuracy) and a field-programmable gate array card (National Instruments, PCI-7833R). Prior to digitization the z signal undergoes a further amplification stage (50–1000X) using a differential amplifier with an offset. After digitization, we used software calibration curves to convert the voltages into position records (see Section 2.3.1). Customized software was written in LabVIEW (National Instruments, version 7.1 or 8.5) on a computer (Dell Dimension 9200) with a fast processor (Intel Core2-Duo, 2.66 GHz).

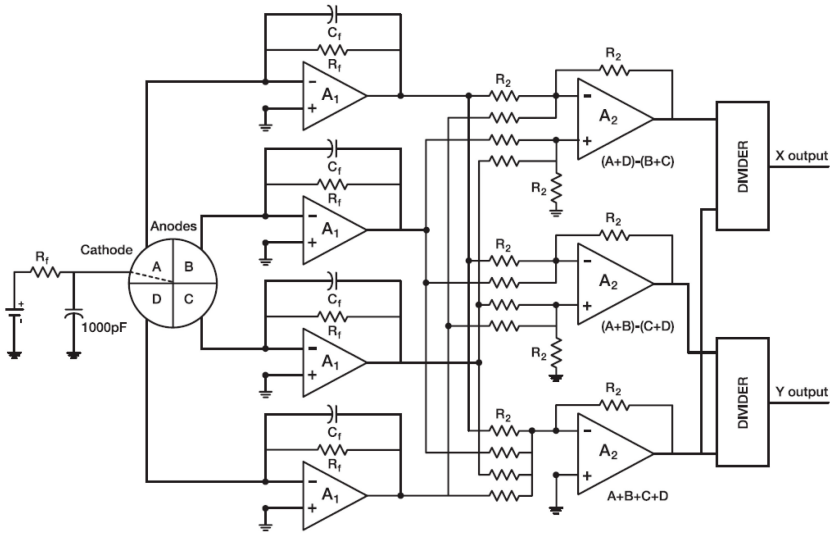

Figure 2.5: Quadrant photodiode circuit. Figure credit: UDT application note "Quadrant/Bi Cell Photodiode".

2.1.4 Laser stabilization

To reduce laser noise, we used active stabilization (Fig. 2.6 **A**). Specifically, we passed the laser sequentially through an AOM, a single-mode, polarization-maintaining fiber, and a polarizing beam splitter. The AOM diffracted the laser and we selected the first order beam using an iris and beam blocks. The combination of the single-mode, polarization-maintaining fiber and the polarizing beam splitter transformed pointing, mode, and polarization noise into intensity noise. We then sampled 10% of the light onto a large-area (10-mm-diameter) photodiode (PerkinElmer Optoelectronics, YAG-444-A). The photodiode signal was analyzed using custom-built feedback electronics that output a voltage signal to the AOM to modulate the power in the diffracted beam so as to stabilize the output laser intensity. The photodiode current was converted to voltage using an analog transimpedance amplifier with a resistance of 10 kΩ. The custom-built feedback electronics consisted of a low-delay, proportional-integral analog servo controller operating at a bandwidth of 200 kHz. The circuit diagram for the feedback electronics is listed in Appendix D.

Simple application of this active stabilization method to the trap laser resulted in a gain inversion when the output intensity of the AOM was changed substantially. The gain inversion was caused by transient heating of the AOM crystal, resulting in index changes that shifted the diffraction angle ($\Delta\theta$) of the beam. Previous measurements of pointing instability after large intensity changes (almost the full range) in a different AOM crystal (germanium) have been as large as 4 mrad in just 2 s [53]. In our experimental geometry, the transient pointing error was converted into a time- and history-dependent intensity error. In other systems, this AOM-induced error would lead to translations of the trap laser focus — uncorrected this could correspond to an 8 μm lateral motion [$\Delta\theta f_{\mathrm{obj}}$, where f_{obj} is the effective focal length of the objective (2 mm)]. To minimize the effects of the AOM pointing instability, we imaged the AOM crystal

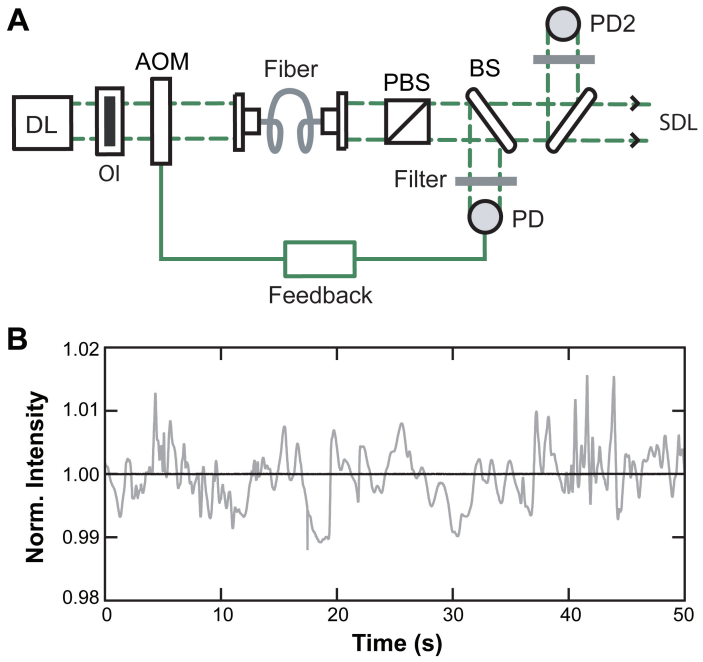

Figure 2.6: Diagram of laser stabilization and performance. (**A**) Optical layout for laser stabilization. Acronyms represent the following: optical isolator (OI), photodiode (PD), beam sampler (BS), polarizing beam splitter (PBS), and acousto-optic modulator (AOM). (**B**) Diode laser intensity prior to stabilization (*gray*) and after stabilization (*black*). Traces were smoothed with a box-car window and decimated to 100 Hz.

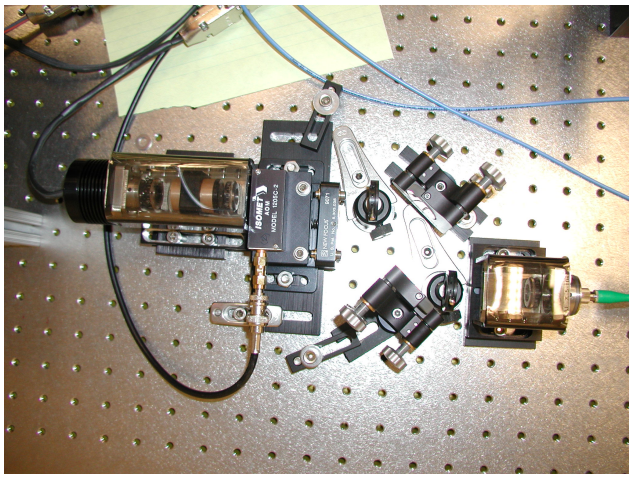

Figure 2.7: Picture of the laser stabilization implemented on the 785-nm diode laser.

(Fig. 2.1) on to the fiber mount coupling lens, eliminating lateral translation of the laser beam on the coupling lens that would otherwise accompany a changing diffraction angle.

To verify the performance of the intensity stabilization, we sampled 10% of the intensity onto a second photodiode (Fig. 2.6 **A**, PD2). Voltages from this second photodiode were digitized, filtered, smoothed with a box-car window and decimated to 100 Hz, and normalized. Without stabilization, the intensity fluctuated 2.5% peak-to-peak for the 785-nm diode laser, greater than the manufacturers specification of 0.5% peak-to-peak (Fig. 2.6 **B**). Measurements of intensity before the AOM were within specification, thus the excess noise probably arose from the other laser noise sources (pointing, mode, or polarization). With stabilization, we decreased the intensity noise by 580-fold to achieve a normalized stability of $1.7\text{x}10^{-5}$ rms at 100 Hz. Similar stabilization of $5\text{x}10^{-5}$ and $4.0\text{x}10^{-6}$ was achieved for the 850-nm laser and trap laser, respectively. This result demonstrates the effectiveness of our scheme whereby a variety of noise sources can be systematically minimized without directly measuring and individually addressing each one.

To maximize the performance of the feedback loop, we tuned the parameters of the AOM, fiber, photodiode, and servo electronics. The AOM diffraction efficiency was maximized at the expense of the loop closure time by passing a collimated, 2-mm-diameter beam through the AOM. At near-infrared wavelengths and this beam diameter, the diffraction efficiency was measured to be ∼70% while the AOM rise time was nominally ∼1 μs. The AOM driver was set so that the "bias adjust" knob was turned all of the way down and the "power adjust" knob was turned such that diffraction efficiency was maximized (all of the way up and then backed off a quarter of a turn). The power efficiency through the fiber was tuned when the AOM output was at 60%, see Appendix E. The photodiode resistance (R, 10 kΩ) was selected so that the incident power (∼1 mW) matched the voltage range (0–10 V) of the servo electronics. Incident

power is related to voltage through the responsivity of the photodiode, which was 0.45–0.5 W/A for our wavelength lasers. In addition, the photodiode resistance was selected to maximize the bandwidth of the photodiode (∼1 MHz), i.e.,

$$\Delta f = \sqrt{\frac{\Delta f_{gain}}{2\pi C R}}, \tag{2.1}$$

where Δf_{gain} is the gain bandwidth (45 MHz) and C is the total capacitance of the circuit (40 pF). We tuned the servo electronics to minimize the noise and maximize the loop closure time, see Appendix E. The feedback loop closure time was limited by the response of the silicon photodiode to infrared light [7, 97]. Increasing the amount of incident light on the photodiode decreased this problem, but limited the output power. We selected a 10% beam sampler as a compromise between bandwidth and output power. Hence, we maximized the performance of the feedback loop by compromising between power efficiency and bandwidth.

2.1.5 Microscope stabilization

Drift between the objective and sample is a long-standing problem in microscopy. However, the introduction of a fiducial mark, or a reference point, into the system provides a means to measure and minimize objective-sample drift. Historically, the fiducial mark has been a micron-sized bead affixed to the microscope cover slip [14, 115]. However, these beads tend to exhibit >1 Å motion relative to the sample (see Section 3.4), so we fabricated micron-sized posts on the cover slip to provide stable fiducial marks (see Section 2.2.1). We measured the position of the fiducial mark using laser-based detection to directly measure the objective-sample distance (the laser focal position is subject to objective drift, while the fiducial mark position is subject to sample drift). Since we have a measure of objective-sample drift we now have a means of reducing it. Previously, our group sought to passively subtract drift [89], however, as the microscope drifts farther out of alignment simple subtraction is not possible. Here, we

actively stabilized the objective-sample position to minimize instrumental drift. Active microscope stabilization was achieved by (*i*) measuring the position of a fiducial mark on the sample, and (*ii*) using this position in a feedback loop to a PZT stage to keep sample position constant (Fig. 2.8).

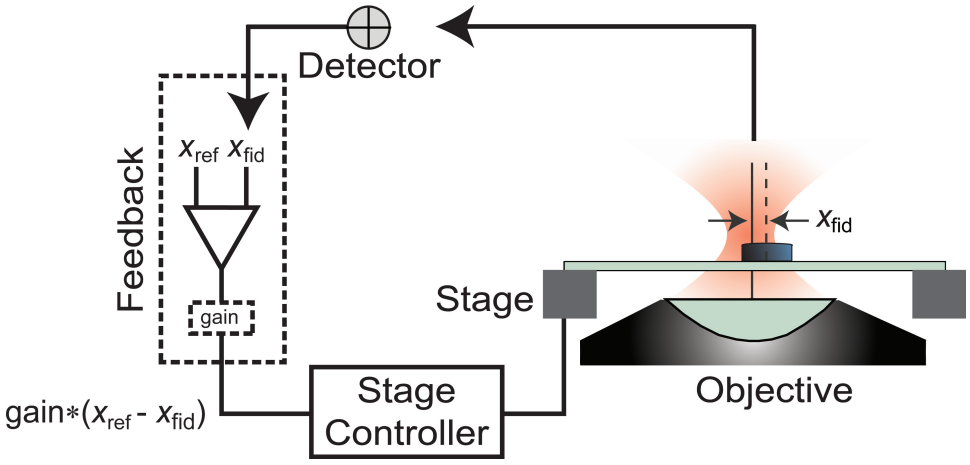

Figure 2.8: Diagram of microscope stabilization. We first detect sample position by scattering a laser beam off a fiducial mark. The light from the scattered beam is collected by a quadrant photodiode detector that outputs a voltage, which is calibrated into position (x_{fid}). A feedback loop compares x_{fid} to a reference position, x_{ref}, and outputs a signal to the piezo stage to keep the sample at the reference position.

To test the performance of the microscope stabilization we used a second laser to monitor the position of a second fiducial mark on the surface. Using this method, we report a microscope stability of 1 Å rms in 3D over 1–25 Hz using forward scattered light (see Ch. 3). We also achieve similar stability using back-scattered light: <1 Å rms in 3D over an order of magnitude larger bandwidth, 0.1–50 Hz (see Ch. 4). The slightly better stability using back-scattered detection is probably due to the more compact optical design and the decreased pointing noise of the lasers, which have been launched out of a single fiber.

To maximize the performance of the microscope stabilization we tuned the parameters of the detection electronics and the feedback loop. The detection electronics

measure the voltage of the incident light on the QPD (see Section 2.1.3), which is then calibrated into a position of the fiducial mark using a calibration curve (see Section 2.3.1). We set the gain on the detection electronics such that the fiducial mark position had a 0.2-nm peak-to-peak noise level, laterally, and a 0.5-nm peak-to-peak noise level, vertically, over a bandwidth of 1–100 Hz (for a micron-sized glass post, x-y gain = 4.5, differential gain = 1, post gain = 1, and vertical gain = 50). Too much gain led to amplification of noise, while bit noise persisted at low gain levels. In addition, we maximized the software feedback loop by tuning the gain and bandwidth parameters. The inputs to the feedback loop were the current position of the fiducial mark (e.g. x_{fid}), the desired position of the fiducial mark (e.g. x_{ref}), the gain (g), and the threshold for loop output. The algorithm calculated the difference between the desired position and the current position. If the difference was above the input threshold value, it was multiplied by the gain, and output as a relative movement of the PZT stage (Fig. 2.8). We set the desired position to zero in 3D, the gain to 0.05 in all dimensions, and the threshold values to 0.05 nm, laterally, and 0.1 nm, vertically, though the gain and threshold values vary with the bandwidth of the feedback loop. To tune the gain values, we increased the gain until oscillation and backed off until the noise decreased to a plateau. The threshold value was set to about a quarter of the peak-to-peak noise level for fiducial mark position over the desired bandwidth; for example, at 100 Hz, the peak-to-peak noise level is 0.2 nm, laterally, so the threshold value is 0.05 nm, laterally. In the optical trapping microscope, the feedback loop was software-based (LabVIEW) with a maximum bandwidth of 100 Hz that was limited by the computer processor and data collection algorithms (see Section 2.3). In the AFM application, the feedback was upgraded to field-programmable gate array control that ran at a 500 Hz bandwidth [21], the resonance frequency of the loaded PZT stage. The larger bandwidth increased performance three-fold.

2.1.6 AFM tip stabilization

AFM tip stabilization was similar to microscope stabilization except for a few key differences. We measured AFM tip position at 300 nm above the surface (see Section 2.3.4), instead of fiducial mark position. Focusing of the lasers and alignment of the beams was done with the aid of micrometer stages to move the fiber tip relative to a collimating lens and to move the fiber tip-lens assembly relative to the piezo mirror. AFM tip position measurements required compensating for crosstalk, which we did with a linear compensation algorithm. The software-based feedback loop was run in LabVIEW 8.5 to accommodate the M-Series data acquisition card, instead of LabVIEW 7.1, though the bandwidth was still 100 Hz. Finally, the gain of each axis of the tip PZT stage had to be individually set. Setting of the PZT stage gain followed published protocols by Physik Instrumente.

In the actual AFM experiment this software-based tip stabilization was upgraded for field-programmable gate array control [21, 51] with an increased bandwidth. In this scheme, the PZT stage position was updated every 1 ms.

2.2 Biological assays

2.2.1 Fiducial mark fabrication

Melted polystyrene beads. The easiest fiducial marks to produce were melted polystyrene beads. We first cleaned microscope cover slips in ethanolic 6 M potassium hydroxide (see Appendix E) and constructed sample chambers (see Section 2.2.2). Second, we flowed in 0.1–1 pM polystyrene beads (Interfacial Dynamics, surfactant-free) in 10 mM Tris buffer. After 5 min, the flow chamber was rinsed with 100 mM magnesium acetate and allowed to sit for 10–20 min. Then, we rinsed with ethanol and removed the excess liquid. When the flow chamber was dry, we heated it in the oven at 100 °C for 15 min, and then filled the chamber with water. Unfortunately, these melted beads were

not firmly affixed to the cover slip and demonstrated significant (>1 Å) motion (see Section 3.4). To address some of this concern the above procedure for melting beads was changed with varying success. The current best procedure for melting polystyrene beads is listed in Appendix E.

Low-index glass posts. Symmetric nano-scale low-index glass posts were fabricated on cover slips using hydrogen silsesquioxane (HSQ, Dow Corning, FOx-16) and e-beam lithography (Fig. 2.9 **A**,**B**). First, we cleaned the cover slips in a 10 min piranha etch (100 mL sulfuric acid and 15 drops hydrogen peroxide at 80 °C, see Appendix E). The cleaned cover slips were spin coated at speeds of 1–5 krpm with HSQ to produce posts with heights ranging from ∼400–1000 nm. Then, thin aluminum films (nominally 15 nm) were vapor deposited to prevent charging during the next step, e-beam lithography (38 keV, 450 μC/cm^2 dose). When exposed to electron irradiation, HSQ cross-links to form glasslike features as small as 20 nm [85]. This fine control allows for highly symmetric, circular structures to be fabricated. Asymmetric structures lead to crosstalk between the x and y motions on the QPD. After e-beam exposure, the aluminum was etched (10 s in 16:1:1:2 phosphoric acid to nitric acid to acetic acid to distilled water), and the HSQ was developed (10 min) by using tetramethylammonium hydroxide. Finally, to ensure the HSQ was fully cross-linked, samples were thermally cured at 400 °C for one hour. A more detailed protocol is listed in Appendix E.

Silicon disks. We fabricated 1 mm^2 arrays of silicon disks in a 6-μm grid (Fig. 2.9 **C**,**D**) on cover slips via physical vapor deposition of silicon through a silicon-nitride shadow mask [54]. Mask fabrication began by spinning e-beam resist (Zeon, ZEP-520) onto 200-nm thick, 2 X 2 mm silicon-nitride membrane windows (Silson). The resist was then exposed via e-beam lithography (38 keV, 15 pA, 50 μC/cm^2) and developed. Holes were then etched through the window in a reactive ion etcher (tetrafluoromethane, 16 sccm, 20 Pa, 100 W, 90 s). Next, 3-μm-tall standoffs were fabricated around the perimeter of the patterned window via optical lithography with SU-8 (Microchem).

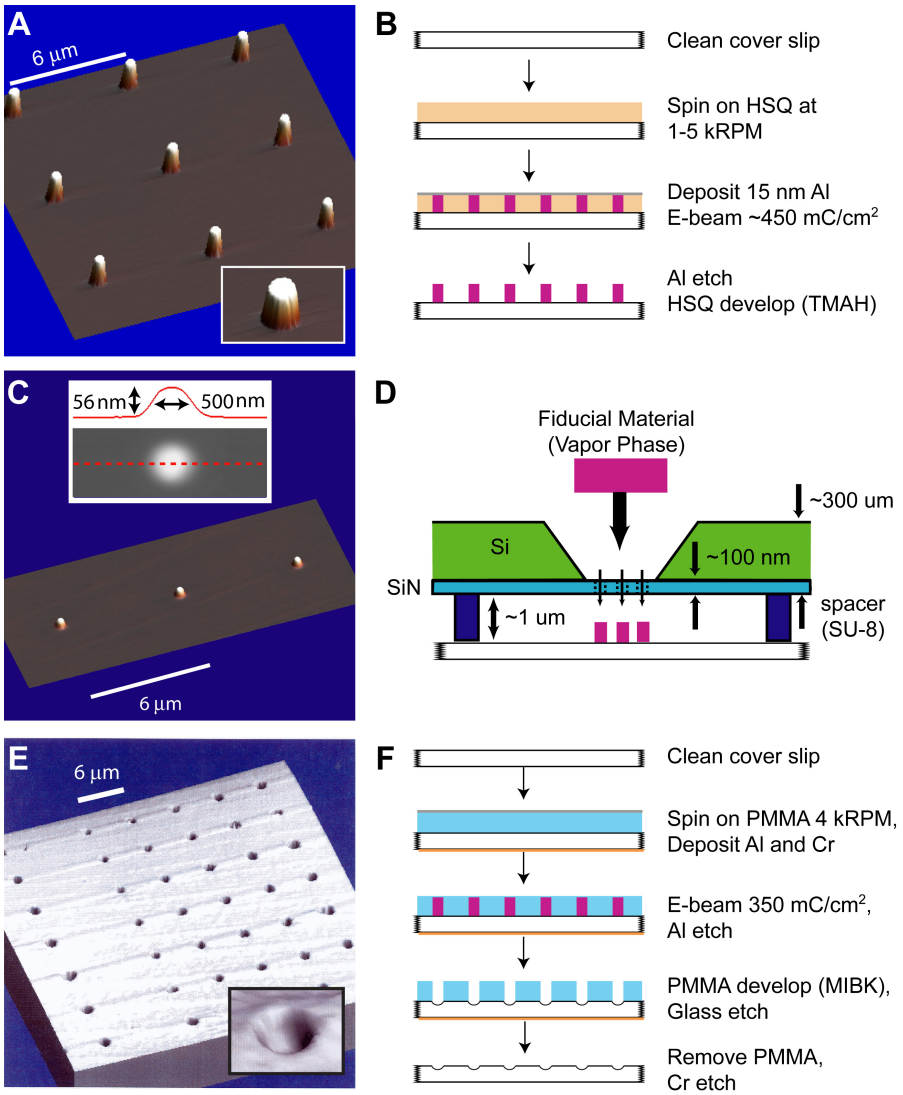

Figure 2.9: Fiducial mark fabrication. (**A**) Atomic force microscope image showing an array of hydrogen silsesquioxane (HSQ) posts (radius, $r = 500$ nm; height, $h = 600$ nm). Inset: zoom-in of post. (**B**) Protocol for making HSQ posts. (**C**) Atomic force microscope image showing three silicon disks ($r = 250$ nm; $h = 56$ nm). Inset: line scan across a disk. (**D**) Cartoon of shadow mask procedure to make silicon disks. (**E**) Atomic force microscope image showing an array of etched holes (patterned $r = 50$–300 nm). Inset: zoom-in of hole. Image credit: Theresa Ulrich. (**F**) Protocol for making etched holes.

Prior to depositing silicon, the glass cover slips were cleaned in ethanolic 6 M potassium hydroxide, see Appendix E. Finally, silicon was deposited through the shadow mask in an evaporation chamber (0.1 nm/s, 1x10^{-4} Pa). The diameter and height of the silicon disks were measured by AFM with a high aspect ratio tip (MikroMasch, STING tip). One general advantage of physical vapor deposition through a shadow mask is that the material composition (and thus the index of refraction) of the disks is highly tunable. Additionally, by using four shadow masks in parallel, four cover slips were made per 30-min cycle, where cycle time was limited by evaporator pumping time. A more detailed protocol is listed in Appendix E.

Etched holes. We etched holes (Fig. 2.9 **E**,**F**) by spin coating cleaned (ethanolic 6 M potassium hydroxide, see Appendix E) cover slips with polymethyl methacrylate resist (300-nm thick) and then vapor depositing a thin layer of aluminum (nominally 15 nm). Next, a chromium layer was deposited to the back side of the cover slip, to prevent etching. Then, we exposed a grid of filled circles with varying radii using e-beam lithography (38 keV, 350 μC/cm^2 dose). After removing the aluminum and developing the resist, we etched the underlying cover slip with buffered hydrofluoric acid to obtain isotropic holes. Finally, the cover slips were cleaned in methyl isobutyl ketone to remove the resist.

2.2.2 Sample preparation

We fabricated fiducial marks (see Section 2.2.1) onto cover slips for use in active stabilization. To enhance usability in single-molecule assays, the cover slips were cleaned with a 10-min piranha etch (100 mL sulfuric acid and 15 drops hydrogen peroxide at 80 °C, see Appendix E) after nanofabrication. We constructed epoxy-rigidified flow chambers (internal volume 15 μL) for enhanced stability using double-stick tape (3M) as a spacer and 5-min epoxy (Devcon) for rigidity. Cover slips were recovered (>20 times) and cleaned after use by soaking the flow chamber in boiling water for 1 hour (to

remove the cover slip) and piranha cleaning the cover slip for 10 min. Surface chemistry after such cleaning was compatible with single-molecule biophysics experiments.

For experiments with only a trapped bead, we used 10-fM polystyrene beads (Interfacial Dynamics, 330-nm-diameter) in WB [25 mM Tris acetate (pH = 7.5), 1 mM magnesium acetate, 1 mM sodium chloride, 1 mM dithiothreitol, 0.4% Tween-20 (BioRad), and 3 mg/ml bovine serum albumin (concentration cited is that before filtration through a 0.2-μm filter)].

2.2.3 DNA preparation

For experiments with a DNA molecule, we prepared double-stranded DNA by polymerase chain reaction (PCR; Applied Biosystems, GeneAmp XL PCR Kit) using one digoxigenin-labeled and one biotin-labeled primer (Integrated DNA Technologies). Labelling the DNA permitted biochemical linkage. We bought M13mp18 plasmid and used this as a template for PCR. To make different lengths (L = 556 nm, 1007 nm, 2413 nm), we used different primers and gel purified the final product. Concentrations cited were spectrally determined (1 absorbance unit at 260 nm = 50 μg/mL of double-stranded DNA) using an ultraviolet-visible absorption spectrometer (Jenway, Genova). Another analytical gel verified the single DNA band of the appropriate size.

Preparation of the 20TS06/T4 DNA hairpin (Fig. 2.10 **A**) followed published protocols [136, 135]. Specifically, we prepared two DNA handles using PCR. Handle A was made using M13mp18 template DNA, a biotin-labeled primer for the top strand, and a bottom-strand primer with an abasic site (deoxyribose spacer) followed by ∼10 nucleotides to create a 5' overhang. Handle B used the same template DNA. The top-strand primer had ∼10 nucleotides that were complementary to the 5' overhang in Handle A, followed by the 20TS06/T4 hairpin, an abasic site, and a complementary region of DNA to the M13mp18 plasmid. The bottom-strand primer was digoxigenin-labeled. After PCR, each handle was gel purified, concentrations were determined, and

a diagnostic gel verified the appropriate lengths. Ligation of the two handles was done by T4 DNA ligase (Invitrogen, 16 °C for 16 hours, 1:1 molar ratio of Handle A to Handle B) resulting in two double-stranded labeled regions flanking the single-stranded hairpin. The final DNA product was gel purified, concentrations were determined, and a final diagnostic gel was run, as above.

For experiments with RecBCD, we prepared DNA by PCR with M13mp18 plasmid template and with one biotin-labeled primer and one unlabeled primer (Fig. 2.10 **A**). This created a blunt-end DNA molecule (L = 2413 nm, 993 nm) void of chi-sites and with only one biochemical linkage for attachment to the optically trapped bead. We then purified the DNA and verified the concentration and length, as above. To make tailed DNA we cut the 993-nm-length blunt-end DNA with BsmBI restriction endonuclease (New England Biolabs) at a restriction site such that the purified product had an L = 901 nm. We purchased two DNA oligos to make a tailed substrate: one with a 3' poly-T tail (dT = 5 or 6) and a 5' end that is complementary to the BsmBI overhang, the other with a 5' poly-T tail (dT = 10) and a sequence that is complementary to the first oligo up until the 5' end (Fig. 2.10 **B**). The two oligos were annealed at 70 °C, slowly cooled (4 °C increments held for 30 s) to room temperature, and ligated using T4 DNA ligase to the cut DNA (16 °C for 16 hours, 50:1 molar ratio of tailed substrate to cut DNA). The final double-stranded DNA length of the tailed substrates was 908 nm. We gel purified the product and concentrations were determined, as above. To verify that the final product was a tailed DNA we further cut an aliquot of the product with a DrdI restriction endonuclease (New England Biolabs) at a site upstream of the BsmBI site. This produced a 829-nm-length DNA molecule containing the biotin label, and a 78-nm-length DNA molecule with the tailed substrate. If the digestion or ligation were faulty then bands would appear at other lengths (a 164-nm length indicated the blunt-end DNA molecule and a 72-nm length indicated the DNA molecule with the BsmBI cut end and no ligation). There were three different tailed substrates that were created:

a GC-rich substrate, an AT-rich substrate, and a substrate with a mixed sequence (Fig. 2.10 **B**).

2.2.4 DNA tethered particle assay

Tethering DNA to the surface required biochemical linkage. DNA was prepared as above with one biotin-labeled primer and one digoxigenin-labeled primer. These labels enabled us to attach a DNA molecule at one end to a streptavidin-coated bead (Spherotech, 320 nm diameter) and at the other end to an antidigoxigenin-coated cover slip (Fig. 2.1). Coated cover slips were made by incubating 20 μg/ml antidigoxigenin antibody (Roche) suspended in 0.1 M sodium phosphate buffer for 1 hour in flow chambers. Bead-DNA complexes were made by incubating streptavidin-coated beads (900 pM) at a 9:1 molar ratio with labeled DNA at room temperature. After washing the flow chamber with WB, the bead-DNA mixture was flowed into the chamber and allowed to incubate for 1 hour before washing again. A more detailed protocol is listed in Appendix E.

2.2.5 RecBCD assay

RecBCD preparation protocols were adapted from those in earlier studies [27, 96] based on the biotinylated RecBCD derivative, RecBCD-bio. RecBCD-bio unwinding rates agree, within experimental uncertainty, to the wild type unwinding rates in both bulk and single molecule experiments [8, 27, 114]. Both RecBCD-bio and RecBCD-bio with a knockout RecD helicase were expressed and purified by our collaborators (Hung-Wen Li and Hsiu-Fang Fan). Streptavidin beads were sonicated, then incubated for 1 hour with DNA (9:1 mol ratio, 900 pM beads) in WB. Concurrently, biotinylated bovine serum albumin (Vector) at 10–100 mg/ml in 100 mM sodium phosphate buffer (pH = 7) was incubated within a flow chamber for 30 min at room temperature to promote adsorption. After washing with WB, the chamber was incubated with 5 mg/ml

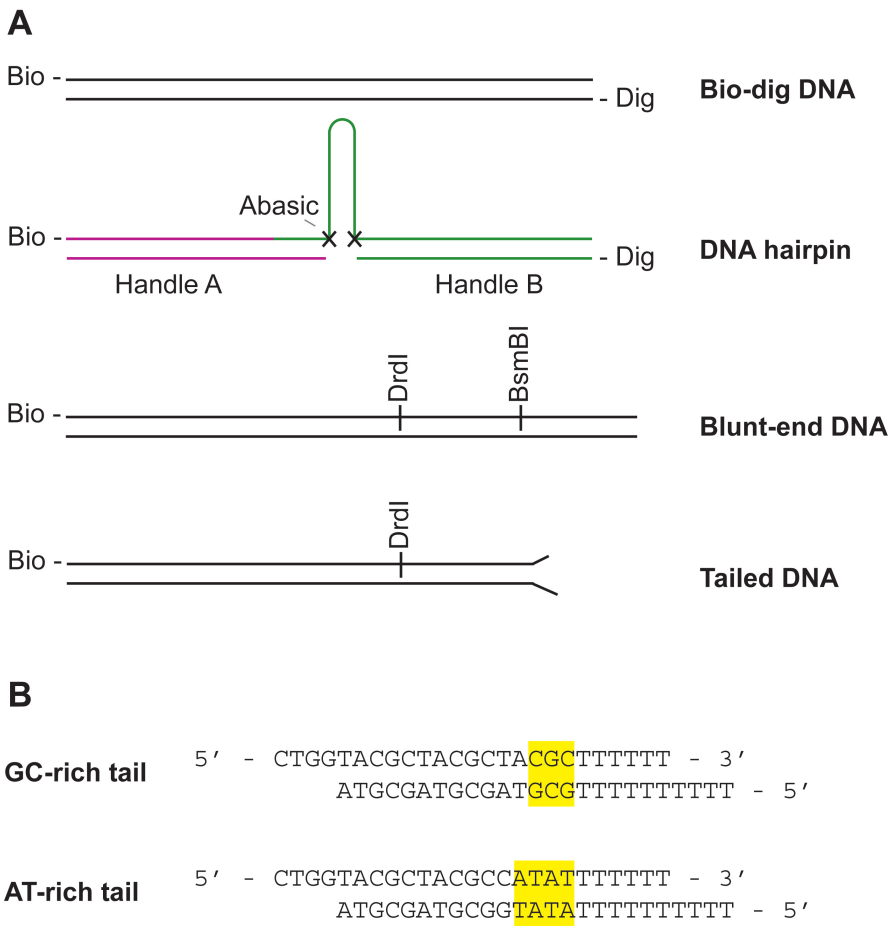

Figure 2.10: DNA constructs. (**A**) We used four DNA constructs. We made DNA tethers using DNA labeled with a biotin (bio) and digoxigenin (dig). For DNA hairpin constructs, we prepared two DNA handles, one with a hairpin, and ligated them together. The abasic sites in the two handles were used to stop the PCR extension reaction. For RecBCD DNA constructs, we made DNA with a blunt-end for RecBCD binding, the other end was biotin labeled for bead linkage. There are two endonuclease sites within this DNA construct for preparation of the last construct, the tailed DNA. The BsmBI site was used to cut the DNA so that tails could be attached, the DrdI site was used to cut the DNA to check ligation. (**B**) DNA tailed substrates had 6 T's on the 3' end and 10 T's on the 5' end, GC-rich constructs contained 3 G-C base-pairs before the tail, while AT-rich constructs contained 4 A-T base-pairs before the tail (*yellow boxes*).

streptavidin (Molecular Probes) for 30 min. After further washing, RecBCD-bio at 15 nM was introduced and incubated for 2 hours. After washing again, the bead-DNA mixture was introduced and incubated for 40 min and then washed with WB. A more detailed protocol is listed in Appendix E. Enzymatic reaction was initiated by flowing in WB supplemented with 2 μM ATP, 1.1 mM E. coli single-stranded binding protein (Promega), and an oxygen-scavenging system (6 mg/ml glucose (MP Biomedicals), 0.2 mg/ml glucose oxidase (Roche Applied Sciences), 30 units/ml catalase), unless otherwise stated. Where indicated, 2 μM ATP was substituted for 2 mM AMP-PNP (adenylyl imidodiphosphate, Sigma-Aldrich) or 2 mM ADP (adenine diphosphate, Sigma-Aldrich) in the above solution.

2.3 Data collection

Data collection relied on data cards (National Instruments, PCI-6052E, PCI-6703, and M-series) and a software suite in LabVIEW (see Appendix C). The methods outlined below were automated for reproducibility and ease of use.

2.3.1 Positional calibration

Data collection requires calibrating the voltage from the QPD into position. To do this, we sequentially scanned the fiducial mark through the detection laser focus in all three axes using the PZT stage and recorded the resulting QPD signals (Fig. 2.11). We fit the QPD lateral response to a 7th-order polynomial over a $\pm$180 nm monotonic range, and the vertical response to a 1st-order polynomial over a $\pm$50 nm linear range. The fit coefficients were then used to calibrate voltage from the QPD into a position in nanometers. Since fiducial marks and conditions vary, this calibration is repeated for each experimental trace. To determine sensitivity, or the slope of the curve, we fit both the lateral and vertical response to a 1st-order polynomial over a $\pm$50 nm range.

Motion in one axis that leads to an optical signal on an orthogonal axis (Fig. 2.11)

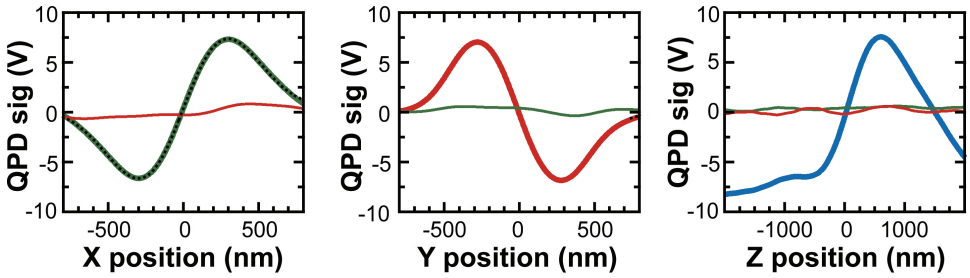

Figure 2.11: Position calibration curves. Calibrations were measured by moving the stage in one axis, while monitoring the on-axis (*thick line*) and off-axis response (*thin line*). Signals in x, y, and z are represented by green, red, and blue, respectively. Centering the fiducial mark in the laser beam required fitting the derivative of a Gaussian to the lateral response (*dashed line*).

complicates detection. Thus, we sought to minimize such optical crosstalk between axes. To remove most of the crosstalk, we precisely centered the fiducial mark relative to the laser beam using an automated routine. Centering was achieved by fitting the lateral response along the horizontal axes to the derivative of a Gaussian and then translating the PZT stage to the Gaussian center point. Further crosstalk removal required careful mechanical adjustments of the fiber tip (translations in x, y, and z) to align the laser focus axially in the microscope. Axial alignment consisted of (*i*) measuring the crosstalk in one axis and determining the slope, (*ii*) translating the fiber in that axis until the slope was minimized, and (*iii*) repeating this minimization for the other axes. Additionally, the back-scattered signals required rotating the quarter-wave plate and the QPD and fixing the mounting angle of the quarter-wave plate such that back reflections off it did not enter the QPD. Using these techniques we obtained ∼2% crosstalk between axes over a 200-nm region. For raster-scanning applications, increased accuracy, or for large displacements, we parameterized the residual crosstalk [24].

2.3.2 Mirror calibration

In the optical trapping microscope we use PZT mirrors to translate the 850-nm and 1064-nm lasers in the image plane. While the PZT mirror input is in voltage, we request these translational movements in nanometers, requiring a mirror calibration. This mirror calibration was done once and was valid unless mirror position on the optical table changed. We calibrated the PZT mirror by scanning a fiducial mark in a grid using the calibrated PZT stage and determined the PZT mirror voltages associated with the center of the fiducial mark at each stage position. We plotted the 2D grid of voltage coordinates, and checked for linearity; a tilted grid means that mirror movement in one axis will generate significant crosstalk on the other axis. The mirror position in the mount was rotated to minimize this crosstalk and create a linear grid. We then determined the calibration for nanometers into volts by linearly fitting the data and

using the slope in each axis along with a linear crosstalk term. To check this calibration, we scanned both the fiducial mark and laser in a grid using the PZT stage and PZT mirror, respectively. The distance of the laser from the fiducial mark center was recorded and verified to be within 5%.

2.3.3 Trap calibration

In the optical trapping experiment we can change the force on the bead (F_{T}) either by changing the bead position (x_{bd}) or the trap stiffness (k_{T}), as $F_{\mathrm{T}} = k_{\mathrm{T}} x_{\mathrm{bd}}$. To change the trap stiffness, we adjust the intensity of the trap (I). This is because the potential of the trapped bead (U) is both proportional to trap stiffness, $|U| = \int F = \frac{1}{2} k_{\mathrm{T}} < x_{\mathrm{bd}} >^2$, and given by the potential of a dipole in an electric field (E), $|U| = \alpha E^2 = \alpha I$, where α is the polarizability. The trap calibration converts trap stiffness (in pN/nm) to a voltage for the trap intensity servo.

There are three methods to calibrate trap stiffness: the equipartition method, the power spectrum method, and the drag method. These three methods have been reviewed extensively [87, 94, 118]. Briefly, the equipartition method draws on the equipartition theorem that allows $\frac{1}{2} k_{\mathrm{B}} T$ of energy per degree of freedom, k_{B} is Boltzmann's constant and T is temperature. Applying this theorem to our trapped bead yields

$$k_{\mathrm{T}} = \frac{k_{\mathrm{B}} T}{< x_{\mathrm{bd}}^2 >}, \tag{2.2}$$

where k_{T} is trap stiffness and x_{bd} is the bead position. The power spectrum method relies on the fact that the responsivity of a trapped bead, as measured by a power spectrum, will roll-off at a particular frequency (f_0) given a particular trap stiffness. The full equation is

$$k_{\mathrm{T}} = 2\pi\beta f_0, \tag{2.3}$$

where β is the drag coefficient of the trapped bead ($\beta = 6\pi\eta r_{\mathrm{bd}}$ far from a surface, η is the viscosity of the liquid and r_{bd} is the bead radius). Finally, in the drag method, the

stage is moved at a particular velocity (v) so as to create a drag force on the trapped bead. By calculating the drag force and measuring the bead position we can determine the trap stiffness,

$$k_{\mathrm{T}} = \frac{\beta v}{x_{\mathrm{bd}}}. \tag{2.4}$$

By calibrating trap stiffness using all three of these methods, we can easily check our stiffness calibration for inconsistencies. The equipartition method does not depend on the drag coefficient (and therefore the bead size or the viscosity of the liquid), the power spectrum method does not depend on the positional calibration, and the drag method will measure the linearity of the trap and so this does not have to be assumed.

We first calibrated the trap stiffness by measuring bead position at ten different voltages of the trap intensity servo. Using this bead position and the resulting power spectrum, we calculated the stiffness given by both the equipartition method and the power spectrum method. For stiffness measurements that were not within 10%, we followed a series of steps to correct the inconsistencies. First, we checked to make sure the measurement axes were aligned with the trapping axes (Fig. 2.12). This is important in the equipartition method where one degree of freedom is measured along the trapping axis. Rotating a half-wave plate moved the trapping axes into alignment. Second, we used all new buffer and sample chambers, since the power spectrum method is sensitive to the viscosity of the liquid. In addition, the power spectrum method is very sensitive to the height above the surface, so we selected the height before every measurement to remove drift or we used a fiducial mark to stabilize the stage in z. Finally, if the trap calibration still did not agree, we rechecked the mirror and positional calibrations, as the equipartition method is sensitive to these calibrations.

We then measured the linearity of the trap and the trap stiffness with the drag method. We measured the bead position at multiple velocities of the stage, plotting drag force vs. bead position. By fitting a line to this curve and measuring the residuals we

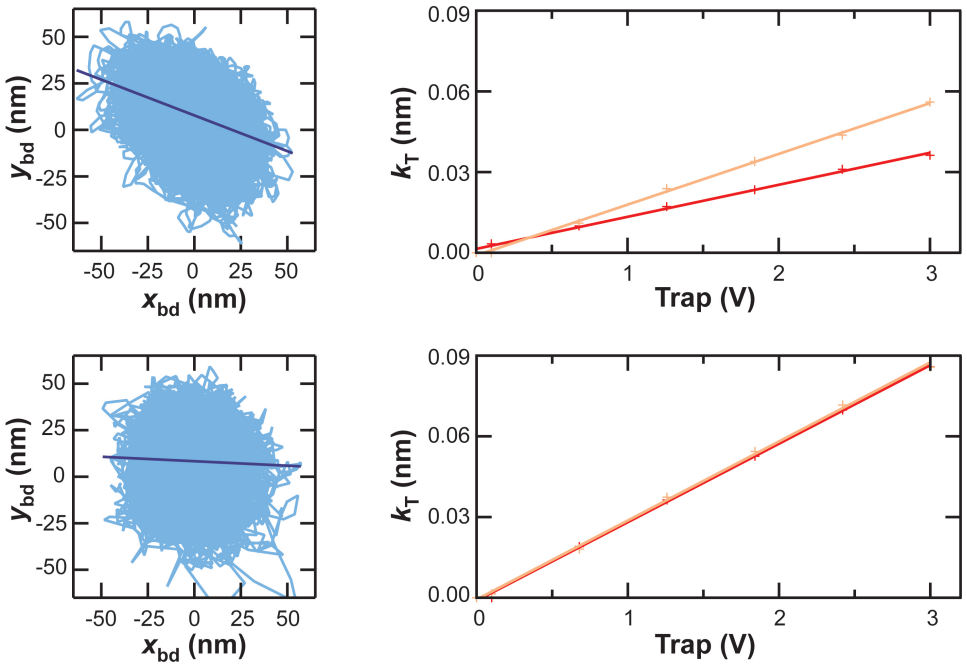

Figure 2.12: Trap calibration is sensitive to polarization. *Left panels.* Trapped bead position (y_{bd} vs. x_{bd}) fit to a line to show polarization orientation. *Right panels.* For the trapped bead in the left panels, the stiffness vs. trap power is shown for both the equipartition method (*orange*) and the power spectrum method (*red*). Polarization orientation must be aligned with the measurement axes for the equipartition method and power spectrum method to agree.

assessed the linearity of the trap; within 5% for ±100 nm. The slope of the line (fit over ±50 nm) was the trap stiffness. It is important when taking this data to account for the slope of the stage and to set the height appropriately. We repeated this measurement of trap stiffness using the drag method at the same ten different intensity servo voltage levels used above.

Finally, using the equipartition, power spectrum, and drag data, we determined the trap calibration. We plotted the trap stiffness measured by each of the three methods against the trap voltage (Fig. 2.13) and verified the stiffness at each value. The data was within 10%. A line was fit to the data (in voltage vs. stiffness) and the linear coefficients were written out as the trap calibration. This calibration was repeated for each bead size and buffer condition, though once taken the calibration is valid as long as the instrument does not change. We checked the calibration by uploading the calibration file and using it to send a voltage to the trap intensity servo. We measured the difference between the desired and measured trap stiffnesses and verified that the difference was ±5%. We also verified that the stiffness of the trap was not sensitive to the position above the surface by measuring trap stiffness at various heights. From 100–1000 nm above the surface the stiffness decreased by ∼2

2.3.4 Positional measurement

We want to measure the position of a fiducial mark over time to both characterize the sample drift and to actively stabilize the sample. In Section 2.3.1 we calibrated the position of a fiducial mark, here we want to use that calibration to take positional measurements over time. To measure fiducial mark position, we first coarsely centered the fiducial mark in the laser focus using a camera. Second, we scanned the sample laterally and fit the resulting QPD voltage curve with a Gaussian to find the fiducial center; we then moved the stage or laser so as to laterally align the fiducial and laser. Next, we scanned the sample in z and selected the center position. We repeated the

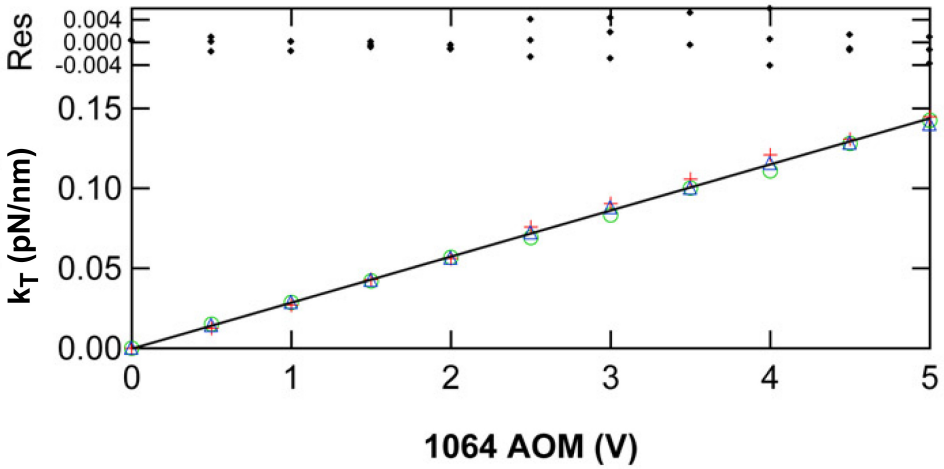

Figure 2.13: Trap calibration. Stiffness is calculated by the equipartition method (*red cross*), the power spectrum method (*green circle*) and the drag method (*blue triangle*). All data points are simultaneously fit with a line (*black*) and the residuals are plotted at the top of the graph (*black diamonds*).

lateral centering and then took positional calibration curves in 3D, see Section 2.3.1. Finally, we used the calibrations to measure the position vs. time. For monitoring the fiducial mark position detected by two laser beams, one beam was aligned using the PZT stage (785-nm laser) and the other was aligned using the PZT mirror (850-nm laser). Note: In the modified microscope for the AFM experiment there were no PZT mirrors so both lasers were aligned using the PZT stage and movement between the lasers was done by turning a mirror knob by hand. A differential measurement was taken by subtracting the positional data recorded by the lasers (e.g. $x_{\mathrm{dif}} = x_{\mathrm{monitor}} - x_{\mathrm{in-loop}}$). Active stabilization was achieved by inputting the in-loop positional data into the software feedback loop and using the monitor positional data as the definitive measure of stability.

In the ultrastable AFM experiment we also want to measure and stabilize tip position. To measure tip position, we first coarsely centered the AFM tip on the 810-nm laser focus using a camera. Second, we touched the tip to the surface and retracted it 300 nm with the AFM PZT translation stage. We then aligned the tip with respect to its laser to minimize crosstalk accompanying lateral motion. This alignment was achieved by dithering the AFM tip along each axis sequentially and changing the center position of the dither. This procedure collapsed the majority of the crosstalk (which was deterministic and reproducible) onto the vertical axis. Next, we translated the tip about its optimum alignment point on each axis sequentially and fit the center portion ($\pm$50 nm) of the resulting curves to first-order polynomials. The linearity of the signal and the crosstalk within this restricted region allowed us to use a linear parametrization. This calibration was then used to convert voltage from the 810-nm QPD into position. Finally, we measured position over time and used this measurement as the in-loop signal to stabilize the tip. When monitoring the stability of the technique, we aligned a second laser, the monitor laser, to the tip to measure position as well. For imaging, we calibrated while in contact with the surface.

2.3.5 DNA elasticity measurement

A DNA elasticity measurement stretches the DNA while recording the force on the DNA at each extension value. This measurement is used to laterally align the tether point to the laser, as well as determine the DNA contour length and persistence length. First, we trapped a DNA-tethered bead. We then determined the vertical location of the surface by monitoring the z voltage on the QPD as the tethered bead was brought into contact with the surface [87], and we lowered the stage 300 nm. Next, bead position was calibrated. Finally, the program laterally moved the stage to stretch the tether, while measuring bead position to determine both force and extension [131]. The resulting elasticity curve was fit with the modified Marko-Siggia formula [71] to determine the tether point, DNA contour length, and DNA persistence length. The tether point, which is the position of the tether anchor relative to the laser focus, was used to align the tether to the laser. We stretched the DNA twice in both lateral directions to center the tether and a third stretching curve was used to determine DNA contour length and persistence length. The error in the tether point and persistence length measurement was $\sim$2 nm, while the error in the DNA contour length was 7 nm rms due to the uncertainty in the bead radius. If the elasticity measurement showed a larger error we rechecked the positional, mirror, and trap calibrations.

2.3.6 DNA length measurement

To measure DNA contour length, we first determined the vertical location of the surface by monitoring the sum signal as a tethered bead was brought into contact with the surface [87]. We calibrated the trapped bead position and then lowered the stage 300 nm. We found the lateral tether point position by performing a 2D elasticity-centering procedure, which also returned the persistence length. Bead-DNA complexes anchored by multiple DNA molecules (determined by a low persistence length) were not studied.

We next centered the 850-nm laser on a nearby fiducial mark by moving the laser with the PZT mirror and calibrated fiducial mark position. Finally, we stretched the DNA along the y-axis using the PZT stage to a specified force (with a corresponding move of the fiducial-tracking laser). After recalibrating the fiducial mark, we actively stabilized the sample using a simple software-based feedback loop with a 100 Hz update rate and a proportional gain of 0.05. Concurrent with measuring fiducial mark position, the software also measured the trapped bead position to determine DNA length [131].

For measuring DNA hairpin dynamics under constant force, we implemented a force clamp in parallel with the above stage stabilization. We modulated k_{T} at 100 Hz such that the force ($F_{\mathrm{T}} = k_{\mathrm{T}} x_{\mathrm{bd}}$) was maintained to $\sim$0.01%. Modulations in k_{T} were about $\sim$20% to maintain constant F_{T}.

For measuring RecBCD movement, we implemented a pseudo force clamp in parallel with the above stage stabilization. RecBCD movement causes motion of the bead relative to the trap center, which changes the force. To keep the force within 15% of the initial value we allowed movement of the trapped bead to $\pm$10 nm from the clamp position (70 nm). Bead motion larger than this triggered the stage to reset the bead position back to the clamp value, with a corresponding movement of the PZT mirror that controls the fiducial-tracking laser.

2.4 Data analysis

2.4.1 Data processing

Raw data was collected at 4 or 10 kHz and filtered using an 8th-order, low-pass, elliptic filter. The data was digitized with a 16-bit, 20-V-range data card in the optical trapping experiment and an 18-bit, 20-V-range data card in the AFM application. We then used a software filtering algorithm in IGOR. We smoothed the data with either a moving box-car window or a moving Savitzky-Golay window [101]. The box-car window

smooths out higher frequency signals and introduces a bias into the data if the signal has a nonzero second derivative, as compared to the Savitzky-Golay window [101]. For an illustration of how the two windows smooth differently see Figure 2.14. Where indicated, we also decimated the smoothed data so that each point was independent, that is we removed all of the overlapping windows from the smooth function.

2.4.2 Noise determination

To determine the noise level of the data, we used three different metrics. The first metric was to take the standard deviation (σ) of the data smoothed with a box-car window; the upper limit in the bandwidth is the smoothing frequency while the lower limit in the bandwidth is the inverse time interval. The second metric was to calculate the integrated noise over a particular bandwidth. We first calculated the power spectrum of the raw data using a scaled power spectrum function (Power Spectral Density.ipf in IGOR), a Hann window, and the largest window size possible. Then, the square root of the integral of the power spectrum over the specified bandwidth was calculated to give the integrated noise. Theoretically, the standard deviation and the integrated noise should be equal given Parseval's theorem; experimentally, they were within 5%. The final metric was to plot the histogram of the data and measure the HWHM. For a Gaussian peak the HWHM is related to the standard deviation by a factor (HWHM = $\sqrt{2\ln 2}\sigma$).

2.4.3 Step detection

To determine steps within the data, we used three different metrics. The first metric was to plot the histogram of the data. Step size was the distance between peaks and the noise level was the HWHM. The second metric we used was a pair-wise distance difference of the data. The pair-wise distance difference is a measure of the distance between pairs of points in the data. By plotting a histogram of the pair-wise distance

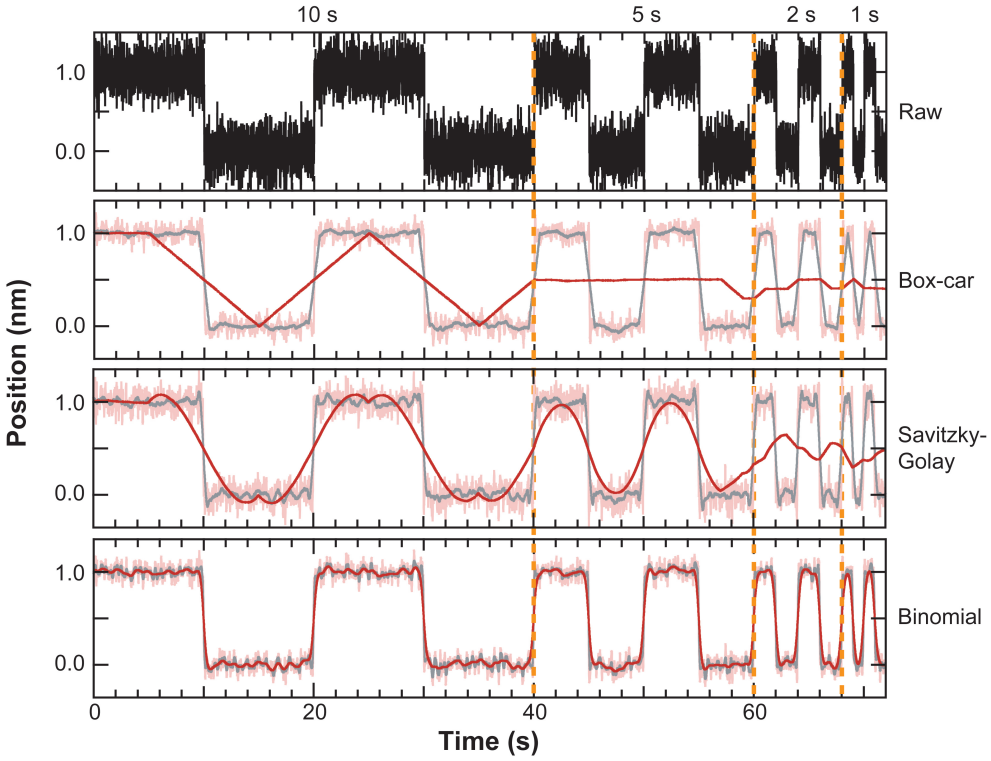

Figure 2.14: Window type affects data smoothing. We simulated 100-Hz, raw, positional data (*black, top*) by adding Gaussian noise to an ideal 1-nm stepping signal. At first, steps occur every 10 s, then 5 s, then 2 s, and finally 1 s, as separated by the orange dashed lines. The raw data is smoothed to 10 Hz (*pink*), 1 Hz (*gray*), and 0.1 Hz (*red*) using a box-car window (*middle top*), a Savitzky-Golay window (*middle bottom*), and a binomial window (*bottom*). Data is presented as back-and-forth steps for clarity. If we instead plot linearly increasing steps (*data not shown*) and fit these steps with a step fitting algorithm [48], we can quantitatively compare the smoothing algorithms. We define the parameter r_{best} as the ratio of the smoothing frequency at which we fit 90% of the steps with the correct height and the dwell time, divided by the stepping frequency of the simulated data. For the box-car window $r_{\text{best}} = 2.7$; for the Savitzky-Golay window $r_{\text{best}} = 1.0$; and for the binomial window $r_{\text{best}} = 0.2$.

difference there will be peaks at intervals of the step size; the noise is defined as the HWHM of the peak. In addition, we took the power spectral density of the pair-wise distance difference histogram; a peak in the power spectrum will occur at the most likely distance-difference, the step size. Finally, we fit the data using a step finding algorithm based on a maximum likelihood parameter [48]. The data was assumed to be either increasing or decreasing. One step was fit to the data and the likelihood parameter was found. Then two steps and so on until the algorithm reached the user defined stopping point (300 steps) and output the plot of likelihood vs. number of steps, which contained a peak. The user then input the number of steps just to the left of the peak and the program output the fit steps, the mean and standard deviation of which was the step size and the accompanying noise level, respectively.

Chapter 3

Microscope stabilization to 1 Å

3.1 Introduction

Mechanical drift between the objective and sample is a long-standing problem in microscopy that occurs in all three dimensions. Typical drift rates, around ∼1 nm/s [52, 89], can be caused by mechanical settling of the objective or stage, thermal heating of the objective or sample, or acoustic vibrations. Such large drift increasingly limits the localization precision of the microscope. Localization of a single object is not limited by the Rayleigh criterion and has been widely used in single molecule experiments to resolve nanometer-scale motion of beads [119], fluorophores [138], and organelles [58]. Localization *in vivo* can also resolve features down to 16 nm [133], well below the diffraction limit (∼200 nm). In addition, there is a strong desire to increase the localization precision to 1 Å for a myriad of biophysical applications [77], including measuring [1] enzymatic motion along DNA. As researchers increase localization precision to measure smaller and smaller distances, the mechanical drift between the microscope objective and the sample becomes increasingly problematic.

Moreover, in surface-coupled optical trapping assays this unwanted mechanical drift is the dominant source of instrumental noise [89]. The goal of our research is to use surface-coupled optical trapping experiments to measure the discrete motion of a helicase as it unwinds the DNA duplex. Motion can be as small as 1 bp (3.4 Å) [61, 125], while mechanical drift limits localization precision to ∼6 bp (20 Å) [89, 96].

In a surface-coupled optical trapping assay (Fig. 2.1), the enzyme is typically anchored to the surface, while an optically trapped bead, indirectly coupled to the enzyme by a protein or a DNA molecule, detects the enzymatic motion [5, 11, 45, 48, 64, 120, 132, 140]. Drift is then coupled into the bead-enzyme distance measurement, obscuring the underlying motion. Ideally, such unwanted drift would be eliminated in all three dimensions, since many experimental geometries are sensitive to both horizontal and vertical drift [96, 130, 131].

The introduction of a fiducial mark, or a reference point, into the system provides a means to measure and minimize objective-sample drift. Commonly, the fiducial mark is a micron-sized bead affixed to the microscope cover slip, the position of which is deduced using video-imaging analysis [14, 115]. Such measurement has been used in a feedback loop to stabilize an optical microscope in three dimensions [14, 115], achieving 0.8-nm stabilization at 25 Hz [14], though without independent verification. Compared to video-based techniques, laser-based detection [33, 37, 128] offers significantly enhanced bandwidth and potentially sub-picometer resolution [23]. Laser-based detection also depends on the relative position of the laser (set by the objective) to a fiducial mark (attached to the cover slip) in three dimensions [100] and is, therefore, a promising candidate for 3D stabilization of the objective-sample position. The problem is that, historically, instrumental noise particularly at low frequencies (0.1–100 Hz) has limited laser-based detection measurements [37, 49, 128].

We overcame this instrumental noise and used laser-based detection to achieve Ångstrom-scale stabilization of an optical microscope in 3D. We first measured the position of a fiducial mark coupled to the microscope sample with a detection laser ($\lambda =$ 785 nm), the in-loop laser. Then, we used a software-based feedback loop to a PZT stage to compensate for drift in the fiducial mark position (Fig. 3.1). Hence, we effectively stabilized the microscope sample position to the in-loop laser focus, which is coupled to the objective, stabilizing the sample-objective distance. Several factors contributed to

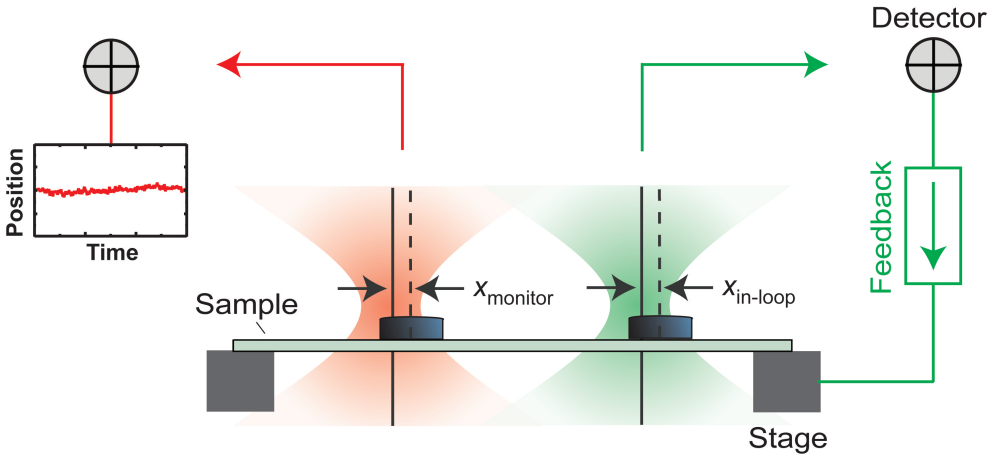

Figure 3.1: Basic principle of microscope stabilization. We measured the position of the sample (e.g. $x_{\mathrm{in-loop}}$) by detecting the scattering of a focused laser beam ($\lambda = 785$ nm) off a fiducial mark. This position is then used in a feedback loop to a piezo-actuated stage to keep sample position constant. To monitor stability, we measured the position of a second fiducial mark (x_{monitor}) using another focused laser ($\lambda = 850$ nm).

this experimental realization: decreasing the low-frequency instrumental noise apparent in laser-based detection, increasing the sensitivity of laser-based detection to vertical motion, and fabricating a fiducial mark that was firmly coupled to the sample (and thus, an accurate representation of sample position). Using this technique, we achieved a stability of 1.1 Å, 1.0 Å, and 0.9 Å (rms, Δf = 1–25 Hz) in x, y, and z, respectively.

The stabilities reported here are independently verified with a second detection laser (λ = 850 nm), the monitor laser, which monitors fiducial mark position (Fig. 3.1). The simple application of feedback loops, without independent verification of their performance, can lead to erroneous conclusions of stability. Let us consider one source of instrumental noise: laser-pointing instability. Such pointing noise causes apparent motion between the objective and the sample that is erroneously compensated for by the feedback loop. Without independent verification, we have no knowledge about this erroneous compensation. We note that the use of a monitor laser is not always a truly independent verification since the monitor laser is immune to common-mode fluctuations that both lasers share, such as air currents and vibrations of optical mounts. However, in our system a large fraction (40%) of the optical path is not common-mode, and the common-mode optical elements (excluding the objective) are rigidly attached to the microscope frame or the optical table by custom-made, large-diameter (38-mm) aluminum posts. Vibrational testing suggests that the limits in the mechanical stability of our system are the fiber launches and the QPDs, which are independent for each laser. Therefore, in our system, the monitor laser did represent an independent measurement of microscope stability.

3.2 Decreasing low-frequency laser noise

More than a decade ago it was shown theoretically that laser-based measurements could achieve subpicometer localization of micron-sized beads [23]. However, instrumental drift, particularly at low frequencies (.01–100 Hz), limited such measurements [128].

To overcome this instrumental drift, we significantly increased the low-frequency stability of laser-based detection by addressing multiple sources of laser noise.

Previously, our group addressed one source of low frequency noise, laser pointing noise, by using fiber-coupled lasers and holding the fiber end in a stable, mechanical mount [89]. However, fiber coupling a laser translates pointing instability into intensity noise. Additionally, coupling a laser into a single-mode polarization-maintaining fiber translates mode and polarization fluctuations into intensity noise. This added intensity noise adversely affects position measurements, particularly in z, where measurements are proportional to intensity.

To minimize the effects of various laser noise sources, we used an AOM-based laser intensity stabilization (see Section 2.1.4). The active stabilization method consisted of passing the laser sequentially through an AOM, a single-mode, polarization-maintaining fiber, and a polarizing beam splitter (Fig. 2.6). Then we sampled 10% of the light onto a photodiode to measure intensity, which was stabilized by a feedback loop to the AOM. This method decreased the intensity noise of both detection lasers to 0.002–0.005% over the low-frequency bandwidth of 0.02–100 Hz. In this manner, a number of noise sources (pointing, mode, and polarization) were minimized by translating them into intensity noise that was also minimized, in turn, by the intensity feedback loop. In addition, we have stabilized the low-frequency laser noise responsible for limiting previous positional measurements.

3.3 Increasing the sensitivity of laser-based detection

Previously, our group showed that laser-based detection is sensitive enough to track the position of a fiducial mark in the lateral directions (x and y) with 1 Å precision at 1 kHz [89]. We now needed to increase the sensitivity of the signal in the vertical direction, z. The z positional signal is deduced from the sum voltage of the QPD (see Section 2.1.3), which is proportional to intensity. More specifically, this vertical signal

arises because laser intensity is phase-shifted by the Guoy phase shift at the focus of the laser [100]. This phase-shifted intensity scatters off the fiducial mark and interferes with the incident beam in the back-focal-plane of the condenser. The interference leads to a small modulation on top of a comparatively large signal that is proportional to intensity. Hence, fluctuations in intensity appear as fluctuations in z.

The inherent sensitivity (in volts per nanometer, see Section 2.3.1) in z was small (0.2 mV/nm), as deduced by moving the fiducial mark vertically through the laser focus (Fig. 3.2 **A**, *purple*). To increase this sensitivity, we used an offset amplifier to optimally match the variable portion of the sum signal to the 20-V dynamic range of the 16-bit data acquisition card. This amplification led to an enhanced sensitivity of 27 mV/nm, sufficient to resolve 1 Å motion (with a digitization of 0.3 mV/bit). Finally, the combination of offset amplification with intensity stabilization yielded an additional benefit: small, periodic oscillations in the sum signal were eliminated. Since intensity was stabilized before the laser entered the microscope, these oscillations are not cavity effects between the bead and the cover slip that are forward-scattered [86]. We speculate that these oscillations result from a small amount of reflected light that feeds back into the diode laser cavity (making it through both the AOM and the optical isolation system) and cause mode-hopping of the laser.

After increasing the sensitivity of the signal in z, we measured the noise level of the signal using differential detection, as was done previously for x and y [89]. In this technique, the position of one fiducial mark is measured with two detection lasers. The difference in the position records is calculated (e.g., $z_{\mathrm{dif}} = z_{\mathrm{in-loop}} - z_{\mathrm{monitor}}$), which computationally removes any mechanical drift and leaves residual laser noise [89]. Even after removing mechanical drift, the original z signal was shown to be too noisy to achieve 1 Å stability in z_{dif} (Fig. 3.2 **B**). This excess noise was primarily intensity noise. Thus, in the intensity-stabilized z_{dif} measurement there was marked improvement. However, only by coupling intensity stabilization with offset amplification

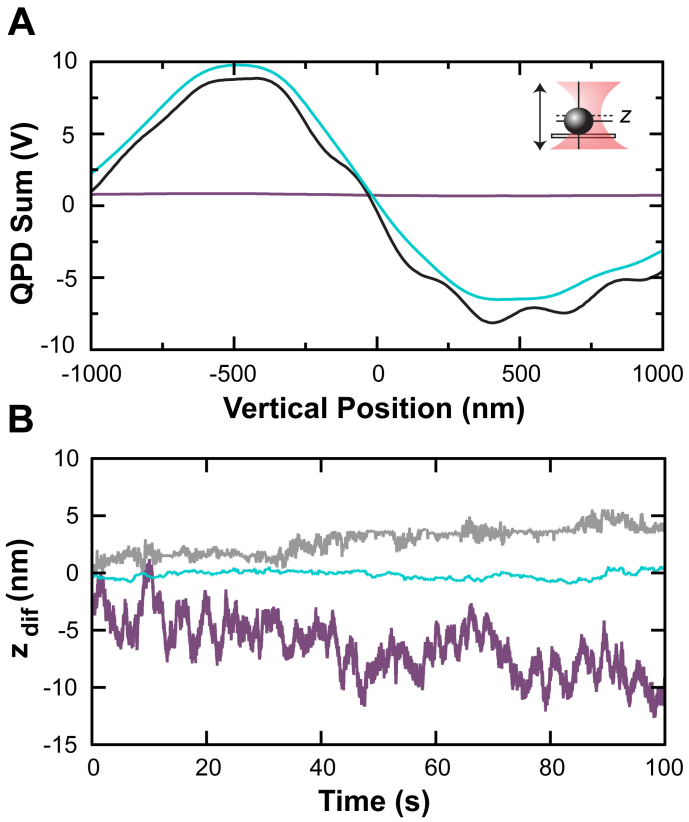

Figure 3.2: Vertical sensitivity enhancement. (**A**) Height calibration signals for an affixed bead that was scanned vertically through the detection laser. The traces represent the inherent signal (*purple*), offset-amplified signal (black), offset-amplified signal with intensity servo active (*blue*). (**B**) Differential measurements of vertical motion ($z_{\mathrm{dif}} = z_{\mathrm{in-loop}} - z_{\mathrm{monitor}}$) using two lasers and a 400-nm-diameter affixed bead as a fiducial mark. Traces represent the inherent signal (*purple*), the intensity-stabilized signal (*gray*), and the offset-amplified signal with intensity servo active (*blue*). Traces displaced vertically for clarity.

did we achieve a 1 Å differential stability. More quantitatively, the average short term (1–25 Hz) differential stability was 1 Å, determined from the average standard deviation of a non-overlapping series of one-hundred 1-s intervals ($\bar{\sigma}_z$). Long-term differential stability was $\leq$3.3 Å as measured by the standard deviation over a 100-s interval (σ_z, $\Delta f = 0.01$–25 Hz). We note that, as before [89], lateral differential stability was excellent (Fig. 3.3), achieving sub-Ångstrom precision ($\bar{\sigma}_x = 0.4$ Å, $\bar{\sigma}_y = 0.4$ Å). Since differential stability is a measure of the residual laser noise in the system, it represents an ultimate limit for microscope stability using this technique.

3.4 Firmly coupling fiducial marks to the sample

The enhancements in laser stabilization and sensitivity can only improve measurements of sample position if the fiducial marks are firmly coupled to the cover slip. Previously [89] and in Figure 3.2, 400-nm-diameter polystyrene beads, melted to the cover slip, were used as fiducial marks. Unfortunately, our melted beads still demonstrated significant motion. When differential detection or video-based detection was used to detect the position of one fiducial mark, fiducial movement relative to the surface was undetected (Fig. 3.3 **A**). However, if differential detection was used to detect two fiducial marks, then fiducial movement relative to the cover slip was visible. In fact, in ~80% of our traces, beads moved $\geq$1 Å relative to the cover slip (Fig. 3.3 **B**). Such motion limited our ability to stabilize the microscope and presumably limited the stability of the work of others as well, though in such cases this added motion would have been unseen without an independent measurement.

To surmount these challenges, we fabricated an array of fiducial marks that were an integral part of the cover slip. Low-index glass posts (see Section 2.2.1) yielded excellent optical signals with sensitivities in x, y, and z sufficient for sub-Ångstrom resolution and were, as expected, stable relative to the cover slip (Fig. 3.3 **C**). To elucidate how these sensitivities scaled with volume, we constructed a range of posts

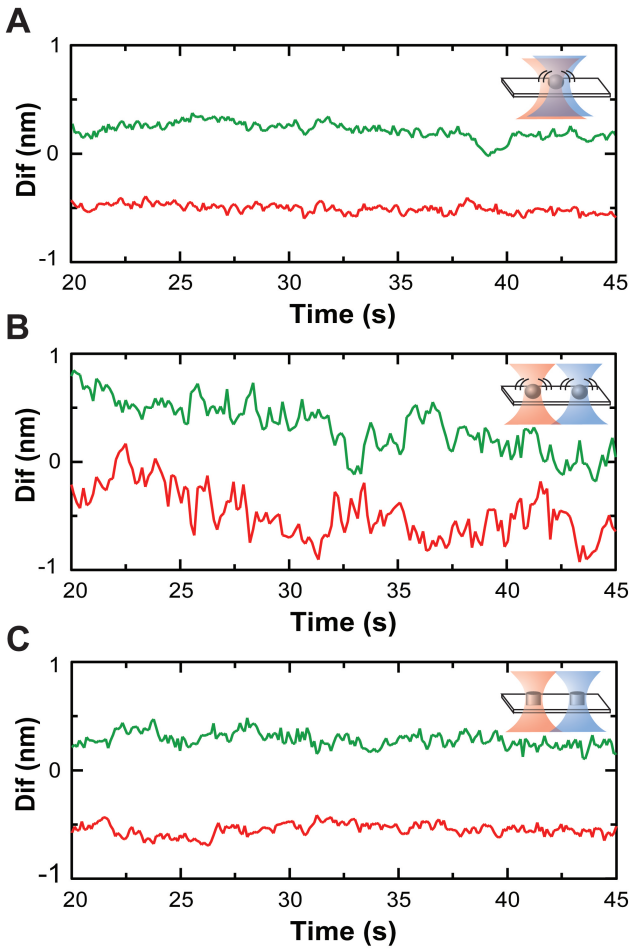

Figure 3.3: Fiducial mark movement as displayed by a differential measurement in x ($x_{\mathrm{dif}} = x_{\mathrm{in-loop}} - x_{\mathrm{monitor}}$, *green*) and y ($y_{\mathrm{dif}} = y_{\mathrm{in-loop}} - y_{\mathrm{monitor}}$, *red*). (**A**) Both lasers measure the position of one affixed bead (inset), masking the underlying bead movement. (**B**) Each laser measures the position of different affixed beads (inset) so that bead motion is apparent. The displayed trace is truly an average response with a noise level that is the median value for ten trials. (**C**) Each laser measures the position of a fabricated post (inset), which does not display movement. Traces displaced vertically for clarity.

with varying w (350-725 nm). Interestingly, the sensitivity was proportional to the volume of the post (Figure 3.4 **A**), agreeing with a model of the post as a point with a polarizability proportional to its volume [37, 100], even though the dimensions for larger posts were comparable to the wavelength of the laser ($\lambda = 785$ nm).

As an alternative fiducial mark, we also investigated etched holes (see Section 2.2.1). Holes with different openings, w, gave different signals (Fig. 3.4 **B**). For the smallest openings investigated, 100 nm, we measured an approximately linear signal over an extended range. However, for larger openings, the response was nonlinear in the middle of the hole. We conclude that hemispherical holes yielded high quality signals, but flat-bottom holes did not. Additionally, holes have their optical center $\sim$1 μm below the plane of the trapped bead, which requires detector beam foci to be in different planes, an added complication.

3.5 Active microscope stabilization

To actively stabilize the microscope, we first measured post position with the in-loop laser. Then the stage position was updated at 100 Hz to keep the position constant in all three axes. The monitor laser, recording the same post, independently determined microscope stability (Fig. 3.5 **A**). We note that this independent verification of microscope stability, once performed, is not necessary in day-to-day stabilization applications. Using the monitor laser, we achieve short-term microscope stabilities, as described in Section 3.3, of $\bar{\sigma}_{\mathrm{x}} = 1.1$ Å, $\bar{\sigma}_{\mathrm{y}} = 1.0$ Å, and $\bar{\sigma}_{\mathrm{z}} = 0.9$ Å (Δf = 1–25 Hz); and long-term stabilities of $\sigma_{\mathrm{x}} = 1.7$ Å, $\sigma_{\mathrm{y}} = 1.2$ Å, and $\sigma_{\mathrm{z}} = 3.5$ Å (Δf = 0.01–25 Hz). We note that the bandwidth of our feedback loop (100 Hz) is limited by the resonance frequency of the stage (unloaded: 450 Hz horizontal and 1100 Hz vertical) and the software-based processing speed. Stiffer PZT stages with higher resonances should lead to lower noise and higher bandwidth stabilization.

The robustness of this 3D stabilization was demonstrated by introducing a large,

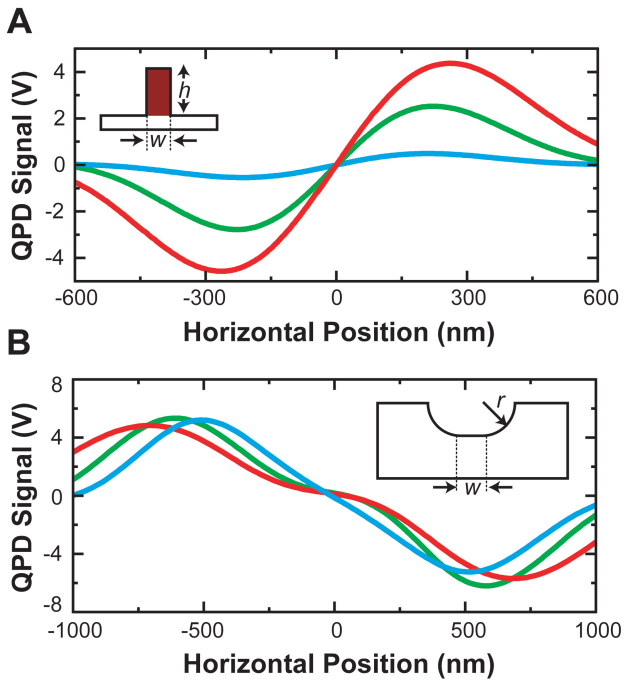

Figure 3.4: Fabricated fiducial mark signals. (**A**) Horizontal response for low-index glass posts of varying size. Posts were a constant height, $h = 600$ nm, with widths (w) of 350 nm (*blue*), 550 nm (*green*), or 725 nm (*red*). Inset, geometry of a post. (**B**) Horizontal response for etched holes of varying size. Holes had a constant radial depth ($r = 500$ nm) with initial openings, w, of 100 nm (*blue*), 200 nm (*green*), or 300 nm (*red*). Inset, geometry of a hole.

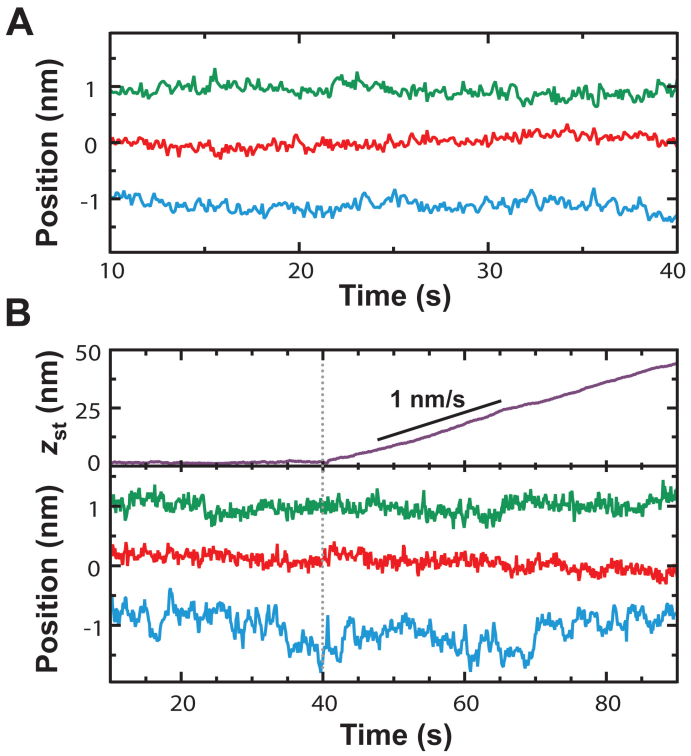

Figure 3.5: Active microscope stabilization to 1 Å. (**A**) Sample positional stability measured by the independent monitor laser, x_{monitor} (*green*), y_{monitor} (*red*), and z_{monitor} (*blue*). (**B**) As in **A**, independent position records with active stabilization before and during heating. At 40 s, the objective was heated, leading to significant vertical drift that was compensated for by moving the PZT stage (e.g., z_{st}, *purple*, vertical stage position). Traces displaced vertically for clarity.

temporally controllable drift. We heated the objective with the trap laser (λ = 1064 nm), which had a transmission of 59% [88]. This type of perturbation is often found in optical-trapping assays [87, 96, 130], and a similar motion arises from the common problem of objective settling. Specifically, we actively stabilized the microscope at a constant low laser power of 50 mW (Fig. 3.5 **B**), then the laser power was increased by a factor of three to 150 mW at 40 s. During the following 50 s, the active stabilization compensated for the thermal expansion of the objective by moving the PZT stage 44 nm to keep the vertical position of the post constant. We note that active stabilization in the presence of substantial drift yielded excellent long term stabilities of 1.5 Å, 1.4 Å, and 2.6 Å (Δf = 0.02–25 Hz) for σ_{x}, σ_{y}, and σ_{z}, respectively. Short-term stability (1–25 Hz) was essentially unchanged at 1.1 Å, 1.0 Å, and 1.0 Å for $\bar{\sigma}_{\mathrm{x}}$, $\bar{\sigma}_{\mathrm{y}}$, and $\bar{\sigma}_{\mathrm{z}}$, respectively.

3.6 Conclusions

The experimental advances presented here allow for 1 Å stabilization of an optical microscope in three dimensions. The keys to achieving this stabilization were decreasing low-frequency laser noise, increasing the sensitivity of the measurement in z, and firmly coupling a fiducial mark to the surface to measure microscope drift. We anticipate that this technique will be useful in precision particle tracking [138] and surface-based fluorescence measurements [11]. More importantly, active microscope stabilization sets the foundation for a precision optical trapping assay. Typically, surface-coupled optical trapping assays have a ∼20-Å noise level [96] that is dominated by mechanical drift [89]. By stabilizing this mechanical drift we reduce the noise so that precision measurements are possible. In particular, measurements of enzymatic motion along DNA (helicase unwinding, polymerase extension, translocase movement), which could be as small as 1 bp (3.4 Å), are especially motivating.

Chapter 4

Modified microscope stabilization for AFM

4.1 Introduction

Drift is a long-standing problem in microscopy. In an AFM, lateral drift between the sample and the AFM tip at ambient conditions is on the order of 5 Å/s [52, 123]. To circumvent drift and achieve Ångstrom-scale resolution, fast, lateral scanning of the tip is necessary, though this reduces the signal-to-noise (S/N) ratio (Fig. 4.1). However, drift must be addressed for long time-scale scanning, for accurate registration of the tip over the sample, for stationary "hovering" of the tip above a point of interest, or for imaging 1D objects (nanotubes) and zero-point objects such as complex protein structures, nanopores, or quantum dots. Thus, there is a clear need for tip-sample control with Ångstrom-scale positional precision, registration, and stability. While such a combination has been achieved passively in scanning probe microscopes at cryogenic temperatures [29] and in ultrahigh vacuum [117], there is no routine method to achieve this triumvirate of requirements in air or fluid at room temperature.

Several existing methods address active tip-sample control with varying success. Commercial, closed-loop PZT stages provide for Ångstrom-scale stability using capacitive sensors to maintain stage position with respect to the frame. However, these sensors are often located many centimeters away from the measurement position, allowing for unseen sample drift. Tracking techniques [2, 99, 116] can yield atomic precision in ultra-high vacuum, but they forfeit scanning or assume unvarying drift rates. Software-

based techniques [43] can reduce drift rates to ∼5 Å/min in ambient conditions [78], but require predictions of future drift or compensate for drift only once per AFM image. External optical techniques, applied in one [102, 113] or more dimensions [81, 79], have not achieved Ångstrom-scale tip-sample stability or image registration (<10-nm overlay precision [79]).

Previously, we demonstrated Ångstrom-scale sample control in 3D for a microscope with an optical-trapping application [17]. Stability was achieved by first detecting the position of a fiducial mark on the sample with a focused laser, then implementing a feedback loop to a PZT stage to keep the position constant. However, since that work used forward-scattered light [128], it is not compatible with AFM applications due to limited or poor quality optical access opposite the imaging objective. Yet, BSD, initially demonstrated over 10 years ago for optically trapped beads [33], is a viable alternative. In this implementation, the sample and tip would be stabilized using the BSD position of each in a feedback loop (Fig. 4.2), though we see three critical criteria to demonstrate before BSD is adopted for tip or sample control in AFM (or in optical trapping applications). These criteria are: (*i*) Ångstrom-scale sensitivity in 3D, (*ii*) similar-scale stability, and (*iii*) low optical crosstalk between detection axes for scanning and registration purposes.

We overcame these limitations and used BSD to actively stabilize a microscope. We first enhanced the BSD signals from the fiducial mark, and minimized the crosstalk between axes (x-y coupling of 3% and x-z coupling of 1%). After establishing these high quality BSD signals (Section 4.2), we then demonstrated active stabilization of a microscope (Section 4.3) to <1 Å rms (Δf = 0.1–50 Hz). This active stabilization allows for stabilized scans (Section 4.4), composed of orthogonal steps, and registration that is maintained to <0.5 Å rms, even after many 100-nm displacements (N = 14). More importantly, this microscope stabilization represents the enabling technology for an ultrastable AFM.

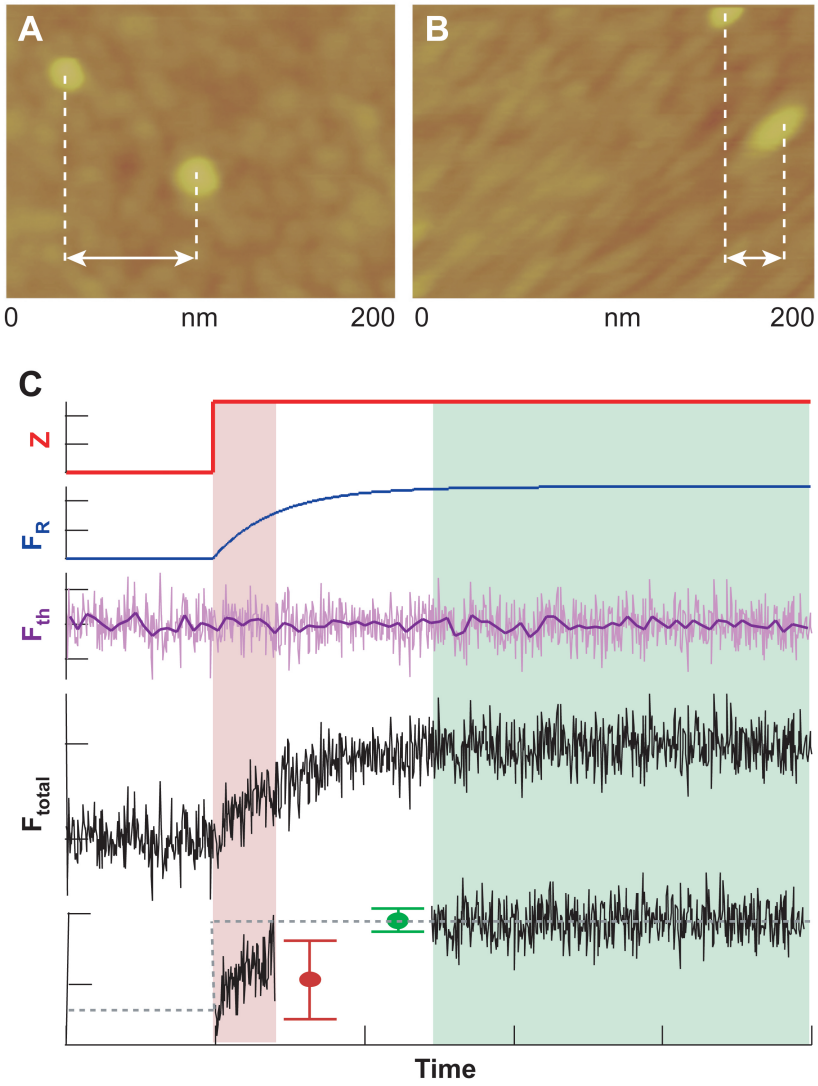

Figure 4.1: One motivation for an ultrastable AFM: fast scans overcome drift but sacrifice S/N ratio. (**A**) AFM image of two gold nano-spheres on the surface taken with a fast scan speed (150 μs/pixel) relative to the cantilever response time (250 μs). (**B**) Same as in **A** with a slower scan speed (10 ms/pixel). Tip-sample drift during imaging distorts the image. (**C**) Scan speeds that have a time per pixel that is shorter than the cantilever response time sacrifice S/N ratio. The force on the cantilever (F_{total}), which is the sum of an ideal force (F_{R}) plus thermal noise (F_{th}), changes when a surface feature (Z) is encountered. If the time per pixel is shorter than the cantilever response time (*red shaded region*), the signal (*red data point*) is lower and the noise (error bars) is higher than if the time per pixel is several cantilever response times (*green shaded region*, *green data point*). Figure credit: Gavin King and Allison Churnside.

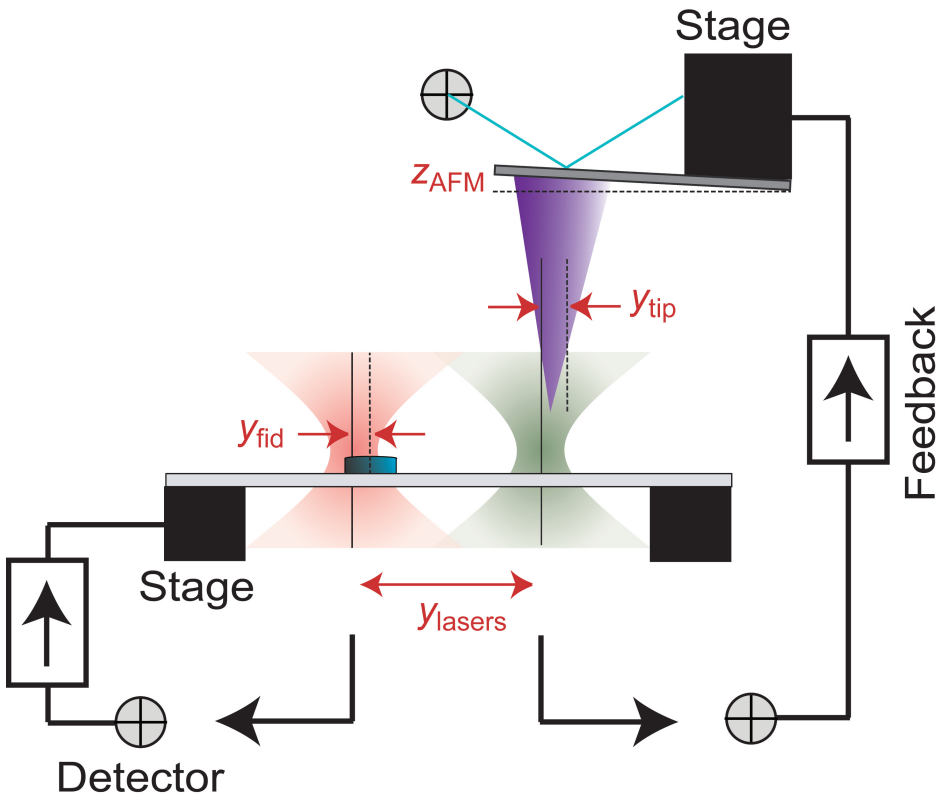

Figure 4.2: Basic principle of AFM stabilization. A focused laser scattered off a fiducial mark on the surface and the back-scattered signal was detected by a QPD to measure fiducial position (y_{fid}). This position was then used in a feedback loop to the sample PZT stage to keep fiducial position constant. Similarly, a second focused laser and QPD measured the position of the apex of the AFM tip (y_{tip}), and a feedback loop to the tip PZT stage stabilized that position. Overall AFM stability relied on the differential pointing stability between the lasers (y_{lasers}), which was 0.2 Å over 0.1–50 Hz. Normal AFM imaging (z_{AFM}) with an optical lever arm detection was not affected.

The application of this active stabilization system in AFM is discussed in Section 4.5. We show that using these BSD signals we can stabilize tip position to ¡1 Å (rms, Δf = 0.01–10 Hz), which allows "hovering" over a region of interest. In addition, by stabilizing both the tip and the sample, we achieved stable scanning and registration of 2.4 Å for one hour. Two-dimensional images taken in this way showed 4-5 pm/min of residual drift, similar to results achieved in cryogenic conditions of 1 pm/min [116].

4.2 Increasing the sensitivity of back-scattered detection

Previously, BSD sensitivity was reported as ∼0.2 mV/nm, which is too small to measure Ångstrom-scale motion (digitization at 0.1 mV/bit). We increased the sensitivity of BSD by both increasing the BSD efficiency so that more light was incident on the detector (see Section 2.1.2) and amplifying the resulting signals (see Section 2.1.3). To check the resulting sensitivity, we sequentially scanned the silicon disk fiducial mark through the laser focus in all three axes using the PZT stage and recorded the resulting detector signals (Fig. 2.11). This yielded sensitivities of 38 mV/nm, 40 mV/nm, and 20 mV/nm in x, y, and z, respectively. Thus, BSD has the sensitivity to detect single-picometer motion, though our differential stability (19 pm) is currently limited by other laser noise sources (see Section 4.3). Additionally, we achieved a low level of crosstalk: 3% between x and y signals and 1% between lateral and z signals over a 200-nm region, similar to the results achieved using forward-scattered light [60]. For raster-scanning applications, increased accuracy, or for large displacements, we parameterized the residual crosstalk [60].

The high sensitivity of BSD is not limited to silicon disks (Fig. 4.3). We directly compared these disks to polystyrene beads (r = 300 nm) at equal amplification and without vertical offset amplification. The resulting records showed comparable BSD signals. The comparable lateral sensitivity ($S_{\mathrm{Si}}/S_{\mathrm{ps}} = -0.8$; where S_{Si} is the sensitivity of the silicon disk and S_{ps} is the sensitivity of the polystyrene bead) was achieved even

though the beads were ten-fold larger by volume than the disks; the sign change in S_{ps} for polystyrene beads has previously been reported [44].

Qualitatively, we would expect a larger sensitivity per unit volume to arise from the higher index of refraction of silicon. To test this hypothesis, we compared the sensitivity of silicon disks and polystyrene beads to the calculated value we might expect given the index of refraction of each. Calculations by Gittes and Schmidt [37] using a first order interference model in the Rayleigh approximation have successfully been applied to quantitatively predict the sensitivity for forward-scattered detection by spherical beads. These authors and others [100] have shown that the magnitude of the sensitivity scales with the polarizability α of the scattering particle. We applied this approximation to the observed lateral back-scattered signals. The polarizability of a spherical scattering particle is:

$$\alpha_{\mathrm{sphere}} = 3V[m^2 - 1]/4\pi[m^2 + 2], \tag{4.1}$$

where V is the volume, and m is the index of refraction ratio ($m = n_{\mathrm{object}}/n_{\mathrm{solvent}}$) [37]. This equation holds for the general case of complex m. By approximating the silicon disk as a sphere and using an index of 3.9 + 0.15i (amorphous silicon at λ = 810 nm) [91], we calculated the ratio of the polarizability between silicon and polystyrene to be:

$$[\alpha_{\mathrm{Si}}/\alpha_{\mathrm{ps}}] = V_{\mathrm{Si}}([m_{\mathrm{Si}}^2 - 1]/[m_{\mathrm{Si}}^2 + 2])/V_{\mathrm{ps}}([m_{\mathrm{ps}}^2 - 1]/[m_{\mathrm{ps}}^2 + 2]) = 7.1V_{\mathrm{Si}}/V_{\mathrm{ps}}. \tag{4.2}$$

The measured ratio of polarizabilities and thus, within our approximation, the ratio of sensitivities is 0.8. After division by 7.1, this yields a predicted volume ratio of 0.11 in agreement with the actual volume ratio of 0.10. Thus, within this approximation, the increased lateral sensitivity of silicon relative to polystyrene was consistent with the higher index of refraction of silicon. As a consequence, by using silicon, we could use substantially smaller fiducial marks while retaining suitable sensitivity.

We note that the success of this first-order approximation does not prove the lateral sensitivity is linear in α nor that an interference model is the correct description

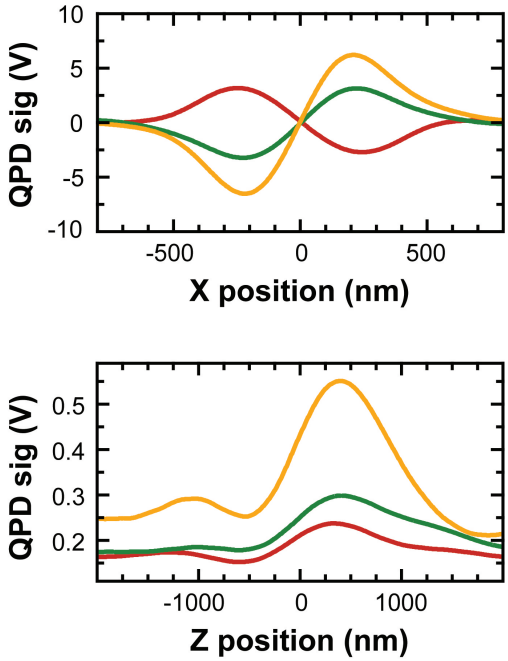

Figure 4.3: BSD signals vary with index of refraction of the medium and fiducial mark. Comparison between silicon disks in water (*green*) and air (*yellow*), with polystyrene beads ($r = 300$ nm) in water (*red*) for both lateral and vertical signals.

of BSD. However, like the interference model for forward-scattered detection [37], our lateral response is quantitatively described by the derivative of a Gaussian (Fig. 4.3), and our 500-nm-diameter, 56-nm-high disks are neither large nor small compared to the wavelength of light and, therefore, the Rayleigh (or Mie) approximation [118] is not strictly correct. Future work, based upon a detailed study of the response for both silicon disks and polystyrene beads as a function of their size and surrounding medium, coupled with improved modeling, should lead to a complete description of BSD.

Vertical response of BSD is distinctly different than that of forward-scattered detection (Fig. 4.3). As the disk was vertically scanned through the beam waist, the back-scattered signal dramatically increased 200% from a low-level baseline to a maximum, and then monotonically decreased towards the baseline over ∼1500 nm (maximal lateral sensitivity occurs at $z = 0$). In contrast, vertical motion in forward scattered detection leads to a small modulation (∼10%) on top of a comparatively large static signal [100]. We also note that the origin of our BSD vertical sensitivity was different than prior BSD reports; we under-filled our 10-mm-diameter QPD with a 6-mm-diameter beam (see Section 2.1.2), whereas prior vertical sensitivity was based on overfilling the QPD [33] or using BSD in combination with a reflective element [50, 49].

One application of this work is in scanning and stabilizing a sample for AFM; many AFM applications occur in air or vacuum. To demonstrate BSD in air (Fig. 4.3, *gold*), we scanned the silicon disk through the detector beam in the flow chamber, prior to measuring the same disks in water. The sensitivities were two-fold higher in air than in water, allowing stabilization in non-aqueous environments.

Overall, BSD detection provides excellent optical signals for both polystyrene beads and silicon disks, and is capable of sensing very small motions with minimal crosstalk. Lateral response was well fit by the derivative of a Gaussian and is similar in shape to the forward-scattered response. Vertical response was distinctly different and inherently more sensitive than the forward-scattered response.

4.3 Active microscope stabilization using back-scattered detection

To demonstrate the stability of BSD, we next actively stabilized the sample (Fig. 4.4) with the in-loop laser ($\lambda = 810$ nm), while measuring the residual motion with the monitor laser ($\lambda = 810$ nm). We achieved average short-term (1–25 Hz) stabilities (as previously calculated in Section 3.3) of $\bar{\sigma}_{\mathrm{x}} = 48$ pm, $\bar{\sigma}_{\mathrm{y}} = 48$ pm, and $\bar{\sigma}_{\mathrm{z}} = 49$ pm. We also achieved a long-term (0.01–25 Hz) stability of $\sigma_{\mathrm{x}} = 50$ pm, $\sigma_{\mathrm{y}} = 49$ pm, and $\sigma_{\mathrm{z}} = 57$ pm.

While previous experiments using BSD do not report real-space stabilities, they do report power spectral densities for their electronic noise floor [33, 44]. In Figure 4.4 **B**, we plot the power spectral density of our actual stabilization records. At higher frequencies (>20 Hz), our achieved stabilities were equal to or better than these previous electronic noise floors. At low frequencies (<20 Hz), our achieved stabilities stayed low; previous BSD work, in contrast, showed a rapidly increasing electronic noise floor as well as a two-fold increase in the power spectral density of an optically trapped bead between 20 and 2 Hz, suggesting significant low frequency noise [44]. Our low broadband noise ($\sim$10 pm/Hz between 0.1 Hz and 1 kHz) demonstrates the significant reduction in instrumental noise achievable with BSD coupled with active reduction in optical and mechanical noise.

An excellent alternative metric for calculating stabilities is to integrate the power spectral density within a specified bandwidth to calculate the integrated noise. We computed the integrated noise from 0.1 to 50 Hz, a broad bandwidth useful for a range of AFM and optical trapping experiments. The resulting stabilities were 88, 79, and 98 pm, in x, y, and z respectively. Calculating the equivalent metric on real-space data yields similar results as required by Parseval's Theorem [101], verifying the appropriate scaling of the power spectral density. Thus, our stability over this real-world useful bandwidth (0.1–50 Hz) is below 1 Å on all three axes.

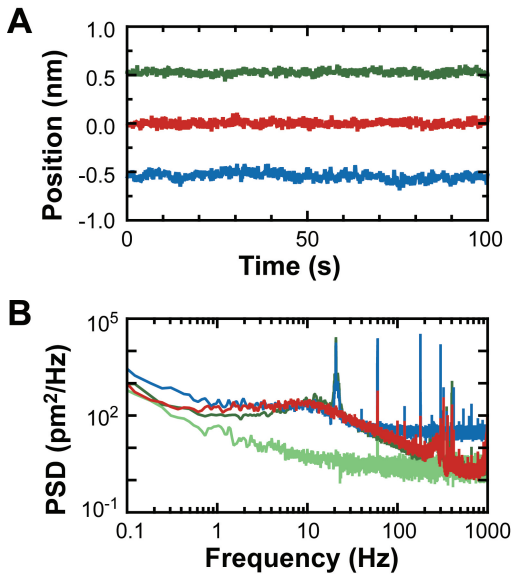

Figure 4.4: BSD active stabilization. (**A**) Sample positional stability as measured by the monitor laser: x_{monitor} (*green*), y_{monitor} (*red*), and z_{monitor} (*blue*). (b) Power spectral densities (PSD) of the stabilized data shown in **A**. The lateral localization precision limit, deduced by measuring the same unstabilized disk with two lasers [89], was substantially lower (*light green*).

The excellent stability achieved here is partially due to the optical conciseness of BSD (see Section 2.1.1 and 2.1.2, which increases the mechanical stability and is one potential advantage over forward-scattered techniques. Mechanical stability enables the substantial, yet zero mean, Brownian motion inherent in many assays to be averaged down to atomic dimensions. Though mechanical stability is an engineering challenge in forward-scattered detection since optics are required at two different vertical levels: that of the input light coupled into the objective and that of the output light on the back side of the condenser incident upon the QPD. For inverted microscopes, this second vertical level is the more technically challenging one; it requires a lightweight, mechanically rigid set of lenses, filters, and QPDs that is often bolted onto the condenser arm of a commercial research microscope (see Section 2.1.1 and Appendix D). In contrast, BSD optics external to the microscope are in a single horizontal plane.

Achieved stabilities do not reflect the ultimate localization precision of BSD. A better metric is the differential measurement (see Section 3.3) between the two lasers [89], which records the residual laser noise and is not dependent on the positional resolution of the PZT stage. We plot the power spectral density of the lateral differential measurement (Fig. 4.4 **B**, *light green*) so that the amplitude of the residual laser noise for different frequencies is easily visible. The integrated noise on the differential signal from 0.1 to 50 Hz was 19 pm in both x and y, and 73 pm in z. Hence, microscope stability using BSD will be ultimately limited by this localization precision.

Improvements in instrumentation to extend sample stabilization to this ultimate localization precision might include better mechanical and optical design as well as enhanced isolation from vibrations (Fig. 4.4 **B**, 23-27 Hz peak]. Low frequency performance can be limited by a number of factors, including non-common-mode optical-mechanical noise (e.g., differential motion between the QPDs or mirrors), variations in index of refraction [1], and thermal stability. We speculate that our low frequency performance is currently limited by the temperature ($>1\,^{\circ}$C) and pressure fluctuations

in the room, which could be alleviated by moving the apparatus to a temperature regulated ($\pm 0.2\,^{\circ}$C), acoustically quiet (NC30) room, as in the optical trapping experiment. High frequency performance is currently limited by our software-based feedback loop (100 Hz). Real-time embedded control (e.g. field programmable gate array) provides a means for deterministic timing and increased bandwidth up to and limited by the PZT stage resonance [21]. For anticipated AFM applications, the loop closure time will limit the scan-rate for stabilized scans, while low frequency noise will limit registration and the ability to "hover" a tip over a specified point on the sample.

4.4 Ultrastable scanning and registration

Ultra-stable scanning of a sample requires precise steps. Ideally, such scanning would occur without drift on any axis. Atom tracking [99], the most popular method for sample stabilization in scanning probe microscopy [121, 123], is fundamentally incompatible with simultaneous scanning and stabilization. In this work, we demonstrate simultaneous scanning and stabilization using BSD to locally measure and thereby control sample location. The basis of scanning is a series of uniform steps. To demonstrate uniformity in the step size, we made a staircase of 0.5-nm steps sequentially in all three axes. The sample position was actively controlled in 3D at all times with the in-loop laser. Changes in the feedback set point led to scanning. The reported results were determined with the monitor laser, which provides an independent verification of feedback-performance. The resulting records show linear motion in one axis with negligible motion on the stationary axes [Fig. 4.5 **A**].

Individual steps were clearly resolved and repeatable in size (Fig. 4.5 **B**). To provide an unbiased measurement of step size and an estimate of the S/N ratio, we computed the histogram of the pair-wise distance difference (Fig. 4.5 **C**), which shows the distance between each pair of points [35]. Ideally, every such difference would be a multiple of 0.5 nm. A Fourier transform of the pair-wise distance difference histogram

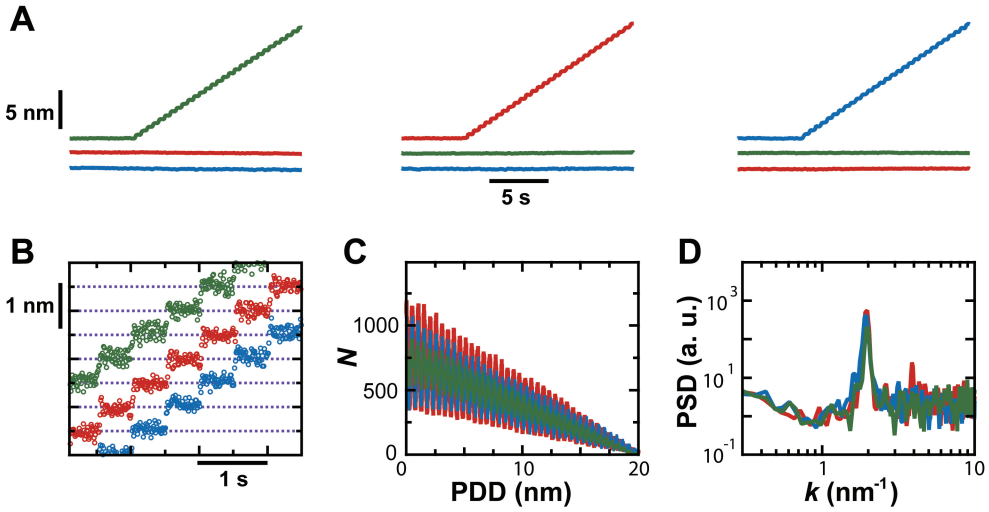

Figure 4.5: Stabilized microscope scanning using BSD. (**A**) The sample was moved in 0.5-nm steps sequentially along each axis under active stabilization. Sample position, independent of the servo-loop, was measured with the monitor laser (x_{monitor}, *green*; y_{monitor}, *red*; z_{monitor}, *blue*). Traces displaced for clarity. (**B**) Individual steps smoothed with a box-car window and decimated to 100 Hz show uniform 0.5-nm motion. Traces displaced for clarity. (**C**) A histogram of pair-wise distance differences (PDD) along each axis shows peaks every 0.5 nm. (**D**) Fourier transform of the PDD histograms in (**C**) reveals the power spectral density (PSD) of the data as it varies with the spatial frequency (k). The peak of the PSD is at 2 nm^{-1}, as expected.

determines the spatial frequency components present in the data (Fig. 4.5 **D**). Peaks occurred at 2.0 ± 0.1 nm^{-1}, 1.9 ± 0.1 nm^{-1}, and 1.9 ± 0.1 nm^{-1} (peak ± FWHM) in x, y, and z, respectively. The S/N ratio for these 0.5-nm steps is 30, 28, and 32, for motion along x, y, and z, respectively, based on the next largest peak. Thus, our implementation of BSD enables both precise and accurate steps as well as scanning concurrent with active stabilization on all axes.

Precision is fundamental to registration — the ability to repeatedly return to a particular sample position. Sample drift limits registration, and therefore, the ability to return to a particular location for subsequent detailed study. To demonstrate registration, we repeatedly moved the sample back and forth in 100-nm steps individually on all three axes for a total of fifteen 6-s cycles (Fig. 4.6 **A**). The average step position ($x^{\mathrm{N}}_{monitor}$) after each movement back to the starting location was compared to the initial step value ($\Delta x^{\mathrm{N}} = x^{\mathrm{N}}_{\mathrm{monitor}} - x^{0}_{\mathrm{monitor}}$) and plotted versus the step number to show the spread in the relative registration (Fig. 4.6 **B**). The standard deviations of the relative position of these steps were 25 pm, 21 pm, and 58 pm in x, y, and z, respectively. The experiment was repeated with 1-nm steps and yielded essentially identical results. Thus, the registration is near to and limited by our long-term, low-frequency stability (σ_{x} = 11 pm, σ_{y} = 16 pm, σ_{z} = 40 pm, in 100 s of data filtered to 0.3 Hz).

4.5 Application to AFM

4.5.1 Measuring tip position to 0.2 Å

Before applying the Ångstrom-scale sample control afforded by BSD to stabilize an AFM tip, we needed to establish that BSD could localize an AFM tip — a highly asymmetric object in comparison to beads and thin silicon disks. Ideally, such a signal would be sensitive to Ångstrom-scale motion in 3D with low cross-talk between axes. To demonstrate these signals, we first positioned a silicon tip 300 nm above a glass

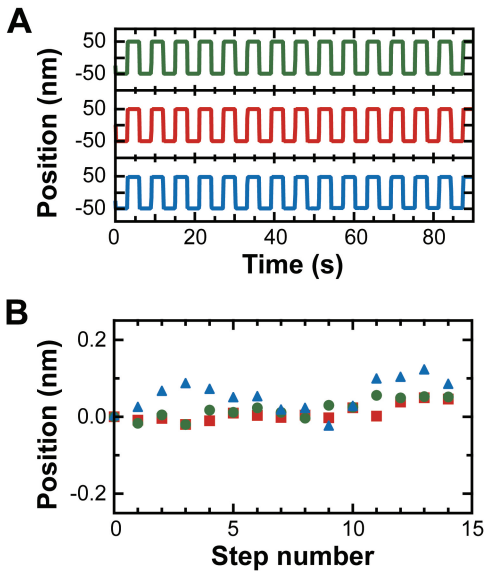

Figure 4.6: Registration with BSD. (**A**). The sample was moved in a series of fifteen back-and-forth 100-nm steps sequentially on each axis. The steps were actively stabilized with the in-loop laser while the resulting motion was verified with the monitor laser [x_{monitor} (*green*), y_{monitor} (*red*), and z_{monitor} (*blue*)]. (**B**) Mean values of the step position subtracted from the initial value are plotted as a function of step number and demonstrates the excellent registration of our technique.

surface in air and then sequentially translated it through the 810-nm laser focus along each axis, yielding a voltage-versus-distance curve (Fig. 4.7). The QPD signal during on-axis motion was approximately linear, whereas the off-axis traces were nearly flat (<10% cross talk over a 50-nm range). A two-fold increase in the laser power used for BSD (from 400 W to 800 W at the tip) did not alter the shape or the magnitude of the BSD signals, but did introduce a slight z offset (<1 nm) on the cantilever. Such BSD signals formed the basis for subsequent tip voltage-to-position calibration (see Section 2.3.1). With active reduction in laser noise (see Section 2.1.4) and electronic amplification (see Section 2.1.3), the resulting sensitivities (>6 mV/nm) were sufficient to detect picometer-scale motion (digitization at 0.1 mV/bit).

In the current implementation, we used transparent substrates in air, but we have also achieved proof-of-principle, tip-based BSD signals in several conditions including in liquid and through both birefringent and thin metallic substrates [51]. In addition, nanometer-scale metallic particles (5-nm height, gold) scanned through the tip-stabilization laser did not degrade the optical signal. Thus, BSD-based tip detection is robust to small optical changes in the local detection volume and, in principle, compatible with several different environments and non-opaque substrates.

4.5.2 Active stabilization achieves 0.3-Å tip stability

We used BSD signals to measure and actively stabilize the position of an AFM tip in 3D. For this demonstration, both detection lasers were focused onto a silicon tip that was 300 nm above the glass surface. We employed the 810-nm signal as the in-loop laser and the 845-nm signal as the independent monitor laser. Long-term stabilities detected by the monitor laser (Fig. 4.8 **A**) were 26 pm, 39 pm, and 25 pm in x, y, and z respectively (σ, Δf = 0.01–10 Hz). Histograms of this data (Fig. 4.8 **B**) provided a complementary analysis and were well fit by Gaussian curves, with standard deviations of 28 pm and 26 pm in x and z, respectively. These reported stabilities represent

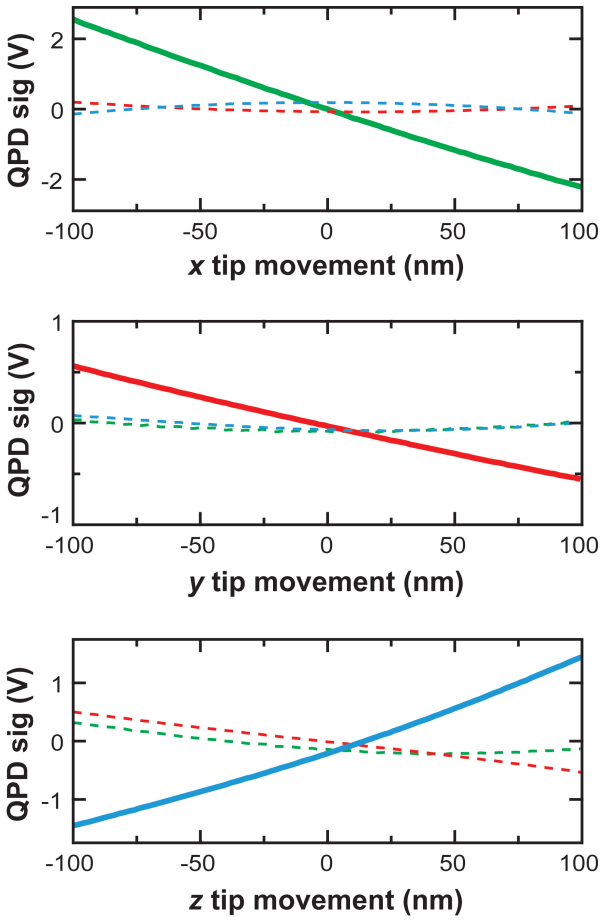

Figure 4.7: AFM tip signals in air. Records of the QPD signal versus tip position are shown for x (*green*), y (*red*) and z (*blue*) on the moving axis (*solid lines*) and the stationary axes (*dashed lines*) from light scattered off a commercial silicon tip. Figure credit: Gavin King and Allison Churnside.

a metric for the ultimate positional control between the tip and sample that can be achieved with our current apparatus and include the uncertainty due to pointing noise between the detection lasers.

With this Ångstrom-scale stabilization, we also show similar-scale tip control (Fig. 4.8 **C**). We scanned the tip in a pattern by updating the feedback set point which changes the position of the tip relative to the lasers while maintaining stability. Measurements of tip position by the in-loop laser show movements on the scale of Ångstroms, an order of magnitude better than previous tip control techniques [81].

4.5.3 Stable AFM scanning and registration

To demonstrate an ultrastable AFM, we stabilized the tip while in contact with the surface and stably scanned (see Section 4.4) a 5-nm gold particle attached to the sample through the tip (Fig. 4.9 **A**). These particles are known to be robust and incompressible in ambient conditions [126] and are often used as AFM calibration standards. To demonstrate tip-sample registration and stability, we located an individual particle on the surface and repeatedly scanned in x, yielding a series of line scans $z(x)$ (Fig. 4.9 **B**). We took a set of three line scans over 60 s and then held the tip stationary ("hovered") 10 nm outside of the scan range for 20 s; this cycle was iterated eight times for a total duration of 640 s. Each scan contained a peak in z corresponding to the particle center point. The peak locations for each set of line scans were averaged. The average peak location (x_{peak}) was stable to 160 pm over eight iterations of hovering and 10 min of time (Fig. 4.9 **C**). Thus, the ability to stably scan and repeatedly return the tip to the same feature demonstrates an ultrastable AFM with both atomic-scale stability and registration.

One succinct visual representation of both registration and stability is to form a kymograph. In this presentation, successive line scans, one every 20 seconds, form the rows of an image. A stationary object maps out a vertical path. We formed such

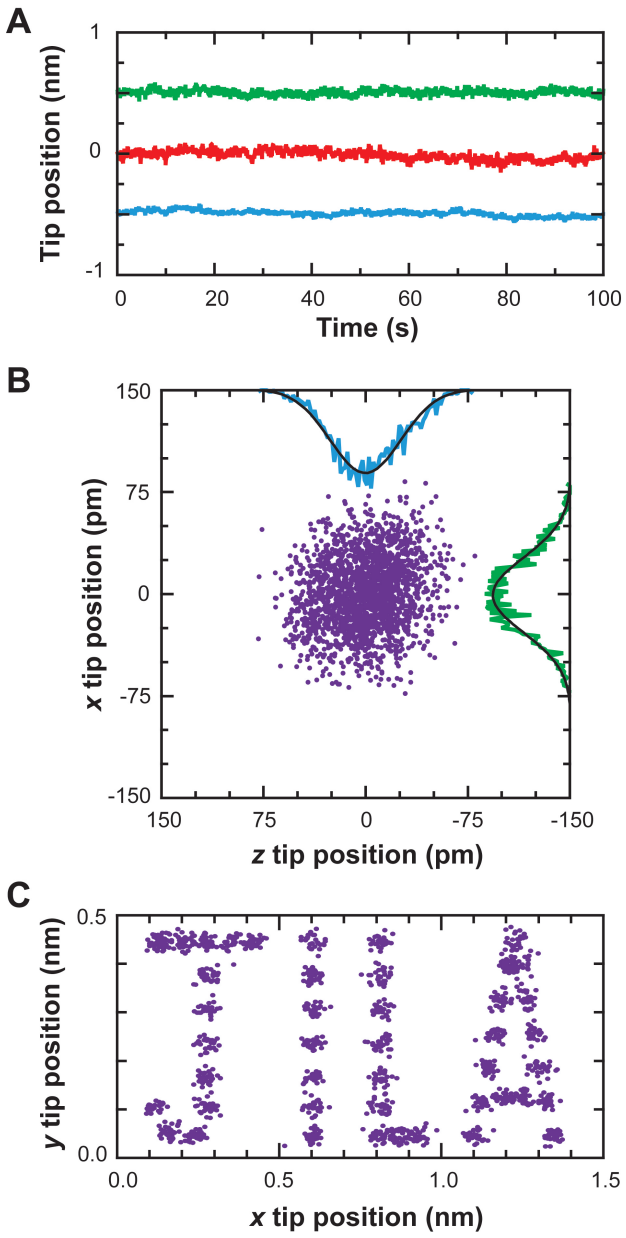

Figure 4.8: Ångstrom-scale AFM tip control in 3D at ambient conditions. (**A**) Tip position records versus time were low-pass filtered to 10 Hz and offset vertically for clarity [x (*green*), y (*red*), z (*blue*)]. Positions were determined by a monitor laser while the tip was actively stabilized with the in-loop laser. (**B**) A scatter plot of the tip position (*purple*) in the x-z plane from the 100-s record in **A**. Histograms of the data projected onto the x and z axes were well fit by Gaussian curves with standard deviations of 28 pm and 26 pm, respectively. (**C**) To demonstrate tip control, the tip position in x and y was recorded as the tip was scanned in a pattern. The in-loop tip position is plotted. Figure credit: Gavin King and Allison Churnside.

kymographs from the above data (Fig. 4.9 **D**) and from an hour of data where the tip was alternatively stabilized at two positions separated by 12 nm (Fig. 4.9 **E**). The stability of the peak location over this hour was 2.4 Å in x.

4.5.4 Stable AFM imaging

To further demonstrate an ultrastable AFM, we show precise, independent control of the tip and sample. We imaged a particle with a silicon-nitride tip while stabilizing the 3D position of the sample (Section 4.3) and the lateral position of the tip (Section 4.5.2). The z position of the tip PZT stage was adjusted to maintain a constant tip-sample interaction force ($F \sim 200$ pN) which was determined via the cantilever-deflection-sensing laser. We acquired seven sequential images. Representative images at the beginning, middle and end of the time course are displayed in Figure 4.10 **A**. Line scans through these images showed no significant lateral motion (Fig. 4.10 **B**).

To demonstrate atomic-scale stability and registration, we performed a 2D cross-correlation analysis [51]. This analysis precisely tracked the location of the particle during the 82 min of continuous imaging (Fig. 4.10 **C**). Over this time scale the stability and registration of our technique was <5 Å. Linear fits to the particle position revealed residual lateral drift rates of 4 and 5 pm/min in x and y, representing a 250-fold reduction of the inherent instrumental drift rate [51]. These residual rates, achieved in air at room temperature, are close to those found in cryogenic conditions (∼1 pm/min, 8 K) [116]. The precision of this control (and analysis technique) are further verified by small average deviations — 23 and 40 pm in x and y, respectively — from the linear fits. While we refer to the time evolution of the correlation-peak position as "residual drift", this apparent motion could also arise from instability of the particle relative to the cover slip [17] or from tip-sample degradation.

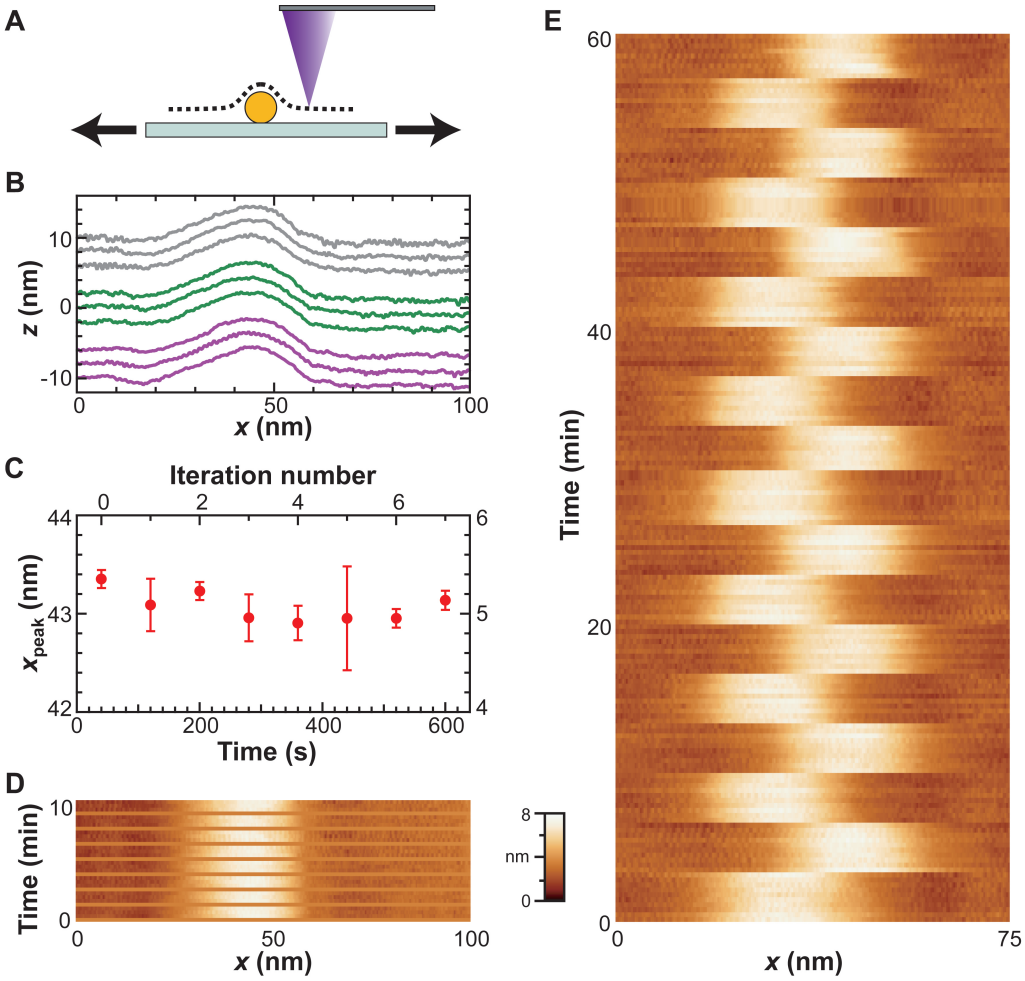

Figure 4.9: AFM scanning and registration. (**A**) Cartoon of AFM scanning over a gold particle. (**B**) Line scans of a gold particle taken every 20 s. Sets of three lines scans were separated by hovering the tip 55 nm away from the particle for 20 s, forming one iteration. The sets of line scans shown represent the first (*purple*), middle (*green*), and final (*gray*) iterations of a 640 s record. Traces are displaced vertically for clarity. (**C**) Atomic-scale stabilization and registration is demonstrated by plotting average peak position (x_{peak}) from the set of scans in **B** vs. iteration number. The standard deviation in x_{peak} was 160 pm over 10 min. (**D**) A kymograph of the above data, where rows in the image are successive line scans. The line in the kymograph associated with hovering is set to uniform color. (**E**) A kymograph of line scans formed from one hour of data where the sample position was alternated between two positions offset by 12 nm, shows both long-term stabilization and registration. The vertical scale bar for both **C** and **D** is shown. Figure credit: Gavin King.

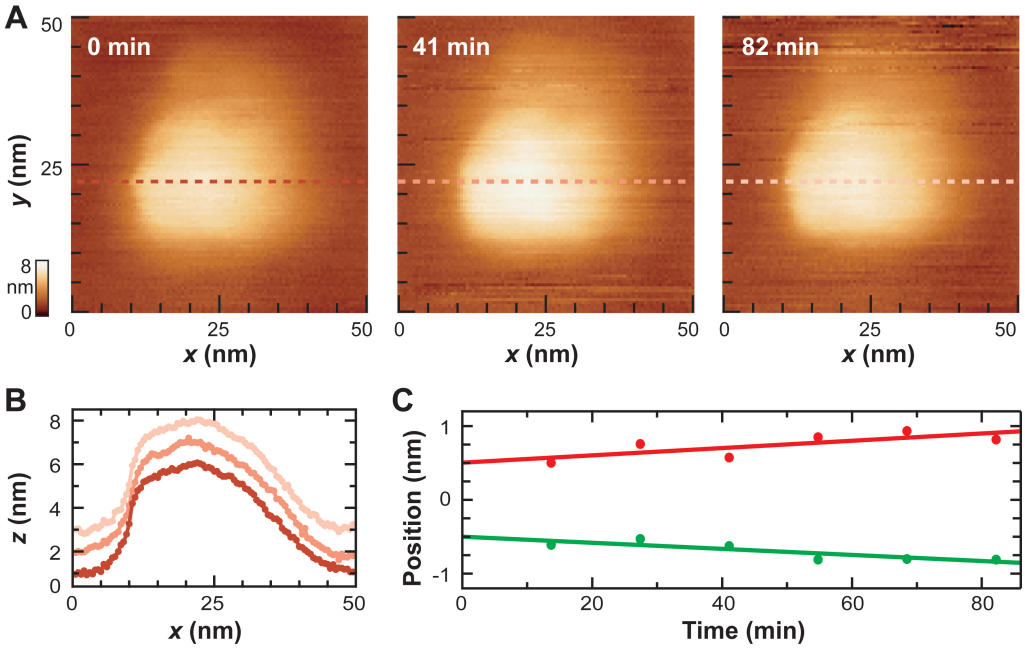

Figure 4.10: Ultrastable AFM imaging. (**A**) Images of a 5-nm gold particle taken at times 0, 41 and 82 minutes, respectively. (**B**) Line scans through the center of each image. (**C**) Relative lateral position of the particle plotted vs. time as determined by a cross-correlation analysis (x, *green*; y, *red*). From linear fits to the data, we deduced residual lateral drift rates of 4 and 5 pm/min in x and y, respectively. Figure credit: Gavin King and Allison Churnside.

4.6 Conclusions

With BSD, we achieved Ångstrom-scale sample localization precision, stability, and registration in all three axes. In addition, we demonstrated that BSD can meet or exceed the best stabilities achieved with forward-scattered detection in all dimensions. In contrast to prior BSD work, we achieved this enhanced sensitivity when underfilling the QPD. Fundamental to this set of state-of-the art metrics, unprecedented in aqueous or ambient conditions, is active stabilization based on a local optical measurement of sample position. Thus, we could scan while actively stabilizing the sample on all three axes.

Moreover, we demonstrate that back-scattered light off the apex of a commercially available AFM tip provides a means to an ultrastable AFM without resorting to low temperatures or ultra-high vacuum environments. Ångstrom-scale stability and registration enable returning to a particular feature in an image, such as a domain of a protein, and hovering the tip over this feature for extended periods — allowing detailed study of vertical motion with high temporal resolution. Feedback is performed at relatively low frequency, so this stabilization technique should be compatible with tapping mode and frequency-modulated cantilever detection methods. The scanning range can be easily extended to several microns by sequential moves of the laser with a PZT mirror. We anticipate that the shape and material properties of the tip and fiducial mark, as well as the wavelength of the laser, can be varied to suit different applications. More specifically, silicon wafers, in lieu of cover glass, can be accommodated by shifting to a longer wavelength detector laser below the silicon band-gap. In cases where changing the wavelength of the laser is not an option a fiducial mark could be engineered into the cantilever that spatially separates the tip from the laser. Such separation would enable strongly scattering, optically opaque, or time-varying specimens [98] to be studied with similar Ångstrom-scale stability and registration.

The optical and mechanical conciseness of BSD makes this technique amenable to a wide variety of applications and underlies its superior stability and optical efficiency. We foresee integration of BSD into many applications seeking ultrastable 3D detection and control, especially those with poor quality or limited optical access opposite of the microscope objective, such as scanning probe microscopy and magnetic tweezers. Though, BSD can be used in optical trapping assays as well. Such detection is more optically compact, and in our experiments, more robust. While we do not apply this technique to our optical trap or use it to measure RecBCD motion, its discussion here represents an interesting side-track and perhaps a future direction to take.

Chapter 5

Precision optical trapping assay sensitive to Ångstrom-scale motion

5.1 Introduction

Detection of single-molecule motion at or near the Ångstrom-scale reveals previously inaccessible details about biomolecular dynamics [77]. Surface-coupled trapping assays have measured the 1-codon step of the ribosome that, with mechanical amplification, corresponds to a 2.7-nm displacement [132]. To resolve smaller motions, such as the 1-base-pair (3.4-Å) step of RNA polymerase [1], researchers decoupled their experiments from the surface using dual-beam optical-trapping assays [1, 76] to reduce surface-induced noise. Yet, the vast majority of single-molecule optical-trapping assays are coupled to surfaces [5, 11, 45, 48, 64, 120, 132, 140]. What is needed is a general method that permits surface-coupled optical-trapping assays to achieve positional precision at the Ångstrom-scale.

Measurements of biological motion by optical-trapping experiments are corrupted by various noise sources (thermal, mechanical, laser, etc). Thermally driven Brownian motion is dominant on short time scales (<0.01–0.1 s). Such motion, which has a zero mean, can be averaged to atomic-scale dimensions at the expense of temporal resolution and sets a theoretical limit for positional precision (i.e. the thermal limit, see Section 5.2). To achieve this thermal limit, other noise sources must be reduced to maintain Ångstrom-scale instrumental stability over the same (or ideally longer) time period.

Current surface-coupled optical-trapping assays lack such Ångstrom-scale instru-

mental stability. A surface-coupled assay is physically connected to its local environment (e.g., cover slip or micropipette) and thus sensitive to mechanical perturbations through this connection. One common application of this class of assays has a DNA molecule attached to a surface at one end while attached to an optically trapped bead at the other (Fig. 2.1). As a first step towards a surface-coupled optical-trapping instrument with atomic-scale sensitivity, we stabilized an optical microscope to 1 Å in 3D [17]. In applying this technique to optical traps, two detection lasers (one monitoring the trapped bead, the other measuring fiducial position) establish a local, differential measurement reference frame. Local detection suppresses motion (e.g., thermal expansion) unmeasured by sensors in closed-loop stages. Differential measurement suppresses noise (e.g., air currents and objective drift) common to both lasers [89]. The ultimate limit on instrumental stability is set by the differential pointing stability between the detection lasers (<0.065 nm laterally, Δf = 0.1–50 Hz).

Mechanical stabilization of the surface alone was insufficient to achieve Ångstrom-scale resolution in our optical trapping apparatus. The trapping laser was also a significant source of instrumental noise. To achieve base-pair resolution, dual beam experiments not only decoupled the assay from the surface, but also reduced laser pointing instability by either encasing the optics in a helium enclosure [1] or by using a differential measurement [76]. In contrast with these passive methods, we adopted an active method to not only reduce pointing noise but also other types of laser noise (intensity, mode, and polarization noise) that affect instrumental stability. We were motivated, in part, by our analysis which shows that trap laser intensity fluctuations of 1% induce apparent motion of 1 bp for a 1 μm long DNA molecule (see Section 5.2).

For studying the dynamics of molecular motors and nucleic acid structures, we sought to achieve atomic-scale stability immediately after changes in applied force. Previous work has only reported base-pair stability at constant force, presumably after any thermal perturbations caused by changes in the trap laser power have subsided. We

demonstrated sensitivity to 1-bp steps along DNA at moderate force and 1-bp stability immediately following a substantial change in force (3.4 pN) as well as sensitivity to 0.1-pN force-induced changes in DNA hairpin unfolding dynamics.

In summary, prior work [1, 76] has removed the surface from the assay and has emphasized the importance of minimizing pointing noise. We stabilized a surface-coupled assay and reduced various laser noise sources, including intensity noise. Calculations show that controlling intensity noise is important when the bead is offset from the trap center.

5.2 Noise in optical trapping assays

5.2.1 Thermal noise

Thermally driven Brownian motion has a zero mean, so time averaging bead position, x_{bd}, reduces the uncertainty in position as long as instrumental drift is negligible over the time span averaged, τ_{avg}. On short time scales ($<1/f_0$; f_0 is the roll-off frequency of trapped bead motion), bead motion is correlated and thus not statistically independent. However, by averaging N independent data points spaced at the correlation time ($1/f_0$), the standard deviation of the data ($\sigma_{\mathrm{D}} = \sqrt{k_{\mathrm{B}}T/k_{\mathrm{T}}}$; $k_{\mathrm{B}}T$ is thermal energy and k_{T} is the trap stiffness [118]) decreases by $\sqrt{N}$. The uncertainty in x_{bd} after averaging a specific time (τ_{avg}) is given by the standard error of the mean (σ_{SEM}),

$$\sigma_{\mathrm{SEM}} = \frac{\sigma_{\mathrm{D}}}{\sqrt{N}} = \sqrt{\frac{k_{\mathrm{B}}T}{k_{\mathrm{T}}}\frac{1}{\tau_{\mathrm{avg}}f_0}} = \sqrt{\frac{k_{\mathrm{B}}T}{(k_{\mathrm{T}})^2}\frac{12\pi^2\eta r_{\mathrm{bd}}}{\tau_{\mathrm{avg}}}}, \tag{5.1}$$

using the relationship $k_{\mathrm{T}} = 12\pi^2\eta r_{\mathrm{bd}} f_0$; where η is the viscosity of the liquid and r_{bd} is the radius of the bead. (Note: This formula assumes that there is not a correction due to proximity to a surface.) Thus, theoretically, in an optical trap with a high trap stiffness of $k_{\mathrm{T}} = 0.53$ pN/nm and $r_{\mathrm{bd}} = 165$ nm, this uncertainty reduces to 3.4 Å (1 bp) in 2.5 ms. At a moderate k_{T} of 0.086 pN/nm, the time to average to $\sigma_{\mathrm{SEM}} = 3.4$ Å increases to 95 ms.

To achieve a noise level that is at the thermal noise limit, other noise sources (i.e. surface or laser noise) must be reduced to maintain instrumental stability over the same (or ideally longer) time period. (Note: Experimentally, our results for the trapped bead example quantitatively matched the predictions above. We achieved 1 bp resolution, $\sigma_{\mathrm{SEM}} = 3.4$ Å, in 2.5 ms and 103 ms, at the respective trap stiffnesses. Thus our ability to measure trapped bead position in an optical trapping assay is close to the thermal noise limit.)

5.2.2 Surface noise

Current surface-coupled optical-trapping assays lack Ångstrom-scale instrumental stability over long time-scales (100 s) [77] because of surface noise [89]. While dual-beam assays have removed the surface from optical trapping experiments to increase resolution, we have stabilized the surface to 1 Å over 1–25 Hz in 3D [17], reducing this noise source.

5.2.3 Laser noise

In assays where lasers are used, multiple types of laser noise degrade instrumental stability. For example, in an optical trapping assay, the trap and detection lasers are prone to mode, polarization, pointing, or intensity noise. Mode and polarization noise generally appear as pointing or intensity noise after the optical element that couples the lasers into the microscope, the dichroic mirror. Thus, we will only discuss pointing and intensity noise.

Pointing noise moves the trap laser relative to the detection laser, which appears as an erroneous trapped bead movement, δx_{bd}. The coupling between the pointing movement and the trapped bead movement is 1:1; so if pointing noise is on the scale of nanometers then this source of laser noise typically dominates over atomic-scale measurements. To reduce pointing noise to the Ångstrom-scale, researchers have enclosed

the laser optics in a Helium-filled box [1], or have mechanically held a fiber-coupled laser in a rigid mount [89]. In addition, researchers have used a differential measurement between two lasers to remove non-common pointing noise [76, 89].

Intensity noise, while important, has not been addressed. Intensity noise appears as a change in trap stiffness, δk_{T}, which causes a change in the potential energy and an erroneous trapped bead movement, δx_{bd}, when the bead is offset from the trap center by a load (Fig. 5.1 **A**). Here we calculate the effect intensity fluctuations have on both x_{bd} and the contour length (L) in a DNA tethered particle assay (Fig. 5.1 **B**).

We used a simplified one-dimensional model where the forces on the bead were balanced. The force exerted by the DNA (F_{DNA}) was equal to the force exerted by the trap (F_{T}) i.e.,

$$F_{\mathrm{DNA}} = F_{\mathrm{T}} = k_{\mathrm{T}} x_{\mathrm{bd}}. \tag{5.2}$$

Initially, F_{DNA} was equal to $F^0_{\mathrm{DNA}} = k^0_{\mathrm{T}} x^0_{\mathrm{bd}}$, where F^0_{DNA} is the initial force, x^0_{bd} is the initial bead position, and k^0_{T} is the initial trap stiffness. If the intensity of the trap (I) fluctuated by δI, this caused a fluctuation in the trap stiffness ($\delta k_{\mathrm{T}} = \frac{\delta I}{I} k_{\mathrm{T}}$), which moved the bead (δx_{bd}) and changed F_{DNA}. To calculate the current F_{DNA}, we used a Taylor series to expand around the initial extension of the DNA, x^0_{DNA},

$$F_{\mathrm{DNA}} = F^0_{\mathrm{DNA}} - k^0_{\mathrm{DNA}} \delta x_{\mathrm{bd}}, \tag{5.3}$$

where we defined the initial DNA stiffness as $k^0_{\mathrm{DNA}} = \frac{\partial F_{\mathrm{DNA}}}{\partial x_{\mathrm{DNA}}}|_{x_{\mathrm{DNA}} = x^0_{\mathrm{DNA}}}$. Thus, after the intensity fluctuation, the balance of forces in Eq. 5.2 was now rewritten as

$$F^0_{\mathrm{DNA}} - k^0_{\mathrm{DNA}} \delta x_{\mathrm{bd}} = (k^0_{\mathrm{T}} + \delta k_{\mathrm{T}})(x^0_{\mathrm{bd}} + \delta x_{\mathrm{bd}}). \tag{5.4}$$

Solving for δx_{bd} gave

$$\delta x_{\mathrm{bd}} = -x^0_{\mathrm{bd}} \delta k_{\mathrm{T}} / (k^0_{\mathrm{DNA}} + k^0_{\mathrm{T}} + \delta k_{\mathrm{T}}). \tag{5.5}$$

After calculating δx_{bd}, we calculated the apparent change in the contour length, δL. We determined the fractional extension of the DNA ($f = x_{\mathrm{DNA}}/L$), which is the

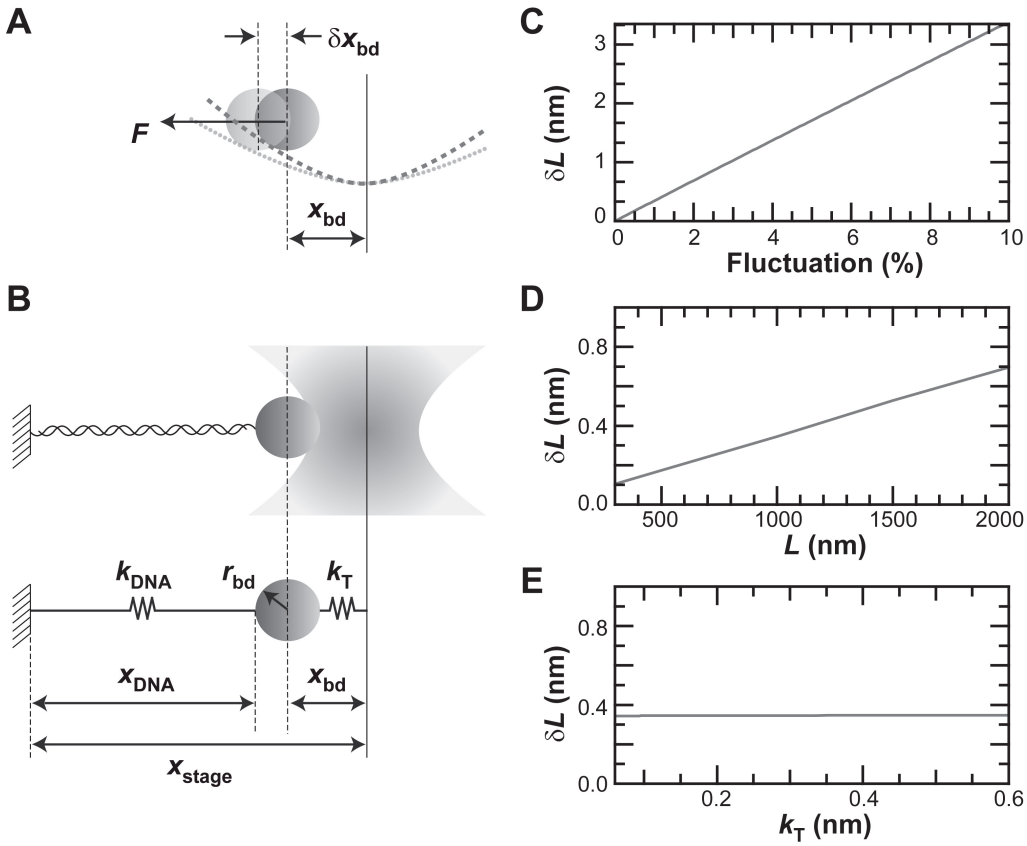

Figure 5.1: Intensity noise affects trapped bead position (x_{bd}) and measurements of DNA contour length (L). (**A**) Unwanted bead motion (δx_{bd}) occurs under constant load (F) when an intensity fluctuation (δI) decreases the trapping potential. (**B**) A one dimensional diagram of the experiment and its mechanical analog. Variables represent the following: k_{DNA} is the nonlinear stiffness of the DNA molecule, k_{T} is the trap stiffness, x_{stage} is the distance between the tether point and the trap center, x_{DNA} is the end-to-end extension of the DNA, and r_{bd} is the bead radius. (**C**–**E**) Based on a first order calculation (Eq. 5.8), the uncertainty in DNA contour length (δL) is linear in intensity fluctuation (**D**) and DNA length (**C**), but independent of k_{T} at constant force (**E**). Calculations were performed with a constant trap force of 6 pN and r_{bd} of 165 nm. When parameters were not varied they were held fixed at the following values: $\delta I = 1\%$, $k_{\mathrm{T}} = 0.086$ pN/nm, $k_{\mathrm{DNA}} = 0.187$ pN/nm, $x_{\mathrm{bd}} = 70$ nm, and $L = 1000$ nm.

ratio of the DNA extension to the contour length. To determine f, we used an inverse formula valid at forces >1 pN [71],

$$f = 1 - (1/\sqrt{4k_{\mathrm{T}}x_{\mathrm{bd}}p/k_{\mathrm{B}}T}). \tag{5.6}$$

Here $k_{\mathrm{B}}T$ is thermal energy (4.1 pN-nm) and p is the persistence length of the DNA (40 nm) at our ionic conditions and contour length (1000 nm) [108]. Then, we used f to find L,

$$L = x_{\mathrm{DNA}}/f = (x_{\mathrm{stage}} - x_{\mathrm{bd}} - r_{\mathrm{bd}})/f, \tag{5.7}$$

where x_{stage} is the distance between the trap center and the tether point of the DNA. Given Eq. 5.6 and Eq. 5.7, δL was found by calculating the initial contour length and subtracting it from the current contour length,

$$\delta L = \frac{(x_{\mathrm{stage}} - x^0_{\mathrm{bd}} - \delta x_{\mathrm{bd}} - r_{\mathrm{bd}})}{(1 - 1/\sqrt{4pk_{\mathrm{T}}(x^0_{\mathrm{bd}} + \delta x_{\mathrm{bd}})/k_{\mathrm{B}}T})} - \frac{(x_{\mathrm{stage}} - x^0_{\mathrm{bd}} - r_{\mathrm{bd}})}{(1 - 1/\sqrt{4pk_{\mathrm{T}}x^0_{\mathrm{bd}}/k_{\mathrm{B}}T})}. \tag{5.8}$$

As expected in a first order approximation, we found that $\delta L \propto \delta I$ (Fig. 5.1 **C**) and $\delta L \propto L$ (Fig. 5.1 **D**). We note that at constant force, δL was independent of k_{T} (Fig. 5.1 **E**). Given the parameters ($F^0_{\mathrm{DNA}} = 6$ pN, $k^0_{\mathrm{T}} = 0.086$ pN/nm, $L = 1000$ nm, $k^0_{\mathrm{DNA}} = 0.187$ pN/nm, $r_{\mathrm{bd}} = 165$ nm), we calculated that a 1% fluctuation in intensity created a $|\delta x_{\mathrm{bd}}|$ of 2.2 Å and a $|\delta L|$ of 3.4 Å. Thus, this calculation motivated us to address intensity noise (which has a typical specification of ±1%) and other types of laser noise in combination with pointing noise to improve long-term instrumental stability.

5.3 Stabilizing trap laser noise

To reduce trap laser noise, we used active stabilization. Specifically, we first minimized multiple types of laser noise by transforming pointing, mode, and polarization noise into intensity noise using the combination of a single-mode, polarization-maintaining fiber and a polarizing beam splitter (see Section 2.1.4). We then sampled 10% of the light onto a photodiode to measure laser intensity. Finally, the intensity

measurement was used in a feedback loop to an AOM (placed before the fiber) that modulated intensity to keep the output intensity constant. Also, to minimize effects of AOM pointing instability, we imaged the AOM crystal on to the fiber coupling lens, eliminating lateral translation of the laser beam on the coupling lens that would otherwise accompany a pointing instability.

With this stabilization, we decreased the steady state trap intensity noise to 0.01% rms at moderate laser powers (200 mW, Δf = 0.03–100 Hz, Fig. 5.2 **A**). Importantly, similar trap intensity control of 0.01% rms was achieved immediately after dynamic changes in intensity (Fig. 5.2, **B**–**D**). Without feedback, there was a substantial, time-dependent AOM-induced error (see Section 2.1.4) between the requested and actual laser intensity that was not present with feedback (Fig. 5.2, **B**,**C**). This long-term systematic error could take from tens of seconds (Fig. 5.2 **B**) to ∼10 min (at the highest change in laser power in Fig. 5.2 **C**) to stabilize. In addition to this long-term error, there was also a short-term (Δf = 0.2–2000 Hz) AOM-induced error of ∼10% (rms) after an intensity change that was reduced by three orders of magnitude to 0.01% (rms) with active intensity stability (Fig. 5.2 **D**).

In summary, prior work [1, 76] has emphasized the importance of minimizing pointing noise. Our calculations showed the importance of controlling intensity noise when the bead is offset from the trap center. Moreover, we found that dynamic changes in laser intensity using an AOM introduced significant errors. Our feedback system successfully minimized both pointing and intensity noise (as well as other sources) during dynamic changes in laser power.

5.4 Ångstrom-scale tracking of trapped bead motion

After reducing both surface perturbations and trap laser noise, we first demonstrated the excellent positional stability of the trap laser relative to the detection laser. One useful metric is to plot the power spectral density of a trapped bead (Fig. 5.3

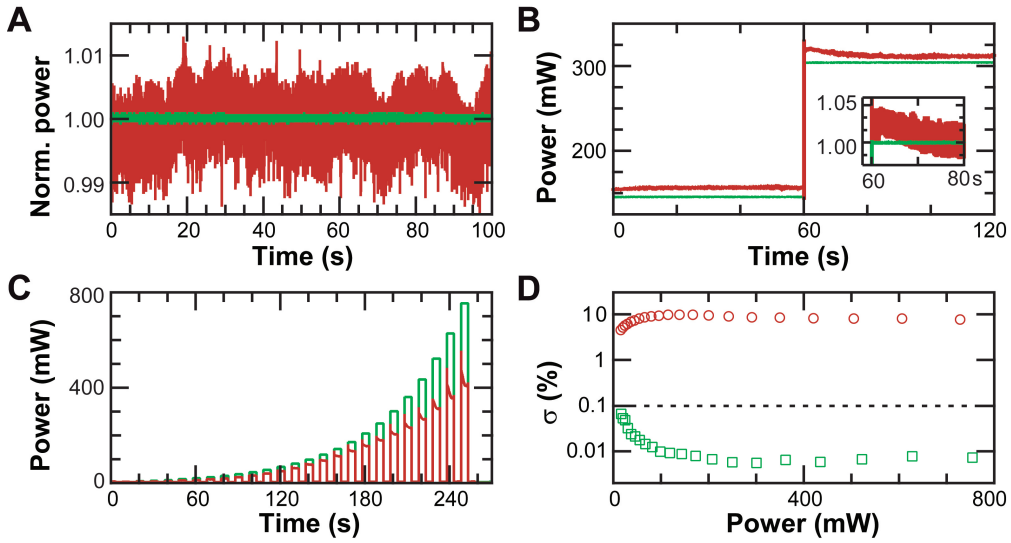

Figure 5.2: Reduction of intensity noise. (**A**) Steady state normalized power of the trap laser with (*green*) and without (*red*) stabilization. Data was taken after 1 hour of equilibration time. (**B**) A step increase in laser power from 150 to 300 mW with and without feedback. Such steps led to a slow (>10 s), substantial (>3%) systematic error. Intensity stabilization effectively minimized this error. Traces offset for clarity. Inset is a zoom-in of the transient noise where the data was normalized. (**C**) Records of power versus time during rapid (5 s) changes in power with and without stabilization. Without stabilization, the final measured power was only 55% of the intended value (750 mW). Only after ∼10 min at the desired power did the unstabilized trace equilibrate to within 1% of the requested power (*data not shown*). (**D**) The short-term (5 s) fractional standard deviation (σ) as a function of each power in **C**. The intensity-stabilized trace shows about three orders of magnitude improvement over the unstabilized trace and is <0.1% (*black dashed line*) over the full range. Traces in **A**–**C** are at 2 kHz and color in **B**–**D** is the same as in **A**.

A, inset), which shows the noise as a function of frequency. Another useful metric for calculating noise is to integrate the power spectral density within a specified bandwidth to produce the integrated noise. This integrated noise (1.7 Å) was a fraction of a base pair over a broadly useful bandwidth (Δf = 0.02–100 Hz) for a 330-nm-diameter bead trapped at a stiffness of 0.53 pN/nm (Fig. 5.3 **A**). The noise level was within 0.5 Å of the thermal noise limit and was maintained over a wide range of trap stiffness (Fig. 5.3 **B**). Interestingly, our integrated trap noise was only ∼0.5 Å higher than the best reported trap stability [1], though our method used a four-fold lower stiffness and did not require the encasement of optics in helium.

Second, we achieved atomic-scale sensitivity to bead motion. Using a PZT mirror, we generated 0.4-nm trap motion (limited by 1 bit changes in a control voltage). The resulting steps were well resolved [0.43 ± 0.08 nm (peak ± HWHM)] with a signal-to-noise ratio of 5 in a trace filtered to 5 Hz using a Savitzky-Golay window (Fig. 5.3 **C**). Thus, by reducing mechanical perturbations and excess trapped-bead noise, we achieved sufficient stability and precision to measure Ångstrom-scale bead motion.

5.5 Stability and resolution of 1-bp along DNA

We next achieved 1-bp stability in a surface-coupled DNA assay (Fig. 2.1) over tens of seconds. Measurements of DNA contour length (L = 556 nm) were taken at a moderate force of 6 pN with and without active stabilization of both the surface and trap (Fig. 5.4 **A**). Active stabilization resulted in a four-fold decrease in the integrated noise to 1.5 Å at 0.1 Hz (Fig. 5.4 **B**). Additionally, we maintained a 1-bp (3.4-Å) positional precision over a useful frequency range (Δf = 0.03–2 Hz). The stability for a ten-fold longer time period (Fig. 5.4 **C**) was slightly larger at 4.8 Å (Δf = 0.003–2 Hz). Such long-term traces contain some noise level changes of ≥1 bp. For analyzing steps of a molecular motor, this noise would only lead to ∼10% erroneous steps when measuring an enzyme movement with a 0.2-Hz stepping rate. As expected, the spatial precision

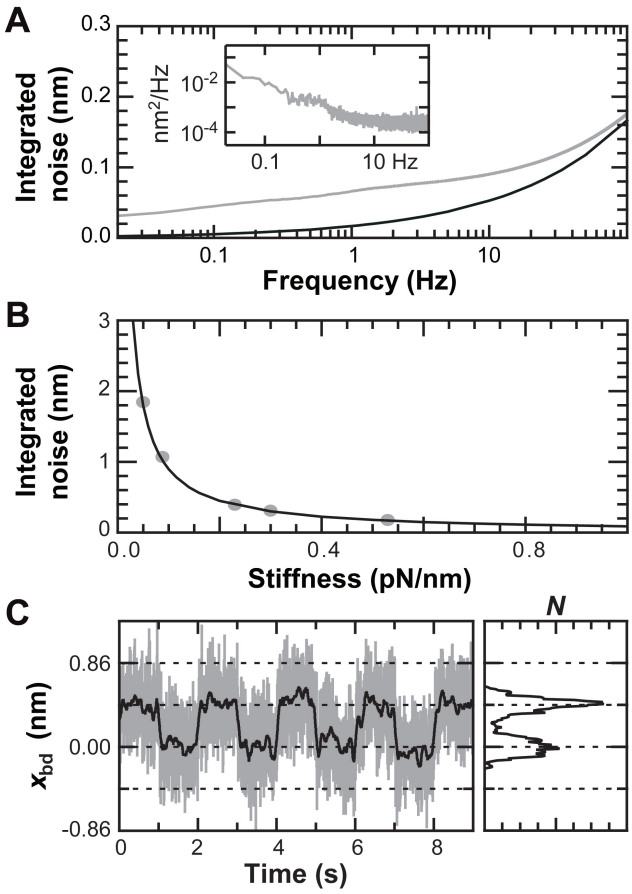

Figure 5.3: Precise tracking of trapped bead position. (**A**) Inset: the power spectral density in x_{bd} for an isolated trapped bead ($k_{\mathrm{T}} = 0.53$ pN/nm). The integrated noise in x_{bd} (*gray*) of the power spectral density was within 0.5 Å of the thermal limit (*black*). (**B**) Likewise, the integrated noise (*gray circles*) over a bandwidth of 0.02–100 Hz at different trap-stiffness values followed the thermal noise limit (*black line*). (**C**) Steps in x_{bd} as the trapping laser was moved back-and-forth relative to the detection laser. Data was filtered with a Savitzky-Golay window to 100 Hz (*gray*) and 5 Hz (*black*). A histogram of the 5 Hz data showed distinct peaks.

increased with increasing force (Fig. 5.4 **D**) for $\Delta f = 0.1$–10 Hz, but is currently limited by the residual error in stage stabilization.

Ideally, we seek to perform high resolution studies of force-sensitive states. For example, the E. coli RecBCD helicase experiences a force-induced backwards slip at a variable time (∼1–10 s) if exposed to $F > 6$ pN [96]. For such states, there is only a limited amount of time to take the measurements and that time may be short compared to the thermal equilibration time (10–1000 s). With active stabilization of the lasers and the microscope, we attained 1-bp stability following dynamic force changes. Specifically, the spatial precision in the 60 s after a force change of 3.4 pN (Fig. 5.4 **E**) yielded a stability of 3.1 Å (rms) for $\Delta f = 0.1$–10 Hz, in quantitative agreement with steady state measurements (Fig. 5.4 **D**). A small (∼2 nm), systematic offset in L accompanied the change in force. Such offsets have been seen previously [96] and are most likely due to the difficulty in correctly modeling the elasticity of short DNA molecules [108].

Finally, we demonstrated sensitivity to steps along DNA by moving the stage in a series of 0.34-nm increments every 5 s (Fig. 5.5 **A**). Conceptually, this stage motion is the signal input (Fig. 5.5 **A**, *blue*). The deduced contour length, calculated without incorporating the stage motion, is the signal corrupted by thermal and mechanical noise. Quantification of steps in single-molecule experiments can be done by a step-fitting algorithm [48]. Such fitting of our data recapitulated the input motion over both a few [0.33 ± 0.08 nm (mean ± SD; $N = 6$)] and many steps [0.38 ± 0.13 nm (mean ± SD; $N = 52$)]. Another metric to demonstrate step detection is a pairwise-distance difference histogram, which revealed a peak at 0.31 ± 0.09 nm (peak ± HWHM) (Fig. 5.5 **B**). Experimentally, the signal-to-noise ratio of the data is ∼4, within the signal-to-noise threshold for accurate determination of steps [129]. Thus, we resolved the smallest known biological step in the widely used surface-coupled assay.

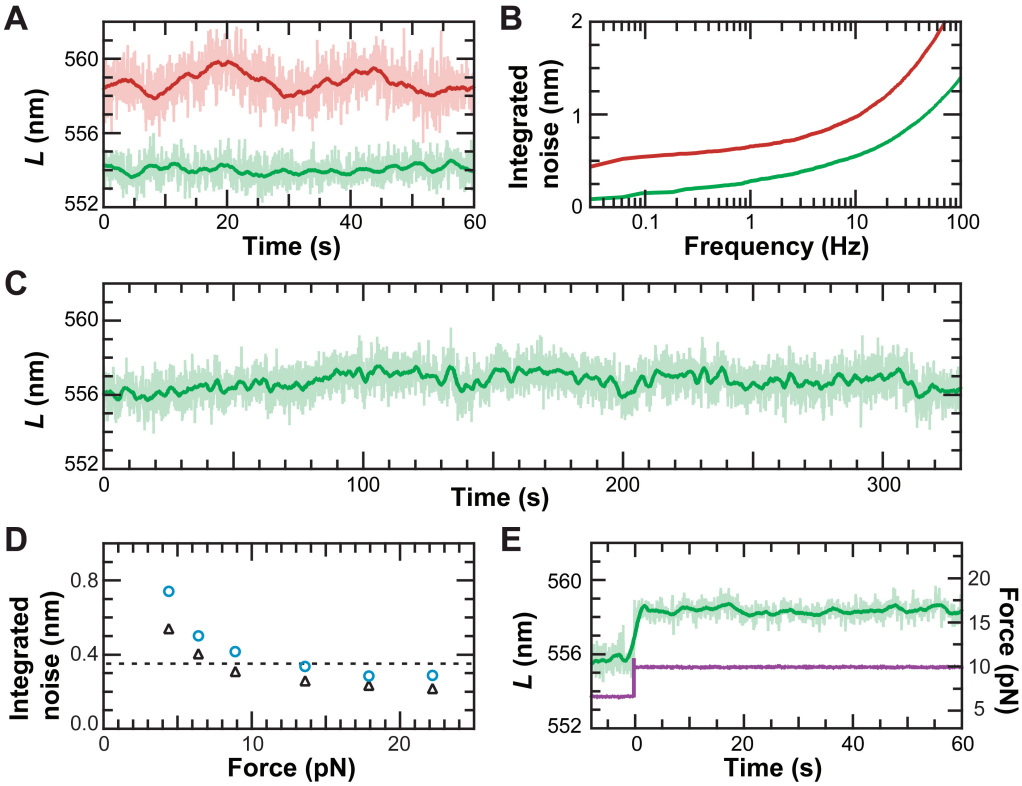

Figure 5.4: Positional stability of 1 bp along DNA. (**A**) DNA contour length (L) measurement with (*green*) and without (*red*) active stabilization of both the trap and surface. Data taken at $F = 6$ pN and $x_{\mathrm{bd}} = 70$ nm, and filtered using a Savitzky-Golay window (*light* = 5 Hz, *dark* = 0.2 Hz). (**B**) The integrated noise for traces in **A**. With active stabilization (*green*), the positional stability of the system increases four-fold at 0.1 Hz and is 1 bp (3.4 Å) over 0.03–2 Hz. (**C**) Record of L vs. time over 5 min, with the same conditions and trace color as in **A**. (**D**) The integrated noise in L ($\Delta f = 0.1$–10 Hz) as a function of force at two different lengths [556 nm (*black triangles*), 1007 nm (*blue circles*)]. (**E**) Record of length versus time during a 3.4 pN step increase in force (*purple*). Trace color and conditions same as in **A**. Traces offset vertically for clarity in **A**, **C**, and **E**.

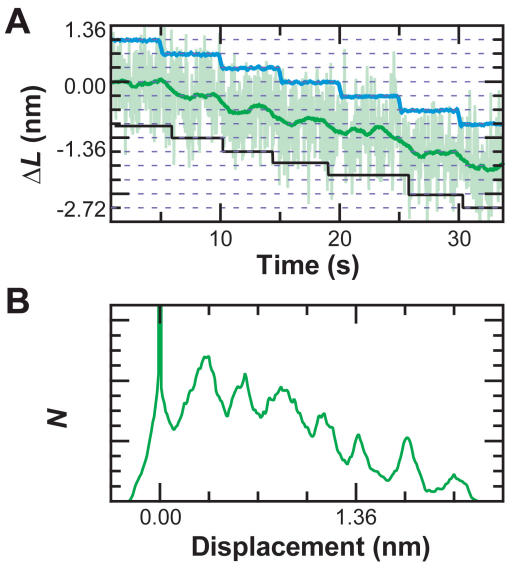

Figure 5.5: Resolution of 1 bp steps along DNA. (**A**) To demonstrate the resolution of the system, the stage was moved in 0.34-nm increments (*blue*) such that the apparent DNA contour length changes (ΔL). A step-fitting algorithm found steps (*black*) at 0.33 $\pm$ 0.08 nm (mean $\pm$ SD, $N = 6$). Data taken at $F = 6$ pN and $x_{\mathrm{bd}} = 70$ nm, and filtered using a Savitzky-Golay window (*light green* = 5 Hz, *dark green* = 0.2 Hz). Traces offset for clarity. (**B**) A pair-wise distance difference histogram of the 0.2 Hz data from **A** shows a peak at 0.31 $\pm$ 0.09 nm (peak $\pm$ HWHM).

5.6 Precision force control

The precise control of force developed here is beneficial to experiments beyond resolving steps of molecular motors. Biological structures are highly sensitive to changes in the applied force [64, 135, 136]. To illustrate the importance of steady-state force control, we studied a previously characterized DNA hairpin, 20TS06/T4 [135], and measured its unfolding dynamics (Fig. 5.6). We obtained an unfolding distance (Δx) of 19.7 nm and a force at which the hairpin has a 50% probability of being unfolded ($F_{1/2}$) of 12.3 pN, in quantitative agreement with previous results [135]. Small force changes (ΔF) of 0.1 pN in either direction substantially shifted the probability of being unfolded (Fig. 5.6). More quantitatively, a force change of <1% ($\Delta F/F_{1/2}$) shifted the probability of being folded by ∼20%. In such cases where the biological molecule under study is exquisitely sensitive to the applied force, precise force control must be maintained. Yet, commercial lasers rarely specify intensity stability to better than 1%. Hence, our reduction in intensity noise to ∼0.01% rms provides a biologically useful increase in precision for force measurements.

5.7 Conclusions

We used active stabilization of both the surface and trap to achieve 1 bp positional precision in a surface-coupled optical-trapping assay. By actively stabilizing multiple forms of laser noise, we tracked bead position to within 0.5 Å of the thermal limit and measured 0.1-pN force-induced changes in DNA hairpin unfolding dynamics. Our current short-term (∼1 s) positional precision is limited by the residual error (1 Å) in surface stabilization. We expect that it is this noise that prevents us from reaching the theoretical limit under these conditions [129]. Further improvements to increase surface stabilization could include a feedback loop with a field-programmable gate array coupled with a stiffer stage to increase the loop closure time [21]. To improve long-term stability,

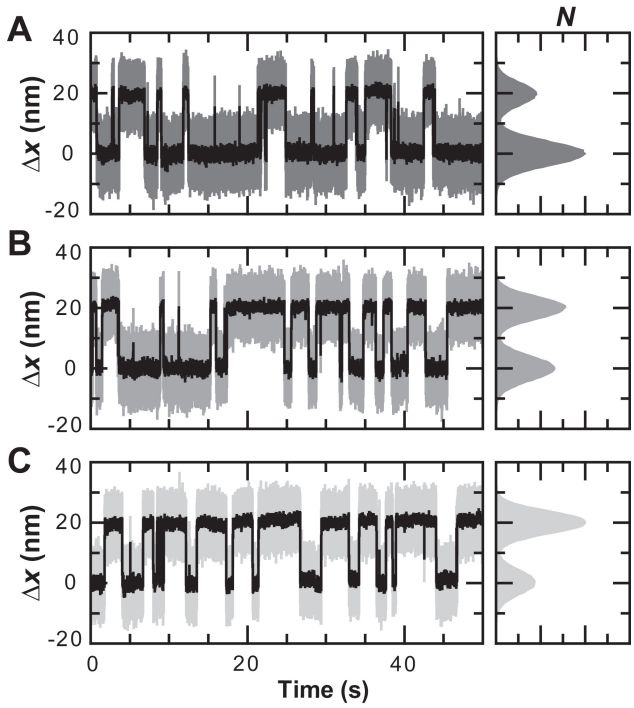

Figure 5.6: DNA hairpin unfolding dynamics show need for force precision. DNA hairpin dynamics under a constant load of (**A**) 12.2 pN, (**B**) 12.3 pN, and (**C**) 12.4 pN. Data filtered using a Savitzky-Golay window (2 kHz, *gray*; 100 Hz, *black*). Histogram of the data shows probability of being unfolded increases from 29% (12.2 pN) to 52% (12.3 pN) and then to 68% (12.4 pN).

differential laser motion could be minimized with a more compact optical design and by launching all three lasers from one fiber. This improved the differential laser stability for two lasers, in a different application, from <65 pm laterally (Δf = 0.1–50 Hz) to 19 pm [16].

In comparison with existing high-resolution dual-beam methods [1, 76], we achieved 1-bp positional precision at a factor of 1.2–3 lower force with a surface-coupled assay and without the encasement of optics in helium. Dual-beam assays enable enhanced measurements using passive force clamps [39]. Dual-beam assays with differential detection offer a small ($\sqrt{2}$), but significant, increase in time resolution [77]. In contrast, our active stabilization method increases force sensitivity, stabilizes the geometry in all three dimensions, and is surface coupled for rapid adoption to a wide variety of existing assays [5, 11, 45, 48, 120, 132, 140]. Dual beam assays would also benefit from increased force precision. Future assays could combine single-molecule force and fluorescence assays using total internal reflection fluorescence, a surface-based technique [11], with the enhancements presented here.

Chapter 6

Conformational dynamics of the RecBCD-DNA complex

6.1 Introduction

Helicases are enzymes that unwind double-stranded nucleic acid in the first steps of nucleic acid processing [111]. One particularly complex helicase, RecBCD, is mechanistically capable of DNA unwinding and digestion, DNA recognition, and protein recruitment [57, 92]. Functionally, it is involved in DNA repair, homologous recombination, and excision of foreign DNA in *E. coli* [57]. This unusual variety of mechanism and function, coupled with a high processivity (36–48 kbp) and speed (∼1 kbp/s) [66], allows for an extraordinary helicase. We are interested in determining how this complex helicase uses the chemical energy of ATP to mechanically unwind the DNA duplex.

The first step in understanding the physical mechanism of any helicase is to determine the step size of movement. Previously, two different methods (crystallography and pre-steady state unwinding assays) yielded two proposed step sizes for SFI helicases (the structural super family that contains RecBCD). Crystallographic studies of the enzyme-DNA complex with and without ATP infer a 1 bp "mechanical step size", which is the translocation per ATP hydrolysis event [61, 125]. Pre-steady state unwinding assays, on the other hand, measure the number of base-pairs per rate-limiting translocation or the "kinetic step size". At rate-limiting ATP concentrations we would expect the mechanical and kinetic step size to be equal. However, for RecBCD unwinding assays at rate-limiting ATP concentrations, the kinetic step size is 4 bp [68, 69, 67]. Thus,

there is a conflict in the field over what the actual step size is for RecBCD and other helicases.

To resolve this conflict, we sought to directly measure the step size of RecBCD using a single molecule optical trapping assay. Single molecule assays measure the dynamics of individual molecules, and therefore, do not require synchronization (as in pre-steady state unwinding assays) or rely on an average behavior (as in both crystallographic studies and unwinding assays). Optical trapping assays can probe the force-dependence of unwinding and allow for measurements of the energy landscape. However, previous measurements of RecBCD movement using this type of assay were limited to a 6-bp resolution [96], which masked the underling 1 or 4 bp steps.

To improve resolution, we built a precision optical trapping assay that was sensitive to 1 bp movements along DNA (see Ch. 5 and Fig. 1.4). In the previous measurement [96], a biotinylated form of RecBCD was attached to a streptavidin surface. The RecBCD then bound a DNA molecule (2.4 μm), which was biochemically linked to a polystyrene bead and stretched using the optical trap. Bead position (x_{bd}) was used to calculate double-stranded DNA contour length (L) [131] and determine RecBCD translocation. Drift in either the position of the sample [89] or trapped bead [18] obscured enzymatic motion. Here in the precision optical trapping assay (Fig. 1.4), we actively stabilized the sample position by detecting the position of a fiducial mark on the sample (x_{fid}) with a detector laser and using this position in a feedback loop to minimize sample drift [17]. We also actively stabilized the trapping laser to decrease multiple sources of laser noise that affected trapped bead position [18]. In samples where the DNA was directly attached to the surface without RecBCD, DNA length measurements were stable to 1 bp (rms, Δf = 0.03–2 Hz) and the precision optical trapping assay was capable of resolving 1-bp movements [18].

Using this precision optical trapping assay, we measured the conformational dynamics of single RecBCD-DNA complexes. RecBCD movement along DNA showed

discrete steps that were variably sized with the average step size of 4.4 bp agreeing with pre-steady state unwinding assays [67, 68, 69]. We also observed backwards motion of the enzyme at low ATP concentrations (2 μM) that were similar to forwards steps in both their variability and average step size (4.3 bp). Additionally, RecBCD exhibited $\pm$3 bp fluctuations at frequencies above the stepping rate ($\sim$0.1–10 Hz). These ATP-independent, force-dependent fluctuations were only present when the RecD helicase was engaged on the DNA template. Moreover, the different conformations were dependent on the upstream double-stranded DNA sequence, suggesting that they were translocations of RecBCD along the DNA template. These observations imply that RecBCD unwinding does not occur through a series of 1 bp translocations, each of which is dependent on ATP hydrolysis, as hypothesized by crystallographic studies [13, 61, 125]. Instead, our data agrees with models of helicase unwinding that have multiple base-pair step sizes [66].

6.2 Discrete motion along DNA

Using our precision optical trapping assay, we measured L as RecBCD unwound the double-stranded DNA (Fig. 6.1). Data was taken at 6 pN of force, unless otherwise noted, and in WB buffer (1 mM magnesium acetate, 1 mM sodium chloride) with 2 μM ATP, 1 mM E. coli single-stranded binding protein, and an oxygen scavenging system to prevent free oxygen radicals. Forward movement caused a decrease in L. RecBCD motion ($N = 20$) at this low ATP concentration displayed pauses and changes in velocity (Fig. 6.1 **A**), as in previous experiments [96]. Traces also displayed discrete steps, which appeared as fast translocations of the enzyme separated by pauses in movement (Fig. 6.1 **B**). To identify steps we used a step-finding algorithm that fit the 1-Hz data based on a maximum-likelihood parameter [48]. Each molecule displayed steps that were variable in size from about 2-6 bp, occasionally larger. A histogram of the forward steps (Fig. 6.1 **C**) was fit by a Gaussian curve with a peak at 4.4 $\pm$ 1.8 bp (mean $\pm$ σ); the peak

step size agreed with pre-steady state unwinding assays that measure an average step size of 3.9 ± 0.5 bp [67]. Interestingly, a two-fold increase in the ATP concentration to 4 μM did not change the average step size, which also agreed with previous results [67].

In addition to forwards motion, we noticed that all of the RecBCD molecules studied took occasional backwards steps at the low ATP concentration used (Fig. 6.1). While backwards steps were similar to forwards steps in both variability (2-6 bp) and average step size (4.3 ± 2.7 bp as determined by a Gaussian fit to a histogram of backwards steps), the probability for a backwards step was 30%, allowing for forward motion of RecBCD. As ATP concentration was increased two-fold, the probability of a backwards step decreased two-fold to 14%, suggesting that backwards motion does not occur at higher ATP concentrations, and therefore, would not have been measured in previous assays [68, 69, 67, 96]. Forward motion after a backwards step was identical in both size and dwell time to regular forward movement. Given this data, we interpret backwards movement as a backwards step of the enzyme coupled with a reannealing of the double-stranded DNA.

6.3 Conformational dynamics in the RecBCD-DNA complex

Unexpectedly, in between steps, measurements of RecBCD motion fluctuated by ±3 bp at 1 Hz, well above the instrumental noise floor of ∼1 bp (Fig. 6.2). A record of DNA length as measured by a digoxigenin-labeled DNA molecule attached to an anti-digoxigenin surface demonstrated the instrumental noise present in the assay. We compared this record to a record of RecBCD motion where the time in between steps was long enough so that comparison was possible (Fig. 6.2 **A**). A histogram of the RecBCD motion at 1 Hz had a HWHM of 1.09 nm (3.2 bp), which was three-fold higher than the instrumental noise (HWHM = 0.29 nm). The power spectral density of the records (Fig. 6.2 **B**) showed that the fluctuations occur over the bandwidth 0.1–10 Hz, just above the above the stepping frequency of 0.1–0.2 Hz. Comparison of the integrated

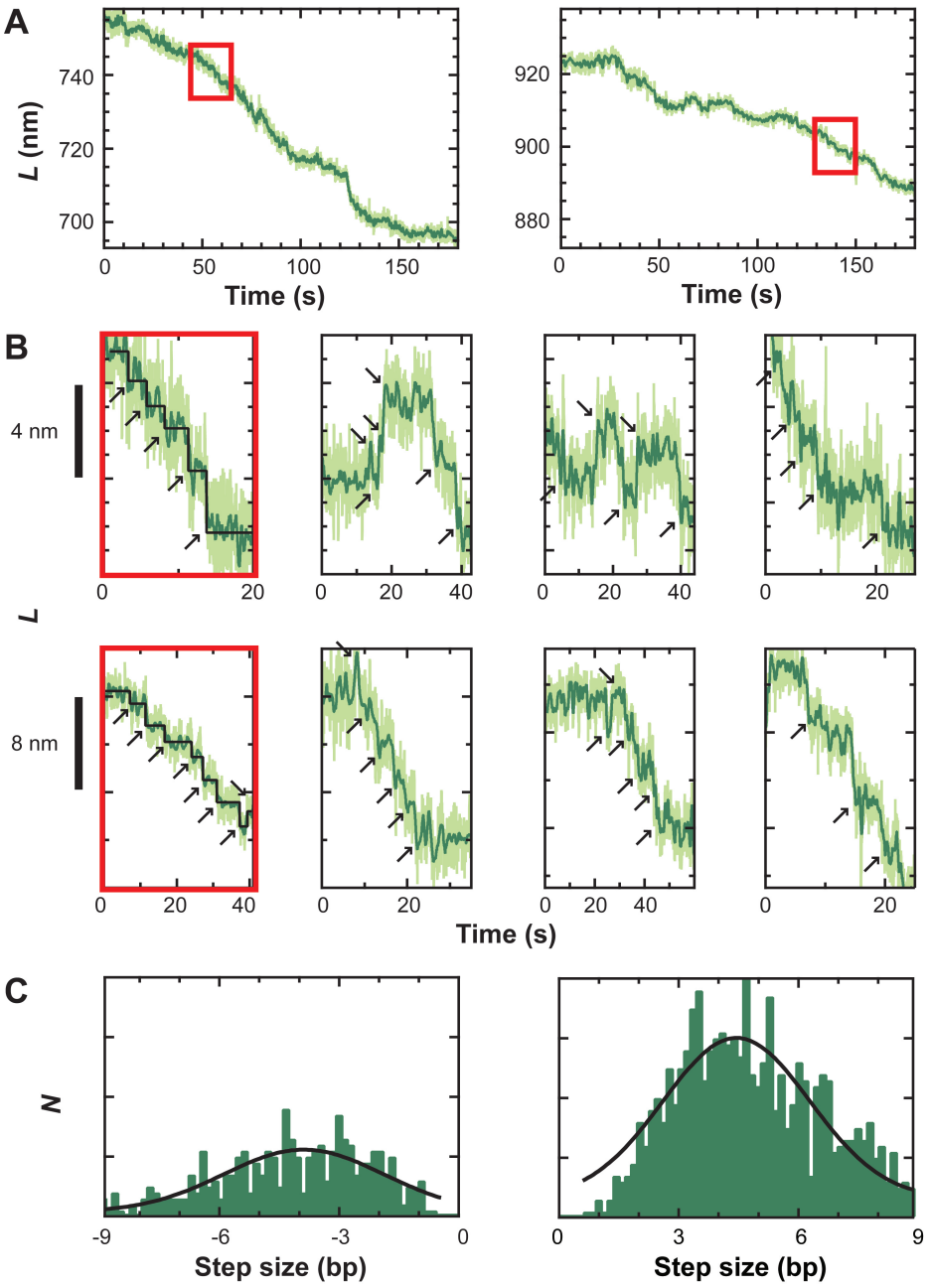

Figure 6.1: RecBCD motion shows forward, backward, and variably sized steps. (**A**) DNA contour length (L) decreases as RecBCD moves forward. Traces taken at 6 pN of force, 2 μM ATP, and smoothed with a Savitzky-Golay window to 10 Hz (*light green*) and 1 Hz (*dark green*). (**B**) Closer view of RecBCD movement shows discrete steps. Zoom-in of traces in **A** in red boxes. Motion was fit with a step-fitting algorithm [48] (*black line*), which determines placement of steps (*black arrows*). Trace color same as in **A**. (**C**) Histograms of the steps show variably sized forward and backward motion. Gaussian fits to the data reveal a peak at 4.4 bp $\pm$ 1.8 bp (mean $\pm$ σ) for forward motion and 4.3 bp $\pm$ 2.7 bp for backward motion. The number of backwards steps are 30% of the total.

noise under the power spectral density was similar to measurements of histogram width. RecBCD fluctuations had an integrated noise level of 0.94 nm (2.8 bp) at 1 Hz, while the integrated noise present in the instrument was 0.28 nm. This same measurement over the entire frequency range of the fluctuations (0.1–10 Hz) gave an integrated noise level of 1.41 nm (4.1 bp) for RecBCD movement in between steps, above the instrumental noise of 0.55 nm (1.6 bp). We posit that the ±3 bp fluctuations are real and enzyme-dependent since measurements of instrumental noise are much lower.

There are four sources of enzyme-dependent movements in our assay that could be causing the fluctuations (Fig. 6.3). We measure the movement of RecBCD along the DNA template through the surface-RecD-DNA attachment point, which has four possible sources of movements: translocations of RecBCD along the DNA template (α), enzymatic movements within RecBCD (β), movements between RecBCD and the biotin tag (γ), and movements within the biotin-streptavidin surface-attachment (δ). We can rule out movements in the biotin-streptavidin surface-attachment, δ, because measurements of a DNA molecule with a biotin linkage attached to a streptavidin surface produced identical noise characteristics as that of a digoxigenin-labeled DNA molecule attached to an anti-digoxigenin surface (i.e. there were no fluctuations). In addition, measurements of DNA contour length for RecBCD bound to a blunt-end DNA molecule did not show fluctuations (Fig. 6.4), eliminating movement between RecBCD and the biotin tag, γ. The integrated noise at 10 Hz for $\geq$5 traces was on average 0.83 ± 0.04 nm (mean ± σ_{error}), below the measurement for fluctuations, although slightly higher than the measured instrumental noise (integrated noise at 10 Hz was 0.53 ± 0.03 nm, mean ± σ_{error}). Thus, we hypothesize that the fluctuations are conformational dynamics in the RecBCD-DNA complex: either translocations of RecBCD along the DNA template or motion within RecBCD.

By measuring the conformational dynamics for different RecBCD-DNA binding conditions, we found that the conformational changes were ATP-independent and only

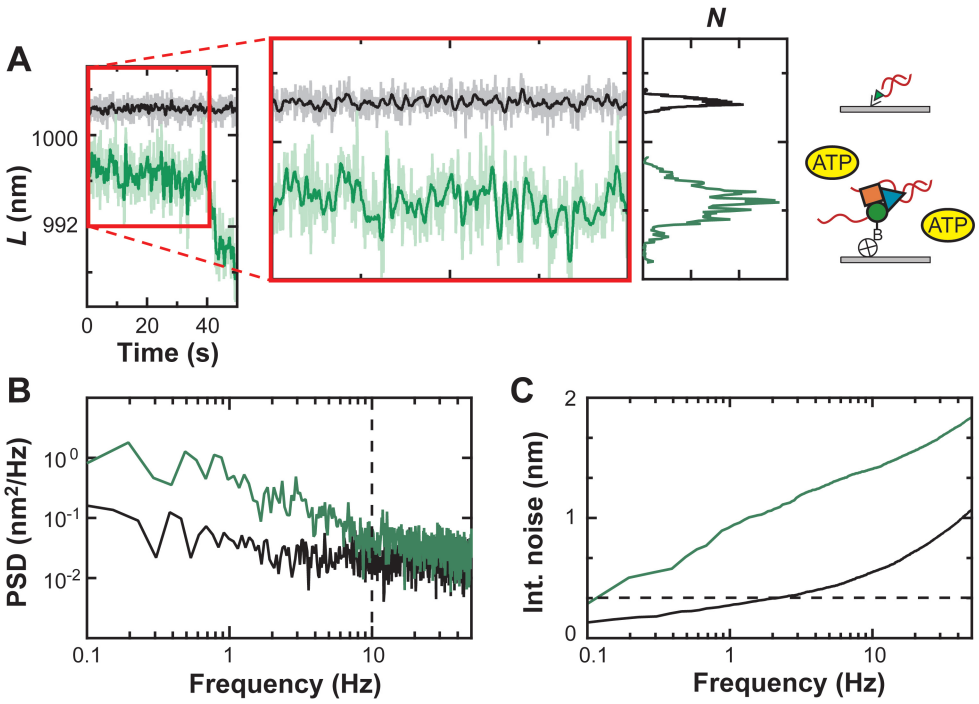

Figure 6.2: RecBCD motion shows ±3 bp fluctuations between stepping events. (**A**) RecBCD motion (*green*), as measured by a RecBCD enzyme attached to the surface (*right bottom cartoon*), shows fluctuations in between steps. Measurement of L (*black*) for a DNA molecule attached to the surface (*right top cartoon*) shows the level of noise present in the instrument. Red box is a zoom-in. Traces smoothed with a Savitzky-Golay window to 10 Hz (*light*) and 1 Hz (*dark*). Histograms of the 1 Hz data have a HWHM of 0.29 nm for instrumental noise and 1.09 nm (3.2 bp) for RecBCD fluctuations. (**B**) Power spectral density (PSD) of the position data in the red box in **A**. RecBCD motion (*green*) shows fluctuations at 0.1–10 Hz that are above the instrumental noise (*black*). (**C**) Integrated noise of the PSD in **B**. Instrumental noise (*black*) is at 0.28 nm at 1 Hz, while RecBCD fluctuations (*green*) are at 0.94 nm (2.8 bp). Over the 10 Hz bandwidth that fluctuations occur, the integrated noise for the RecBCD motion between stepping events is 1.41 nm (4.1 bp), above the instrumental noise of 0.55 nm (1.6 bp).

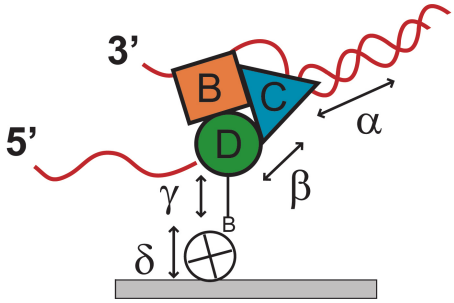

Figure 6.3: Fluctuations are conformational dynamics in the RecBCD-DNA complex. Conformational dynamics in the RecBCD-DNA complex are either translocations of RecBCD along the DNA (α) or movements within the RecBCD enzyme (β) or both. The fluctuations are not movements in the biotin attachment to enzyme (γ) or motion of the attachment to the surface (δ).

occurred when RecD engaged the DNA template (Fig. 6.4). To measure the effects of ATP, we stalled RecBCD in the middle of the DNA template after it had translated ∼1 μm by washing WB buffer without ATP through the sample. Measurements of L did not display RecBCD forward motion, but did display different conformations (Fig. 6.4 **A**). The integrated noise of the conformational changes (Fig. 6.4 **B**,**C**) for ∼5 traces at 10 Hz was 1.40 ± 0.04 nm (mean ± σ_{error}), similar to the integrated noise for RecBCD conformational dynamics in between steps (1.39 ± 0.02 nm, mean ± σ_{error}). Since the conformational changes were ATP-independent, we then hypothesized that engaging the RecD subunit might cause these dynamics. To check this hypothesis, we used a DNA substrate that engaged the RecD subunit upon RecBCD binding. This DNA substrate has an end possessing a pre-existing single-stranded $(\text{dT})_N$ tail, where N represents the number of T's in the tail (see Section 2.2.3). A substrate with a 5'-$(\text{dT})_{10}$ tail contacts the RecD subunit [105] and eliminates the initial RecBCD unwinding steps [137], whereas a 5'-$(\text{dT})_6$ tail does not. We measured DNA length for RecBCD bound to a substrate with a 5'-$(\text{dT})_{10}$ and 3'-$(\text{dT})_5$ tail and for RecBCD bound to a DNA end with a 5'-$(\text{dT})_6$ and 3'-$(\text{dT})_6$ tail. The RecBCD bound to the 5'-$(\text{dT})_{10}$ tail exhibited conformational dynamics (integrated noise at 10 Hz was 1.40 ± 0.05 nm, mean ± σ_{error}), whereas the RecBCD bound to the 5'-$(\text{dT})_6$ tail did not (integrated noise at 10 Hz was 0.84 ± 0.04 nm, mean ± σ_{error}). This is consistent with previous measurements that show substrates with both a 5'-$(\text{dT})_6$ and 3'-$(\text{dT})_6$ tail act like blunt-end DNA, whereas substrates with a 5'-$(\text{dT})_{10}$ tail act like threaded DNA [105, 137]. Thus, the conformational dynamics occur when the DNA template engages RecD.

We expect that conformational dynamics in the RecBCD-DNA complex would be force-dependent, with increasing force showing less conformations. Experimentally, this was the case. We measured the conformational dynamics for RecBCD stalled in the middle of the DNA template without ATP as a function of force (Fig. 6.5). Conformational changes at 4 pN decreased from an integrated noise level at 10 Hz of

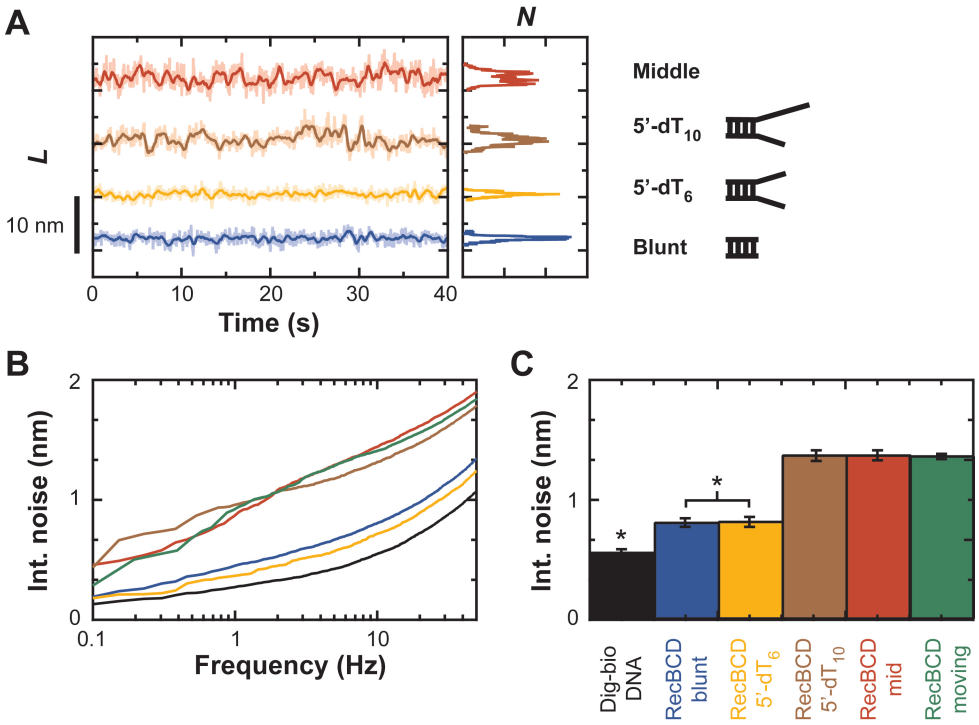

Figure 6.4: Conformational dynamics were ATP-independent and occur when RecD is engaged. (**A**) Measurement of L for different RecBCD-DNA complexes: RecBCD bound to blunt-end DNA (*blue*), RecBCD bound to a DNA end possessing pre-existing single-stranded $(dT)_6$ tails [134] (*orange*), RecBCD bound to a DNA end with a 3'-$(dT)_5$ and 5'-$(dT)_{10}$ tail (*brown*) that engages the RecD subunit [105], and RecBCD stalled in the middle of the DNA molecule (*red*) after translocation and RecD engagement. All conditions without ATP. Traces smoothed with a Savitzky-Golay window to 10 Hz (*light*) and 1 Hz (*dark*). Histograms of the 1 Hz data show the noise level of each case. (**B**) Integrated noise for the traces in **A** (trace color same as in previous) shows that fluctuations occur when RecD is engaged (*brown*, *red*). Traces from Fig. 6.2 for reference. (**C**) Bar graph of the integrated noise at 10 Hz for the conditions in **A** and in Fig. 6.2 with $N \sim 5$. Trace color same as in **A** and Fig. 6.2. Points that are statistically significant (95

1.69 ± 0.17 nm to 0.84 ± 0.05 nm at 10 pN. This decrease was 2.6-fold higher than the decrease in instrumental noise that also accompanies a force change. Measurements at forces higher than 10 pN were not available due to RecBCD backsliding along the DNA template [96].

6.4 Conformational dynamics were ATP-independent

RecBCD-DNA conformational dynamics were independent of changes in the ATP-binding site. In Figure 6.4 we observed that conformational changes occurred even without ATP. We checked these results by measuring RecBCD conformational dynamics (Fig. 6.6) with 2 mM AMP-PNP (an ATP analog) and 2 mM ADP (the hydrolyzed product of ATP) on DNA substrates where RecD was engaged. Conformational dynamics in both cases had a similar integrated noise level at 10 Hz of 1.4 ± 0.07 nm and 1.36 ± 0.15 nm, respectively. We note that ADP may not be binding the enzyme and would therefore represent the same state as without ATP. We also tested a mutant RecBCD enzyme ($\text{RecBCD}^{\text{K177Q}}$) where the RecD ATP-binding pocket [25] had a lysine to glutamine substitution at position 177 in the Walker A box (helicase motif I) [38]. This well established mutation decreases ATP hydrolysis and helicase activity [25]. We did not measure a change in the level of conformations in the mutated $\text{RecBCD}^{\text{K177Q}}$ enzyme; the integrated noise at 10 Hz was 1.29 ± 0.06 nm. Likewise, a four-fold increase in the magnesium acetate concentration to 4 mM did not change the conformational dynamics either (integrated noise at 10 Hz was 1.38 ± 0.06 nm). This evidence suggests that the conformational dynamics are not due to changes in the RecD ATP-binding site.

We note that sometimes the measured conformational dynamics did show an ATP-dependence. Up until this point we have only discussed one type of conformational dynamics, type I conformational dynamics. These dynamics have an integrated noise level of 1.40 nm at 10 Hz and appeared 85% of the time. In addition, type I conformational dynamics were always ATP-independent and only occurred when the

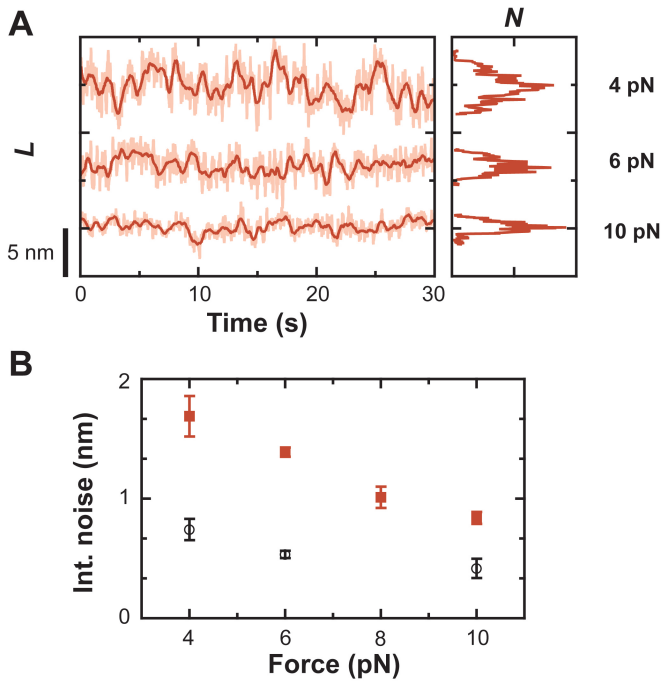

Figure 6.5: Conformational dynamics were force-dependent. (**A**) Measurement of L for RecBCD stalled in the middle of the DNA molecule (*red*) after translocation and RecD engagement at three different forces (*top* = 4 pN, *middle* = 6 pN, *bottom* = 10 pN). Traces smoothed with a Savitzky-Golay window to 10 Hz (*light*) and 1 Hz (*dark*). Histograms of the 1 Hz data show the conformational changes of each case. (**B**) Integrated noise at 10 Hz as it varies with force for the condition in **A** (*red*) and for the condition of a digoxigenin-labeled DNA molecule attached to an anti-digoxigenin surface (*black*). Data collected for $N \sim 5$, center point is mean, error bars are the standard deviation.

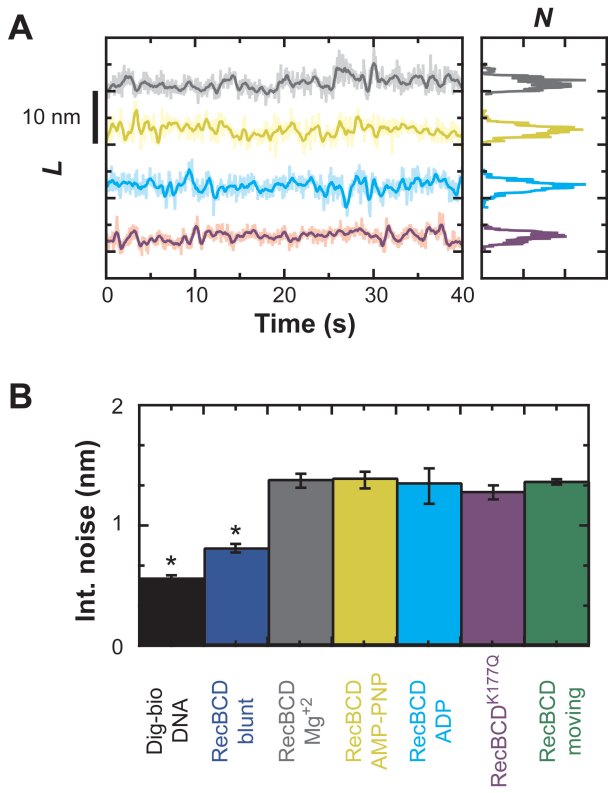

Figure 6.6: Conformational dynamics are independent of changes in the ATP-binding site. (**A**) Measurement of L for different conditions of RecBCD bound to DNA: RecBCD bound to 5'-dT$_{10}$ tail DNA with a four-fold increase in Mg^{+2} to 4 mM (*gray*), RecBCD bound to 5'-dT$_{10}$ tail DNA with 2 mM AMP-PNP (*yellow*), RecBCD stalled in the middle of the DNA with 2 mM ADP (*cyan*), and RecBCD^{K177Q} (RecBCD with a mutation in the RecD ATP-binding site) bound to 5'-dT$_{10}$ tail DNA. Traces smoothed with a Savitzky-Golay window to 10 Hz (*light*) and 1 Hz (*dark*). Histograms of the 1 Hz data show the width of the conformational dynamics. (**B**) Bar graph of the integrated noise at 10 Hz for the conditions in **A** with $N \sim 5$ shows that the conformation dynamics do not change in each condition. Plus, the two conditions from Fig. 6.4 **C** are shown for reference (RecBCD moving along DNA in between steps, *green*, and DNA bound to the surface, *black*) and the condition for Fig. 6.4, RecBCD bound to blunt-end DNA, *blue*. Otherwise, color same as in **A**. Points that are statistically significant (95

RecD subunit was engaged. We also observed type II conformational dynamics, which occurred without ATP and when the RecD subunit was engaged (Fig. 6.7 **A**). However, type II conformational dynamics were much larger (the integrated noise at 10 Hz was 3.30 ± 0.83 nm, Fig. 6.7 **B**), only occurred 15% of the time, and were suppressed by adding 2 mM AMP-PNP (Fig. 6.7). Likewise, we do not observe type II conformational changes in the RecBCD movement assay, probably because ATP suppresses these conformations as well. While these ATP-dependent type II conformational dynamics are potentially interesting, they are not relevant in the RecBCD movement assay and were not studied further.

6.5 Conformational dynamics were DNA sequence-dependent

RecBCD-DNA conformational dynamics were dependent on the upstream double-stranded DNA sequence. We measured the conformations of RecBCD bound to two tailed DNA substrates with differing double-stranded G-C content. The DNA substrates both contained a single-stranded 5'-$(dT)_{10}$ tail to engage the RecD subunit and create conformational changes, yet on one substrate the first four double-stranded base-pairs after the tail were A-T (AT-rich), while in the other, the first three double-stranded base-pairs after the tail were G-C (GC-rich, see Section 2.2.3 and Fig. 6.8 **A**–**C**). We prepared samples with RecBCD bound to each substrate and measured L (Fig. 6.8) to see if the conformational dynamics depended on the double-stranded G-C content. RecBCD bound to the AT-rich tailed substrate exhibited larger conformational dynamics (integrated noise at 10 Hz was 1.75 ± 0.07 nm) than RecBCD bound to the GC-rich tailed substrate (integrated noise at 10 Hz was 1.10 ± 0.06 nm). Thus, the conformations depend on the sequence of the upstream double-stranded base-pairs.

This result implies that RecBCD is interacting with the upstream double-stranded base-pairs to unwind them and that the conformational dynamics that we measured are really translocations of RecBCD along the template. The difference between an A-T

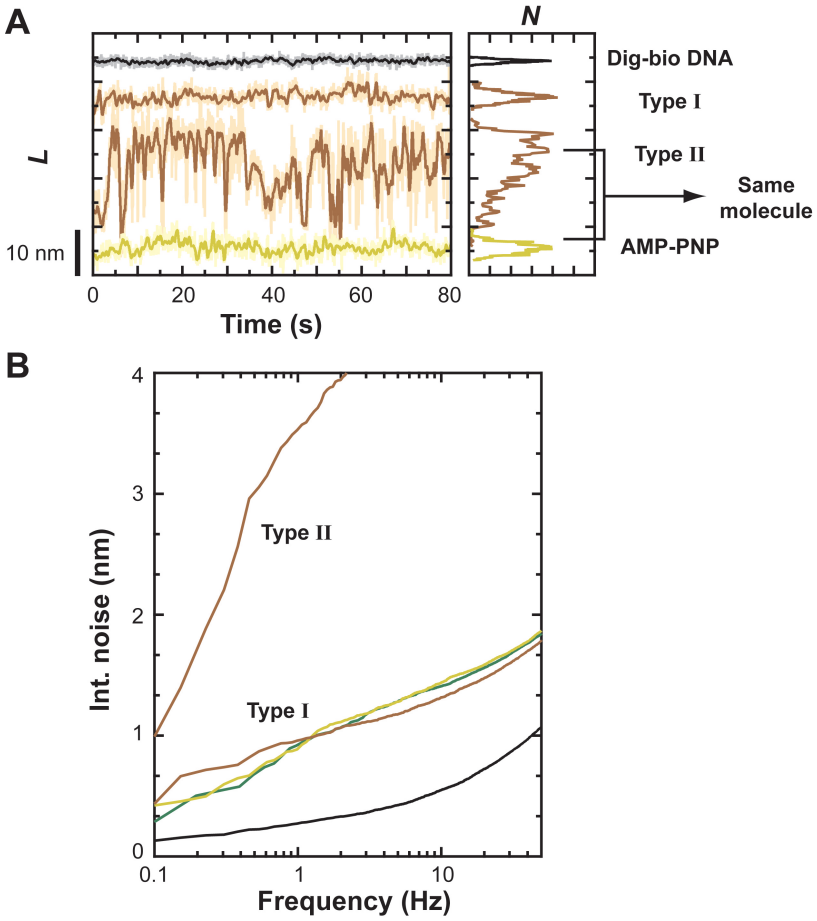

Figure 6.7: Type II conformational dynamics were dependent on ATP but were not studied. (**A**) Measurements of L for RecBCD bound to DNA with RecD engaged (RecBCD bound to 5'-$(dT)_{10}$ tailed DNA) and without ATP (*brown*) showed two different types of conformations. Type I conformational dynamics (*top*) occur 85% of the time and are smaller than type II conformational dynamics (*middle*). Type II conformational dynamics stopped when 2 mM AMP-PNP was added to the molecules that displayed the behavior (*yellow*). Measurement of L for digoxigenin-labeled DNA bound to an anti-digoxigenin surface (*black*) for reference.Traces smoothed with a Savitzky-Golay window to 10 Hz (*light*) and 1 Hz (*dark*). Histograms of the 1 Hz data show the width of the conformational changes. (**B**) The integrated noise for the conditions in **A** and the two conditions from Fig. 6.2 (RecBCD moving along DNA in between steps, *green*, and DNA bound to the surface, *black*). Type II conformational dynamics are four-fold higher at 1 Hz than type I conformational dynamics and are not present in conditions with AMP-PNP (*yellow*) or ATP (*green*). Since type II conformational dynamics are not present during RecBCD motion these conformations were not studied. Color same as in **A** and Fig. 6.2.

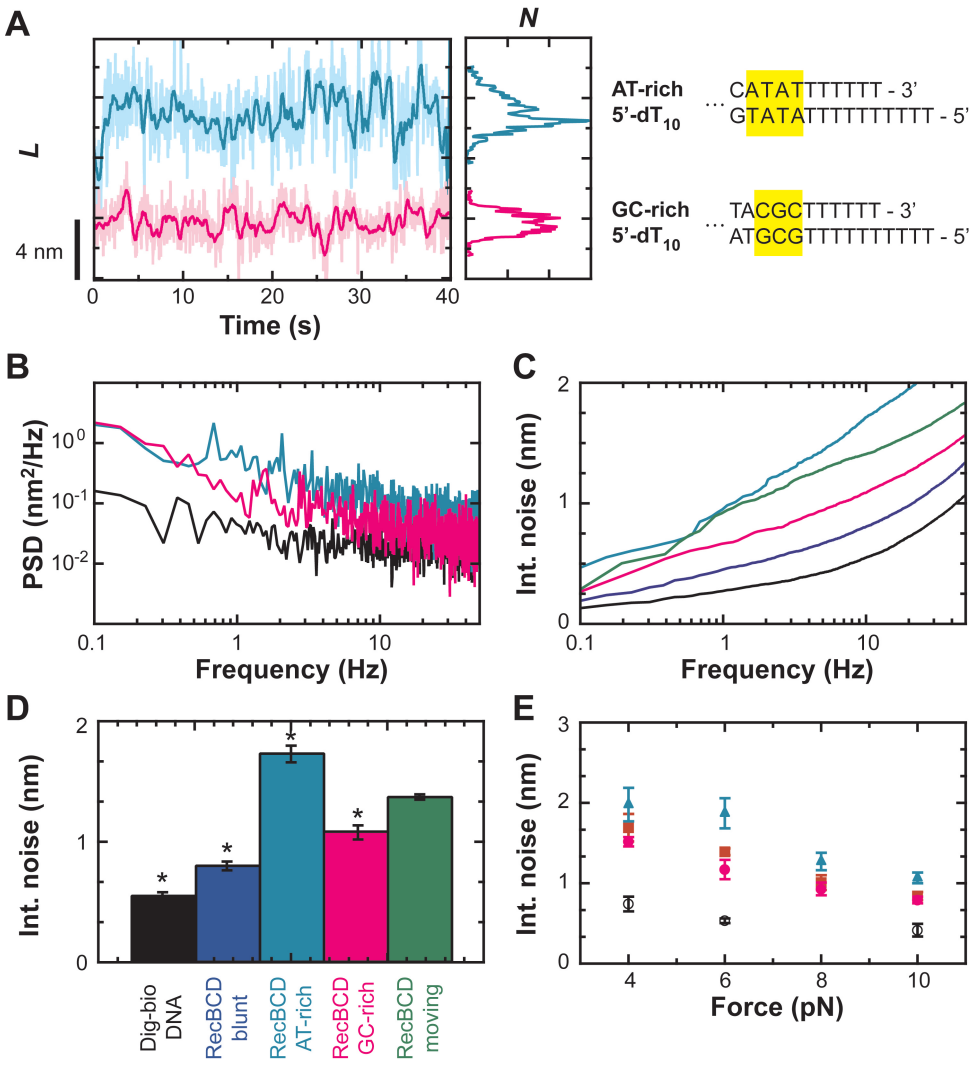

Figure 6.8: Conformational dynamics are dependent on the upstream double-stranded DNA sequence. (**A**) Measurement of L for RecBCD bound to 5'-$(dT)_{10}$ tailed DNA substrates with either the first three upstream base-pairs as A-T (*teal*) or G-C (*pink*). Traces smoothed with a Savitzky-Golay window to 10 Hz (*light*) and 1 Hz (*dark*). Histograms of the 1 Hz data have a HWHM of 1.23 nm and 0.83 nm for the A-T and G-C rich cases, respectively. (**B**) PSD of the position data in **A**, plus the instrumental noise trace from Fig. 6.2 **B** (*black*). (**C**) Integrated noise for the traces in **A**, plus two traces from Fig. 6.2 **C** for reference (RecBCD moving along DNA in between steps, *green*, and DNA bound to the surface, *black*). Trace from Fig. 6.4 **B**, RecBCD bound to blunt-end DNA (*blue*), added for reference as well. At 1 Hz the integrated noise is 0.98 nm and 0.67 nm for the A-T and G-C rich cases, respectively. This increases to 1.61 nm and 1.09 nm at 10Hz, respectively. Color in **B**,**C** same as in **A**. (**D**) Bar graph of integrated noise at 10 Hz for the conditions in **A** (color the same, $N \sim 5$). Plus, the three conditions from Fig. 6.4 **C** are shown for reference (RecBCD moving along DNA in between steps, *green*, RecBCD bound to blunt-end DNA, *blue*, and DNA bound to the surface, *black*). Points that are statistically significant (95

base-pair and a G-C base-pair is the addition of an extra hydrogen bond in the G-C case so that the energy needed to open an A-T base-pair is less than the energy needed to open a G-C base-pair. This difference in energy creates a difference in the amount of base-pairs that can be unwound given a particular energy. Thus, the conformations would be dependent on DNA sequence if they were actually unwinding events without ATP. To check this hypothesis, we compared this data to RecBCD conformational dynamics while in between steps (Fig. 6.8 **D**), which should see an average G-C content of 50%. The integrated noise at 10 Hz was 1.39 ± 0.02 nm, revealing that the conformational dynamics on the AT-rich tailed substrate are slightly higher, while conformational changes on the GC-rich tailed substrate are slightly lower, as expected. In addition, the conformational dynamics in each case are force dependent (Fig. 6.8 **E**), with smaller conformational dynamics occurring as the force was increased and the AT-rich tailed substrate having the largest conformational dynamics at each force level, as expected. These observations, taken together, indicate that the conformational dynamics are translocations of RecBCD along the DNA template without ATP.

We note that we could not rule out the possibility that RecBCD was both translocating along the DNA template and movement within RecBCD was occurring. When we compared the integrated noise at 10 Hz for conformational dynamics with RecBCD bound to the AT-rich tailed substrate, the GC-rich substrate, and blunt-end DNA (1.75 nm, 1.10 nm, and 0.84 nm, respectively), we noticed that we could not account for all of the conformational dynamics as translocations. The difference between the AT-rich tailed substrate and the GC-rich tailed substrate of 0.65 nm was due to translocations that are more energetically favorable for the AT-rich tailed substrate. However, the difference of 0.26 nm between blunt-end DNA and the GC-rich tailed substrate could be due to movement within RecBCD or translocations. In the former case, the GC-rich tailed substrate prevents translocation, whereas in the latter case the GC-rich tailed substrate allows for some translocation. Future studies with tailed substrates that pre-

vent translocation (i.e. cross-linked substrates) will resolve this issue.

6.6 Conclusions

Using a precision optical trapping assay, we measured the motion of RecBCD along the DNA template. Forward motion consisted of a series of steps, with an average step size of 4 bp, agreeing with previous pre-steady state unwinding assays that also measure a kinetic step size of 4 bp [67]. These findings are consistent with multi-base-pair stepping models [61, 62, 66], but not with models that require an ATP-rate-limited, 1-bp translocation step size [13, 61, 125].

We also observed backwards steps of the enzyme at 6 pN and a low ATP concentration that were variably sized and had an average step size of 4 bp, similar to forwards motion. Since forwards motion after a backwards step was identical to typical forward unwinding, we posit that backwards motion is movement of the enzyme in the backwards direction along the DNA template coupled with a reannealing of the double-stranded DNA. Structural studies indicate that backwards motion may be possible because the RecD subunit lacks the helicase 1a motif, which is thought to control directionality of the motor [110]. We also observed that backwards motion decreased at higher ATP concentrations, suggesting that backwards movement probably does not occur during regular unwinding *in vivo*, because the predicted probability from our data at such high concentrations of ATP would be vanishingly small. However, backward motion may occur at a barrier (a bound protein, etc.) or when the enzyme pauses at a chi site, since forward motion would be decreased. We note that we currently can not distinguish backward motion from conformational fluctuations in the backward direction. Future assays that determine the force dependence of backward motion might elucidate the difference since we might expect the amount of backward steps to increase under load and the amount of conformational fluctuations to decrease.

In between RecBCD steps, we observed ± 3 bp fluctuations that were conforma-

tional dynamics in the RecBCD-DNA complex. The conformational dynamics were ATP-independent, required engaging the RecD subunit, and were dependent on the upstream double-stranded DNA sequence. These findings suggest that the conformational dynamics are translocations of RecBCD along the DNA template by the RecD subunit. Thus, RecBCD is able to move substantially along the DNA without ATP, indicating the mechanism for a multi-base-pair step may be ATP-independent. Future work will determine whether the amount of base-pairs unwound is an active or passive mechanism by comparing the theoretical number of base-pairs unwound given thermal energy to the experimentally determined value. We anticipate that the mechanism will be active, given the high velocities of the enzyme ($\sim$1 kbp), though previous helicases have been shown to be passive [62].

Hence, we have shown that RecBCD, a structurally complex helicase [110], is also mechanistically diverse. With ATP, it is able to move both forwards and backwards in multi-base-pair steps, and without ATP, RecBCD is capable of translocational conformational dynamics along the DNA template. This diverse mechanism may be useful during processes which require high processivity, pausing, DNA recognition, and velocity changes. In addition, the larger step size may be mechanistically why RecBCD has one of the highest helicase velocities known [66].

Chapter 7

Conclusions

In summary, we have used single molecule assays to elucidate how helicases convert the chemical energy from ATP hydrolysis into a translocation along DNA. To measure these Ångstrom-scale translocations, we first developed a precision surface-coupled optical trapping assay that actively stabilized the sample to 1 Å [17] and removed multiple sources of trap laser noise [18]. Using this stabilized assay, we directly measured the conformational dynamics of the *E. coli* helicase, RecBCD, bound to DNA with and without ATP. With ATP, RecBCD moved both forward and backward in variably sized steps. The peak step size, 4.4 bp, agrees with the previously measured kinetic step size of 3.9 ± 0.5 bp [68, 67]. Without ATP, RecBCD showed ± 3 bp conformational dynamics that occurred when RecD was engaged. These conformations were ATP-independent, indicating that they were not conformational dynamics of the helicase ATP-binding site. However, the conformational dynamics were dependent on the sequence of the upstream double-stranded DNA, suggesting that they were RecBCD translocations along the DNA template, without ATP. These observations imply that RecBCD movement occurs in large steps without ATP, while ATP addition biases forwards movement. As such, our findings are consistent with multi-base-pair models of helicase movement [61, 62, 66], but not models that assume an ATP-rate-limited, 1-bp translocation [13, 61, 125].

Future work will be needed to determine an exact model. Single molecule assays could be performed with different mutations or attachment points of the enzyme to

change the conformational dynamics. In addition, single molecule measurements of RecBCD motion after chi site recognition will be particularly illuminating because the lead helicase in the heterotrimeric complex changes from RecD to RecB. Bulk structural studies of RecBCD crystallized with different ATP analogs will also be important in defining the different possible states of the helicase. Thus, we anticipate that the data we have presented is only the beginning of a multitude of measurements on RecBCD and helicases in general. These new measurements will be aided by single molecule techniques with 1 bp resolution [1, 76, 18], and by coupling optical trapping assays with fluorescent-based measurements [11].

Bibliography

[1] E. A. Abbondanzieri, W. J. Greenleaf, J. W. Shaevitz, R. Landick, and S. M. Block. Direct observation of base-pair stepping by RNA polymerase. Nature, 438:460–465, 2005.

[2] M. Abe, Y. Sugimoto, T. Namikawa, K. Morita, N. Oyabu, and S. Morita. Drift-compensated data acquisition performed at room temperature with frequency modulation atomic force microscopy. Appl. Phys. Lett., 90:203103, 2007.

[3] J. A. Ali and T. M. Lohman. Kinetic measurement of the step-size of DNA unwinding by Escherichia coli UvrD helicase. Science, 275:377–380, 1997.

[4] J. M. Antonietti, J. Gong, V. Habibpour, M. A. Rottgen, S. Abbet, C. J. Harding, M. Arenz, U. Heiz, and C. Gerber. Micromechanical sensor for studying heats of surface reactions, adsorption, and cluster deposition processes. Rev. Sci. Instrum., 78:054101, 2007.

[5] C. L. Asbury, D. R. Gestaut, A. F. Powers, A. D. Franck, and T. N. Davis. The Dam1 kinetochore complex harnesses microtubule dynamics to produce force and movement. Proc. Natl. Acad. Sci. U. S. A., 103:9873–9878, 2006.

[6] J. R. Barnes, R. J. Stephenson, C. N. Woodburn, S. J. Oshea, M. E. Welland, T. Rayment, J. K. Gimzewski, and C. Gerber. A Femtojoule Calorimeter Using Micromechanical Sensors. Rev. Sci. Instrum., 65:3793–3798, 1994.

[7] K. Berg-Sorensen, E. J. G. Peterman, T. Weber, C. F. Schmidt, and H. Flyvbjerg. Power spectrum analysis for optical tweezers. II: Laser wavelength dependence of parasitic filtering, and how to achieve high bandwidth. Rev. Sci. Instrum., 77:063106, 2006.

[8] P. R. Bianco, L. R. Brewer, M. Corzett, R. Balhorn, Y. Yeh, S. C. Kowalczykowski, and R. J. Baskin. Processive translocation and DNA unwinding by individual RecBCD enzyme molecules. Nature, 409:374–378, 2001.

[9] G. Binnig, C. F. Quate, and C. Gerber. Atomic Force Microscope. Phys. Rev. Lett., 56:930–933, 1986.

[10] G. Binnig, H. Rohrer, C. Gerber, and E. Weibel. 7X7 Reconstruction on Si(111) Resolved in Real Space. Phys. Rev. Lett., 50:120–123, 1983.

[11] R. R. Brau, P. B. Tarsa, J. M. Ferrer, P. Lee, and M. J. Lang. Interlaced optical force-fluorescence measurements for single molecule biophysics. Biophys. J., 91:1069–1077, 2006.

[12] C. Bustamante. In singulo Biochemistry: When Less Is More. Annu. Rev. Biochem., 77:45–50, 2008.

[13] K. Buttner, S. Nehring, and K. Hopfner. Structural basis for DNA duplex separation by a superfamily-2 helicase. Nat. Struct. Mol. Biol., 14:647–652, 2007.

[14] M. Capitanio, R. Cicchi, and F. S. Pavone. Position control and optical manipulation for nanotechnology applications. Eur. Phys. J. B, 46:1–8, 2005.

[15] A. R. Carter, M. Hosotani, H. Fen, H. Li, M. D. Betterton, and T. T. Perkins. Direct measurement of individual RecBCD movement and conformational dynamics along DNA. in preparation, 2009.

[16] A. R. Carter, G. M. King, and T. T. Perkins. Back-scattered detection provides atomic-scale localization precision, stability, and registration in 3D. Opt. Express, 15:13434–13445, 2007.

[17] A. R. Carter, G. M. King, T. A. Ulrich, W. Halsey, D. Alchenberger, and T. T. Perkins. Stabilization of an optical microscope to 0.1 nm in three dimensions. Appl. Opt., 46:421–427, 2007.

[18] A. R. Carter, Y. Seol, and T. T. Perkins. Precision surface-coupled optical-trapping assay with 1 base-pair resolution. submitted, 2008.

[19] W. Cheng, S. Dumont, I. Tinoco Jr., and C. Bustamante. NS3 helicase actively separates RNA strands and senses sequence barriers ahead of the opening fork. Proc. Natl Acad. Sci. U. S. A., 104:13954–13959, 2007.

[20] A. B. Churnside. Ph. D. Thesis. in progress, 2011.

[21] A. B. Churnside, G. M. King, A. R. Carter, and T. T. Perkins. Improved performance of an ultrastable measurement platform using a field programmable gate array for deterministic, real-time control. Proc. of SPIE, 7042:704205, 2008.

[22] H. J. Dai, J. H. Hafner, A. G. Rinzler, D. T. Colbert, and R. E. Smalley. Nanotubes as nanoprobes in scanning probe microscopy. Nature, 384:147–150, 1996.

[23] W. Denk and W. W. Webb. Optical measurement of picometer displacements of transparent microscopic objects. Appl. Opt., 29:2382–2391, 1990.

[24] M. N. Dessinges, T. Lionnet, X. G. Xi, D. Bensimon, and V. Croquette. Single-molecule assay reveals strand switching and enhanced processivity of UvrD. Proc. Natl. Acad. Sci. U. S. A., 101:6439–6444, 2004.

[25] M. S. Dillingham, M. Spies, and S. C. Kowalczykowski. RecBCD enzyme is a bipolar DNA helicase. Nature, 423:893–897, 2003.

[26] M. S. Dillingham, M. R. Webb, and S. C. Kowalczykowski. Bipolar DNA translocation contributes to highly processive DNA unwinding by RecBCD enzyme. J. Biol. Chem., 280:37069–37077, 2005.

[27] K. M. Dohoney and J. Gelles. χ-Sequence recognition and DNA translocation by single RecBCD helicase/nuclease molecules. Nature, 409:370–374, 2001.

[28] S. Dumont, W. Cheng, V. Serebrov, R. K. Beran, I. Tinoco Jr., A. M. Pyle, and C. Bustamante. RNA translocation and unwinding mechanism of HCV NS3 helicase and its coordination by ATP. Nature, 439:105–108, 2006.

[29] D. M. Eigler and E. K. Schweizer. Positioning single atoms with a scanning tunnelling microscope. Nature, 344:524–526, 1990.

[30] R. L. Eoff and K. D. Raney. Intermediates revealed in the kinetic mechanism for DNA unwinding by a monomeric helicase. Nat. Struct. Mol. Biol., 13:242–249, 2006.

[31] J. T. Finer, R. M. Simmons, and J. A. Spudich. Single myosin molecule mechanics: piconewton forces and nanometre steps. Nature, 368:113–119, 1994.

[32] L. Finzi and J. Gelles. Measurement of lactose repressor-mediated loop formation and breakdown in single DNA molecules. Science, 267:378–380, 1995.

[33] M. E. J. Friese, H. Rubinsztein-Dunlop, N. R. Heckenberg, and E. W. Dearden. Determination of the force constant of a single-beam gradient trap by measurement of backscattered light. Appl. Opt., 36:7112–7116, 1996.

[34] E. A. Galburt, S. W. Grill, A. Wiedmann, L. Lubkowska, J. Choy, E. Nogales, M. Kashley, and C. Bustamante. Backtracking determines the force sensitivity of RNAP II in a factor-dependent manner. Nature, 446:820–823, 2007.

[35] J. Gelles, B. J. Schnapp, and M. P. Sheetz. Tracking kinesin-driven movements with nanometre-scale precision. Nature, 331:450–453, 1988.

[36] F. J. Giessibl. Advances in atomic force microscopy. Rev. Mod. Phys., 75:949–983, 2003.

[37] F. Gittes and C. F. Schmidt. Interference model for back-focal-plane displacement detection in optical tweezers. Opt. Lett., 23:7–9, 1998.

[38] A. E. Gorbalenya and E. V. Koonin. Helicases: amino acid sequence comparisons and structure-function relationships. Curr. Opin. Struct. Biol., 3:419–429, 1993.

[39] W. J. Greenleaf, M. T. Woodside, E. A. Abbondanzieri, and S. M. Block. Passive all-optical force clamp for high-resolution laser trapping. Phys. Rev. Lett., 20:208102, 2005.

[40] K. M. Herbert, A. La Porta, B. J. Wong, R. A. Mooney, K. C. Neuman, R. Landick, and S. M. Block. Sequence-resolved detection of pausing by single RNA polymerase molecules. Cell, 125:1083–1094, 2006.

[41] M. M. Hingorani and M. O'Donnell. A Tale Of Toroids In DNA Metabolism. Nat. Rev. Mol. Cell. Biol., 1:22–30, 2000.

[42] B. W. Hoogenboom, H. J. Hug, Y. Pellmont, S. Martin, P. L. T. M. Frederix, D. Fotiadis, and A. Engel. Quantitative dynamic-mode scanning force microscopy in liquid. Appl. Phys. Lett., 88:193109, 2006.

[43] I. Horcas, R. Fernandez, J. M. Gomez-Rodriguez, J. Colchero, J. Gomez-Herrero, and A. M. Baro. WSXM: a software for scanning probe microscopy and a tool for nanotechnology. Rev. Sci. Instrum., 78:013705, 2007.

[44] J. H. G. Huisstede, K. O. van der Werf, M. L. Bennink, and V. Subramaniam. Force detection in optical tweezers using backscattered light. Opt. Express, 13:1113–1123, 2005.

[45] D. S. Johnson, L. Bai, B. Y. Smith, S. S. Patel, and M. D. Wang. Single-molecule studies reveal dynamics of DNA unwinding by the ring-shaped T7 helicase. Cell, 129:1299–1309, 2007.

[46] C. Joo, H. Balci, Y. Ishitsuka, C. Buranachai, and T. Ha. Advances in single-molecule fluorescence methods for molecular biology. Annu. Rev. Biochem., 77:51–76, 2008.

[47] A. N. Kapanidis, E. Margeat, S. O. Ho, E. Kortkhonjia, S. Weiss, and R. H. Ebright. Initial transcription by RNA polymerase proceeds through a DNA-scrunching mechanism. Science, 314:1144–1147, 2006.

[48] J. W. Kerssemakers, E. L. Munteanu, L. Laan, T. L. Noetzel, M. E. Janson, and M. Dogterom. Assembly dynamics of microtubules at molecular resolution. Nature, 442:709–712, 2006.

[49] U. F. Keyser, B. N. Koeleman, S. Van Dorp, D. Krapf, R. M. M. Smeets, S. G. Lemay, N. H. Dekker, and C. Dekker. Direct force measurements on DNA in a solid-state nanopore. Nature Phys., 2:473–477, 2006.

[50] U. F. Keyser, J. van der Does, C. Dekker, and N. H. Dekker. Optical tweezers for force measurements on DNA in nanopores. Rev. Sci. Instrum., 77:105105, 2006.

[51] G. M. King, A. R. Carter, A. B. Churnside, L. Eberle, and T. T. Perkins. Ultra-stable atomic force microscopy: atomic-scale stability and registration in ambient conditions. submitted, 2008.

[52] G. M. King and J. A. Golovchenko. Probing nanotube-nanopore interactions. Phys. Rev. Lett., 95:216103, 2005.

[53] J. Kobayashi, Y. Izumi, M. Kumakura, and Y. Takahashi. Stable all-optical formation of bose-einstein condensate using pointing-stabilized optical trapping beams. Appl. Phys. B, 83:21–25, 2006.

[54] J. Kohler, M. Albrecht, C. R. Musil, and E. Bucher. Direct growth of nanostructures by deposition through an Si_3N_4 shadow mask. Physica E, 4:196–200, 1999.

[55] F. Korangy and D. A. Julin. Efficiency of ATP hydrolysis and DNA unwinding by the RecBC enzyme from Escherichia coli. Biochemistry, 32:4873–4880, 1993.

[56] S. C. Kowalczykowski. Initiation of genetic recombination and recombination-dependent replication. Trends Biochem. Sci., 25:156–165, 2000.

[57] S. C. Kowalczykowski, D. A. Dixon, A. K. Eggleston, S. D. Lauder, and W. M. Rehrauer. Biochemistry of homologous recombination in Escherichia coli. Microbiol. Rev., 58:401–465, 1994.

[58] C. Kural, H. Kim, S. Syed, G. Goshima, V. I. Gelfand, and P. R. Selvin. Kinesin and dynein move a peroxisome in vivo: a tug-of-war or coordinated movement? Science, 308:1469–1472, 2005.

[59] A. Kuzminov. Recombinational repair of DNA damage in Escherichia coli and bacteriophage lambda. Microbiol. Mol. Biol. Rev., 63:751–813, 1999.

[60] M. J. Lang, C. L. Asbury, J. W. Shaevitz, and S. M. Block. An automated two-dimensional optical force clamp for single molecule studies. Biophys. J., 83:491–501, 2002.

[61] J. Y. Lee and W. Yang. UvrD helicase unwinds DNA one base pair at a time by a two-part power stroke. Cell, 127:1349–1360, 2006.

[62] M. K. Levin, M. Gurjar, and S. S. Patel. A Brownian motor mechanism of translocation and strand separation by hepatitis C virus helicase. Nat. Struct. Mol. Biol., 12:429–435, 2005.

[63] M. Li, H. X. Tang, and M. L. Roukes. Ultra-sensitive NEMS-based cantilevers for sensing, scanned probe and very high-frequency applications. Nature Nanotech., 2:114–120, 2007.

[64] J. Liphardt, B. Onoa, S. B. Smith, I. Tinoco, and C. Bustamante. Reversible unfolding of single RNA molecules by mechanical force. Science, 292:733–737, 2001.

[65] T. M. Lohman and K. P. Bjornson. Mechanisms Of Helicase-Catalyzed DNA Unwinding. Annu. Rev. Biochem., 65:169–214, 1996.

[66] T. M. Lohman, E. J. Tomko, and C. G. Wu. Non-hexameric DNA helicases and translocases: mechanisms and regulation. Nat. Rev. Mol. Cell. Bio., 9:391–401, 2008.

[67] A. L. Lucius and T. M. Lohman. Effects of temperature and ATP on the kinetic mechanism and kinetic stepsize for E. coli RecBCD helicase-catalyzed DNA unwinding. J. Mol. Biol., 339:751–771, 2004.

[68] A. L. Lucius, A. Vindigni, R. Gregorian, J. A. Ali, A. F. Taylor, G. R. Smith, and T. M. Lohman. DNA unwinding step-size of E. coli RecBCD helicase determined from single turnover chemical quenched-flow kinetic studies. J. Mol. Biol., 324:409–428, 2002.

[69] A. L. Lucius, C. Jason Wong, and T. M. Lohman. Fluorescence stopped-flow studies of single turnover kinetics of E. coli RecBCD helicase-catalyzed DNA unwinding. J. Mol. Biol., 339:731–750, 2004.

[70] V. MacKay and S. Linn. The mechanism of degradation of duplex deoxyribonucleic acid by the recBC enzyme of Escherichia coli K-12. J. Biol. Chem., 249:4286–4294, 1974.

[71] J. F. Marko and E. D. Siggia. Stretching of DNA. Macromol., 28:8759–8770, 1995.

[72] C. R. K. Marrian and E. S. Snow. Proximal probe lithography and surface modification. Microelectron. Eng., 32:173–189, 1996.

[73] A. D. Mehta, R. S. Rock, M. Rief, J. A. Spudich, M. S. Mooseker, and R. E. Cheney. Myosin-V is a processive actin-based motor. Nature, 400:590–593, 1999.

[74] E. Meyer, H. Heinzelmann, D. Brodbeck, G. Overney, R. Overney, L. Howald, H. Hug, T. Jung, H.-R. Hidber, and H.-J. Gntherodt. Atomic resolution on the surface of LiF(100) by atomic force microscopy. J. Vac. Sci. Technol. B, 9:1329–1332, 1991.

[75] G. Meyer and N. M. Amer. Novel optical approach to atomic force microscopy. Appl. Phys. Lett., 53:1045–1047, 1988.

[76] J. R. Moffitt, Y. R. Chemla, D. Izhaky, and C. Bustamante. Differential detection of dual traps improves the spatial resolution of optical tweezers. Proc. Natl. Acad. Sci. U. S. A., 103:9006–9011, 2006.

[77] J. R. Moffitt, Y. R. Chemla, S. B. Smith, and C. Bustamante. Recent advances in optical tweezers. Annu. Rev. Biochem, 77:205–228, 2008.

[78] B. Mokaberi and A. A. G. Requicha. Drift Compensation for Automatic Nanomanipulation With Scanning Probe Microscopes. IEEE T. Autom. Sci. Eng., 3:199–207, 2006.

[79] E. E. Moon, J. Kupec, M. K. Mondol, H. I. Smith, and K. K. Berggren. Atomic-force lithography with interferometric tip-to-substrate position metrology. J. Vac. Sci. Technol. B, 25:2284–2287, 2007.

[80] E. E. Moon, M. K. Mondol, P. N. Everett, and H. I. Smith. Dynamic alignment control for fluid-immersion lithographies using interferometric-spatial-phase imaging. J. Vac. Sci. Technol. B, 23:2607–2610, 2005.

[81] E. E. Moon and H. I. Smith. Nanometer-precision pattern registration for scanning-probe lithographies using interferometric-spatial-phase imaging. J. Vac. Sci. Technol. B, 24:3083–3087, 2006.

[82] D. J. Muller, K. T. Sapra, S. Scheuring, A. Kedrov, P. L. Frederix, D. Fotiadis, and A. Engel. Single molecule studies of membrane proteins. Curr. Opin. Struct. Biol., 16:489–495, 2006.

[83] S. Myong, M. M. Bruno, A. M. Pyle, and T. Ha. Springloaded mechanism of DNA unwinding by hepatitis C virus NS3 helicase. Science, 317:513–516, 2007.

[84] S. Myong, I. Rasnik, C. Joo, T. M. Lohman, and T. Ha. Repetitive shuttling of a motor protein on DNA. Nature, 437:1321–1325, 2005.

[85] H. Namatsu, Y. Takahashi, K. Yamazaki, T. Yamaguchi, M. Nagase, and K. Kurithara. Three-dimensional siloxane resist for the formation of nanopatterns with minimum linewidth fluctuations. J. Vac. Sci. Technol. B, 16:69–76, 1998.

[86] K. C. Neuman, E. A. Abbondanzieri, and S. M. Block. Measurement of the effective focal shift in an optical trap. Opt. Lett., 30:1318–1320, 2005.

[87] K. C. Neuman and S. M. Block. Optical trapping. Rev. Sci. Instrum., 75:2787–2809, 2004.

[88] K. C. Neuman, E. H. Chadd, G. F. Liou, K. Bergman, and S. M. Block. Characterization of photodamage to Escherichia coli in optical traps. Biophys. J., 77:2856–2863, 1999.

[89] L. Nugent-Glandorf and T. T. Perkins. Measuring 0.1-nm motion in 1 ms in an optical microscope with differential back-focal-plane detection. Opt. Lett., 29:2611–2613, 2004.

[90] F. Ohnesorge and G. Binnig. True Atomic-Resolution by Atomic Force Microscopy through Repulsive and Attractive Forces. Science, 260:1451–1456, 1993.

[91] E. D. Palik, editor. Handbook of optical constants of solids. Academic Press, 1997.

[92] S. S. Patel and I. Donmez. Mechanisms of helicases. J. Biol. Chem., 281:18265–18268, 2006.

[93] S. S. Patel and K. M. Picha. Structure and Function Of Hexameric Helicases. Annu. Rev. Biochem., 69:651–697, 2000.

[94] T. T. Perkins. Optical traps for single molecule biophysics: a primer. Las. Phot. Rev., 2008.

[95] T. T. Perkins, R. V. Dalal, P. G. Mitsis, and S. M. Block. Sequence-dependent pausing of single lambda exonuclease molecules. Science, 301:1914–1918, 2003.

[96] T. T. Perkins, H. W. Li, R. V. Dalal, J. Gelles, and S. M. Block. Forward and reverse motion of single RecBCD molecules on DNA. Biophys. J., 86:1640–1648, 2004.

[97] E. J. G. Peterman, M. A. van Dijk, L. C. Kapitein, and C. F. Schmidt. Extending the bandwidth of optical-tweezers interferometry. Rev. Sci. Instrum., 74:3246–3249, 2003.

[98] R. D. Piner, J. Zhu, F. Xu, S. Hong, and C. A. Mirkin. "Dip-Pen" Nanolithography. Science, 283:661–663, 1999.

[99] D. W. Pohl and R. Moller. Tracking tunneling microscopy. Rev. Sci. Instrum., 59:840–842, 1988.

[100] A. Pralle, M. Prummer, E. L. Florin, E. H. K. Stelzer, and J. K. H. Horber. Three-dimensional high-resolution particle tracking for optical tweezers by forward scattered light. Microsc. Res. Tech., 44:378–386, 1999.

[101] W. H. Press, S. A. Teukolsky, W. T. Vetterling, and B. P. Flannery. Numerical Recipes in C, The Art of Scientific Computing. Cambridge University Press, 1992.

[102] R. Proksch and E. D. Dahlberg. Optically stabilized, constant-height mode-operation of a magnetic force microscope. J. Appl. Phys., 73:5808–5810, 1993.

[103] M. Radmacher, M. Fritz, H. G. Hansma, and P. K. Hansma. Direct observation of enzyme activity with the atomic force microscope. Science, 265:1577–1579, 1994.

[104] L. J. Roman and S. C. Kowalczykowski. Characterization of the adenosine triphosphatase activity of the Escherichia coli RecBCD enzyme: relationship of ATP hydrolysis to the unwinding of duplex DNA. Biochemistry, 28:2873–2881, 1989.

[105] K. Saikrishnan, S. P. Griffiths, N. Cook, R. Court, and D. B. Wigley. DNA binding to RecD: role of the 1B domain in SF1B helicase activity. Embo J., 27:2222–2229, 2008.

[106] S. Scheuring and J. N. Sturgis. Chromatic adaptation of photosynthetic membranes. Science, 309:484–487, 2005.

[107] T. Schimmel, T. Koch, J. Kuppers, and M. Lux-Steiner. True atomic resolution under ambient conditions obtained by atomic force microscopy in the contact mode. Appl. Phys. A: Mater. Sci. Process., 68:399–402, 1999.

[108] Y. Seol, J. Li, P. C. Nelson, T. T. Perkins, and M. D. Betterton. Elasticity of Short DNA Molecules: Theory and Experiment for Contour Lengths of 0.6-7 m. Biophys. J., 93:4360–4373, 2007.

[109] B. Sikora, R. L. Eoff, S. W. Matson, and K. D. Raney. DNA unwinding by Escherichia coli DNA helicase I (TraI) provides evidence for a processive monomeric molecular motor. J. Biol. Chem., 281:36110–36116, 2006.

[110] M. R. Singleton, M. S. Dillingham, M. Gaudier, S. C. Kowalczykowski, and D. B. Wigley. Crystal structure of RecBCD enzyme reveals a machine for processing DNA breaks. Nature, 432:187–193, 2004.

[111] M. R. Singleton, M. S. Dillingham, and D. B. Wigley. Structure and Mechanism of Helicases and Nucleic Acid Translocases. Annu. Rev. Biochem., 76:23–50, 2007.

[112] G. R. Smith. Homologous recombination near and far from DNA breaks: alternative roles and contrasting views. Annu. Rev. Genet., 35:243–274, 2001.

[113] A. W. Sparks and S. R. Manalis. Scanning probe microscopy with inherent disturbance suppression. Appl. Phys. Lett., 85:3929–3931, 2004.

[114] M. Spies, P. R. Bianco, M. S. Dillingham, N. Handa, R. J. Baskin, and S. C. Kowalczykowski. A molecular throttle: the recombination hotspot chi controls DNA translocation by the RecBCD helicase. Cell, 5:647–654, 2003.

[115] W. Steffen, D. Smith, R. Simmons, and J. Sleep. Mapping the actin filament with myosin. Proc. Natl. Acad. Sci. U. S. A., 98:14949–14954, 2001.

[116] B. C. Stipe, M. A. Rezaei, and W. Ho. Single-molecule Vibrational Spectroscopy and Microscopy. Science, 280:1732–1735, 1998.

[117] Y. Sugimoto, M. Abe, S. Hirayama, N. Oyabu, O. Custance, and S. Morita. Atom inlays performed at room temperature using atomic force microscopy. Nature Materials, 4:156–159, 2005.

[118] K. Svoboda and S. M. Block. Biological Applications of Optical Forces. Annu. Rev. Biophys. Biomol. Struct., 23:247–285, 1994.

[119] K. Svoboda, C. F. Schmidt, B. J. Schnapp, and S. M. Block. Direct observation of kinesin stepping by optical trapping interferometry. Nature, 365:721–727, 1993.

[120] K. Svododa and S. M. Block. Force and velocity measured for single kinesin molecules. Cell, 77:773–784, 1994.

[121] B. S. Swartzentruber. Direct measurement of surface diffusion using atom-tracking scanning tunneling microscopy. Phys. Rev. Lett., 76:459–462, 1996.

[122] A. F. Taylor and G. R. Smith. RecBCD enzyme is a DNA helicase with fast and slow motors of opposite polarity. Nature, 423:889–893, 2003.

[123] N. H. Thomson, M. Fritz, M. Radmacher, J. P. Cleveland, C. F. Schmidt, and P. K. Hansma. Protein tracking and detection of protein motion using atomic force microscopy. Biophys. J., 70:2421–2431, 1996.

[124] E. J. Tomko, C. J. Fischer, A. Niedziela-Majka, and T. M. Lohman. A nonuniform stepping mechanism for E. coli UvrD monomer translocation along single-stranded DNA. Mol. Cell, 26:335–347, 2007.

[125] S. S. Velankar, P. Soultanas, M. S. Dillingham, H. S. Subramanya, and D. B. Wigley. Crystal structures of complexes of PcrA DNA helicase with a DNA substrate indicate an inchworm mechanism. Cell, 97:75–84, 1999.

[126] J. Vesenka, S. Manne, R. Giberson, T. Marsh, and E. Henderson. Colloidal gold particles as an incompressible atomic force microscope imaging standard for assessing the compressibility of biomolecules. Biophys. J., 65:992–997, 1993.

[127] M. B. Viani, T. E. Schaffer, A. Chand, M. Rief, H. E. Gaub, and P. K. Hansma. Small cantilevers for force spectroscopy of single molecules. J. Appl. Phys., 86:2258–2262, 1999.

[128] K. Visscher, S. P. Gross, and S. M. Block. Construction of multiple-beam optical traps with nanometer-resolution position sensing. IEEE J. Sel. Top. Quant. Electr., 2:1066–1076, 1996.

[129] A. E. Wallin, A. Salmi, and R. Tuma. Step length measurement — theory and simulation for tethered bead constant-force single molecule assay. Biophys. J., 93:795–805, 2007.

[130] M. D. Wang, M. J. Schnitzer, H. Yin, R. Landick, J. Gelles, and S. M. Block. Force and velocity measured for single molecules of RNA polymerase. Science, 282:902–907, 1998.

[131] M. D. Wang, H. Yin, R. Landick, J. Gelles, and S. M. Block. Stretching DNA with optical tweezers. Biophys. J., 72:1335–1346, 1997.

[132] J. D. Wen, L. Lancaster, C. Hodges, A. C. Zeri, S. H. Yoshimura, H. F. Noller, C. Bustamante, and I. Tinoco. Following translation by single ribosomes one codon at a time. Nature, 452:598–603, 2008.

[133] V. Westphal and S. W. Hell. Nanoscale resolution in the focal plane of an optical microscope. Phys. Rev. Lett., 94:143903, 2005.

[134] C. J. Wong, A. L. Lucius, and T. M. Lohman. Energetics of DNA End Binding by E. coli RecBC and RecBCD Helicases Indicate Loop Formation in the 3'-Single-stranded DNA Tail. J. Mol. Biol., 352:765–782, 2005.

[135] M. T. Woodside, P. C. Anthony, W. M. Behnke-Parks, K. Larizadeh, D. Herschlag, and S. M. Block. Direct measurement of the full, sequence-dependent folding landscape of a nucleic acid. Science, 314:1001–1004, 2006.

[136] M. T. Woodside, W. M. Behnke-Parks, K. Larizadeh, K. Travers, D. Herschlag, and S. M. Block. Nanomechanical measurements of the sequence-dependent folding landscapes of single nucleic acid hairpins. Proc. Natl. Acad. Sci. U. S. A., 103:6190–6195, 2006.

[137] C. G. Wu and T. M. Lohman. Influence of DNA end structure on the mechanism of initiation of DNA unwinding by the Escherichia coli RecBCD and RecBC helicases. J. Mol. Biol., 382:312–326, 2008.

[138] A. Yildiz, J. N. Forkey, S. A. McKinney, T. Ha, Y. E. Goldman, and P. R. Selvin. Myosin V walks hand-over-hand: single fluorophore imaging with 1.5-nm localization. Science, 300:2061–2065, 2003.

[139] A. Yildiz, M. Tomishige, R. D. Vale, and P. R. Selvin. Kinesin walks hand-over-hand. Science, 303:676–678, 2004.

[140] H. Yin, M. D. Wang, K. Svoboda, R. Landick, S. M. Block, and Jeff Gelles. Transcription Against an Applied Force. Science, 270:1653–1657, 1995.

[141] J. Yu, T. Ha, and K. Schulten. Structure-Based Model of the Stepping Motor of PcrA Helicase. Biophys J., 91:2097–2114, 2006.

[142] X. D. Zhang, S. X. Dou, P. Xie, J. S. Hu, P. Y. Wang, and X. G. Xi. Escherichia coli RecQ is a rapid, efficient, and monomeric helicase. J. Biol. Chem., 281:12655–12663, 2006.

[143] J. G. Ziegler and N. B. Nichols. Dynamic Accuracy in Temperature Measurement. Science, 110:361–363, 1949.

Appendix A

Acronym Index

2D two dimensional.

3D three dimensional.

A adenine, DNA base.

ADP adenosine diphosphate.

AFM atomic force microscope.

AMP-PNP adenylyl imidodiphosphate

AOM acousto-optic modulator.

ATP adenosine triphosphate.

bp base-pair.

BS beam sampler.

BSD back-scattered detection.

C cytosine, DNA base.

CCD charged-coupled device.

DL diode laser.

DNA deoxyribonucleic acid.

FSD forward-scattered detection.

FWHM full width at half maximum.

G guanine, DNA base.

HWHM half width at half maximum.

HSQ hydrogen silsesquioxane, spin-on glass.

Obj objective.

OI optical isolator.

PBS polarizing beam splitter.

PCR polymerase chain reaction.

PD photodiode.

PDD pair-wise distance difference.

pH power of hydrogen.

PSD power spectral density.

PZT piezo-electric lead zirconate titanate.

QPD quadrant photodiode.

RNA ribonucleic acid.

rms root mean square.

SD standard deviation.

SDL stabilized diode laser.

SEM scanning electron microscope.

SF super family.

S/N signal to noise ratio.

STL stabilized trap laser.

T thymine, DNA base.

TL trap laser.

VDC direct current voltage.

WB wash buffer.

$\lambda/2$ half-wave plate.

$\lambda/4$ quarter-wave plate.

Appendix B

Variable Index

C capacitance.

d diameter.

F force.

F_0 initial force on the bead.

$F_{1/2}$ force at which a hairpin has a 50% chance of being in the unfolded state.

F_{DNA} force on bead from the DNA.

F_{R} ideal force response of cantilever.

F_{T} force on bead from the trap.

F_{total} total force response of cantilever.

F_{th} force response of cantilever due to thermal motion.

ΔF change in force.

f fractional extension.

f_0 roll-off frequency.

f_{obj} focal length of the objective.

Δf bandwidth.

Δf_{gain} gain bandwidth.

g gain.

h height.

k spatial frequency.

k_{B} Boltzmann constant.

k_{DNA} nonlinear stiffness of the DNA.

k^0_{DNA} initial nonlinear stiffness of the DNA.

k_{T} trap stiffness.

k^0_{T} initial trap stiffness.

δk_{T} change in trap stiffness.

L DNA contour length.

δL change in DNA contour length.

ΔL the difference between the current DNA contour length and the initial DNA contour length.

m ratio of the object refractive index to the solvent refractive index.

m_{ps} index of refraction ratio for the polystyrene fiducial mark.

m_{Si} index of refraction ratio for the silicon fiducial mark.

N number.

n index of refraction.

n_{object} index of refraction of the object.

n_{solvent} index of refraction of the solvent.

p persistence length of DNA.

R resistance.

r radius.

r_{bd} bead radius.

r_{best} ratio of the highest smoothing frequency that allows for accurate fitting of the data to the actual signal frequency of the data.

S positional sensitivity.

T temperature.

V volume.

V_0 reference voltage.

V_{Si} volume of the silicon fiducial mark.

V_{ps} volume of the polystyrene fiducial mark.

V_{QPD} QPD voltage.

V_{z} the QPD sum signal voltage, which measures position in z.

v velocity.

w width.

x one of the three dimensional coordinates, lateral motion.

x_{bd} bead position.

x_{bd}^{0} initial bead position.

x_{C} clamp position for the trapped bead.

x_{DNA} DNA extension.

x_{DNA}^{0} initial DNA extension.

x_{dif} differential position in x.

x_{fid} fiducial mark position in x.

$x_{\mathrm{in-loop}}$ position in x as measured by the in-loop laser.

x_{monitor} position in x as measured by the monitor laser.

x_{monitor}^{0} the average initial position in x as measured by the monitor laser.

x_{monitor}^{N} the average position in x at step number N as measured by the monitor laser.

x_{peak} position of correlation peak in x in AFM image analysis.

x_{ref} reference position in x inside of the feedback loop.

x_{stage} distance between tether point and trap center.

x_{tether} tether point position .

x_{tip} AFM tip position in x.

Δx unfolding distance.

Δx^{N} the difference between the average position in x at step number N and the initial value as measured by the monitor laser.

δx_{bd} change in trapped bead position.

y one of the three dimensional coordinates, lateral motion.

y_{dif} differential position in y.

$y_{\mathrm{in-loop}}$ position in y as measured by the in-loop laser.

y_{lasers} lateral distance between the laser foci in the image plane.

y_{monitor} position in y as measured by the monitor laser.

y_{tip} AFM tip position in y.

Z height of surface.

z one of the three dimensional coordinates, axial motion.

z_{AFM} position in z of AFM cantilever as measured by a standard optical lever arm.

z_{dif} differential position in z.

$z_{\mathrm{in-loop}}$ position in z as measured by the in-loop laser.

z_{monitor} position in z as measured by the monitor laser.

z_{st} movement of the stage in z.

z_{tip} AFM tip position in z.

α_{ps} polarizability of the polystyrene fiducial mark.

α_{Si} polarizability of the silicon fiducial mark.

α_{sphere} polarizability of a sphere.

β drag coefficient.

η viscosity.

λ wavelength.

π pi.

σ standard deviation.

σ_{D} standard deviation of the trapped bead data.

σ_{error} standard error.

σ_{SEM} standard error of the mean for the trapped bead data.

σ_{x} standard deviation in x.

σ_{y} standard deviation in y.

σ_{z} standard deviation in z.

$\bar{\sigma}$ average standard deviation.

$\bar{\sigma}_{\mathrm{x}}$ average standard deviation in x.

$\bar{\sigma}_{\mathrm{y}}$ average standard deviation in y.

$\bar{\sigma}_{\mathrm{z}}$ average standard deviation in z.

τ_{avg} time interval to average over.

$\Delta\theta$ change in angle of laser beam due to AOM pointing instability.

Appendix C

Software Index

This is an index of the top level LabVIEW programs used to collect data for this thesis. Programs are located on the optical trapping experiment computer in B1B42 or the AFM experiment computer in B2B17. The top level directory of all LabVIEW programs is C:\users\perkins\labview\; programs list the further location address. Some programs were used in both experiments with minor differences between the two versions (initialize instrument.vi, BeamAlignment.vi, and StageDrift_1_Beam_Multi.vi), and thus, only described once. In the AFM experiment these programs are located in .\Gavin\ and are called Gavin_initialize_instrument.vi, Gavin_BeamAlignment_lv8.vi, and Gavin_StageDrift_1_Beam_Multi.vi, respectively. The software programs listed in this index do not represent my original work and were updated by many other people, please see the Acknowledgements. They are included for completeness.

C.1 Optical trapping experiment

initialize instrument.vi

Location: .\JILA\

Description: Initializes the PZT stage, PZT mirrors, and intensity servos. First writes zero to the mirrors, then uploads mirror positions from file (DeltaV780.dat, DeltaV850.dat, Delta1064.dat in location C:\users\perkins\trap\data\), and

updates the position. The stage is initialized to the middle of the range. The intensity servos are initialized with the values in TrapInitialize.vi.

Typical parameters: The mirrors are generally set to (5 V, 5 V), which is the middle of the range. The intensity set points are -3 V, -9.5 V, and -2.54 V, for the 785 nm, 850 nm, and 1064 nm lasers.

BeamAlignment.vi

Location: .\JILA\

Description: Centers the PZT mirror on a fiducial mark or trapped bead. Sweeps the "beam PZT" mirror in x and y over the range given by plus or minus "Sen cal amplitude" nanometers, while simultaneously measuring the output voltage of the "beamdetect" x and y channels. Fits the voltage vs. nanometer curve and determines the center point in x and y. Moves the PZT mirror to the center point and updates the mirror position file (DeltaV780.dat, DeltaV850.dat, Delta1064.dat in location C:\users\perkins\trap\data\).

Typical parameters: "beam PZT" is either 1064 or 850, while "beamdetect" is 785 or 850, for centering the trapped bead or fiducial mark, respectively. "Sen cal amplitude" is usually 200-800 nm.

2DHistogram.vi

Location: .\JILA\Yeonee\

Description: Plots the 2D histogram, y vs. x, of the trapped bead position. Reads the binary data output file with extension ".eqp" from StiffnessCalbyPF&EQP.vi. Plots the 2D graph and fits a line to determine the slope of the data, which should be <0.01.

Typical parameters: Input the binary ".eqp" file from StiffnessCalbyPF&EQP.vi.

pow vs Stiff_Optional z-PositionLock.vi

Location: ..\JILA\Yeonee\

Description: Takes the trap calibration data. Measures stiffness of the trap using both the power spectrum and equipartition methods over a series of intensity servo voltages. Fits a line to the stiffness vs. voltage curve. These coefficients then need to be input by hand into a stiffness calibration file located in C:\users\perkins\trap\data\Powercal\. Naming of the file is usually "rXXXstiff-to-volt.dat" where XXX is the bead radius in nanometers. For different buffer conditions or other special situations the name can be extended after "volt". The user sets a height for the measurement, the parameters for taking the power spectrum, the number of data points to be taken, the voltage range to take data over, and whether to pick the height each time or use a fiducial mark on the surface to maintain height.

Typical parameters: "Measurement Height" is usually 0.3 or 1.0 μm. "Low power", "High Power", and "Num steps" set the voltage range and are typically 1.0 V, 7.0 V, 9 steps. "bead r" is the bead radius, 0.165 μm. Parameters to set the power spectrum settings are in yellow; "Frame Size", "Samp Rate", "Num avg", "Num pts skip at beg", "Num pts skip end", "Num pts avg", and "Aq rate" are 131072, 100 kHz, 15, 5, 5000, 200, and 8 kHz, respectively. To select using the fiducial mark click "Position Clamp?" as true, otherwise click "Height?" as true to select the height each time; usually we select the height. "Detector beam", "Trapped bead BeamControl", "Marker beam control" are set to 785, 1064, and 850, respectively.

StiffnessCalbyPF&EQP.vi

Location: .\JILA\Yeonee\

Description: Measures the stiffness using both the power spectrum and equipartition methods at the particular height selected and the current intensity servo voltage. You can optionally choose to use only the equipartition method by

changing the "POWER SPECTRUM" button to false, or to use the current height by changing the "Height" button to false. Data for the equipartition calculation continues to compile until the "stop Equipartition" button is pressed.

Typical parameters: The parameters "Bead Height", "Bead radius", "Beam detect", "beam PZT", "Height Detect", "Sampling Rate", and "Frame Size" are set to 0.3 μm or 1.0 μm, 0.165 μm, 785, 1064, 785, 100 kHz, and 131072, respectively.

StiffnessCalCheck.vi

Location: .\JILA\Calibration Routines\

Description: Checks the stiffness calibration. First, uploads the stiffness calibration file from C:\users\perkins\trap\data\Powercal\ and converts the desired stiffness values to intensity servo voltages. Then measures the stiffness value using the equipartition and power spectrum methods at each desired stiffness. Finally, compares the measured stiffness to the desired stiffness and outputs a percentage. Data should be within 5% to check as normal. Data analyzed by program is sometimes wrong. It is better to do analysis in IGOR using AnalyzeStiffCheck.ipf.

Typical parameters: Parameters are set the same as in pow vs Stiff_Optional z-PositionLock.vi. The stiffness range can be set to mimic the voltage range values by using the calibration file conversions.

CalibratePZTMirrorUsingStageAndStuckBead.vi

Location: .\JILA\Calibration Routines\

Description: This routine calibrates the PZT mirror using the calibrated PZT stage and a fiducial mark. First, the program opens up the PZT mirror calibration file PZTCalMulti.dat in C:\users\perkins\trap\data\ and reads the calibration. If this file does not exist or the values are wrong you can estimate

the calibration, more on this later. Second, the laser is centered on a fiducial mark using the PZT mirror. Then both the PZT stage and the PZT mirror are incrementally moved the same amount in a series of positions outlining a grid. At each position the laser is recentered on the fiducial mark and the center voltage is output. Finally, the program outputs the mirror center voltages as a 2D grid. The data is read by either MirrorCalResult.vi or pztCalibration Analysis.ipf, which calculates the movement in x of the laser in nanometers divided by the voltage change on the mirror in x, the same thing in y, and the crosstalk terms. These numbers then need to be input by hand into PZTCalMulti.dat in the order of movement x divided by voltage x, movement y divided by voltage y, movement x divided by voltage y, movement y divided by voltage x; for the 785 nm PZT mirror, then the 850 nm PZT mirror, and finally, the 1064 nm PZT mirror. To make an estimate of this calibration, you can simply move the stage and mirror by hand and follow the program's protocol. Programs to move the stage or laser by hand can be found in initialize instrument.vi. Usually, the mirror calibration is run for a small grid to make sure everything is working and then a larger grid is used to calibrate the mirror.

Typical parameters: "NumIterationsPerSide" is 1 for the small grid and 5 for the larger grid. "VoltageRangePerSide" is either 1 or 2 V. "BeamControl" is the beam for the corresponding PZT mirror that needs to be calibrated, 850 or 1064.

CheckPZTCalibrateMirrorUsingStageAndStuckBead.vi

Location: .\JILA\Calibration Routines\

Description: This program checks the PZT mirror calibration. First, it uploads the calibration file PZTCalMulti.dat from C:\users\perkins\trap\data\ and reads in the calibration. Next, the laser is centered on a fiducial mark on

the sample. Both the PZT stage and PZT mirror are moved the same amount in a series of positions outlining a grid. At each position the fiducial mark is swept through the laser to determine the fiducial center position and calculate the difference between the fiducial center position and the actual laser position. Hence, we are checking the laser movement against the stage movement to tell if the calibration is correct. The program outputs the difference between the stage and laser positions and the desired laser movement in a table. If the difference is within 5% of the desired movement the PZT calibration is working.

Typical parameters: To define the grid the user specifies "Range" and "Step-size", which are generally 500 nm and 50 nm. "BeamControl" is the beam for the corresponding PZT mirror that needs to be checked, 850 or 1064.

MirrorCalResult.vi

Location: .\JILA\Calibration Routines\

Description: Plots the 2D voltage grid from CalibratePZTMirrorUsingStage-AndStuckBead.vi and calculates the mirror calibration. The calibrations will need to be multiplied by -1 before inputting them by hand into PZTCalMulti.dat located in C:\users\perkins\trap\data\.

Typical parameters: Inputs the output file of CalibratePZTMirrorUsingStage-AndStuckBead.vi, first y data then x data.

Zcal_2_beams_1 bead_Rezero.vi

Location: .\Z calibration\

Description: This program measures the position of one or two fiducial marks using two lasers. The user will first align the two lasers to look at one fiducial mark or two fiducial marks. Then the program centers the lasers and calibrates the fiducial mark position. Finally, the program measures fiducial position vs. time until the "Stop" button is pressed. The program will output the differential

measurement and will also actively stabilize the fiducial position.

Typical parameters: The user defines the "DAQ rate", typically 10.4 kHz, and "DAQ Num pnts to avg", typically 104. These two numbers define the feedback loop rate, which works the best at 100 Hz. The user also need to define the "beam PZT", which is the beam that will be calibrated by moving the PZT mirror (850), and the "beam control", which is the beam that will be calibrated by moving the stage (785).

StageDrift_1_Beam_Multi.vi

Location: .\JILA\StageDrift\

Description: This program takes positional calibration curves in 3D. The program centers the fiducial mark and then outputs the calibration curve. If any of the position calibration subvi's are stopped during data acquisition then sometimes the LabVIEW stage program will freeze. This is because the stage is trying to send data while LabVIEW is writing data. To fix this, run the program E710_Recieve.vi.

Typical parameters: The user defines the "beam control" laser to detect position, usually 850 or 785. To save the calibration data the user will need to flag the various subvi's with a true write statement.

DNAPulling_v1.vi

Location: .\JILA\DNA stretching\

Description: This routine takes a DNA elasticity curve. First, a DNA-tethered bead is trapped and bead position is calibrated. Then the program moves the stage in y to stretch the tether. This continues until the bead reaches the "clamp position", at which time, the stage continues to move while the stiffness in the trap increases to maintain bead position. The program stops stretching when the "high force" is reached and begins stretching in the opposite direction. The

resulting elasticity curve is fit with a modified Marko-Siggia formula [71] to determine the tether point, DNA contour length, and DNA persistence length. The stage is readjusted in y to center the tether point. The program then repeats the stretching measurement in x. Usually two stretching measurements will center the tetherpoint, while the last stretching measurement will take the final DNA elasticity curves.

Typical parameters: "clamp position" is typically 70 nm, while "high force" is usually between 6–10 pN. "Bead Radius" is 0.16 μm. "Moving Beam" is 1064 and "Beam to measure" is set to 785.

Measure freebead with steps.vi

Location: .\JILA\freebead meas\

Description: This routine measures the trapped bead position and thus the name of the vi is somewhat of a misnomer. The trapped bead position is calibrated and then position vs. time is measured until the "Stop" button is pressed.

Typical parameters: "Beam Detect" is 785. "beam PZT" is 1064. "Bead Height" is either 0.3 μm or 1.0 μm.

InfiniteBWForceClamp_ys.vi

Location: .\JILA\inf bandwidth clamp ys\InfiniteBWForceClamp_ys\

Description: This is a passive force clamp used to take the DNA hairpin data. First, a DNA-tethered bead is trapped and bead position is calibrated. Second, multiple DNA elasticity measurements are taken to center the tether point relative to the laser beam. Next, the PZT mirror centers a detection laser on a fiducial mark. Then the stage is moved to stretch the DNA and pull the bead to an intermediary position where position is recalibrated. The stage moves further, stretching the DNA and pulling the bead out of the trap, until each

stage movement moves the bead out of the trap the same amount (bead position = ∼240 nm). At this point, there is a corresponding move of the PZT mirror to recenter the laser onto the fiducial mark and fiducial mark position is calibrated. Finally, the program begins taking bead positional data vs. time and calculating the corresponding DNA contour length vs. time. While taking data, the program actively stabilizes the stage while clamping the bead position by changing the trap stiffness. For taking DNA hairpin data without the passive force clamp we used a clamped bead position of 70 nm, instead of 240 nm. The output ".tim" data file can be viewed using NA_Tanalysis.ipf.

Typical parameters: The user defines the "DAQ rate", typically 4 kHz, and "DAQ Num pnts to avg", typically 40. These two numbers define the feedback loop rate, which works the best at 100 Hz. "Bead Radius" is typically 0.16 μm. The "Desired stiffness value" is the force at which you want to pull (6 pN) divided by the "Clamp position" (240 nm), 0.025 pN/nm. "Moving Beam" is 1064 and "Beam to measure" is set to 785.

RecBCDPulling_v1.vi

Location: .\JILA\RecBCD\RecBCDPulling_v1\

Description: This routine measures DNA contour length vs. time using active stabilization. The program was used to take control measurements of DNA tethers, as well as RecBCD data. First, a tethered bead is trapped and bead position is calibrated. Second, multiple DNA elasticity measurements are taken to center the tether point relative to the laser beam. Next, the PZT mirror centers a detection laser on a fiducial mark. Then the stage moves in y, stretching the DNA and pulling the bead out of the trap until the bead position is at the "Clamp position"; there is a corresponding move of the PZT mirror to keep the detection laser centered on the fiducial mark. To make sure, the fiducial mark

position is calibrated at this point. Finally, the program begins taking bead positional data vs. time and calculating the corresponding DNA contour length vs. time. While taking data, the program actively stabilizes the stage, if the bead position changes by more than 10 nm, the stage and mirror are readjusted so that bead position returns to the initial value. This clamp on bead position is termed the pseudo clamp. The output ".dat" data file can be viewed using AnalyzeDNAPulling.ipf.

Typical parameters: The user defines the "DAQ rate", typically 4 kHz, and "DAQ Num pnts to avg", typically 40. These two numbers define the feedback loop rate, which works the best at 100 Hz. "Bead Radius" is typically 0.16 μm. The "Desired stiffness value" is the force at which you want to pull (6 pN) divided by the "Clamp position" (70 nm), 0.086 pN/nm. The "Feedback Mode control" is pseudo. "Moving Beam" is 1064 and "Beam to measure" is set to 785.

calibrate_free_bead.vi

Location: .\

Description: This program measures stiffness using the drag method. The user positions a trapped bead at one end of the stage range. The program begins moving the stage at a particular velocity, which displaces the bead from the trap center. Using this measurement, the program calculates the stiffness of the trap at the current intensity servo voltage. The program will need to be repeated over several voltages to get a calibration for stiffness to voltage.

Typical parameters: "End Velocity" sets the velocity and depends on the force you want to use. "Range" is how many microns you want to move the stage and is typically 90 μm. "dz/dx" is the tilt of the stage and can be found by measuring the change in fiducial mark z position as the stage is moved laterally.

"Angle" picks whether to move the stage in x or y, 0 degrees = x and 90 degrees = y.

C.2 AFM experiment

Gavin_1beam_Rezero.vi

Location: .\Z calibration\

Description: This program measures the position of one or two fiducial marks using two lasers. The user will first align the two lasers to look at one fiducial mark or two fiducial marks. Then the program centers the lasers and calibrates the fiducial mark position. Finally, the program measures fiducial position vs. time until the "Stop" button is pressed. The program plots the differential measurement and will also actively stabilize the fiducial position. It is also outfitted to allow for an optional linear crosstalk compensation, scanning of the sample, and back-and-forth movement of the sample. The output ".dtf" data file can be viewed using AnalyzeStabData.ipf.

Typical parameters: The user defines the "DAQ rate", typically 10.4 kHz, and "DAQ Num pnts to avg", typically 104. These two numbers define the feedback loop rate, which works the best at 100 Hz.

AFM 3D stabilization.vi

Location: .\JILA\Gavin\AFM 3D Stabilization\

Description: This routine measures the position of the tip using two lasers. The user will first align the two lasers to look at one tip. Then the program moves the tip stage back-and-forth relative to both lasers, while the user moves the tip to center it. The program calibrates the tip position and measures the crosstalk. Finally, the program measures tip position vs. time using a linear algorithm to compensate for crosstalk. Active stabilization of the tip is optional. The output

".dtf" data file can be viewed using AnalyzeStabData.ipf.

Typical parameters: The user defines the "DAQ rate", typically 10.4 kHz, and "DAQ Num pnts to avg", typically 104. These two numbers define the feedback loop rate, which works the best at 100 Hz. The 810-nm beam measures the AFM tip, while the 845-nm beam measures the fiducial mark.

AA_Top_Level_77PicoDrift 2D stabilization Multi wiggle FPGA.vi

Location: .\JILA\Gavin\AFM VI's Reorganized 20070713\

Description: This is a surface imaging program using the stabilized AFM. A more in depth description is elsewhere [20]. Briefly, the program centers both the tip and fiducial mark to their respective lasers and calibrates position (with a crosstalk compensation method). Then the program calibrates the AFM tip position using the optical lever arm. Active stabilization of both the tip in 3D and sample in 2D is controlled through writes to a field-programmable gate array card. The sample position in z is locked using the optical lever arm to maintain a constant force on the tip. The sample is scanned while the z error signal is output as the surface map. To view the ".stm" data file use AnalyzeAFMImage.ipf or sub routine of this procedure.

Appendix D

Hardware Index

This is an index of the custom-built hardware on the optical trapping instrument. Hardware for the AFM experiment will be described elsewhere [20]. There are drawings and designs of various machined microscope and optics mounts, as well as electronic diagrams for our custom electronics. These items do not represent my original work and were mostly made by the JILA machine and electronic shops, please see the Acknowledgements for a more complete reference. The drawings are included for completeness.

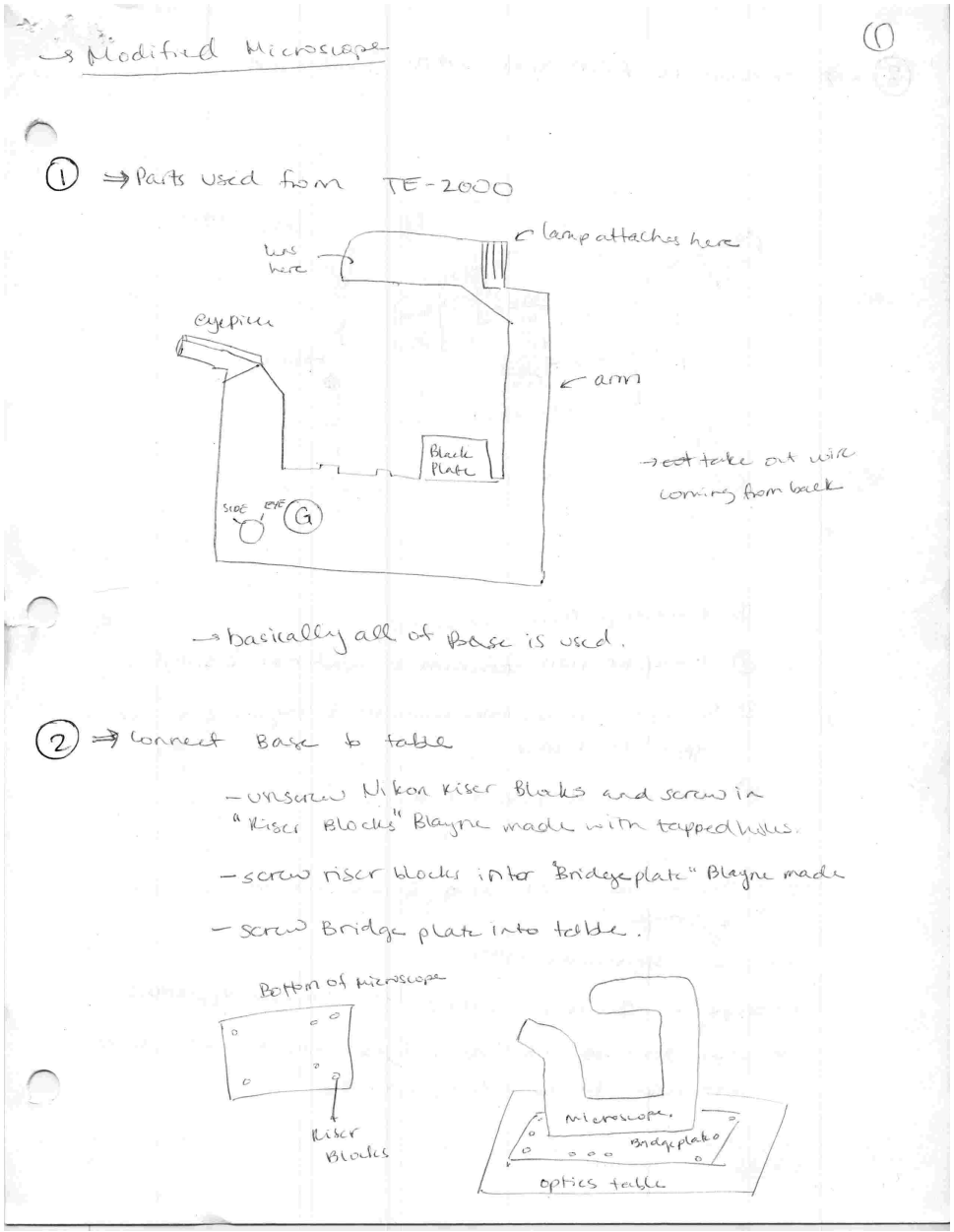

Figure D.1: Building the microscope part 1.

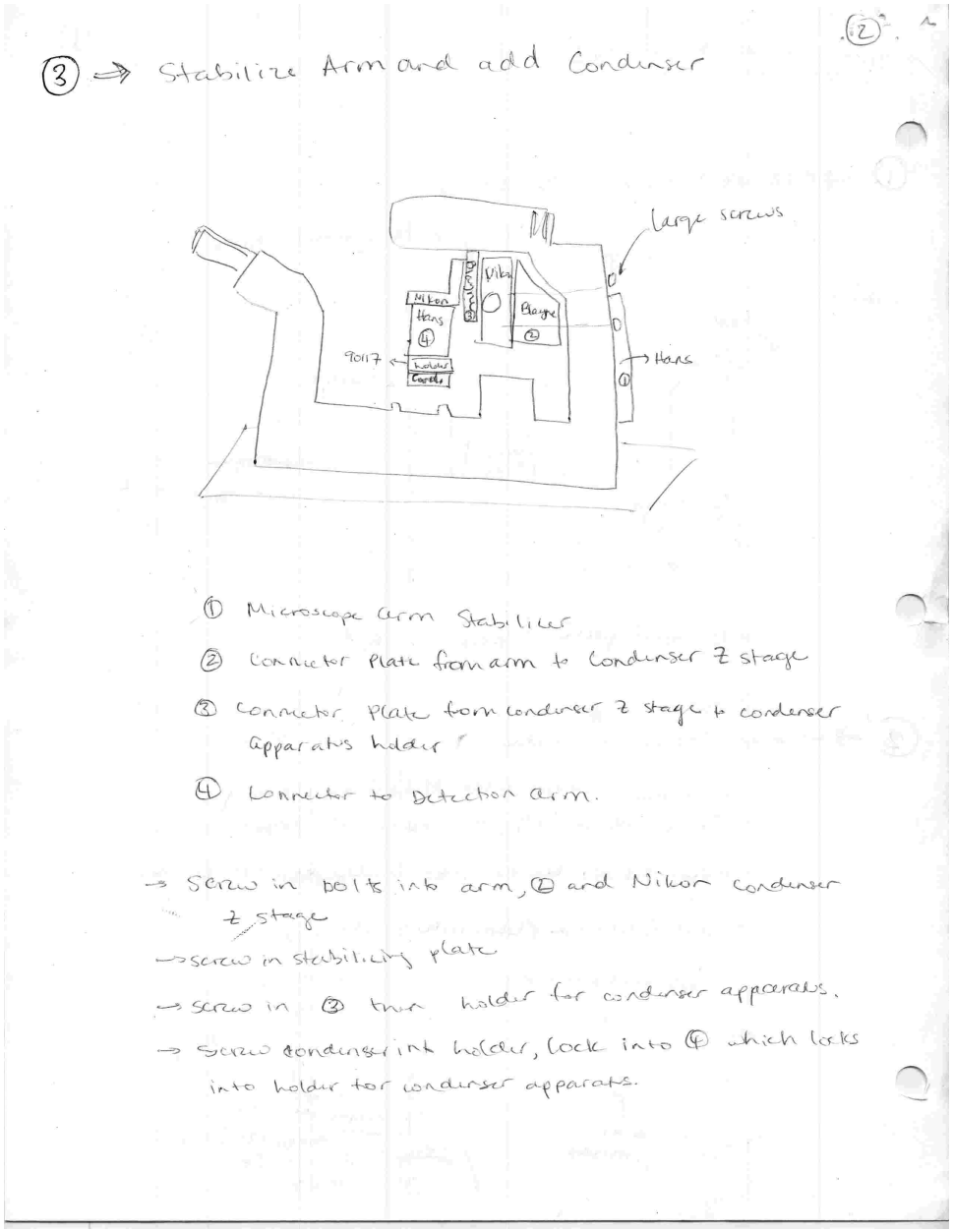

Figure D.2: Building the microscope part 2.

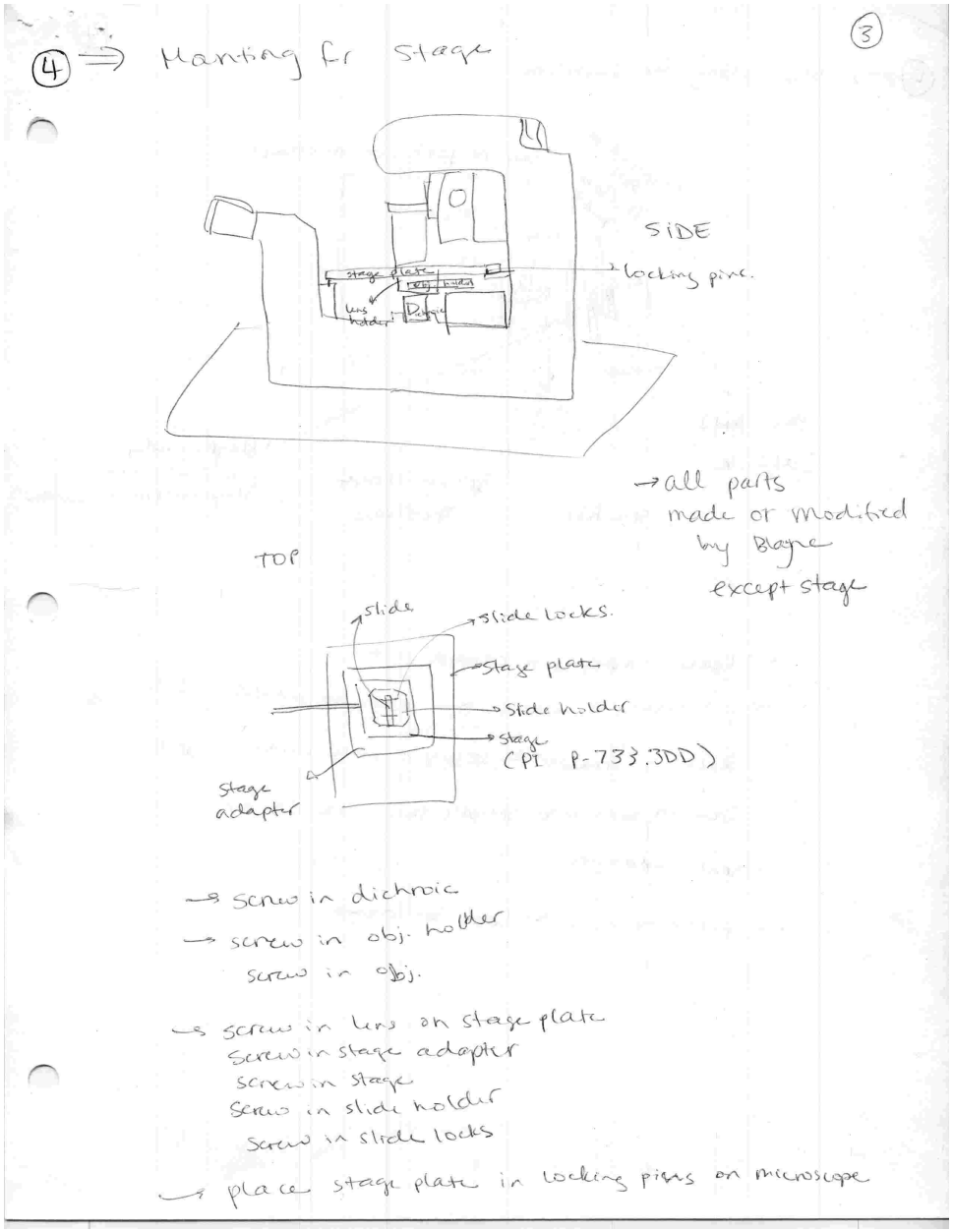

Figure D.3: Building the microscope part 3.

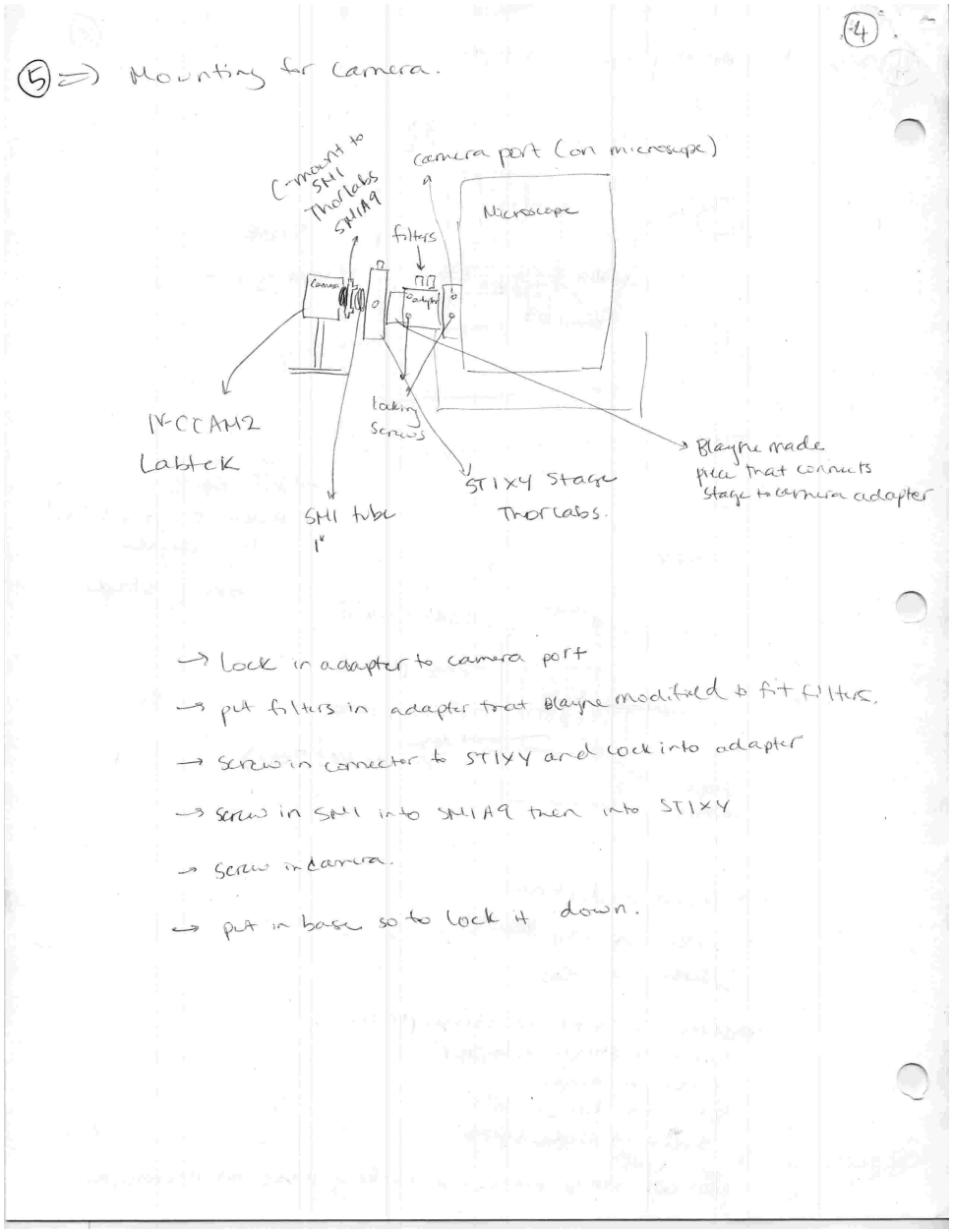

Figure D.4: Building the microscope part 4.

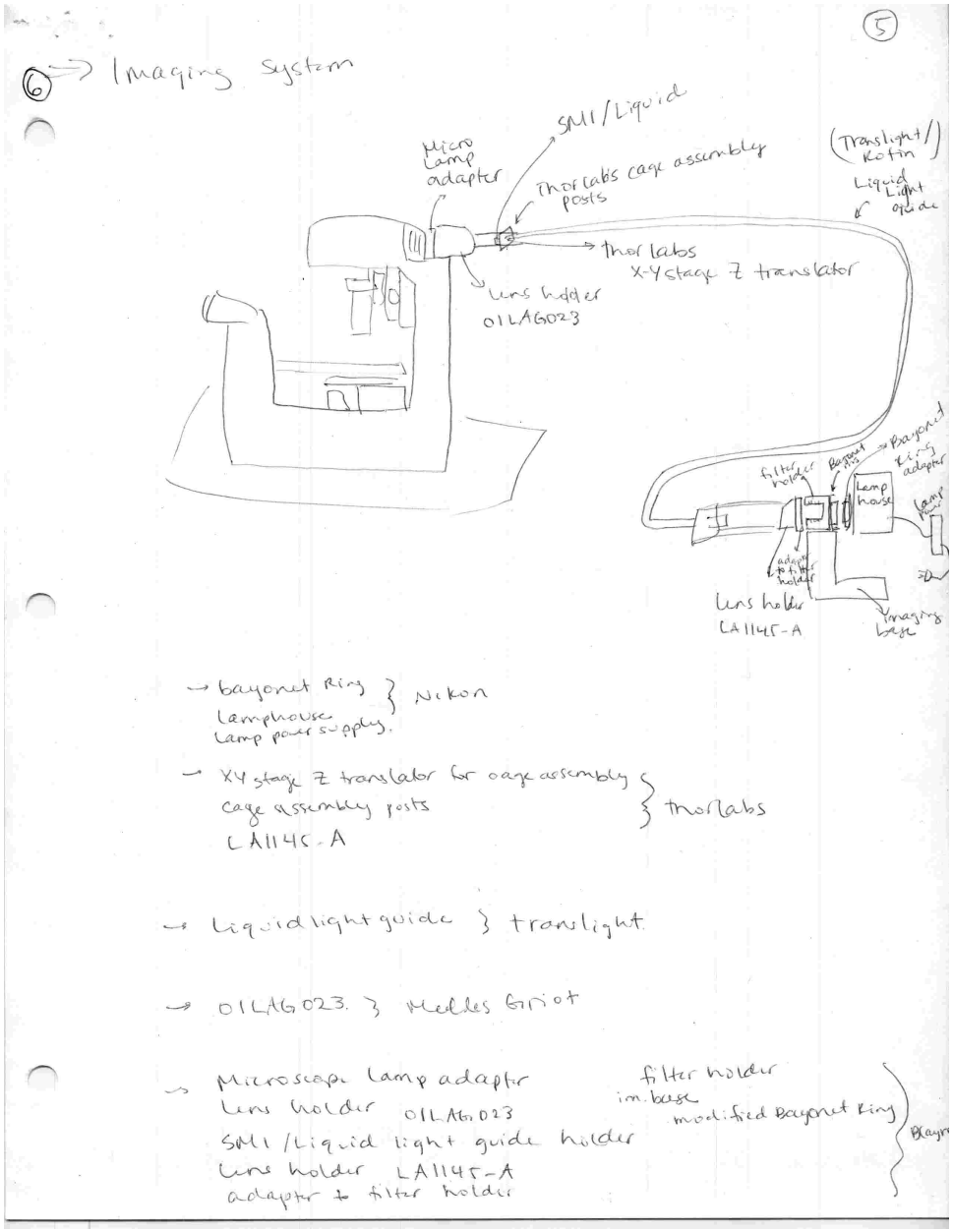

Figure D.5: Building the microscope part 5.

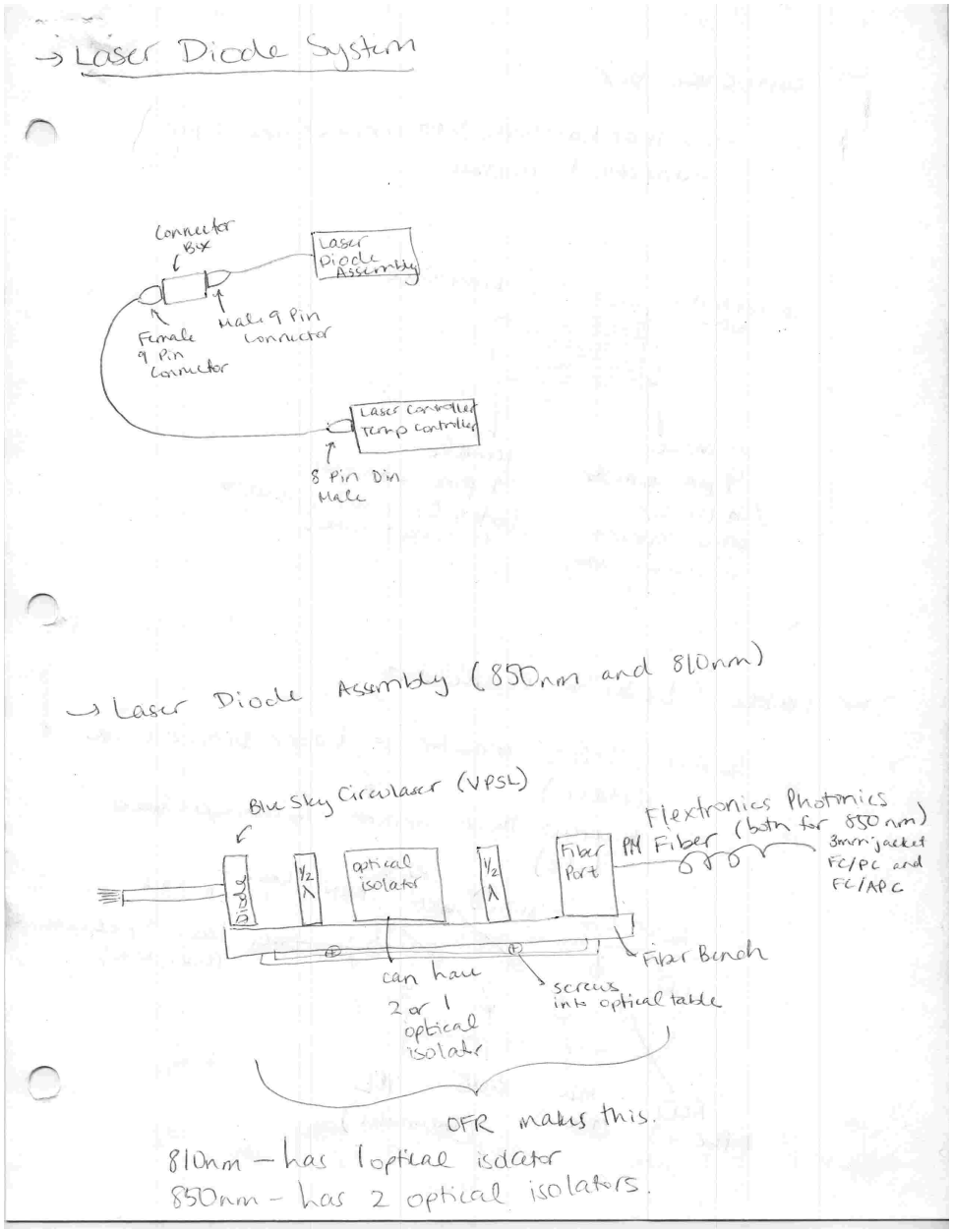

Figure D.6: Building the diode laser system part 1.

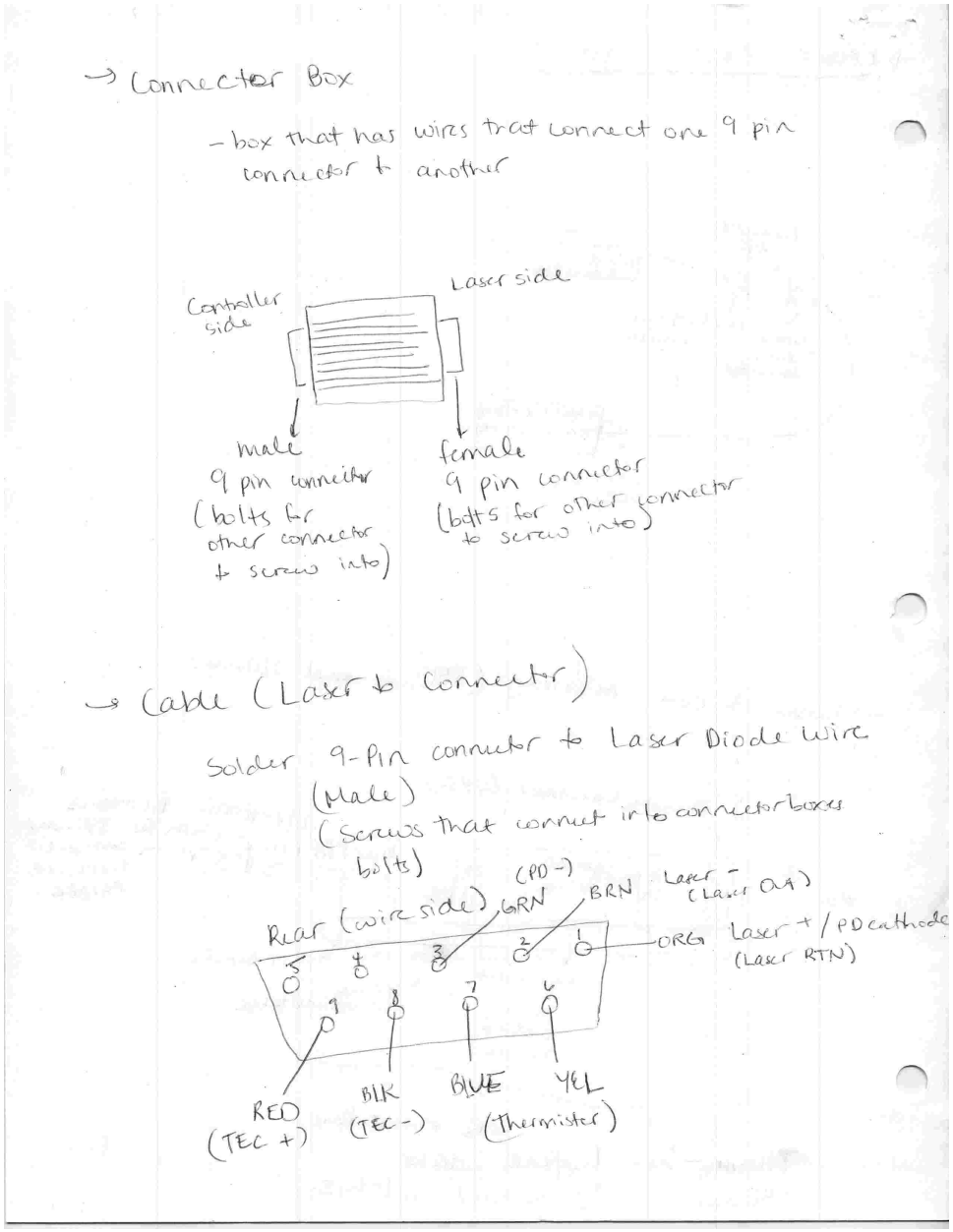

Figure D.7: Building the diode laser system part 2.

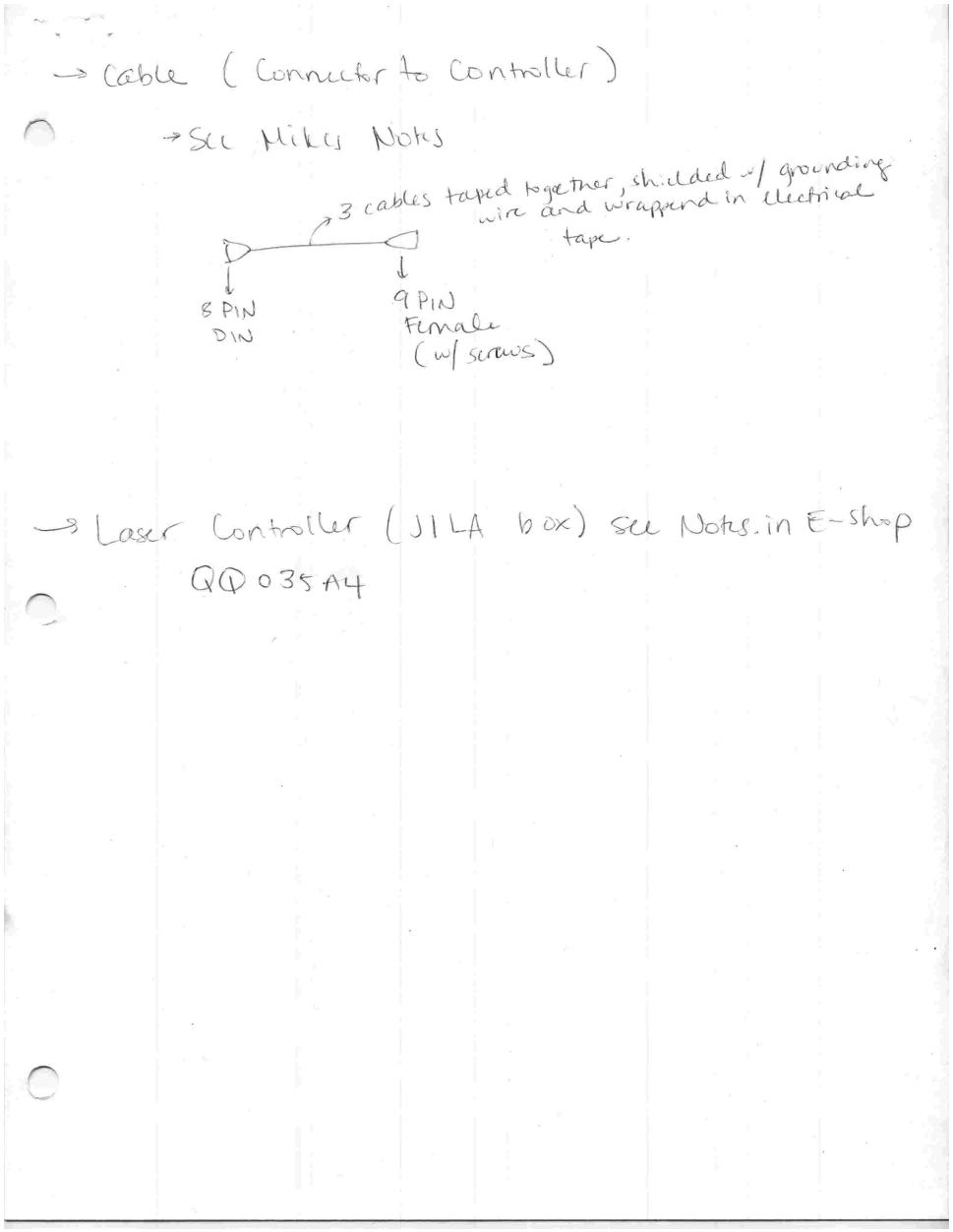

Figure D.8: Building the diode laser system part 3.

Figure D.9: Microscope base plate.

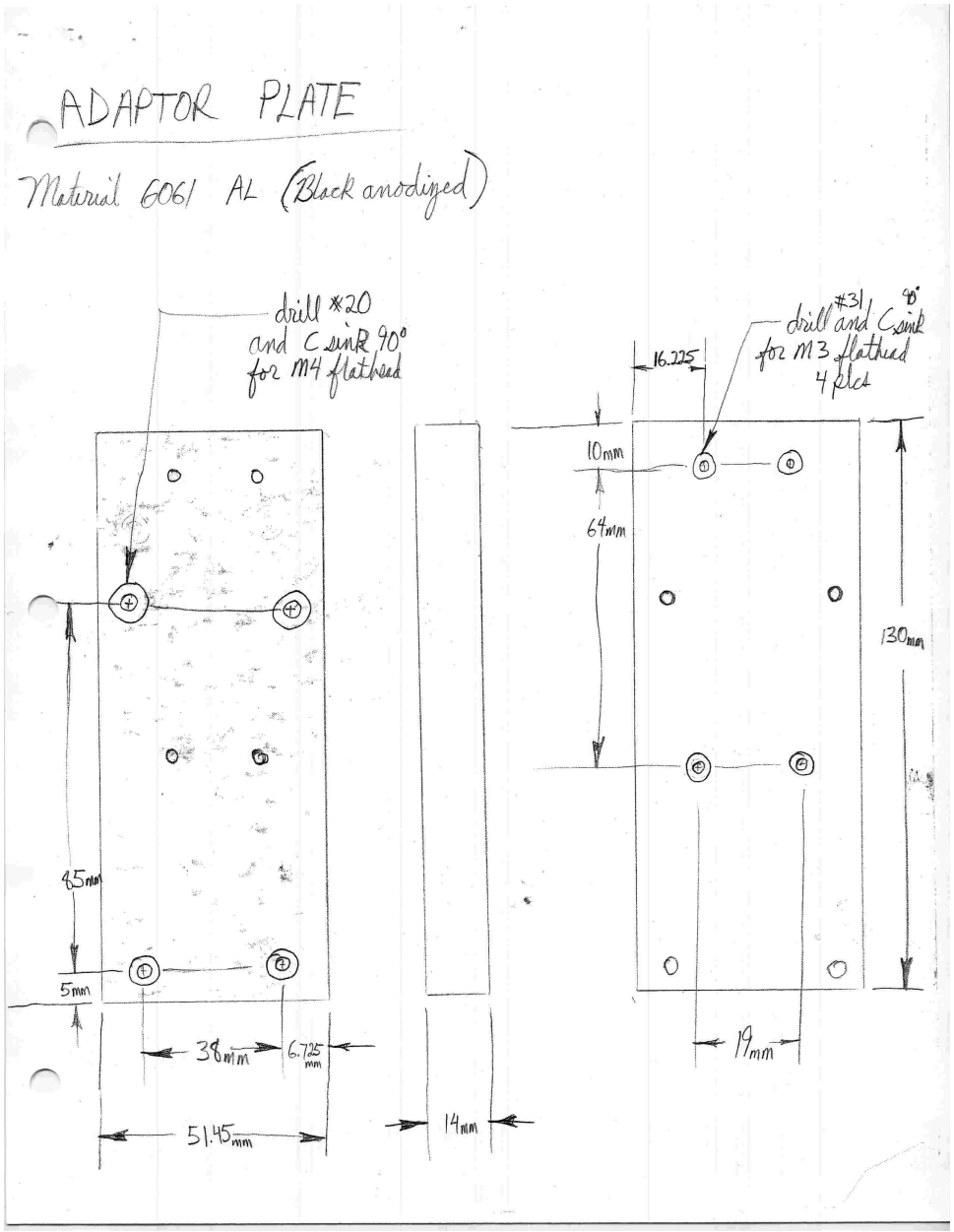

Figure D.10: Condenser arm focusing plate adapter.

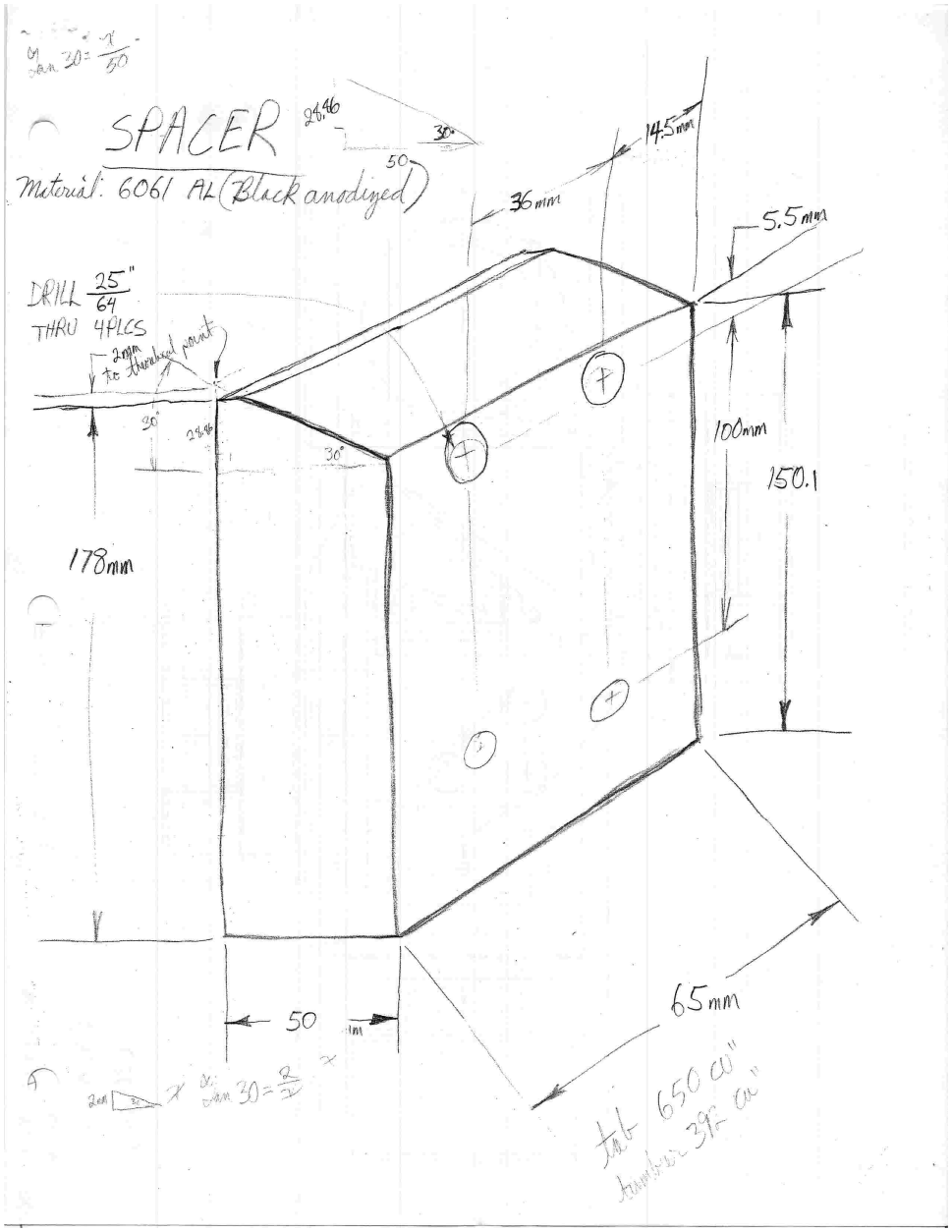

Figure D.11: Condenser arm focusing plate spacer.

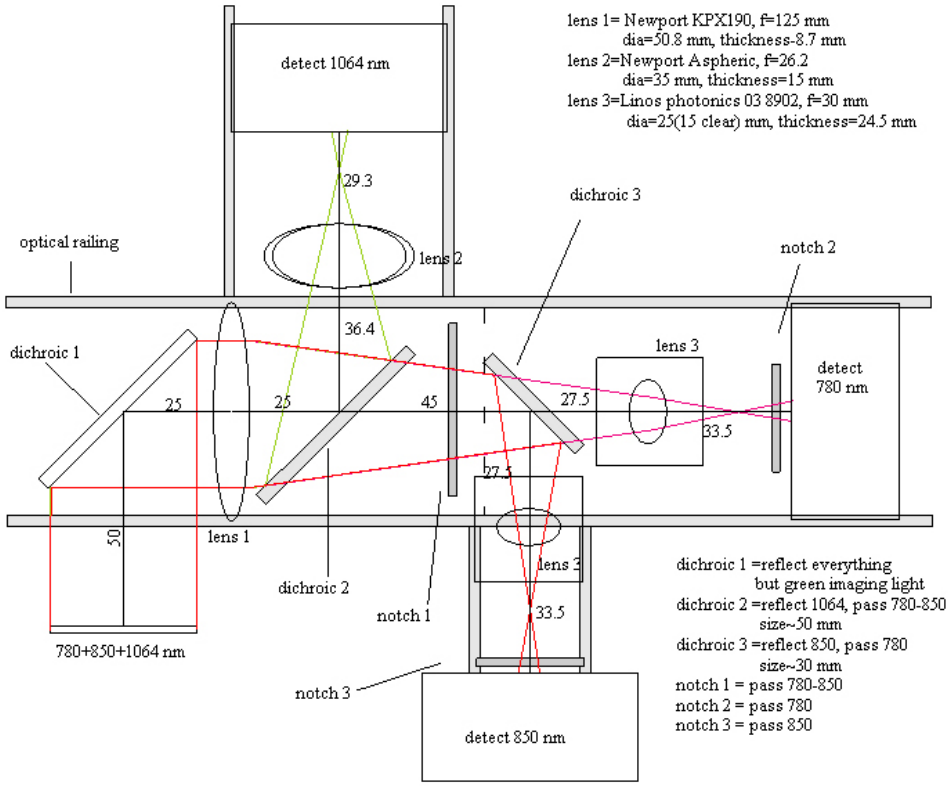

Figure D.12: Detection mount off condenser arm.

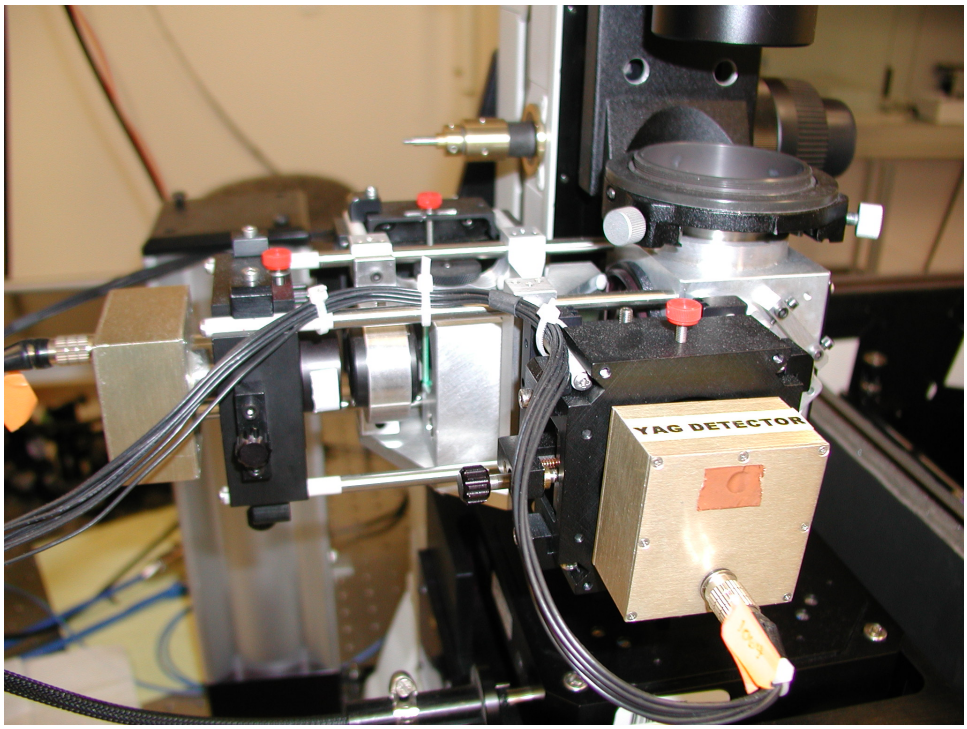

Figure D.13: Detection mount off condenser arm picture.

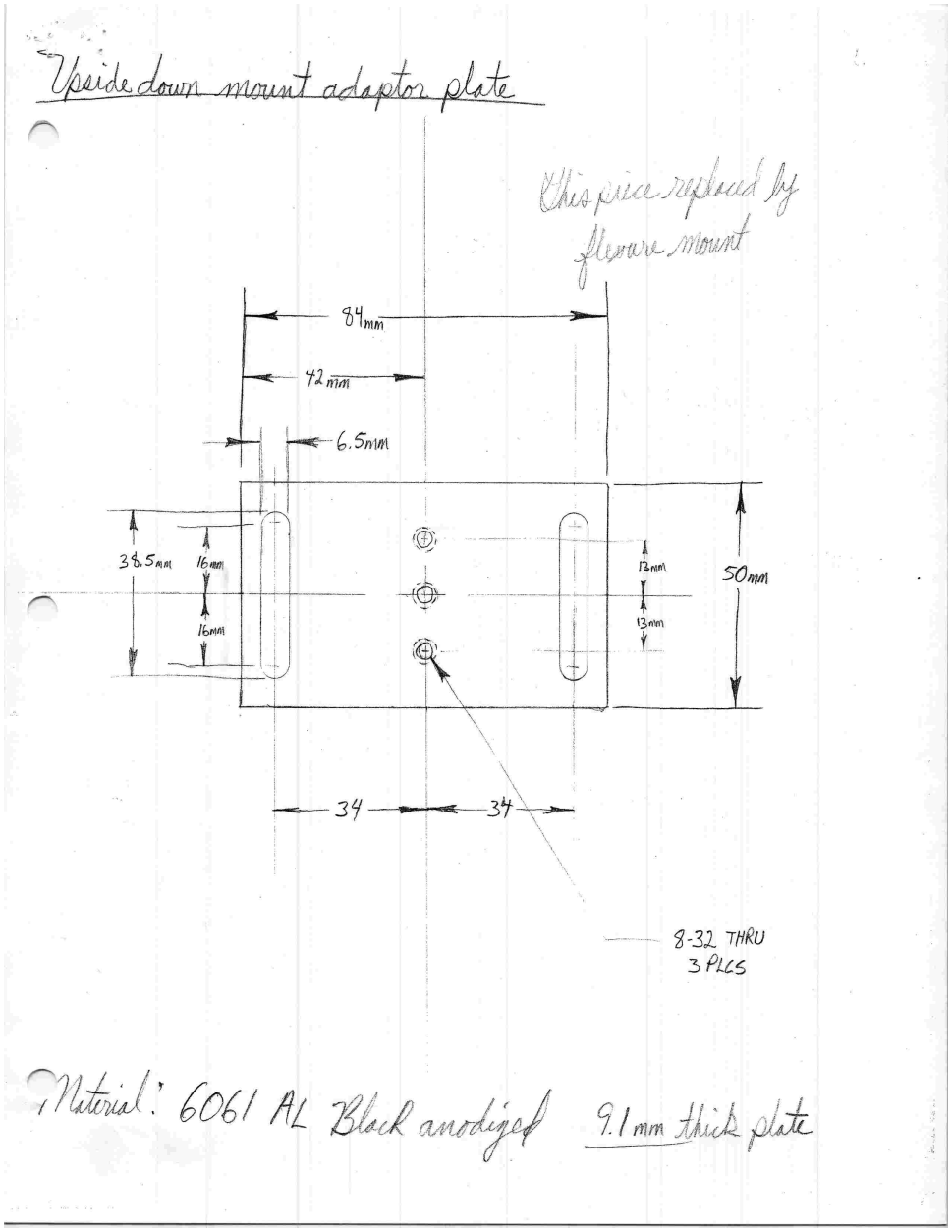

Figure D.14: Upside down lens adaptor plate part 1.

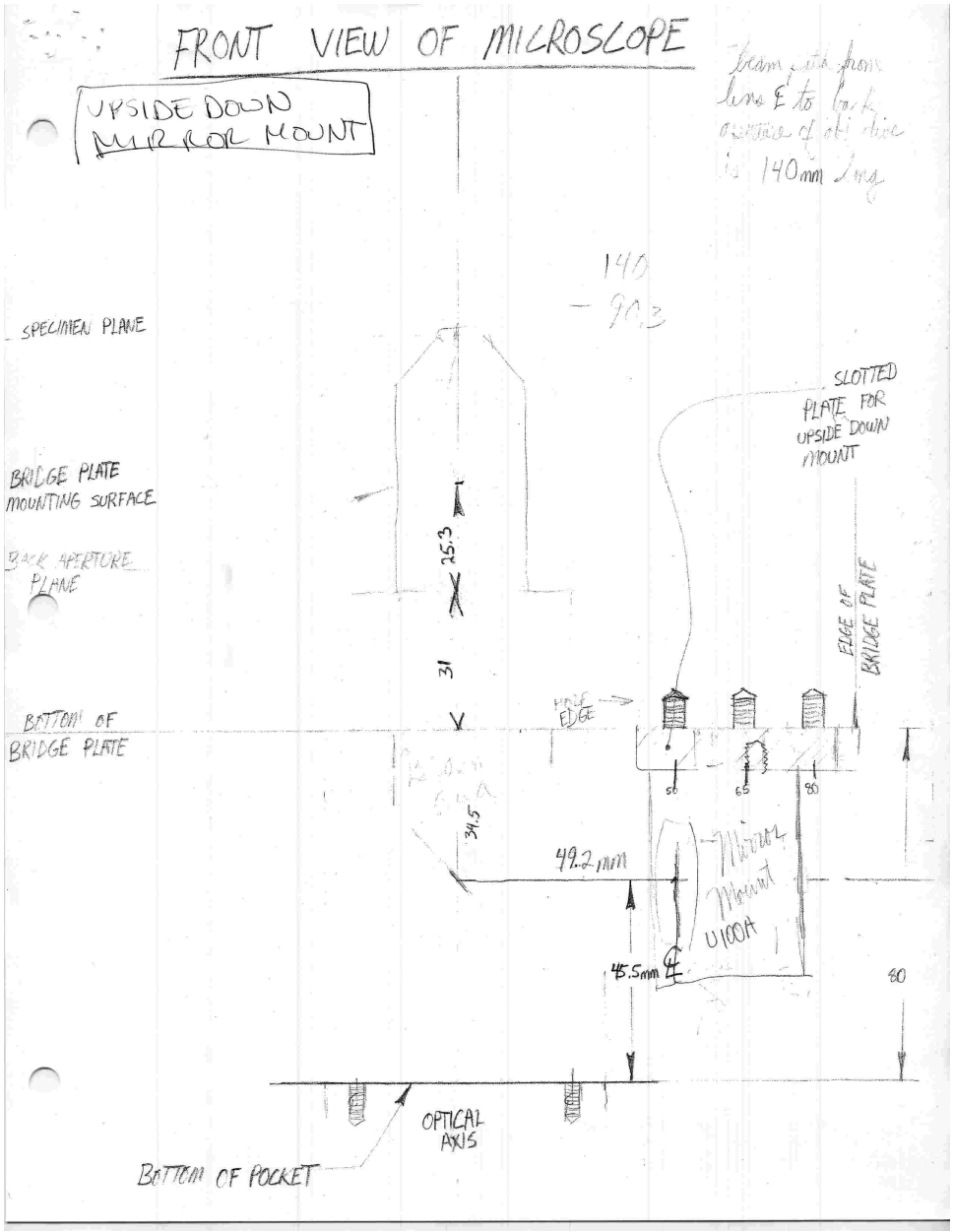

Figure D.15: Upside down lens adaptor plate part 2.

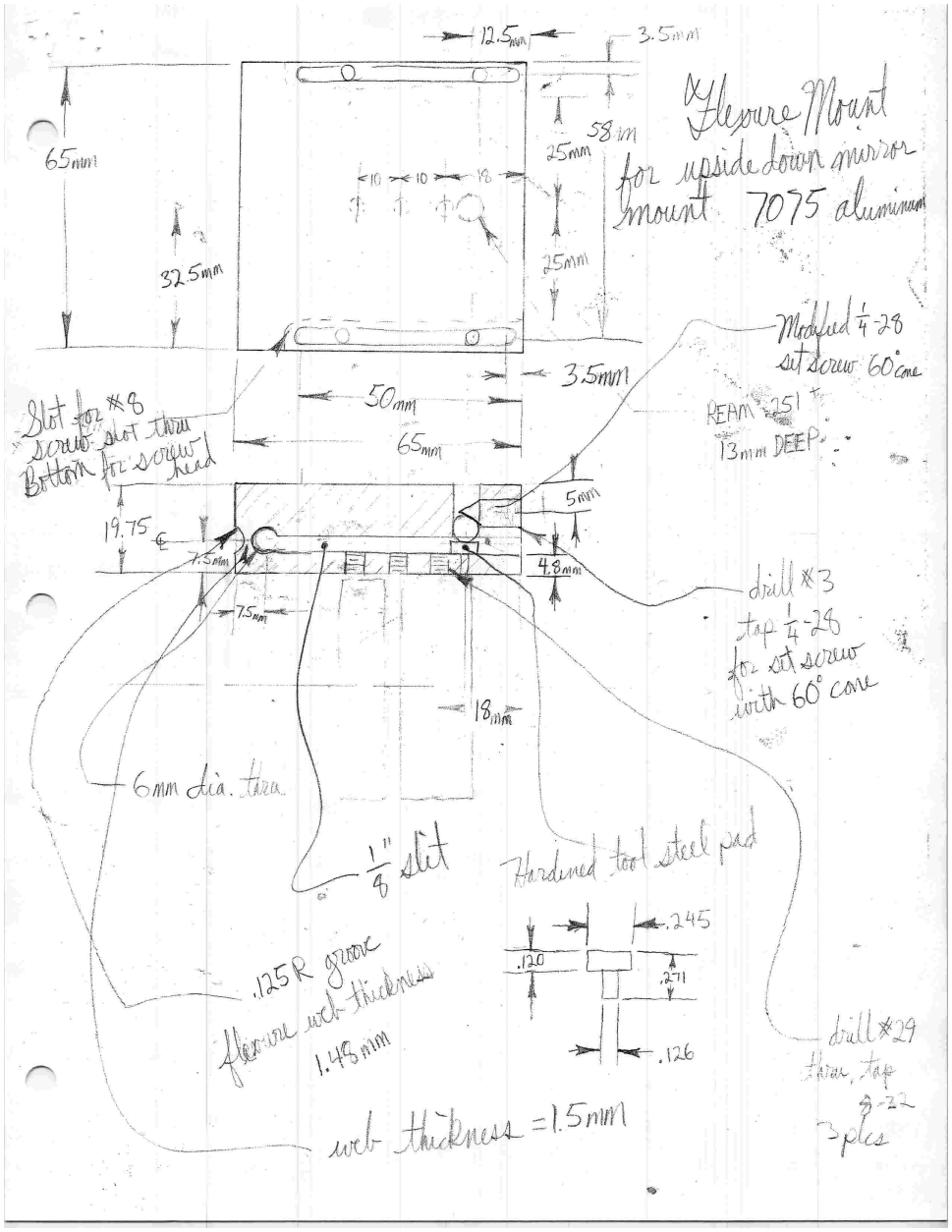

Figure D.16: Upside down lens adaptor plate part 3.

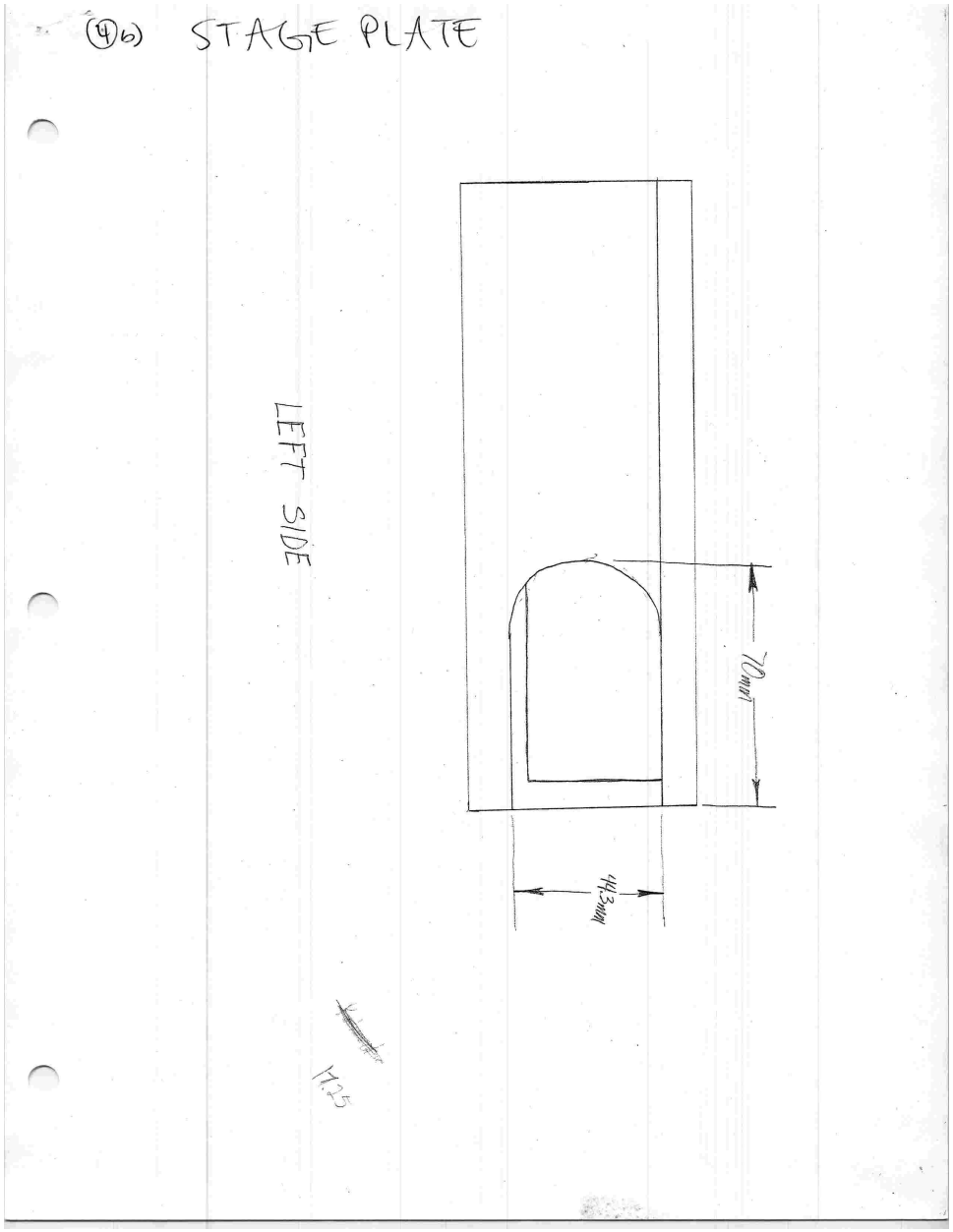

Figure D.17: Microscope bridge plate part 1.

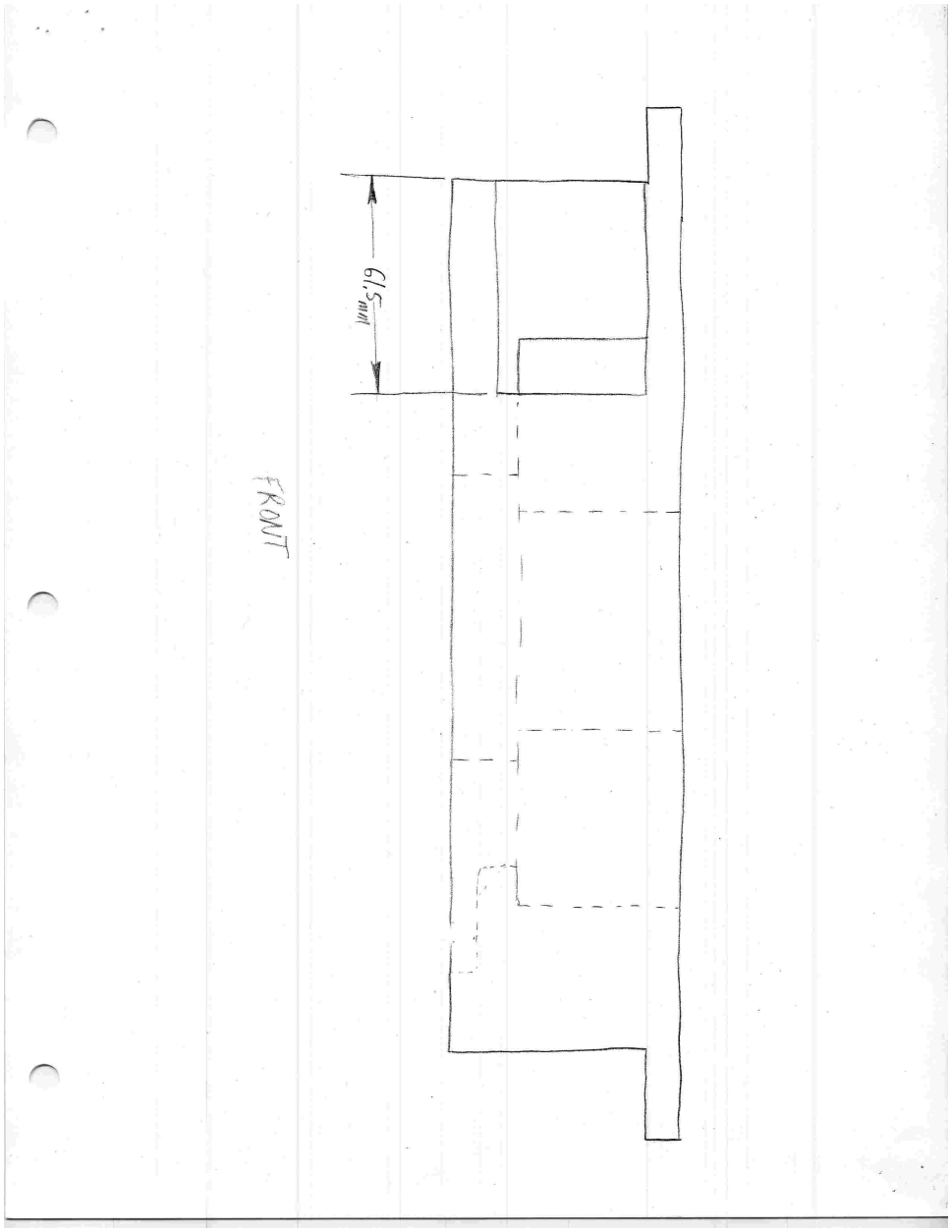

Figure D.18: Microscope bridge plate part 2.

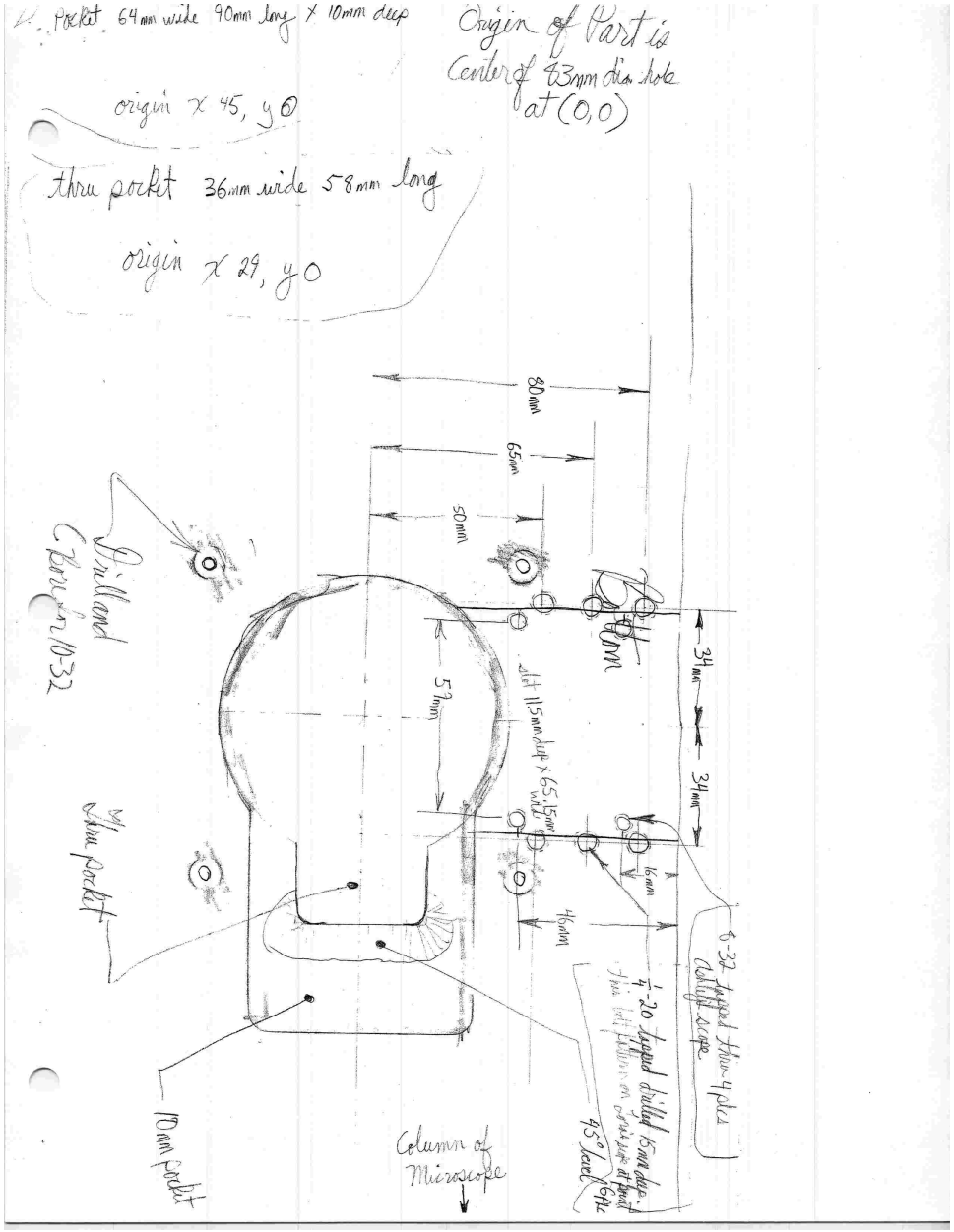

Figure D.19: Microscope bridge plate part 3.

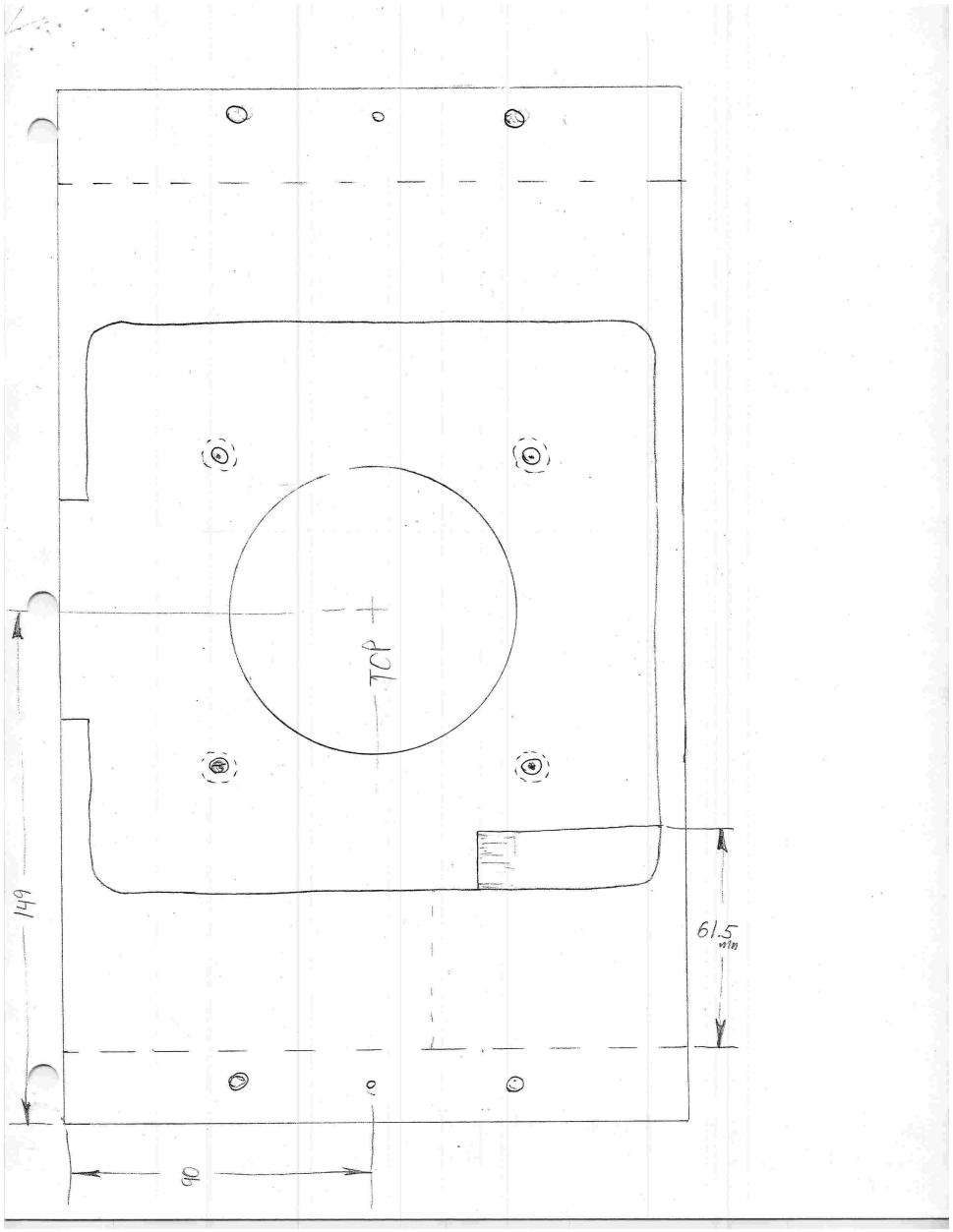

Figure D.20: Microscope bridge plate part 4.

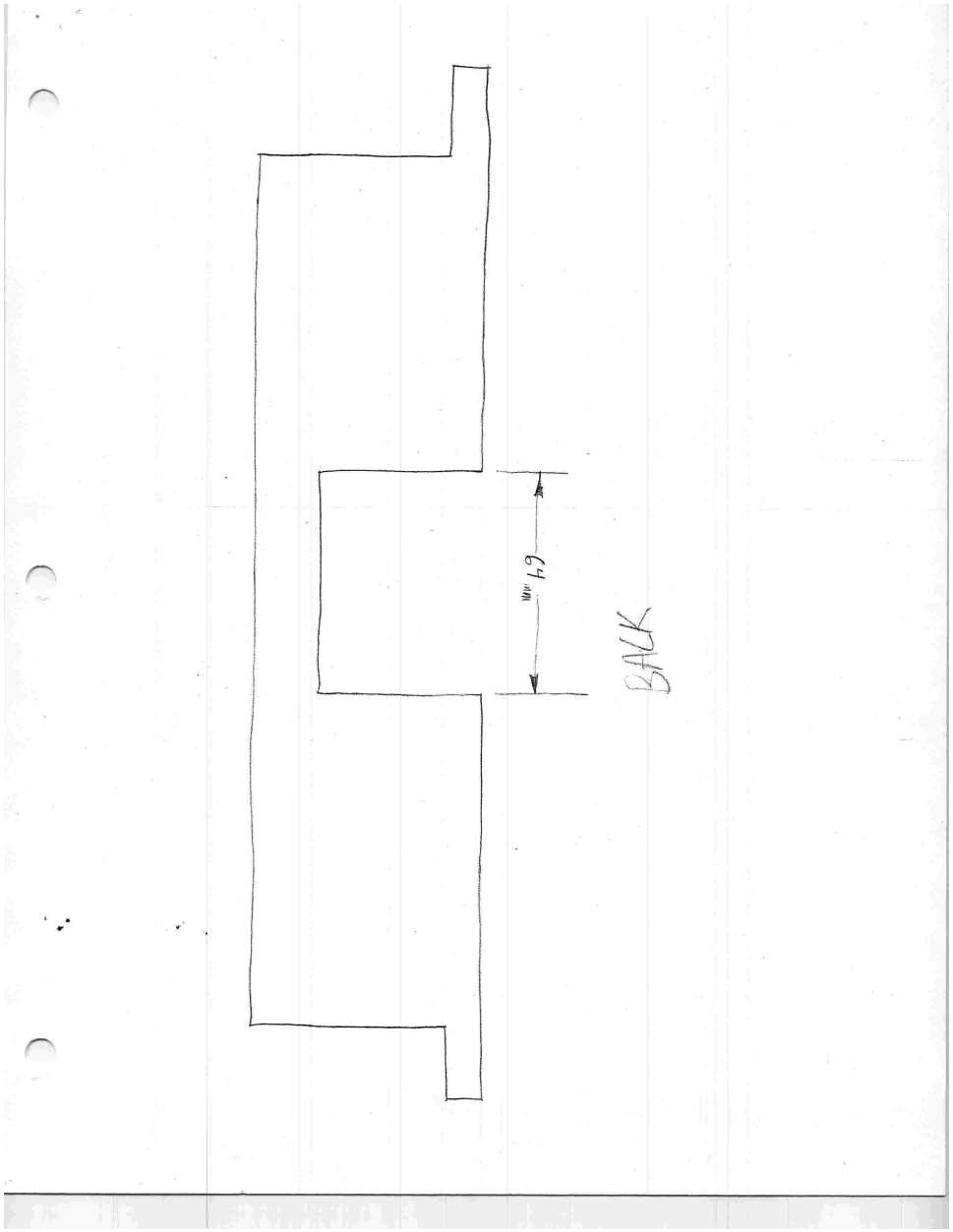

Figure D.21: Microscope bridge plate part 5.

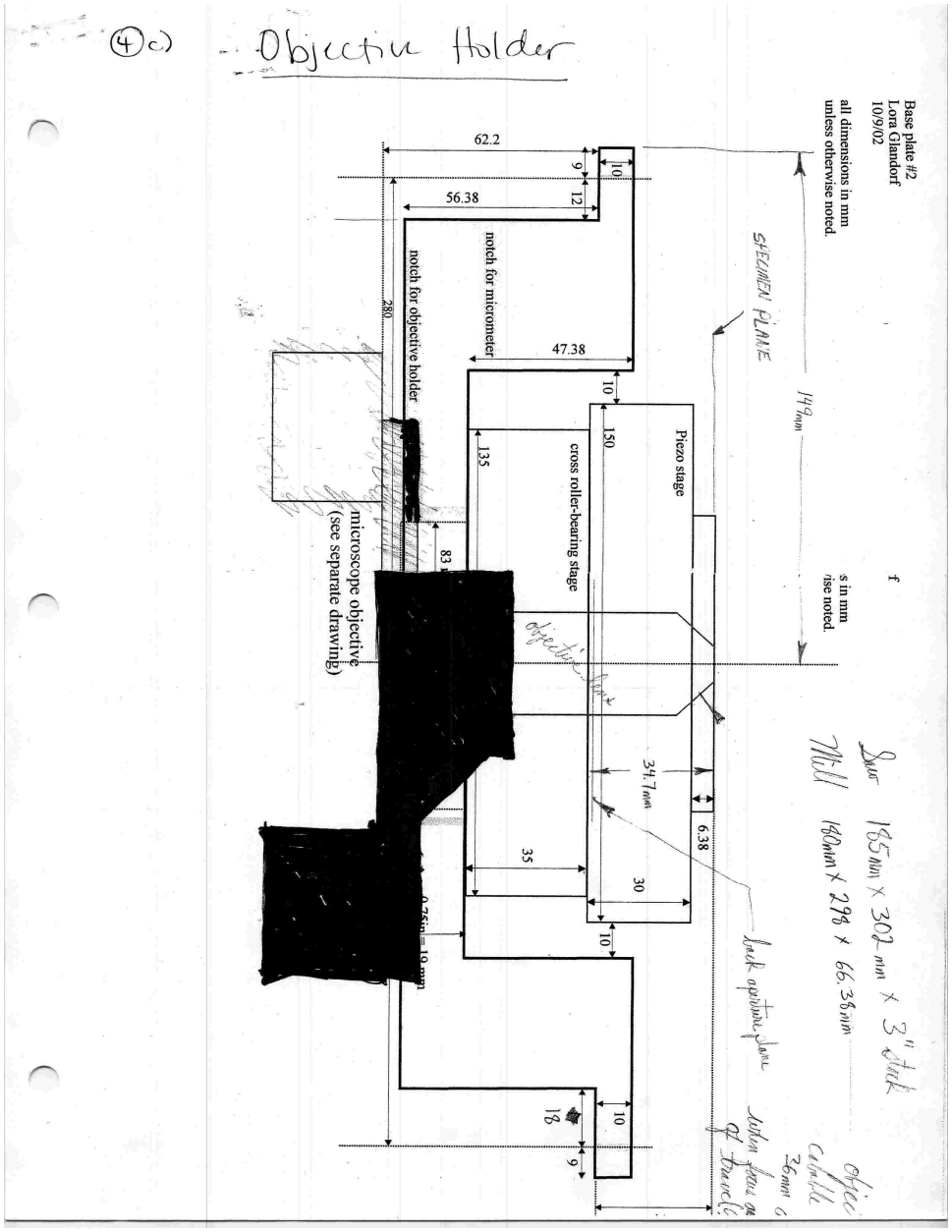

Figure D.22: Objective holder part 1.

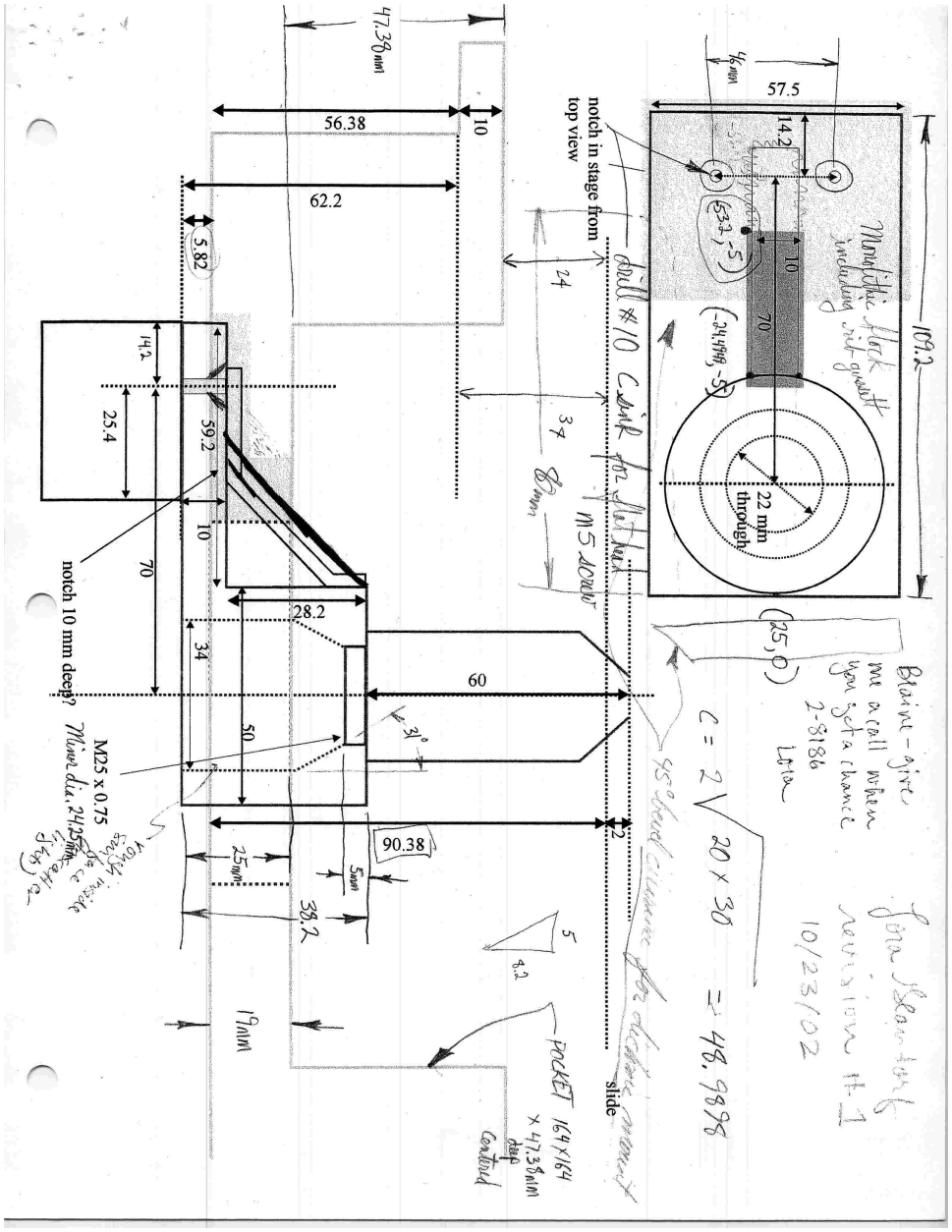

Figure D.23: Objective holder part 2.

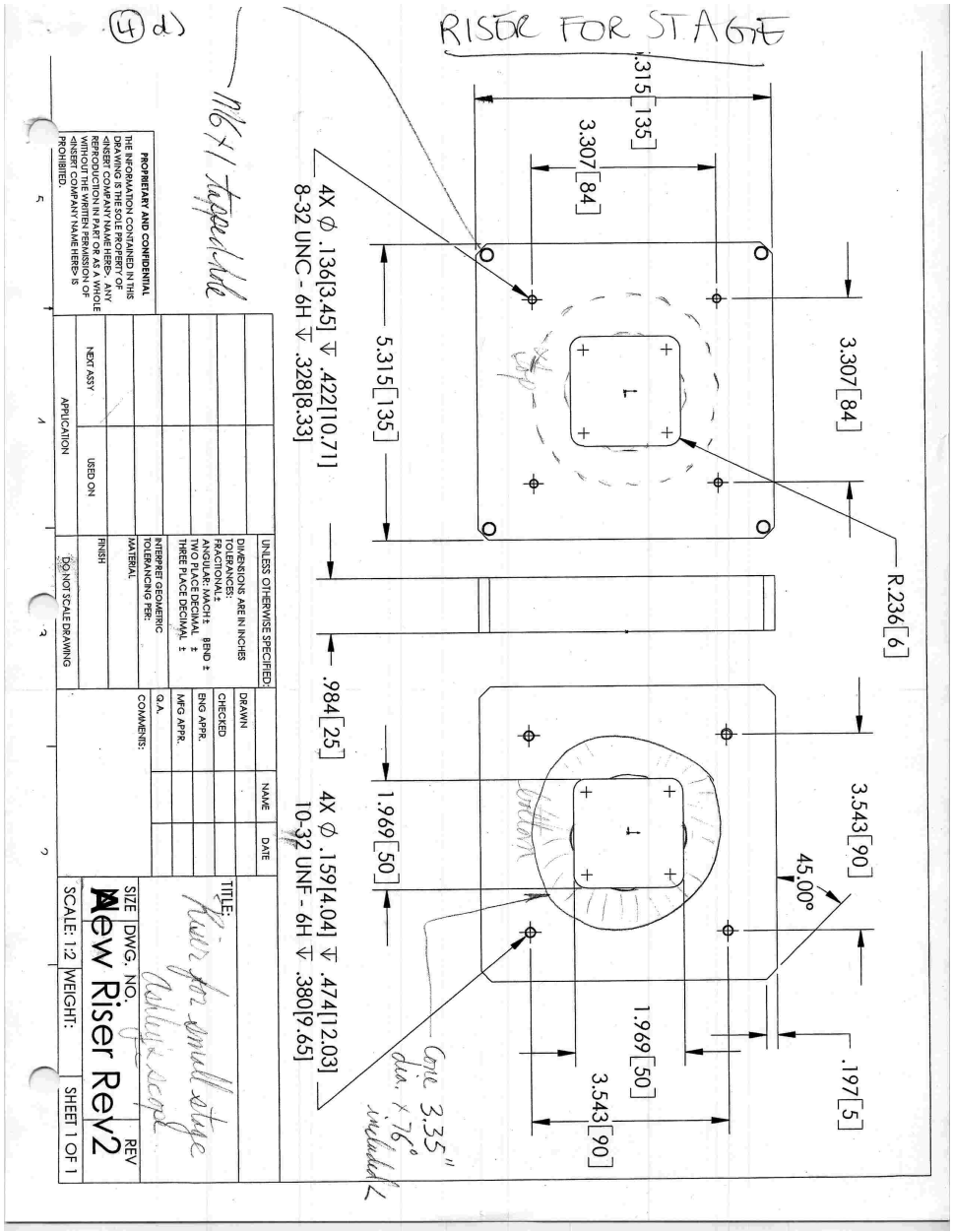

Figure D.24: Riser for 733.3D Physik Instrumente stage.

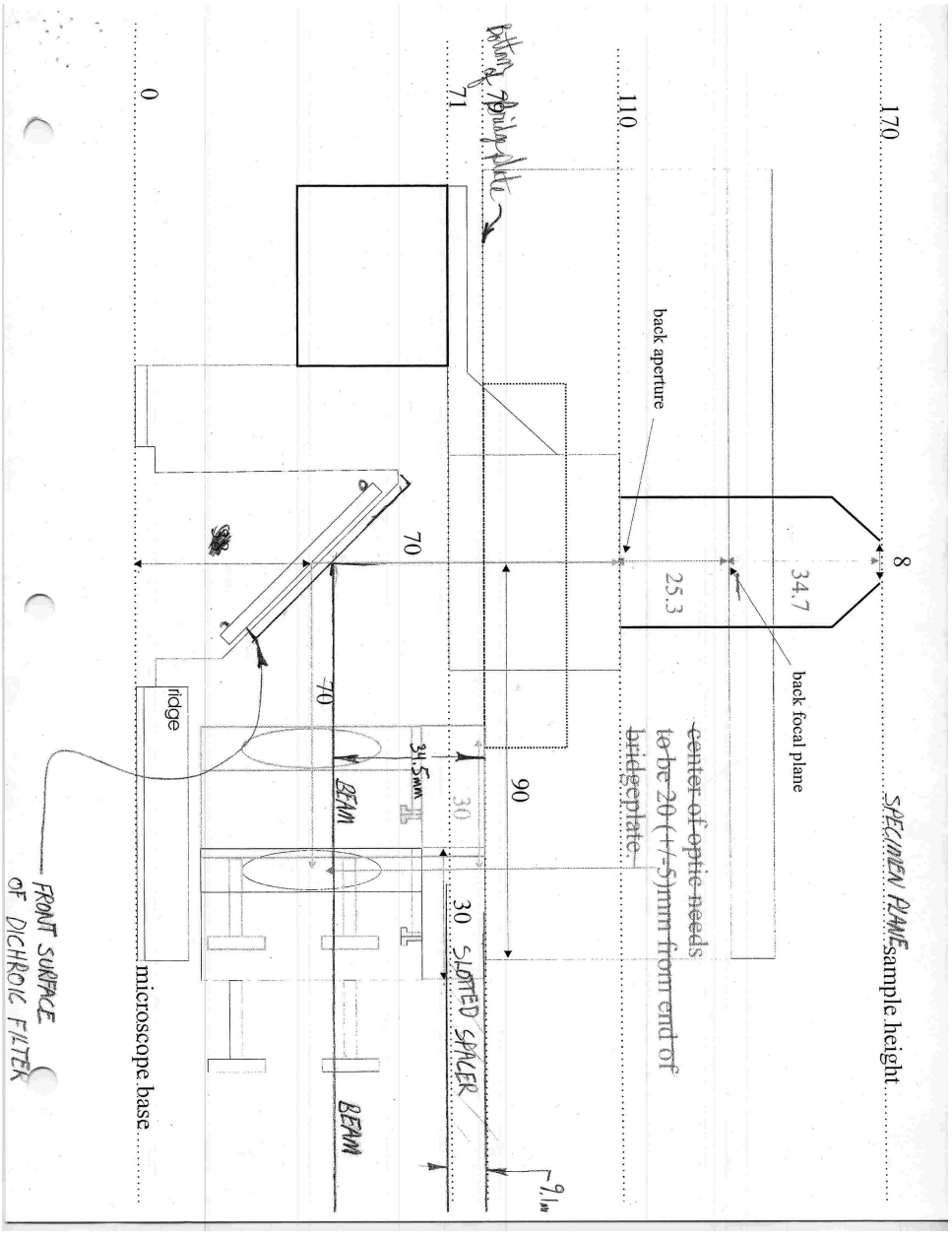

Figure D.25: Microscope dichroic holder part 1.

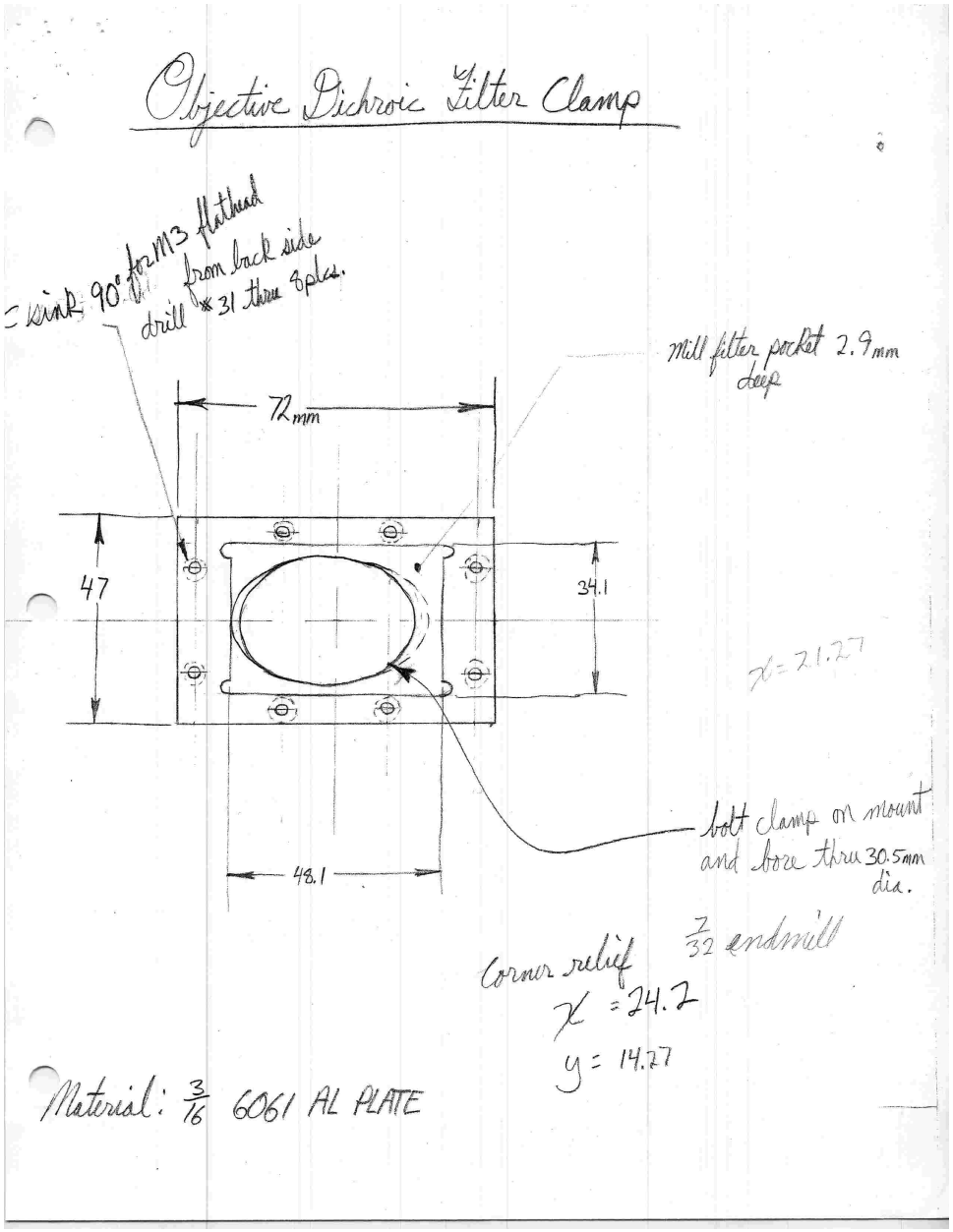

Figure D.26: Microscope dichroic holder part 2.

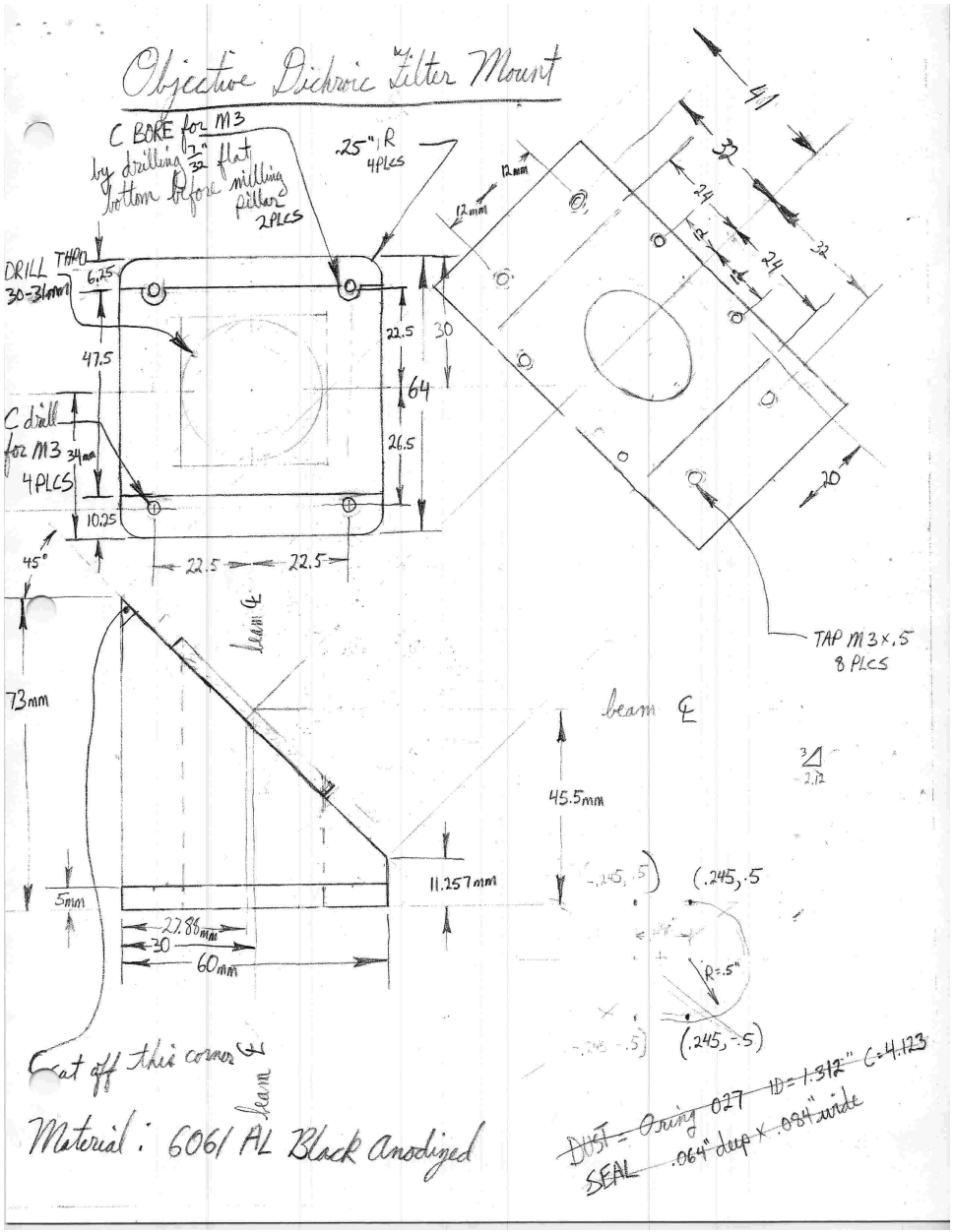

Figure D.27: Microscope dichroic holder part 3.

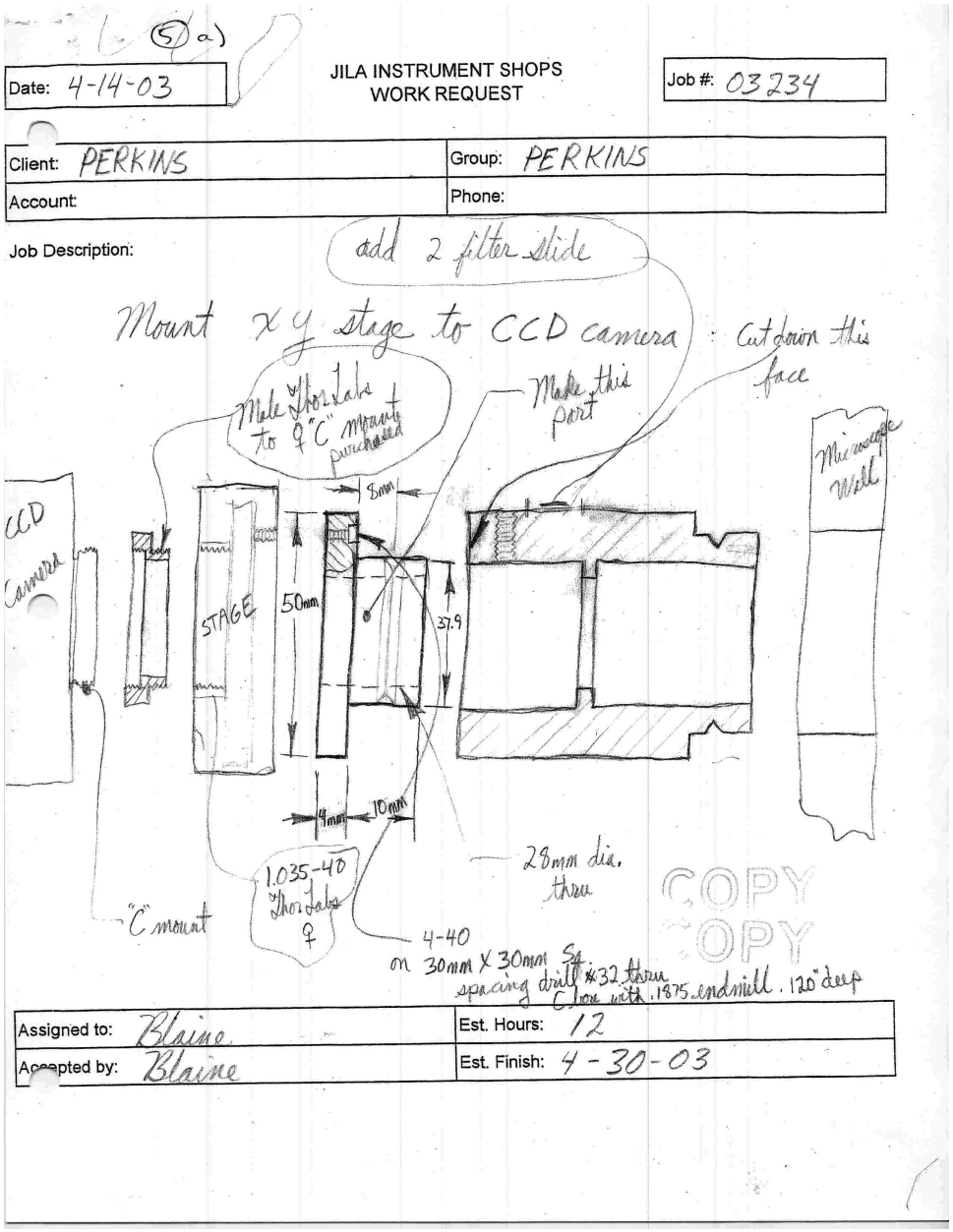

Figure D.28: Microscope camera mount.

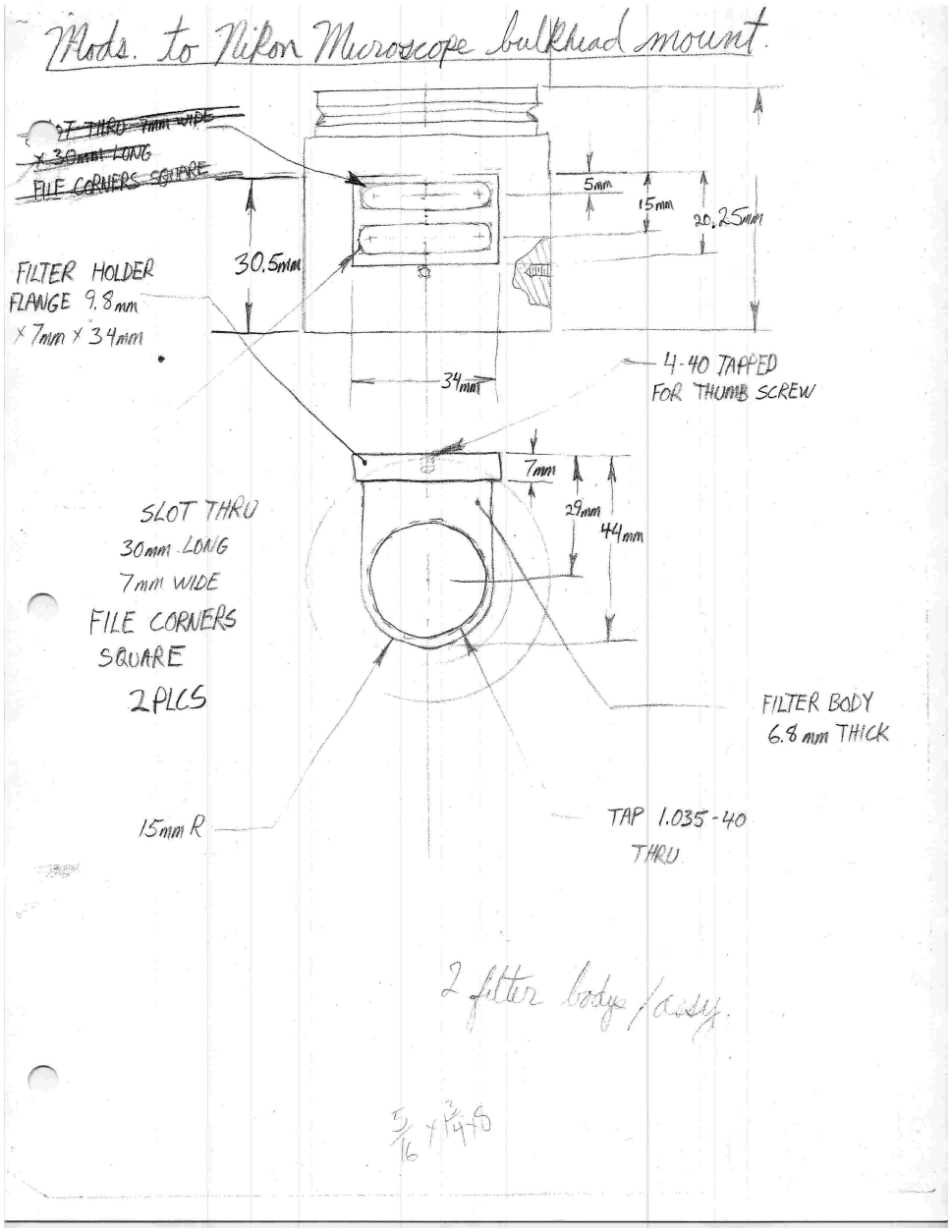

Figure D.29: Color filter holder.

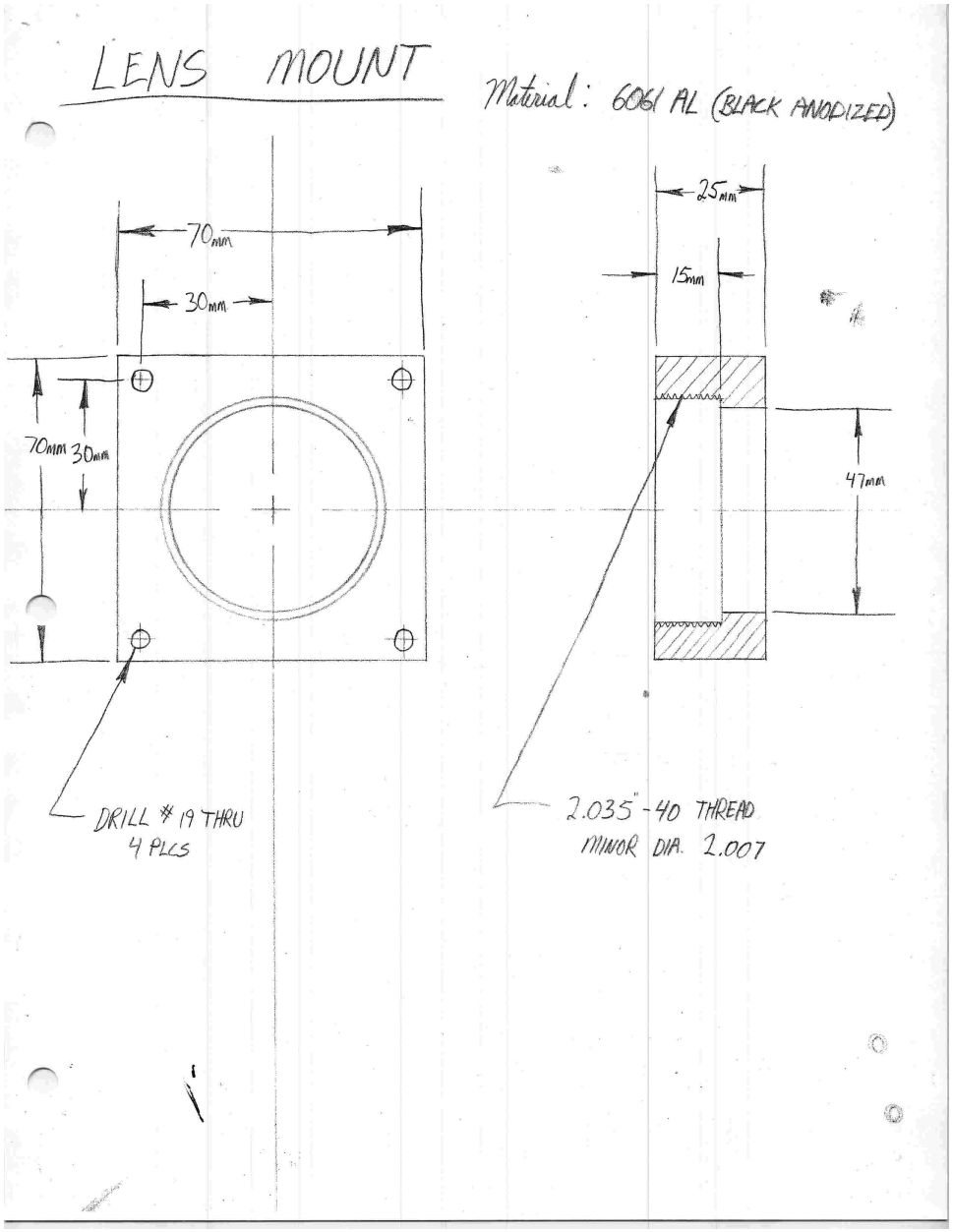

Figure D.30: Lens mount.

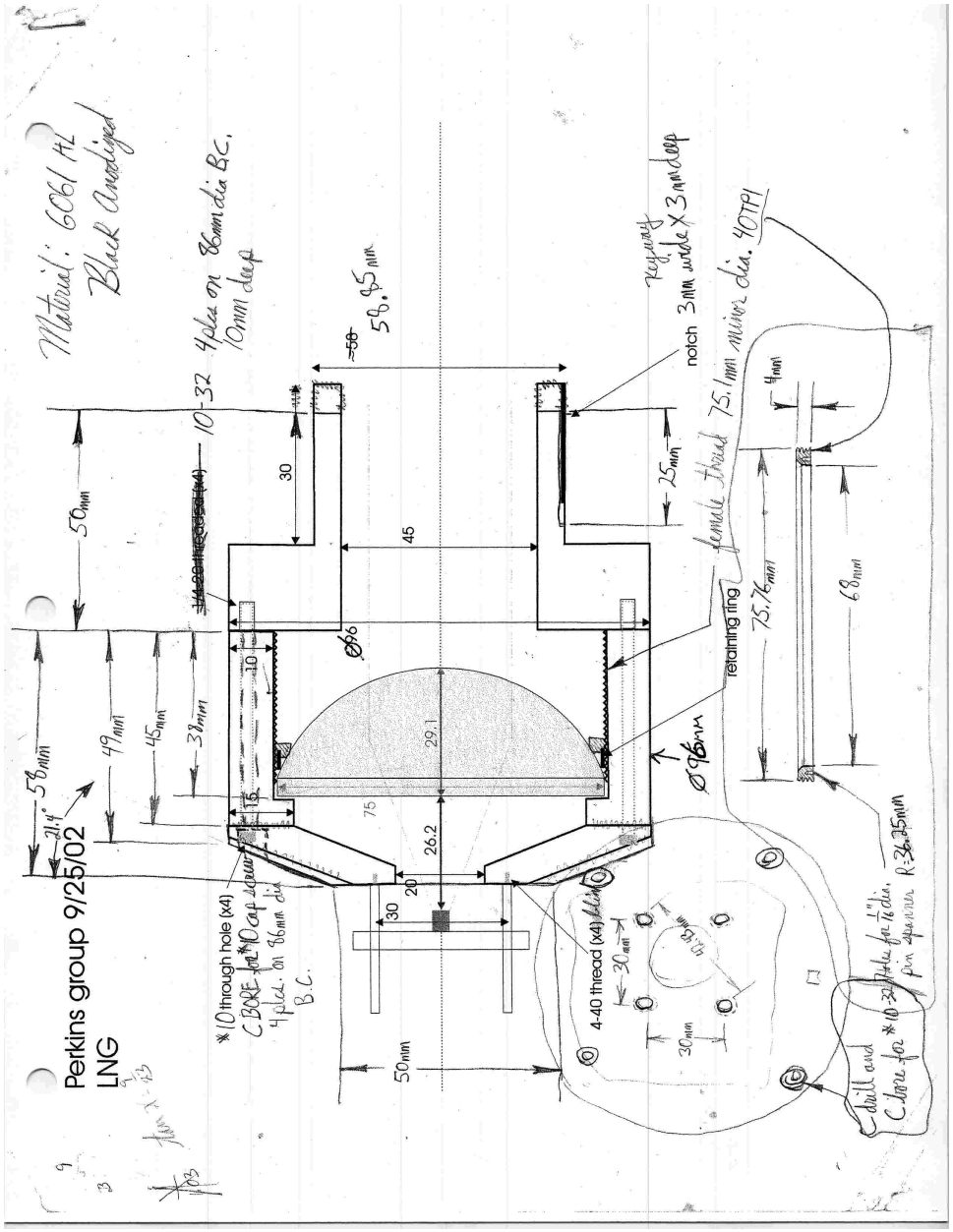

Figure D.31: Mercury lamp to liquid light guide mount part 1.

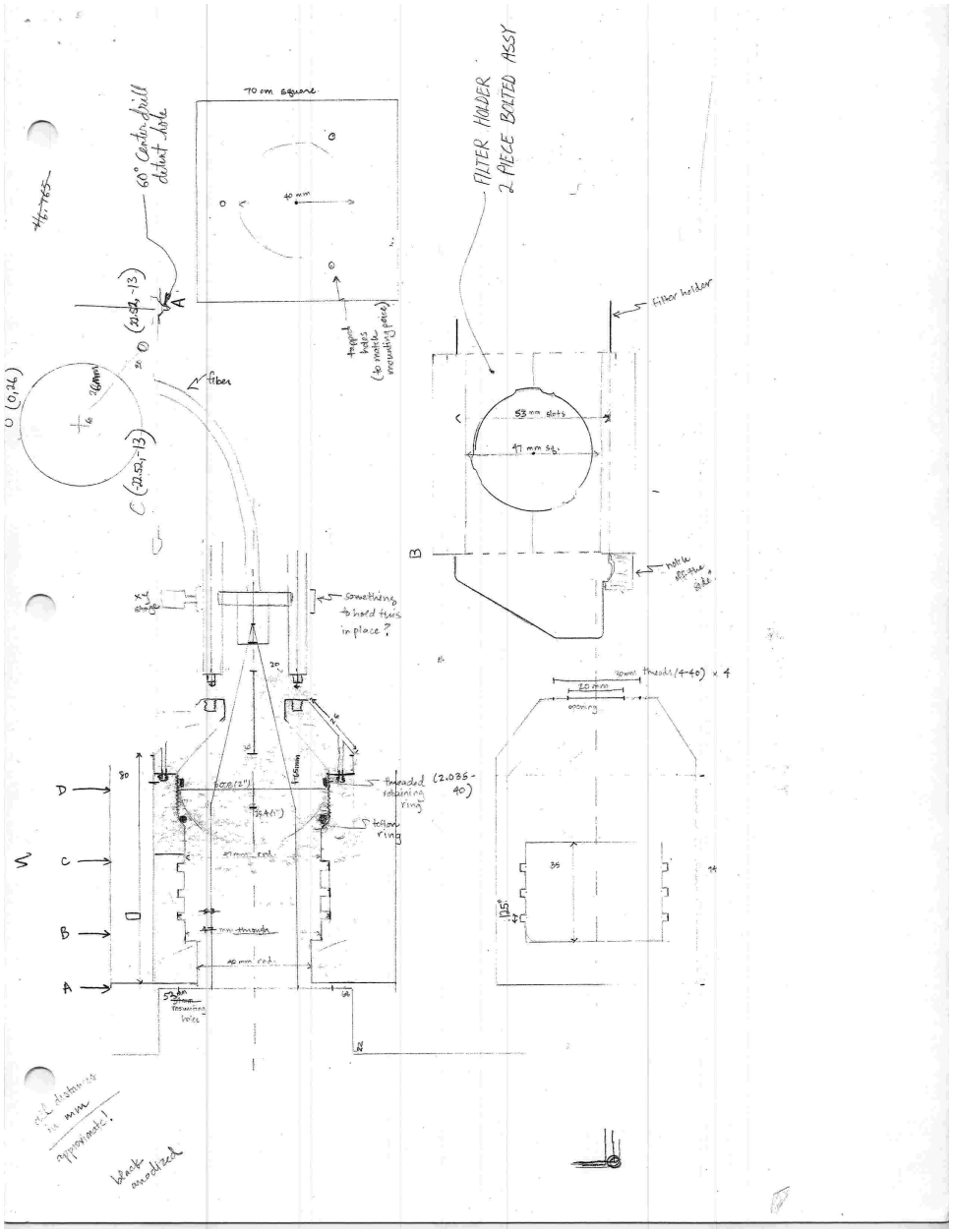

Figure D.32: Mercury lamp to liquid light guide mount part 2.

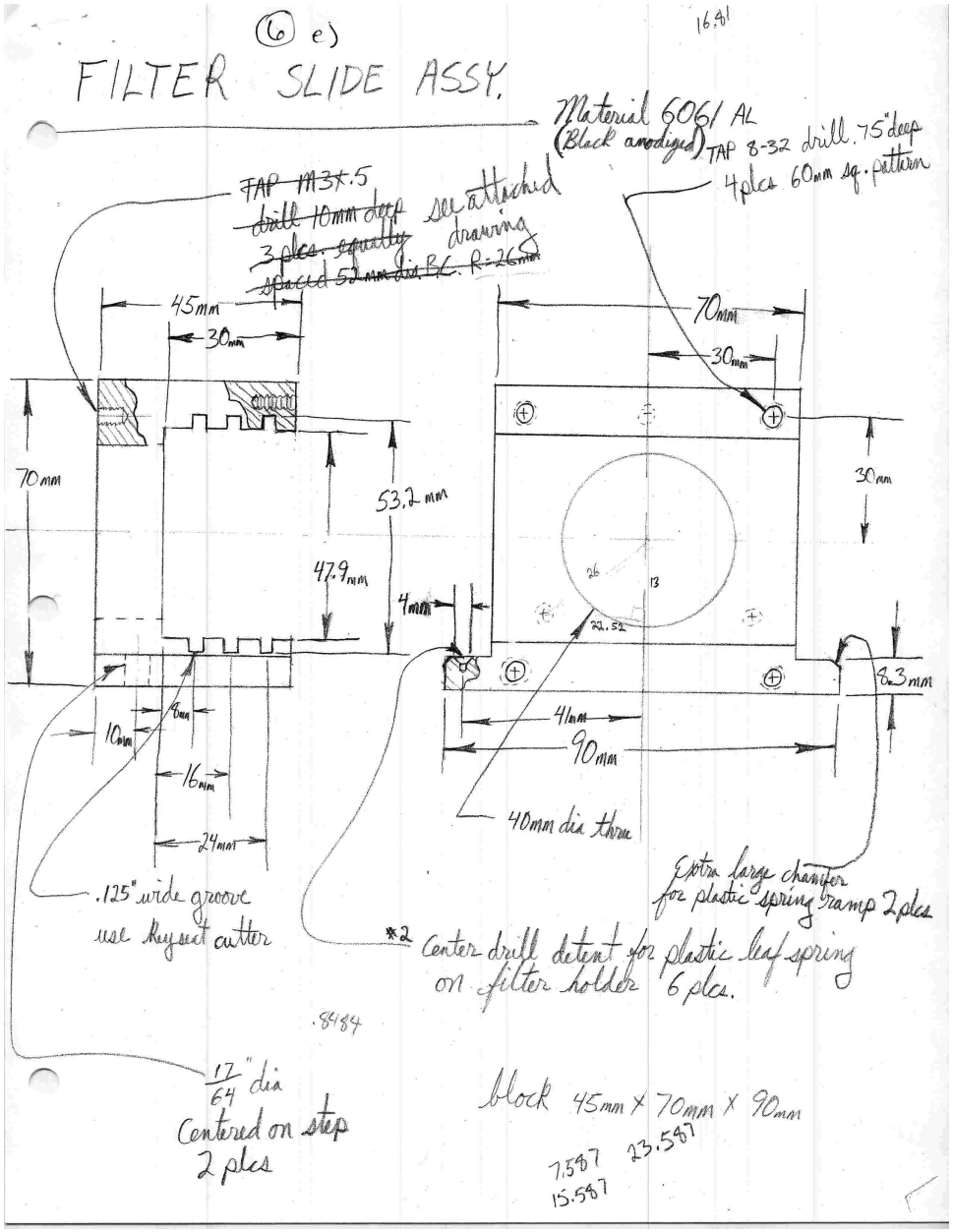

Figure D.33: Mercury lamp to liquid light guide mount part 3.

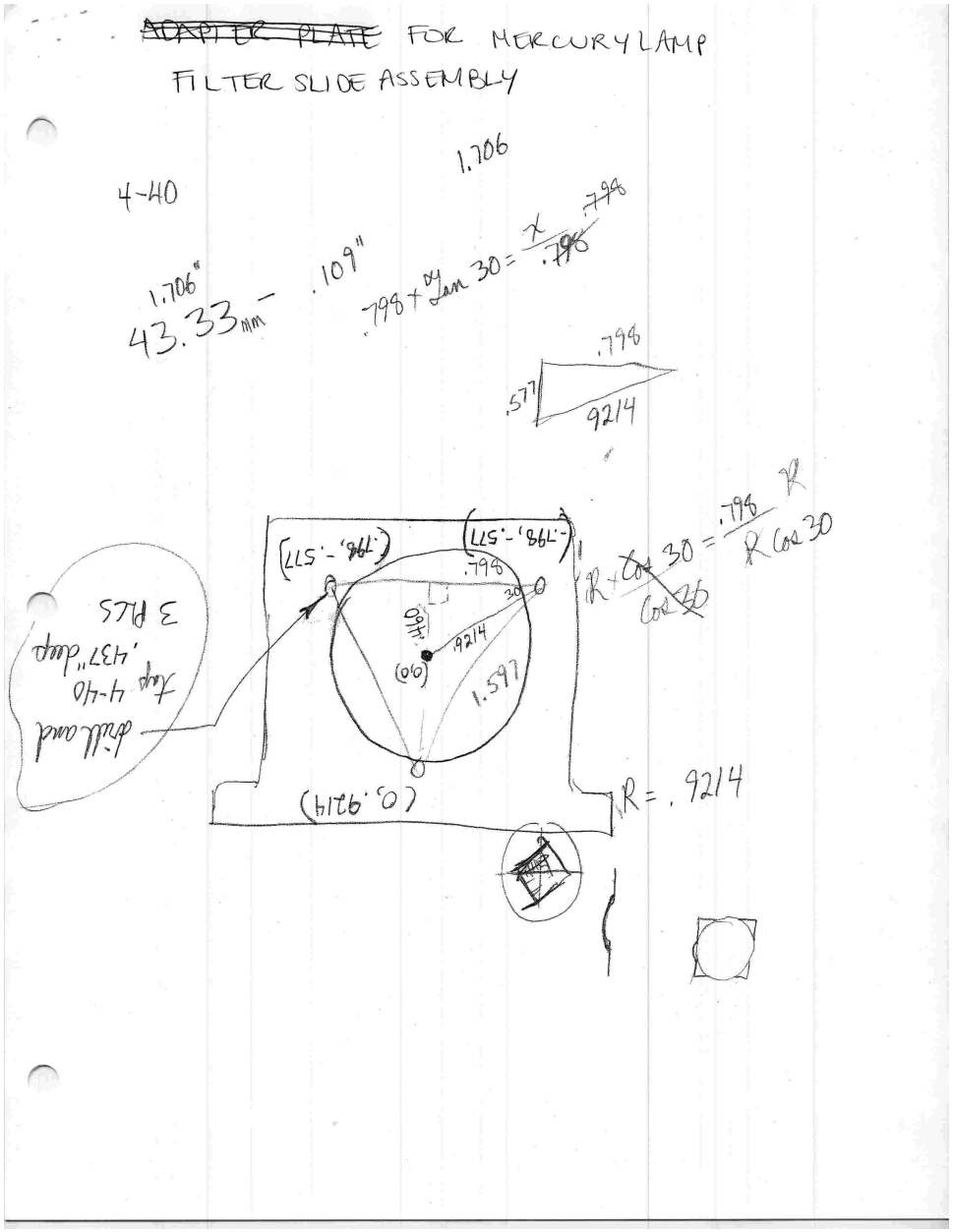

Figure D.34: Mercury lamp to liquid light guide mount part 4.

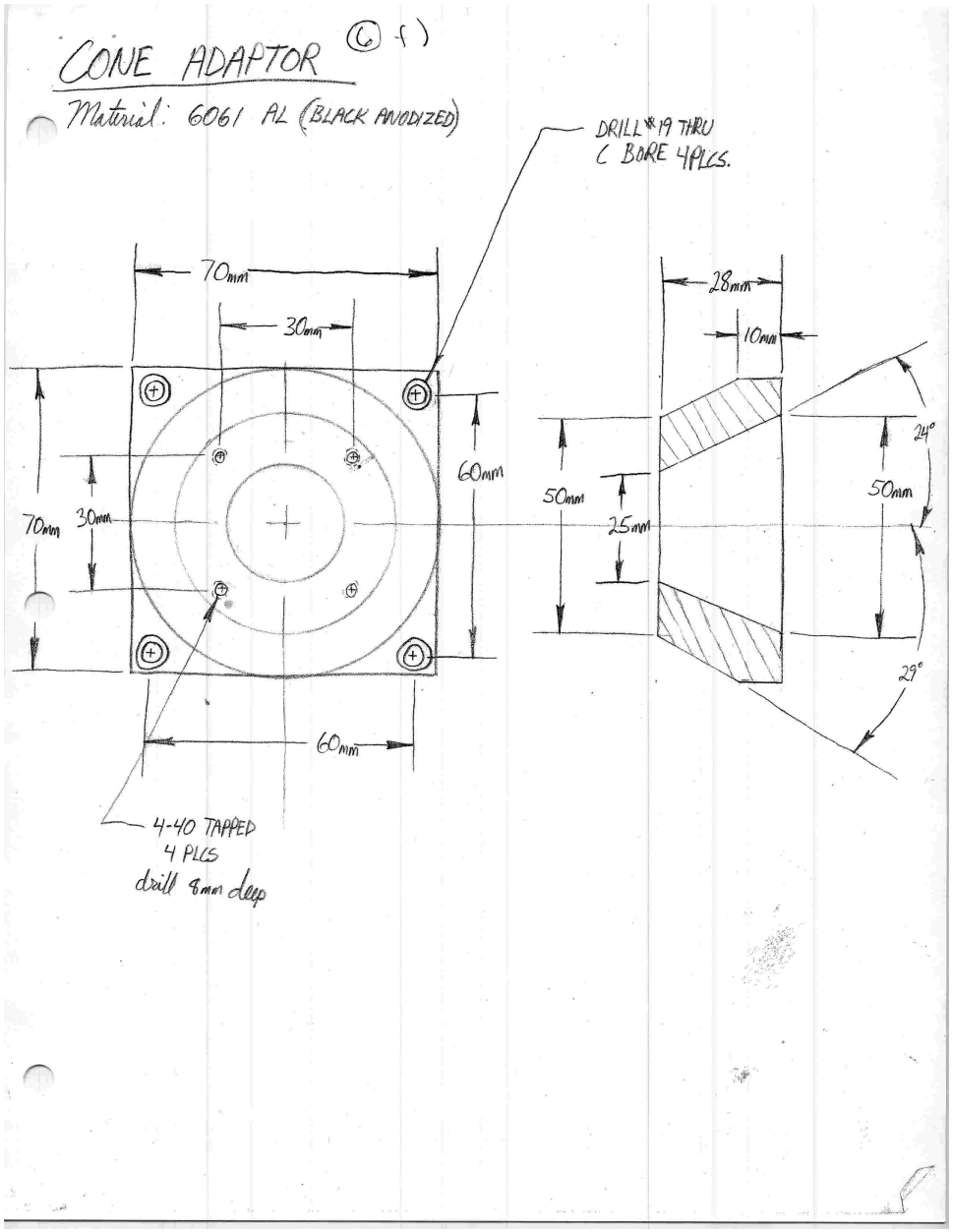

Figure D.35: Mercury lamp to liquid light guide mount part 5.

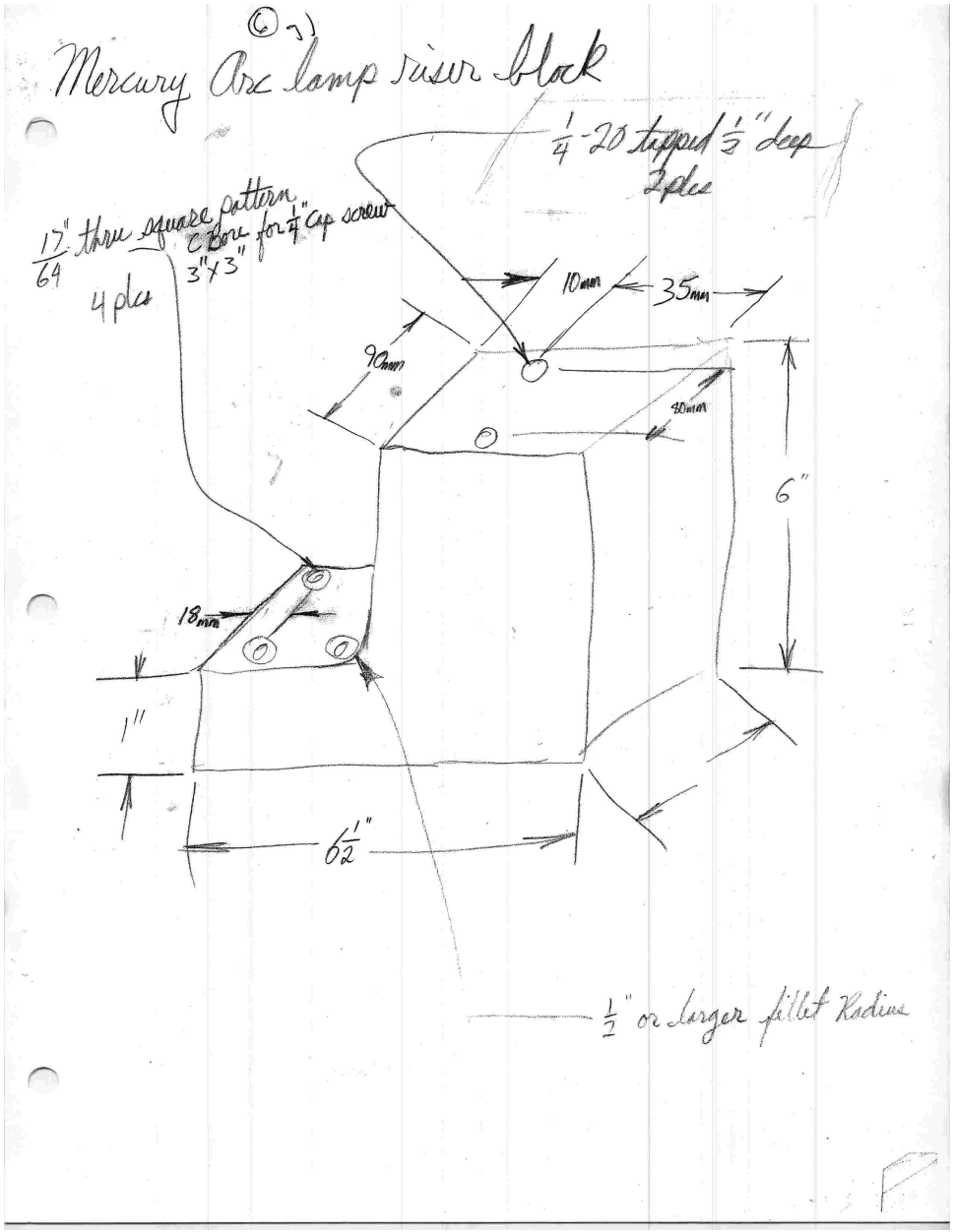

Figure D.36: Mercury lamp to liquid light guide mount part 6.

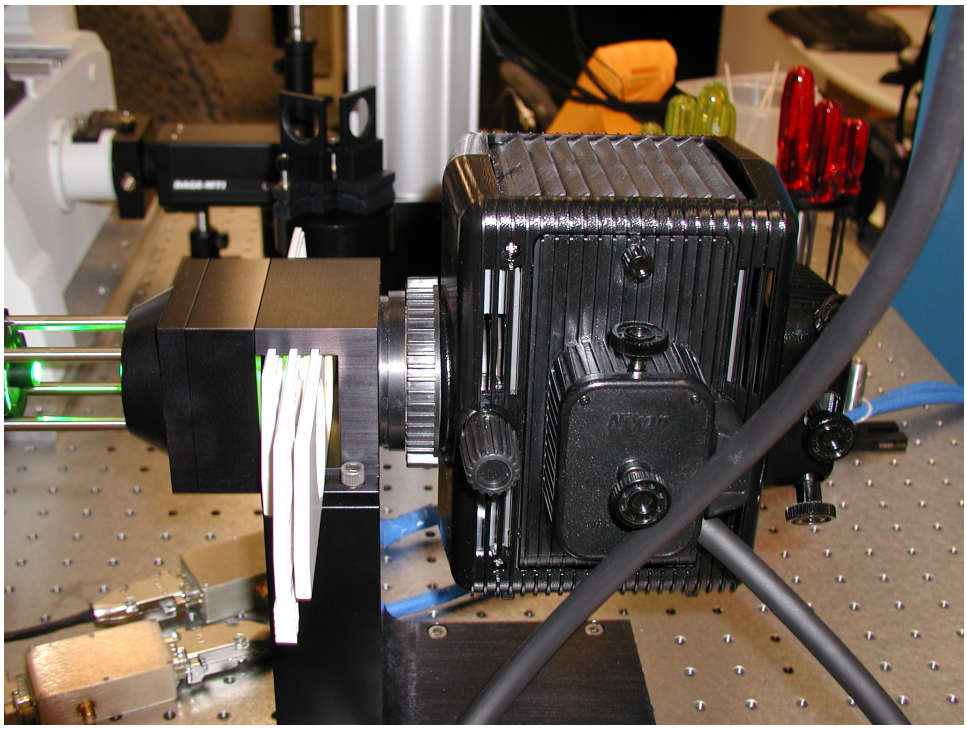

Figure D.37: Mercury lamp to liquid light guide mount picture.

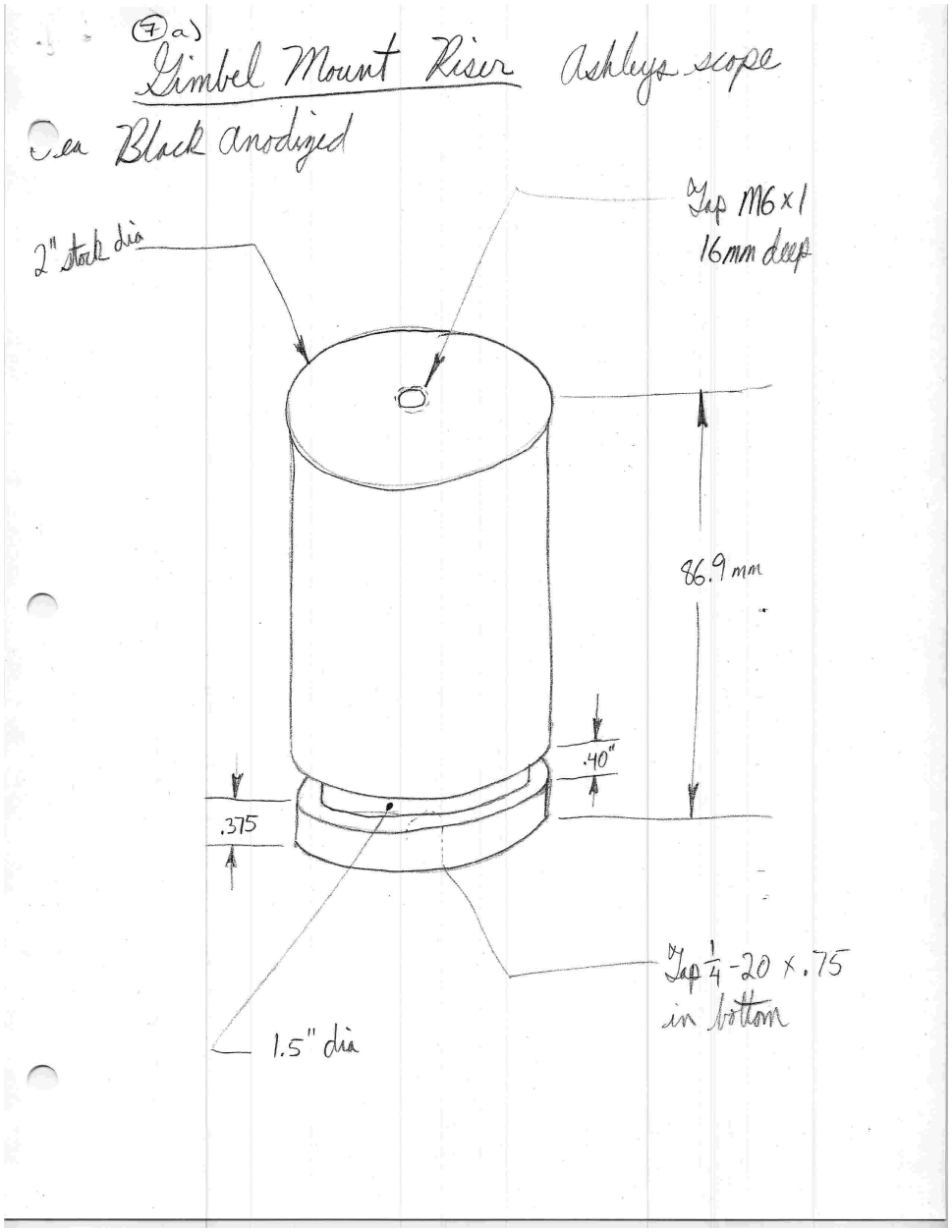

Figure D.38: Gimbal mirror mount part 1. The height is incorrect for the optical trapping experiment part 1.

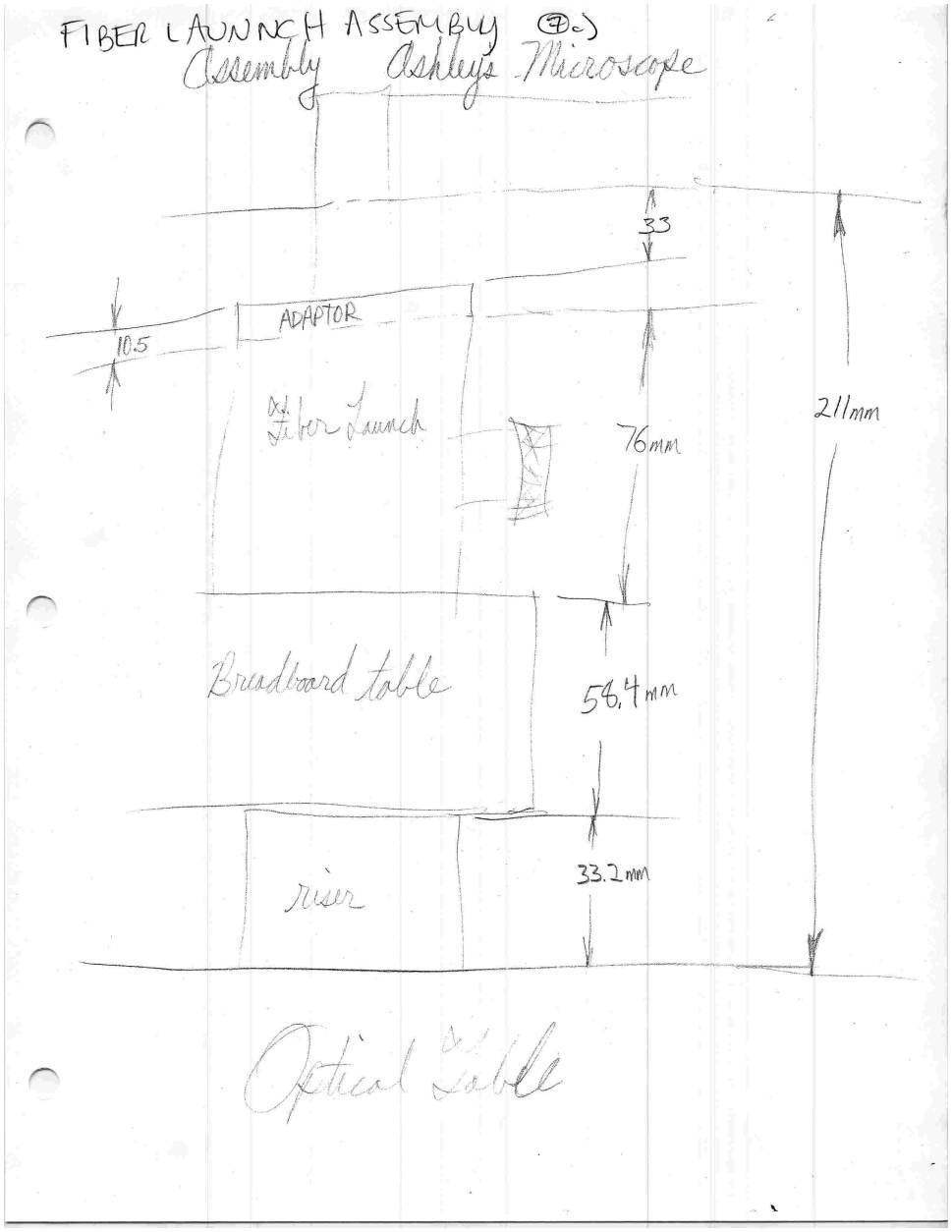

Figure D.39: Gimbal mirror mount part 2.

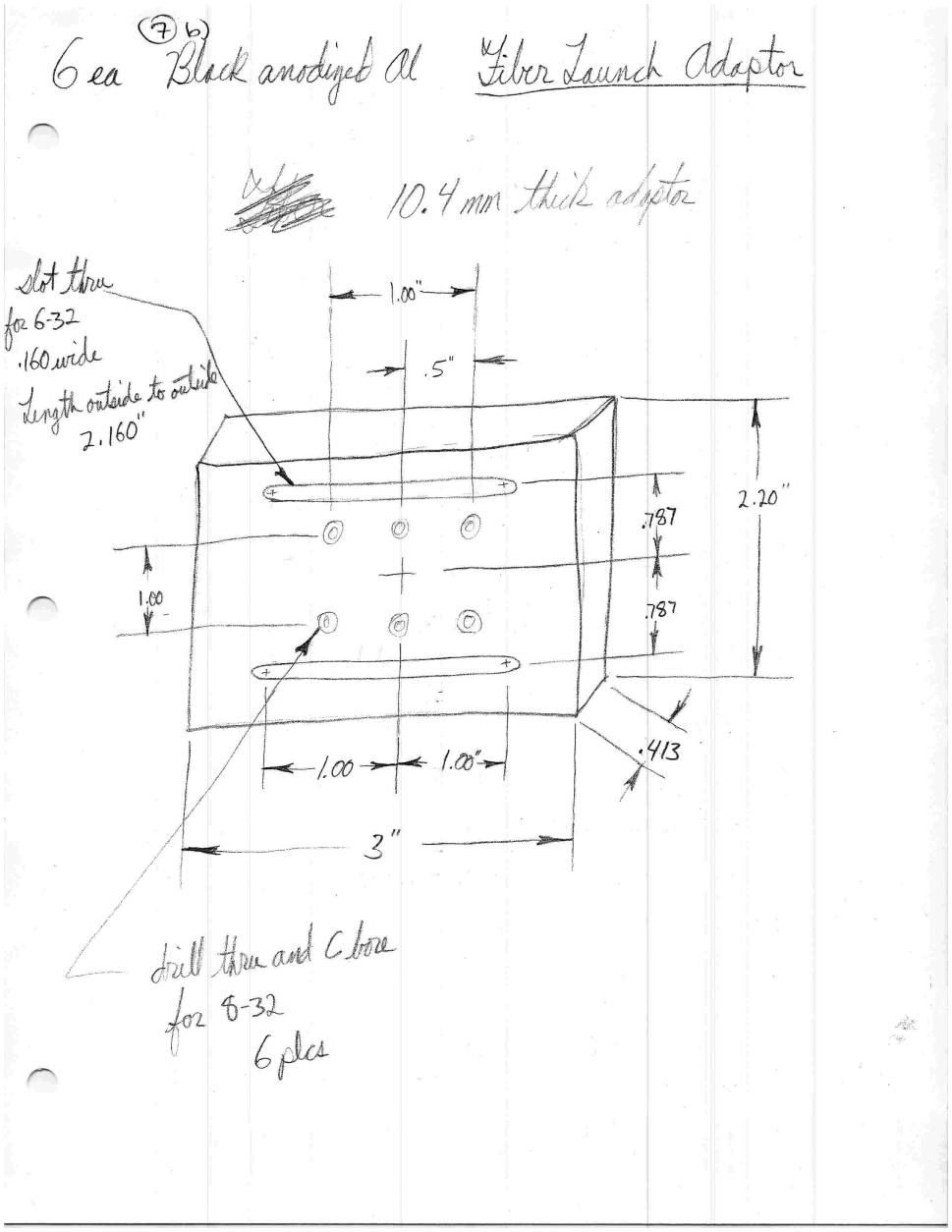

Figure D.40: Fiber launch to 3D translation stage adaptor.

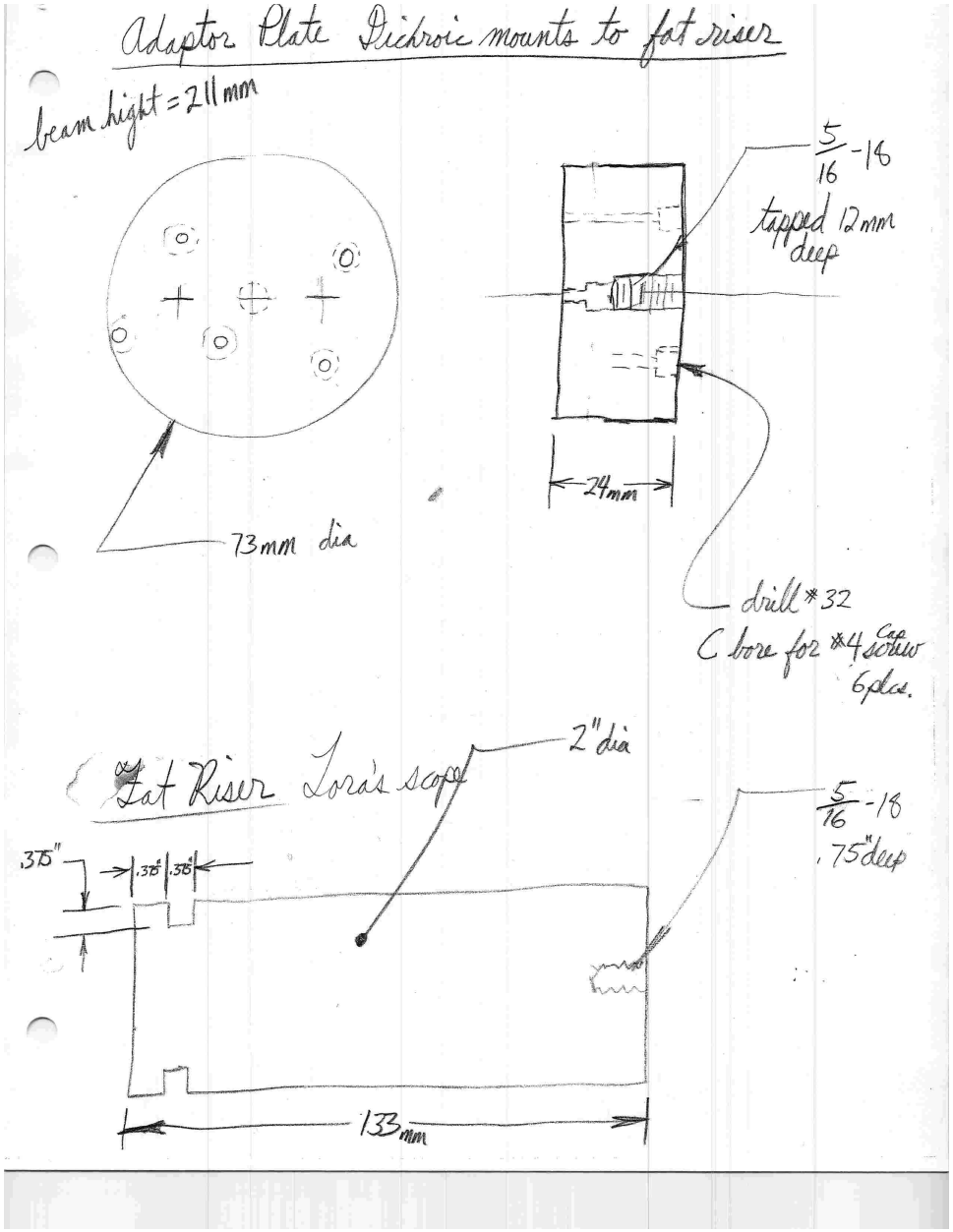

Figure D.41: Double dichroic mount part 1.

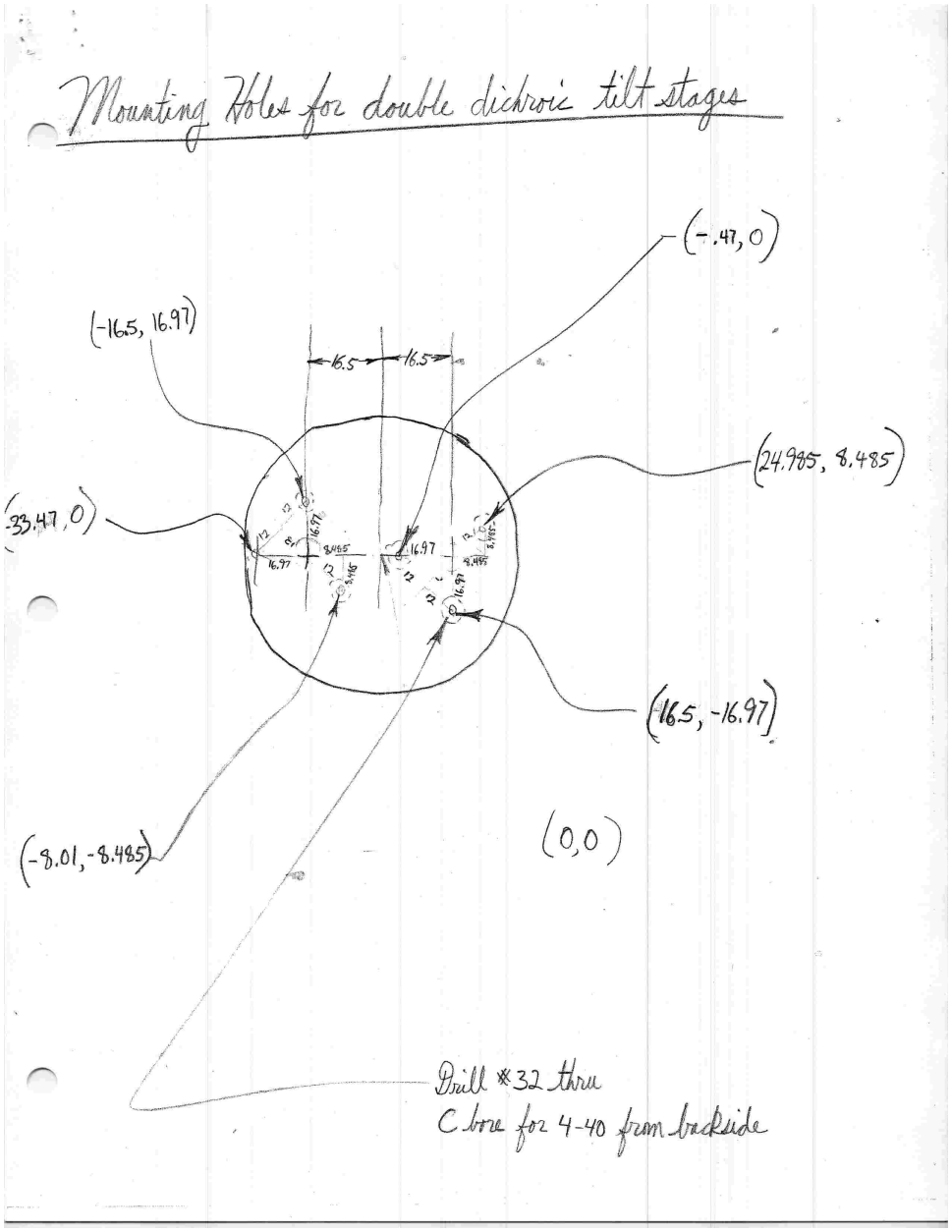

Figure D.42: Double dichroic mount part 2.

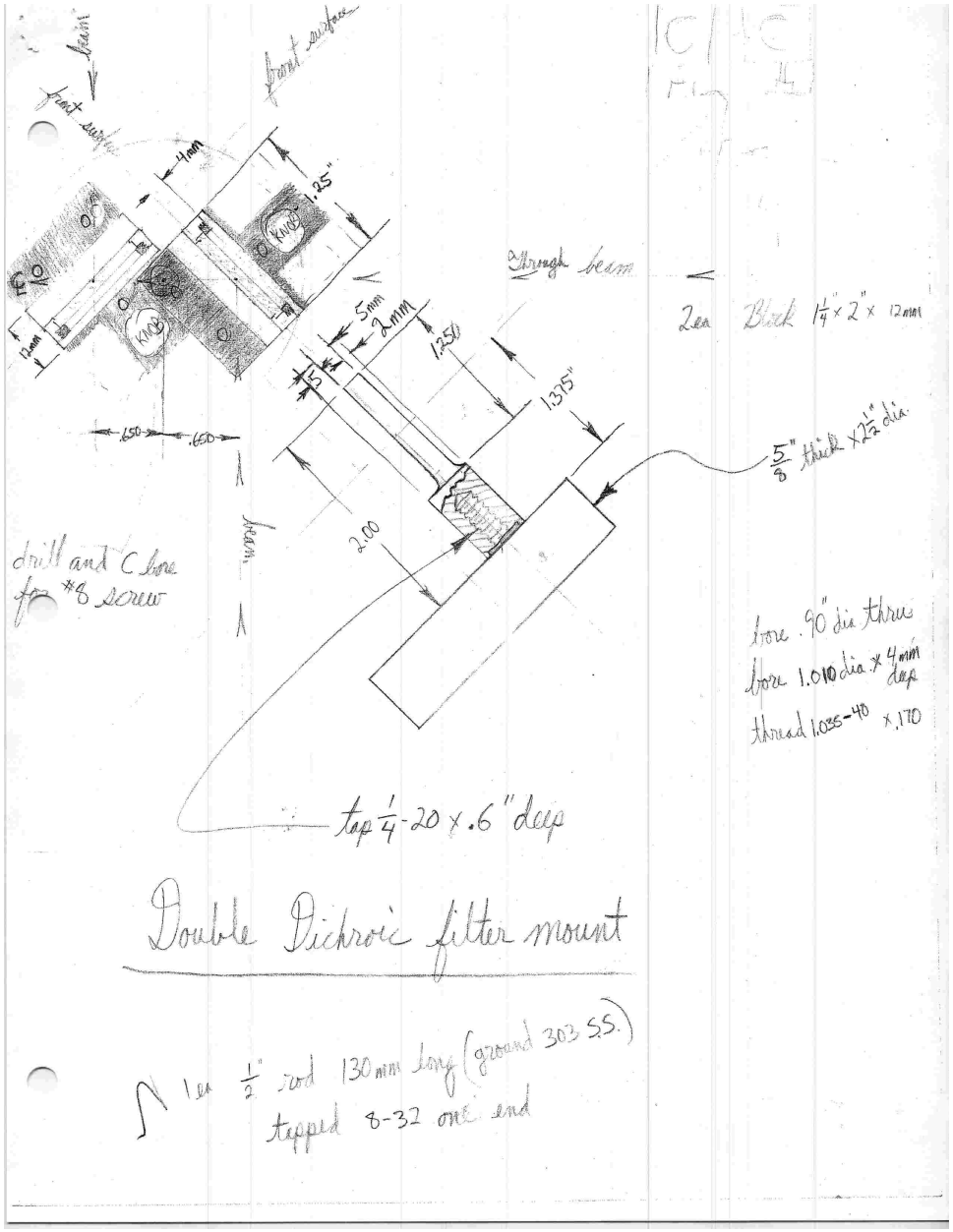

Figure D.43: Double dichroic mount part 3.

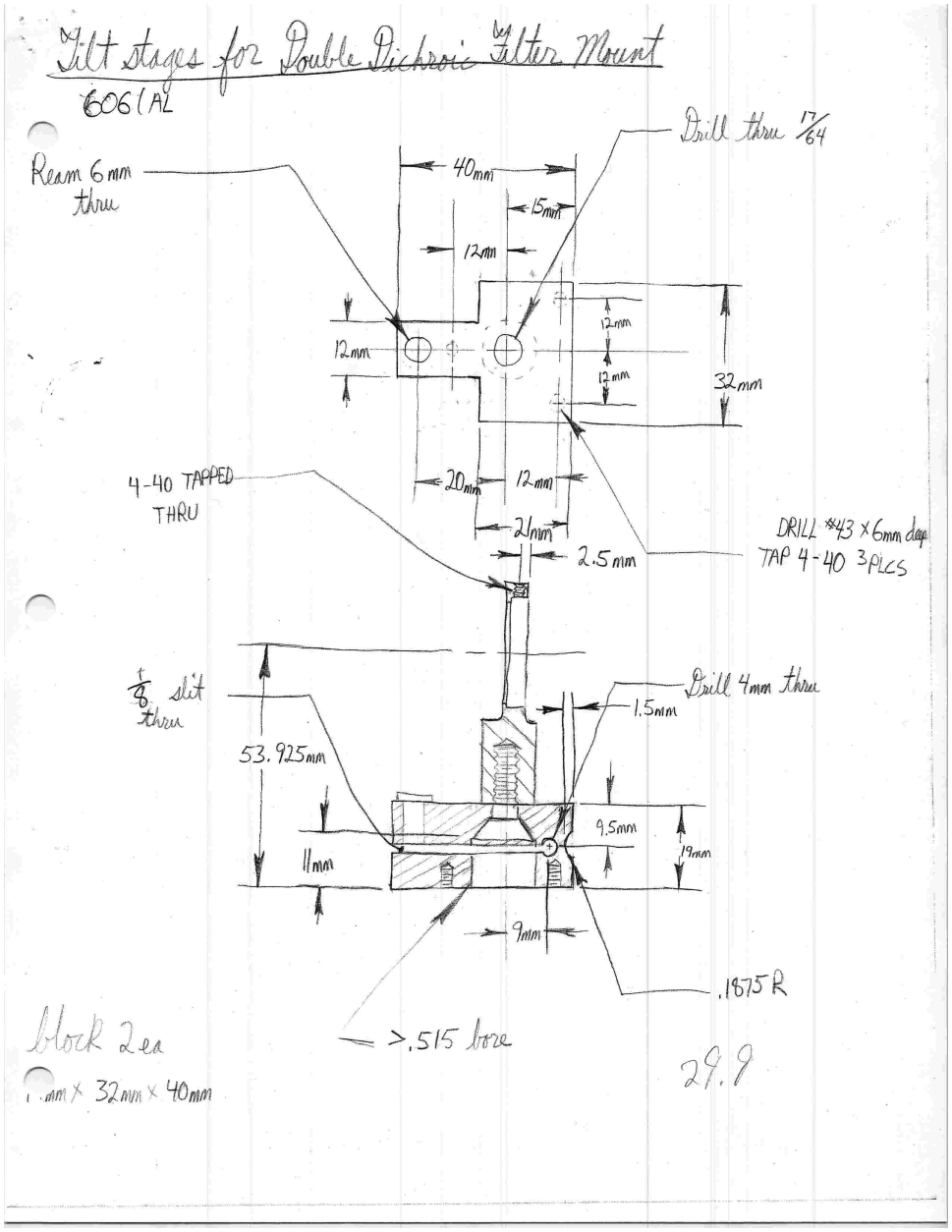

Figure D.44: Double dichroic mount part 4.

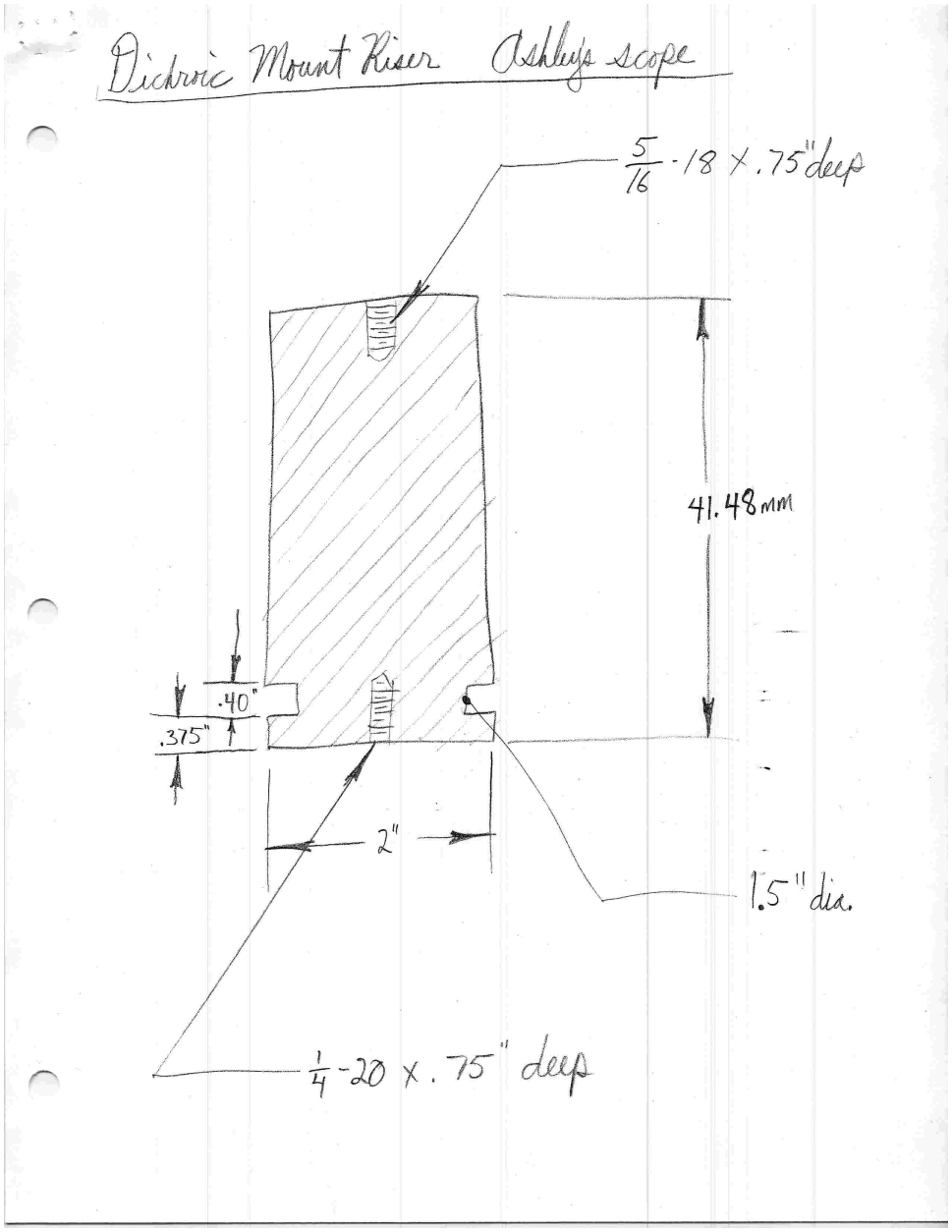

Figure D.45: Double dichroic mount part 5.

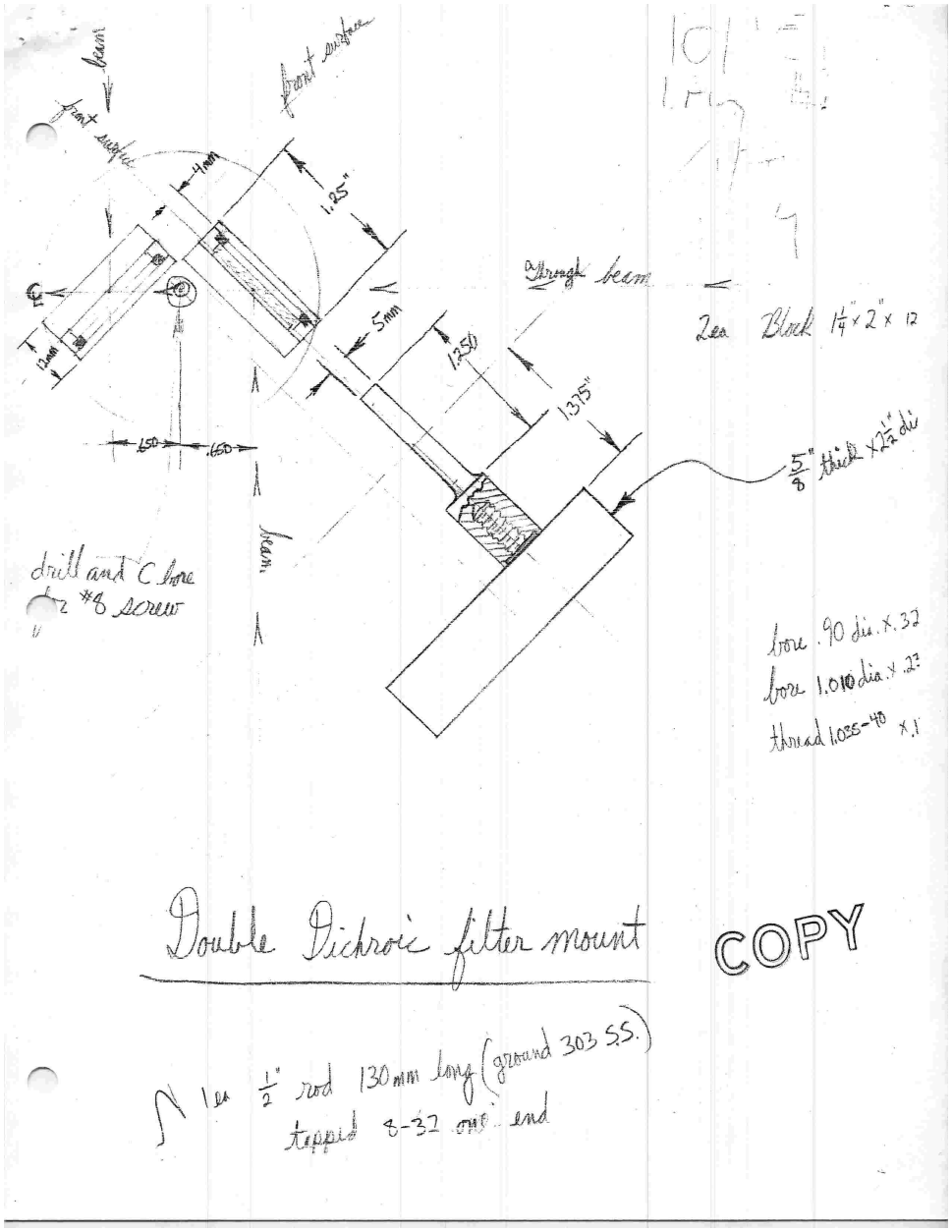

Figure D.46: Double dichroic mount part 6.

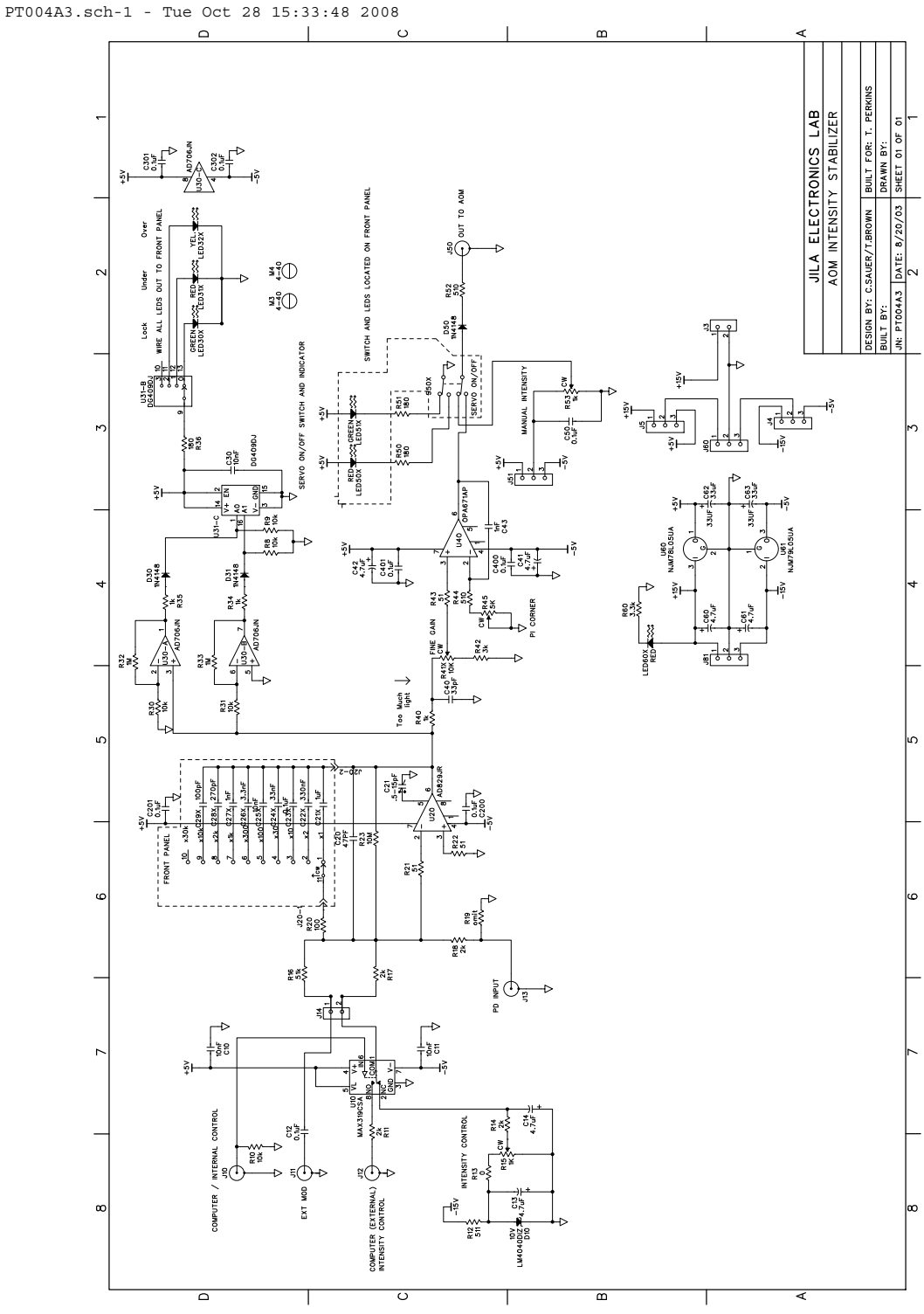

Figure D.47: Intensity servo electronic diagram.

Figure D.48: Intensity servo picture.

Appendix E

Protocol Index

This is a protocol index that lists detailed, step-by-step instructions for various preparations. Most protocols have been developed to prepare a biological assay. However, there are some protocols for how to use various instruments at JILA required in sample preparation and other protocols on how to do various procedures on our instrument. The protocols do not represent my original work, please see the Acknowledgements for a more complete reference. They are included for completeness.

E.1 Potassium hydroxide-clean cover slips

(1) Put on protective clothing: eyewear, lab coat, gloves, and close-toed shoes.

(2) Put small stir bar, 250 mL denatured ethanol, 80 g potassium hydroxide pellets into a 1 L washed beaker. Cover with parafilm.

(3) Put on stirrer. Set at medium stirring speed (slow enough so that there is no sloshing), no heat.

(4) Load cover slip basket with cover slips and attach handle.

(5) Fill Branson 5200 degasser quarter full with distilled water using autoclaved beaker.

(6) Place two 1 L washed beakers half full of distilled water in degasser.

(7) Place potassium hydroxide-alcohol solution beaker in degasser. Hold potassium hydroxide beaker down with tape. Turn on degasser power, but not heat.

(8) Using cover slip basket, place cover slips in solution for 3 min, and invigorate cover slips by moving basket up and down and side to side.

(9) Rinse cover slips over sink with distilled water squirt bottle.

(10) Place cover slips in beaker of distilled water in degasser for 3 min.

(11) Rinse over sink with distilled water again.

(12) Place in other beaker of distilled water in degasser for 3 minutes.

(13) Rinse over sink with distilled water and shake water off.

(14) Dry in microwave, checking ever 30 s or so to see if dry, usually 5 min.

(15) Place in plastic container and remove handle. Write the date on the plastic container.

(16) Repeat steps 8-14 for the rest of the cover slips, changing the distilled water in the beakers in the degasser every three baskets.

(17) Clean-up. Dispose of distilled water in sink, potassium hydroxide solution in organic hazardous waste, and clean empty beakers.

E.2 Piranha-clean cover slips

(1) Put on protective clothing: eyewear, lab coat, two pairs of gloves (nitrile and rubber), and closed-toed shoes.

(2) In the fume hood, Pour ∼400 mL piranha solution (15 drops hydrogen peroxide per 100 mL sulfuric acid) into a 1 L beaker and heat on a hot plate. Set at high heat so that piranha begins to slowly bubble. Do not get piranha too hot

as this is dangerous. The hood should be empty; make sure there are not any alcohols as this mixture is highly reactive.

(3) Load cover slip basket with cover slips and attach the long handle.

(4) Place cover slip basket in piranha for 10 min. There should be many small bubbles around the basket for a good etch. If not, add more hydrogen peroxide. Solution should be clear when etch is finished.

(5) Remove cover slip basket from piranha and place in 1 L beaker of distilled water. Turn off hot plate.

(6) Rinse cover slip basket in sink with distilled water for 1 min, followed by denatured ethanol for 1 min. Place in microwave for 2 min to dry.

(7) Remove piranha from hot plate and allow to cool. Once cool, pour the piranha into a teflon or glass container with a loose teflon lid. Store in secondary containment in fume hood. Piranha can be used multiple times.

(8) Clean used 1 L beakers.

E.3 Affix stuck beads

(1) Prepare 100X diluted 770 nm beads in distilled water.

(2) Prepare sodium bicarbonate solution (84–90 mg of sodium bicarbonate and 10 ml of distilled water). You don't need to measure it precisely.

(3) Mix 480 μL of sodium bicarbonate solution with 20 μL of beads. Vortex.

(4) Introduce this bead-solution to a preassembled sample chamber. Wait at least 10–20 min. Check under microscope to see if there are a decent number of stuck beads for your application.

(5) Wash out bead-solution from the sample chamber with 200 μL of 100 mM magnesium acetate, 10 mM Tris, and 100 mM potassium chloride. Wait at least 30 min.

(6) Dry out the sample chamber with ethanol (i.e., take 20 μL of ethanol and flow it through, sucking out all the liquid completely). This prevents clumping of stuck beads since the water surface tension is large enough to move the stuck beads if allowed to evaporate. Wait 10 min.

(7) Put the sample chamber in the oven at 110 °C for 13 min. Let cool for 30 min.

(8) Repeat last step three more times, but bake for only 7 min to avoid "pancake" stuck beads.

E.4 Fabricate HSQ fiducial marks

(1) Piranha clean cover slips for 10 min.

(2) Pre-bake on hotplate at 200 °C for 2 min.

(3) Spin HSQ on to cover slip at 1200 rpm for 60 s, make 1-μm-tall post.

(4) Post-bake on hotplate at 120 °C for 2 min and again at 200 °C for 2 min.

(5) Thermally evaporate 15 nm of aluminum on to cover slip. HSQ is sensitive to light and electron beams so the evaporation must be thermal and the cover slips should be covered when leaving the clean room.

(6) Use the scanning electron microscope to expose an array of dots. Use the run file to pattern a 1.5 mm X 1.5 mm array of dots with a diameter of 750 nm and a 15-μm spacing. Dosage is 450 μC/cm^2; current is 25 pA; voltage is 38 keV.

(7) Etch the aluminum in a solution with 80 mL phosphoric acid, 5 mL acetic acid, 5 mL nitric acid, and 10 mL distilled water for about 10 s or until aluminum

disappears. Rinse in distilled water and nitrogen dry.

(8) Develop HSQ in tetramethylammonium hydroxide (2% solution) for 10 min; the 25% solution is better and takes 2 min. Place in beaker of 9:1 isopropyl alcohol to tetramethylammonium hydroxide for 30 s, then in isopropyl alcohol, and finally, in distilled water. Rinse in distilled water and nitrogen dry. Check posts under microscope to see if development is complete. If not, repeat development.

(9) Cure in oven at 400 °C for 60 min. Cover slips will need to be placed in glass racks below oven in clean room; teflon will melt.

(10) Piranha clean cover slips for 10 min.

E.5 Fabricate silicon fiducial marks

This protocol can also be used as a guide to evaporation with the electron gun.

(1) Load sample holder with four masks and four cover slips. Load the masks so that the window is over the opening in the rubber pad. Load cover slips so they abut the alignment pins. Pull down the sample holder arm and lightly tighten the screw to clamp, do not touch the screw that holds the spring-loaded pad.

(2) Vent the evaporator by pushing “Vent”. Make sure the gate between the upper and lower chamber is open.

(3) Load the silicon crucible into the crucible holder. Push “Remote” to open shutter before installing crucible, then push “Remote” again to close shutter.

(4) Load sample holder into upper evaporator chamber. Unscrew the 8 pins that hold the side flange on and remove flange. Remove the thermal evaporator sample rod. Gently place the sample holder into the upper chamber and align to the flange screw holes. Screw the 8 pins into the sample holder. Place the flange off to the side.

(5) Close the upper and lower chamber door.

(6) Pump down the chamber by pressing "Cycle". Pump down to 10^{-7} Torr.

(7) Check program parameters. Density should by 2.32 for silicon; amount to deposit is 150 nm.

(8) Turn on electron gun. Make sure set to "1", then push "On/off" and wait for power light, and then press "Gun" and wait for gun light. Turn on current to 30 and slowly ramp it up. The crucible should glow red hot.

(9) Deposit material. Wait until crystal shows 1 nm/s and then push "Run". When 150 nm have been deposited turn gun current down to 30 and let sit for 1 min.

(10) Turn off gun. Press "gun" and then "On/off".

(11) To do another sample you only need to vent and pump the upper chamber. Vent the upper chamber by pushing "Gate close" and "Vent". Take out evaporator holder, load, and replace. Close the upper chamber door. Press "Rough" and wait until pressure is at $3X10^{-1}$. Press "Hi Vac" and wait for two clicks. Push "Gate open", "Reset", "Process", and wait until chamber pumps down to 10^{-7}. Then follow steps 7-10.

(12) Turn off when finished. Vent the upper chamber by pushing "Gate close" and "Vent". Take out evaporator holder and replace the flange. Close the upper chamber door. Press "Rough" and wait until pressure is at $3X10^{-1}$. Press "Hi Vac" and wait for two clicks. Push "Gate open", "Reset", "Vent", and the full chamber should vent. When vented take silicon crucible out of the lower chamber and replace rod. Pump down by pressing "Cycle". Make sure chamber pumps down to 10^{-7}.

E.6 Fabricate etched holes

Please see Theresa Ulrich's notebook for a more detailed procedure.

(1) Piranha clean cover slips for 2 min.

(2) Thermally evaporate 15 nm of chromium on to the bottom of coverslip.

(3) Spin isopropyl alcohol on the cover slip at 4000 rpm for 45 s.

(4) Pre-bake cover slip on hotplate at 180 °C for 20 min.

(5) Spin polymethyl methacrylate resist at 4000 rpm for 45 s.

(6) Post-bake cover slip on hotplate at 180 °C for 5 min.

(7) Thermally evaporate 15 nm of aluminum.

(8) Use the scanning electron microscope to expose an array of filled circles. Use the run file "perkdot4" to pattern a 2 mm X 2 mm array of filled circles with widths of 50 nm, 100 nm, and 150 nm and 6 μm spacing. Dosage is 350 μC/cm^2; voltage is 38 keV; current is 10 pA; magnification is 500X.

(9) Etch the aluminum in a solution with 20 mL distilled water and 3 mL sodium hydroxide (50% w/w) for about 10 s or until aluminum disappears. Rinse in distilled water and nitrogen dry. Sodium hydroxide solution can go down the drain with extra water.

(10) Develop the resist using 1:3 methyl isobutyl ketone to isopropyl alchohol for 3 min, 1:9 solution for 15 s, and distilled water for 30 s. Nitrogen dry. Check for holes in resist using microscope.

(11) Etch in buffered hydrofluoric acid. Wear neoprene gloves. Put 40 mL buffered hydrofluoric acid in 50 mL beaker with stir bar on stirrer at medium stir speed.

Dip coverslip in acid for an amount of time appropriate for the depth of hole needed (1 μm per min etch rate). Rinse in beaker of water for 30 s, rinse in sink, nitrogen dry.

(12) Remove resist. Heat "Nano Remover PG" to 60 °C (flash point is 88 °C). Hold cover slip over remover for 10 s to heat it up and prevent cracking, before placing in remover for 5 min. Rinse in beaker of water for 30 s, rinse in sink, nitrogen dry.

(13) Remove the chromium layer. Place in beaker of "Amtron ETC-212S chrome photomask etchant" (perchloric acid) until chromium disappears. Rinse in beaker of water for 30 s, rinse in sink, nitrogen dry.

E.7 Prepare DNA tethered particle assays

(1) Prepare 10 mL of WB. To a 15 mL falcon tube add: 8.45 mL distilled water, 250 μL 1 M Tris pH = 7.5, 10 μL 1 M magnesium acetate, 10 μL 1 M sodium chloride, 400 μL 10% Tween-20, 870 μL 35 mg/mL bovine serum albumin (filtered), 10 μL 1 M dithiothreitol. To make 10 mL 35 mg/mL bovine serum albumin add the following to a 15 mL falcon tube: 9.4 mL distilled water, 200 μL 1 M Tris pH = 7.5, 400 μL 10% Tween-20, 350 mg bovine serum albumin. Hand mix the bovine serum albumin solution and filter using a 10 mL syringe and a 0.2-μm filter.

(2) Vortex streptavidin bead stock.

(3) Add 30 μL streptavidin bead stock (408 pM 440-nm-diameter beads; 920 pM, 320-nm-diameter beads) to an eppendorf tube per 2 slides.

(4) Wash beads three times. Add 200 μL 0.4% phos-tween, centrifuge (400-nm bead, 5 min, 10 krpm; 500-nm bead, 5 min, 7 krpm; 320-nm bead, 2 min,

12krpm), and remove supernatant.

(5) Resuspend in 30 μL of WB (400-nm beads, 408 pM; 320-nm beads, 920 pM).

(6) Sonicate beads for 40 mins at 20 °C. Parafilm the tube before sonicating. Pulse mode (2 s on, 2 s off).

(7) In the mean time, make flow chambers and allow epoxy to dry.

(8) Once sonication is done, check beads for monodispersion. Dilute 1 μL of beads in 100 μL of WB. Flow through a slide and check under the microscope.

(9) Make 30 μL of 100 pM DNA in WB per two slides. If two dilutions are necessary, first dilution should be in 10 mM Tris (this dilution can be kept and used for weeks). For the second dilution, dilute into WB. This solution can be used that day.

(10) Mix 30 μL bead solution (400-nm bead, 408 pM; 320-nm bead 920 pM) with 30 μL 100 pM DNA per two slides. Mix by pipetting. Let sit for 60 min at room temperature.

(11) Concurrently, make 100 μL of 20 μg/mL anti-digoxigenin solution (90 μL 100 mM sodium phosphate buffer pH = 7, 10 μL of 200 μg/mL anti-digoxigenin full antibody) per 2 slides. Spin anti-digoxigenin stock and then mix by vortexing before using. Vortex final solution as well.

(12) Flow 50 muL per slide of 20 μg/mL anti-dig solution through slides. Sit for 60 min in humidity chamber at room temperature.

(13) Wash 2 times per slide with 200 μL WB. Sit for 10 min.

(14) Flow 30 μL of bead/DNA mixture per slide. Sit 60 min at room temperature.

(15) Wash 2 times with 200 μL of WB.

E.8 Prepare RecBCD assays

(1) Make flow chambers and allow epoxy to dry.

(2) Dilute 200 μL of 125 μg/mL biotinylated bovine serum albumin solution (195 μL 100 mM sodium phosphate buffer pH = 7, 5 μL of 5 mg/mL solution), which makes enough for 10 slides.

(3) Flow 20 μL per slide of 125 μg/mL biotinylated bovine serum albumin solution through slides. Sit for 20 min in humidity chamber at room temperature.

(4) Prepare 10 mL of WB. To a 15 mL falcon tube add: 8.45 mL distilled water, 250 μL 1 M Tris pH = 7.5, 10 μL 1 M magnesium acetate, 10 μL 1 M sodium chloride, 400 μL 10% Tween-20, 870 μL 35 mg/mL bovine serum albumin (filtered), 10 μL 1 M dithiothreitol. To make 10 mL 35 mg/mL bovine serum albumin add the following to a 15 mL falcon tube: 9.4 mL distilled water, 200 μL 1 M Tris pH = 7.5, 400 μL 10% Tween-20, 350 mg bovine serum albumin. Hand mix the bovine serum albumin solution and filter using a 10 mL syringe and a 0.2-μm filter.

(5) Wash 2 times per slide with 200 μL WB. Sit for 10 min.

(6) Make 300 μL of 10 μg/mL streptavidin solution (297 μL WB, 3 μL of 1 mg/mL streptavidin), which makes enough for 6 slides.

(7) Flow 50 μL per slide of 10 μg/mL streptavidin solution. Sit for 20 min in humidity chamber at room temperature.

(8) Concurrent with flow chamber preparation, begin preparing beads. Vortex streptavidin bead stock.

(9) Add 30 μL streptavidin bead stock (408 pM 440-nm-diameter beads; 920 pM, 320-nm-diameter beads) to an eppendorf tube per 2 slides.

(10) Wash beads three times. Add 200 μL 0.4% phos-tween, centrifuge (400-nm bead, 5 min, 10 krpm; 500-nm bead, 5 min, 7 krpm; 320-nm bead, 2 min, 12krpm), and remove supernatant.

(11) Resuspend in 30 μL of WB (400-nm beads, 408 pM; 320-nm beads, 920 pM).

(12) Sonicate beads for 40 mins at 20 °C. Parafilm the tube before sonicating. Pulse mode (2 s on, 2 s off).

(13) By this time the streptavidin solution incubating in the flow chamber should be done. Wash 2 times per slide with 200 μL of WB. Sit for 10 min.

(14) Make 600 μL of 15 nM biotinylated RecBCD solution (600 μL WB, 0.45 μL 10 μM or 34 μM biotinylated RecBCD).

(15) Flow 20 μL 15 nM biotinylated RecBCD solution. Sit for 2 hours in humidity chamber at room temperature.

(16) Wait for the bead sonication to finish. Once it is done, check beads for monodispersion. Dilute 1 μL of beads in 100 μL of WB. Flow through a slide and check under the microscope.

(17) Make 30 μL of 100 pM DNA in WB per two slides. If two dilutions are necessary, first dilution should be in 10 mM Tris (this dilution can be kept and used for weeks). For the second dilution, dilute into WB. This solution can be used that day.

(18) Mix 30 μL bead solution (400-nm bead, 408 pM; 320-nm bead 920 pM) with 30 μL 100 pM DNA per two slides. Mix by pipetting. Let sit for 60 min at room temperature.

(19) When biotinylated RecBCD is done incubating, wash 2 times with 200 μL of WB. Sit for 10 min.

(20) Flow 30 μL of bead/DNA mixture per slide. Sit for 40 min in humidity chamber at room temperature.

(21) Wash 2 times with 200 μL of WB.

E.9 How to guide: thermal evaporator

(1) Align sample (i.e. cover slips) on sample holder and affix with metal pins.

(2) Vent chamber with "Vent" button.

(3) Need to remove the electron beam gun and line the gun area with aluminum foil. Generally, Dave Alchenburger does this. Put a sign on the evaporator that says that thermal evaporation is underway.

(4) Insert the thermal crucible with what you would like to evaporate (e.g. one pellet of aluminum).

(5) Screw the sample rod into the upper chamber through the tube between the lower and upper chambers.

(6) Insert sample holder into the rod using an M6 screw and by holding the rod fixed from above the evaporator.

(7) Check quartz crystal to see if it needs replacing.

(8) Make sure the shutter is closed and on auto (push "S1" and "Remote" in).

(9) Close the door and pump down the chamber by pushing "Cycle". If the vacuum remains at 10^{-8} press "Cycle" again. Chamber pressure should decrease to 10^{-7}.

(10) Check system parameters: density (aluminum is 2.7), tooling (1.3), termination depth (15 nm).

(11) Heat crucible. Turn knob to "LT" and begin slowly increasing current. The outer surface of the material will melt and fall to the bottom of the crucible when it is time to evaporate. Be careful not to turn up the current too much because the material will wick around the side of the crucible and leak out.

(12) Press "Run" to start the evaporation. This should automatically open the shutter and the crystal will record the amount of deposition. Tune the current so that 1 nm of material per second is deposited. The shutter will automatically close when finished.

(13) Turn the current slowly down and move the knob back to "0". Wait until the chamber temperature reaches $\sim$40 °C to vent the chamber by pushing "Vent".

(14) Remove sample from chamber and insert the electron beam gun back into the chamber.

(15) Close the door and pump down the chamber by pushing "Cycle". If the vacuum remains at 10^{-8} press "Cycle" again. Chamber pressure should decrease to 10^{-7}.

E.10 How to guide: scanning electron microscope

(1) Make sure vacuum is sufficient (10^{-6} Torr). If not, fill trap with liquid nitrogen.

(2) Log on to computer. Turn on the "SEM Motion Controller" (stage software), "NPGS menu" (run file editor), and "Flashbus" (video) programs.

(3) Check instrument settings (see Figs. E.1, E.2, E.3, and E.4 for a detailed description of instrument. Turn on the chamber camera by flipping the unlabeled switch, unless sample is sensitive to light. Turn up the brightness and contrast on both monitors. Press "FAST" to switch to fast monitor updating. Bring up the "EOS menu" on the right monitor and the standard screen on the left monitor. Check the parameters on the "EOS menu" to see if correct; voltage = 38

keV, condenser lens coarse adjust = 8–10, magnification = 80–200X. Make sure the "SEM/NPGS" switch is in the "SEM" position. The filament knob should be all the way counter-clockwise and "Accel Voltage" should be off. Check that the manual stage knobs are at 25, 35, 39, for x, y, and z.

(4) Mount the cover slip on the machined cover slip holder so that the calibration standard is at the bottom. Wear gloves. Unscrew the clamps and push the cover slip against the alignment posts located on the right and bottom sides. Screw in the clamps. Screw in the sample loading stick.

(5) Load the sample. Insert the sample with the loading stick into the outer chamber. Press the white button which pumps down the outer chamber. Wait for two clicks (this when the roughing pump switches over to the fine pump). Open the outer chamber gate using the "open" knob, and slide the sample into the inner chamber stage. Unscrew the loading stick and detract it to the outer chamber. Close the gate and push the white button.

(6) Turn the z knob from 39 to 8, raising the sample. In the "EOS menu" change the working distance to 8 mm.

(7) Move the stage to a safe place on your sample or to the calibration standard using the "SEM Motion Controller". Should also be a place where there are features.

(8) Turn on the filament. To do this, turn on the "Accel Voltage". "Fila" button should be glowing green, if not press the button. Change the standard screen on the monitor to a line scan. Slowly turn up the filament current while watching the feature amplitude in the line scan. If there are not any features, check to see if the magnification is low enough (100X), the current is high enough (60 pA), and you are at the correct spot on your sample. The linescan amplitude

should increase, then decrease, then increase, and finally plateau. Leave the filament current right at the start of the plateau. Change the monitor back to the standard image screen.

(9) Tune the electron beam for high resolution images and writes. Find a feature on the surface and increase the magnification while tuning the focus knob. Once a feature is in focus at 70,000X, slowly turn the x and y astigmatism knobs to more clearly focus the image. The "Wobbler" will wobble the focus for easier tuning of the astigmatism knobs. When the beam is tuned, the feature will be sharp at 100,000X.

(10) Turn on the "PCD", which blanks the beam, and move to a location on your sample that is close to the write field. Turn off the "PCD" to image. Make sure that a feature is still in focus at 100,000X.

(11) Turn on the "PCD" button and move to the center of the cover slip or the start of the write field.

(12) Set the correct probe current for the write (10-12 pA).

(13) Set the correct magnification for the write (500X).

(14) Switch "SEM/NPGS" to "NPGS".

(15) Switch "Beam Blanking" to "EXT".

(16) Turn off the "PCD".

(17) Select the correct run file in the "NPGS menu" and push start. The pattern will begin writing.

(18) Once the writing is done, turn off the beam. Slowly turn the filament knob to the full counter-clockwise position. Turn off "Accel Voltage". Return the "SEM

Motion Controller" to absolute home. "Beam Blanking" to off. "SEM/NPGS" switch to "SEM". Turn off "PCD".

(19) Remove the sample. Move the z manual knob to 39. Reverse load the sample. Unscrew the clamps to remove the cover slip from the sample holder.

(20) Shut down the instrument. Clear both monitors and turn the contrast and brightness down. Turn off the camera. Press "PF5".

E.11 How to guide: fiber alignment

(1) Using the translatable lens or an imaging system collimate the free-space laser beam at a diameter that would produce a focal beam width that matches the core diameter of the fiber. Typically beam diameters can be selected to match either the numerical aperture of the fiber or the core diameter. We match the core diameter to minimize the effects of beam translations while still maintaining reasonable power efficiency through the fiber.

(2) Without the fiber attached to the fiber mount, maximize the output power through the mount using the mirrors.

(3) Attach a fiber-coupled laser to the fiber mount such that the fiber-coupled laser beam is output where the free-space laser beam is input. Move the fiber mount tip, tilt, and axial stage such that the fiber-coupled laser beam aligns with the input free-space laser.

(4) Disconnect the fiber laser from the mount and connect the fiber, measuring the light out of the fiber with a power meter.

(5) If there is not any measurable output light recheck steps 2–4.

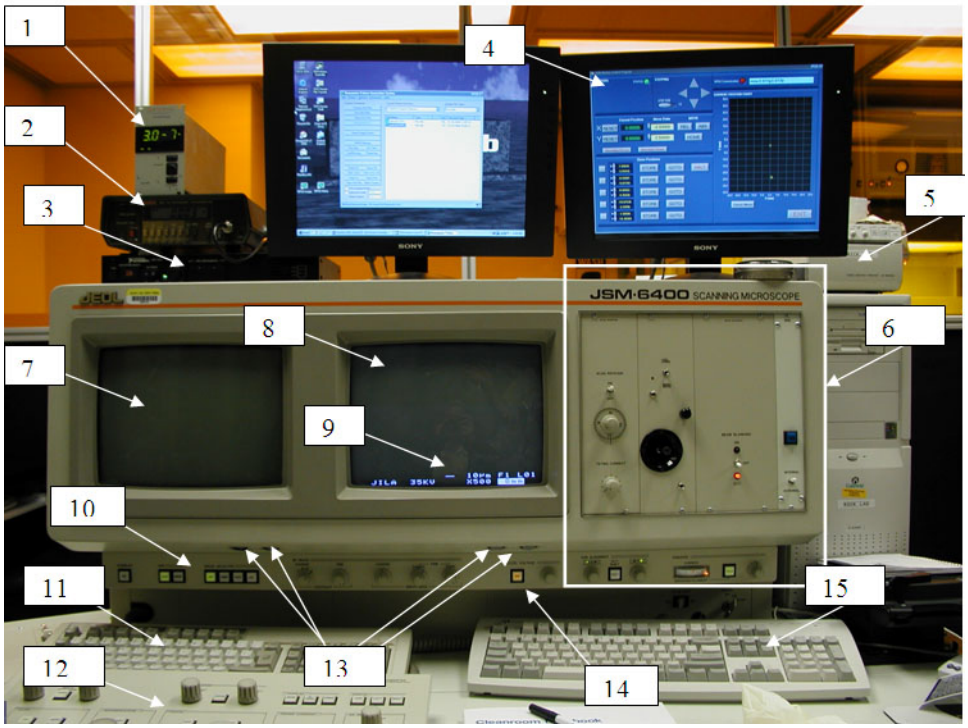

Figure E.1: Scanning electron microscope (SEM) display and controls. (1) Vacuum inside the specimen chamber. (2) Current in nA. (3) Enable switch. (4) SEM Motion Controller Program. (5) Printer for SEM images. (6) Portion of the SEM auxiliary control panel. (7) Analog monitor. (8) Digital monitor. (9) The "standard display" on a monitor. (10) Auxiliary control panel. (11) SEM control keyboard. (12) Primary control panel. (13) Brightness and contrast dials for the analog and digital monitors. (14) "ON" button for ACCEL VOLTAGE. (15) SEM computer keyboard. Figure credit: Theresa Ulrich.

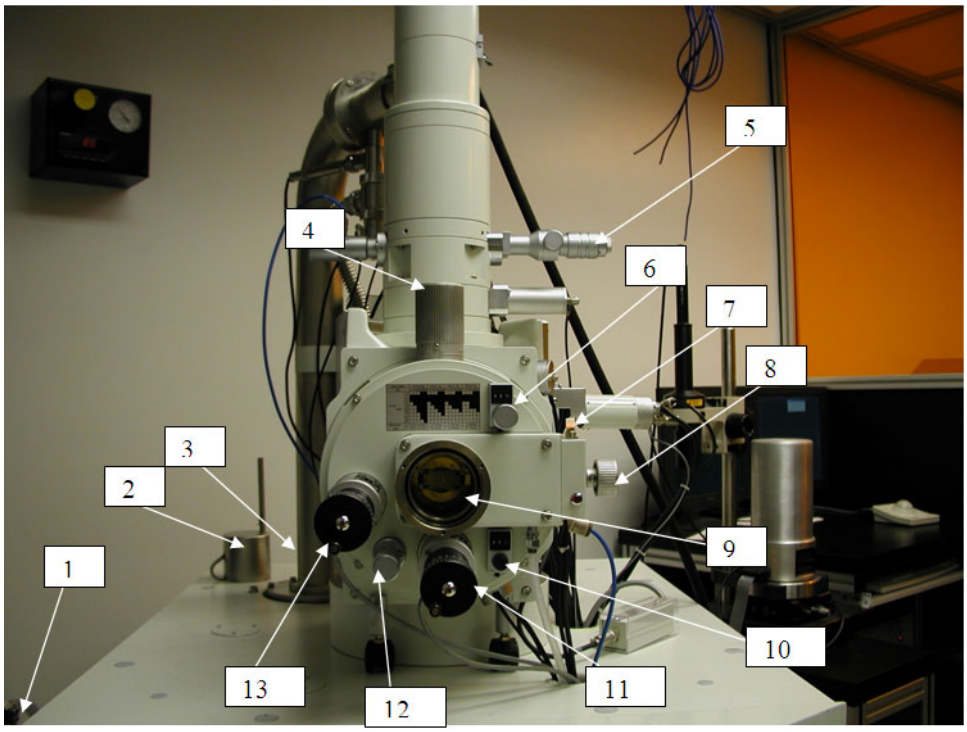

Figure E.2: SEM column. (1) Dewar for liquid nitrogen sits on the floor here. (2) Funnel for liquid nitrogen. (3) Location of small pipe that gets filled with liquid nitrogen. (4) Coarse z control for the stage. (5) Condenser controls. (6) Tilt controls. (7) White button to push when loading a sample. (8) "Open" knob for opening the gate into the specimen chamber. (9) Outer chamber for initial loading of sample. (10) Rotation controls. (11) x control. (12) Fine z control. (13) y control. Figure credit: Theresa Ulrich.

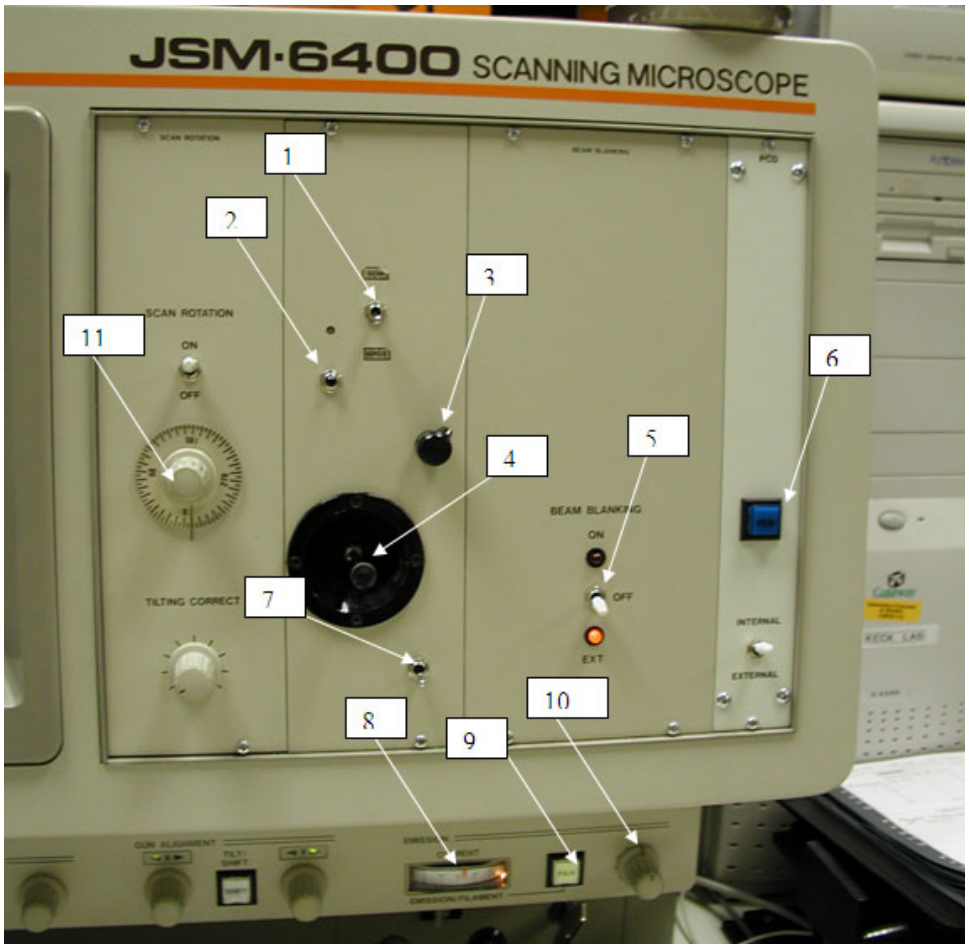

Figure E.3: SEM auxiliary control panel. (1) SEM/NPGS switch. (2) Press this button to see your pattern writing on the analog screen. (3) Speed control for the joystick motion controller. (4) Joystick motion controller. (5) Beam blanking switch. (6) PCD button. (7) Chamber View System switch to turn on the camera. (8) Filament gauge, lit on the right side. (9) Filament button. (10) Filament knob. (11) Scan Rotation knob. Figure credit: Theresa Ulrich.

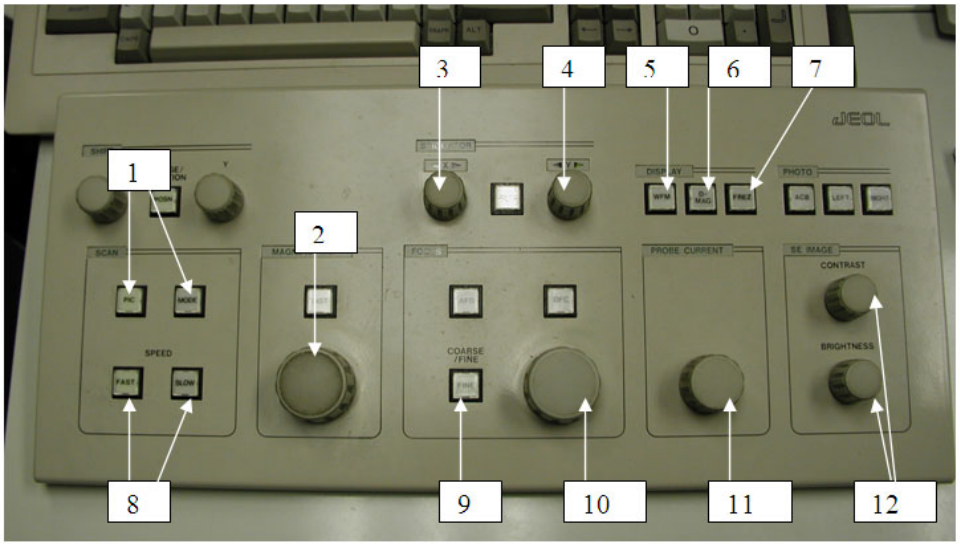

Figure E.4: SEM primary control panel. (1) PIC and MODE buttons, useful during filament saturation. (2) Magnification knob. (3) x astigmatism knob. (4) y astigmatism knob. (5) WFM button, useful for checking brightness and contrast values. (6) D-MAG button, useful for focusing at high magnification. (7) FREZ button, useful for freezing the screen. (8) Speed controls to change scan rate from FAST to SLOW. (9) Coarse/Fine switch for the focus knob. (10) Focus knob. (11) Probe Current knob. (12) Brightness and Contrast knobs. Figure credit: Theresa Ulrich.

(6) Translate the fiber mount axially by turning the three z screws equally. The measured power should reach a maximum value and then decline, go through the maximum and then back to it.

(7) Move the fiber mount in x and y in tiny increments until the power is maximized; do not move more than one turn and do not touch these screws again.

(8) Begin moving the three z screws individually and in order while maximizing the power each time. Two screws you will not have to turn very much, while the third screw, the "magic" screw, will be rotated more. This is because the fiber is angle-cleaved and the "magic" screw is tilting the mount to accommodate for this angle.

(9) Once the power has reached 10% of the input value begin adjusting the two mirrors individually and in order along with the three fiber mount z screws.

(10) Once the power has reached ∼70% of the input power begin translating the lens in small increments while adjusting the mirror and fiber screws to maximize the power at each lens position. This should experimentally determine the width of the beam at the fiber input. Once this procedure is done there should be ∼80% of the input light at the fiber output. One important note: do not get frustrated, sometimes things have to get worse before they get better.

E.12 How to guide: intensity servo tuning

(1) To tune the servo, the fine and coarse gain along with the proportional-integral corner were turned all of the way down. For this intensity servo the proportional-integral corner is somewhat of a misnomer since the corner is really between a single integral (20 dB per decade) and a double integral (40 dB per decade).

(2) The in-loop photodiode voltage was T-ed off to an electronic spectrum analyzer

operating over the bandwidth of 0–1 MHz.

(3) While monitoring the noise using the electronic spectrum analyzer, the coarse gain was turned up until the system began to oscillate and then backed off.

(4) Step 3 was then repeated with the fine gain and, finally, the proportional-integral corner.

(5) To further make sure the system wasn't oscillating, the photodiode output voltage was checked using an oscilloscope.

(6) When finished, the spectrum analyzer should show a noise peak at the bandwidth of the feedback loop (200 kHz for all three lasers), and a measurement of the noise level should reproduce the quoted values in Section 2.1.4.